Synthesis of Multi-Segmented TiO_2/Pt Nanorods for Photocatalytic Hydrogen Production

Gladys Teo Yanru

2014

Supervised by Prof. Jason D. Riley and Prof. Mary P. Ryan

A thesis presented for the degree of Doctor of Philosophy in the Department of Materials of Imperial College London and the Diploma of Imperial College London

I, Gladys Teo Yanru, declare that the work presented in this thesis is my own. Where information has been derived from other sources, I confirm that this has been indicated in the thesis.

The copyright of this thesis rests with the author and is made available under a Creative Commons Attribution Non-Commercial No Derivatives license. Researchers are free to copy, distribute or transmit the thesis on the condition that they attribute it, that they do not use it for commercial purposes and that they do not alter, transform or build upon it. For any reuse or redistribution, researchers must make clear to others the license terms of this work.

Abstract

Photovoltaic modules are under active consideration as a major contributor to future energy requirements. Coupled with an electrolyzer, this energy system converts energy harvested from the sun into chemical power. As the demand for a sustainable yet efficient and cost effective approach of producing hydrogen increases, researchers are seeking ways to improve the technology of forming solar fuel. Mimicking the idea of how nature collects and stores solar energy in chemicals bonds through photosynthesis, economically viable water splitting cells capable of splitting water directly at the semiconductor surface are being developed. The catalytic semiconductor is designed to be both a light absorber and an energy converter to store solar energy in the simplest chemical bond, H_2, thereby eradicating significant fabrication and system costs involved with the use of separate electrolyzers wired to photovoltaic cells.

In this work, water-splitting materials have been designed to consist of multi-component nanorods of titanium dioxide and platinum with well-defined nanostructures to function as photocatalytic cell for hydrogen production. As the TiO_2-Pt nanorods are irradiated with light in the presence of a water source, oxygen and hydrogen are evolved at the anode TiO_2 and cathode Pt segments of the nanorods respectively. The alternating segments of TiO_2 semiconductor and Pt metal enable the control of the direction of charge movement and light absorption pathways in the material, thereby presenting a solution to improving the overall efficiency of photocatalytic hydrogen production.

By employing templated electrodeposition, homogeneous multi-segmented TiO_2/Pt nanorods have been successfully fabricated in anodic aluminium oxide membrane (AAM). This simple method of synthesis permits an easier control of the position and composition of TiO_2 and Pt along the length of the nanorods, which allows for a customizable and highly reproducible method of obtaining segmented rods with uniformly distributed active sites for efficient catalytic activity. The morphology and material composition of the as-prepared Pt-TiO_2 multi-segmented nanorods were characterized using the scanning electron microscope (SEM), transmission electron microscope (TEM) and the x-ray diffraction (XRD); and the photocatalytic properties of these multi-segmented TiO_2/Pt nanorods are then examined by carrying out absorption studies using Rhodamine B (RhB).

Two different Ti precursors, $TiOSO_4$ and $TiCl_3$ were employed in the successful fabrication of TiO_2 nanorod segments. High potentiostatic conditions of -1.2 V (vs. 3 M Ag/AgCl) using $TiOSO_4$ precursor resulted in TiO_2 nanorods, but at the same time had promoted hydrogen evolution, which made it challenging for TiO_2 nanorods to be deposited onto noble metal surfaces such as Pt; while lowering the

potentiostatic voltages resulted in the growth of TiO_2 nanotubes. Cyclic voltammetry and chemical tests were carried out to determine the detailed mechanisms of their respective growth, and the difference in the formation of TiO_2 nanorods and nanotubes was attributed to be the regeneration of high amounts of NO_3- species occurring at more negative deposition voltages. Using $TiCl_3$, a protocol has been developed for the electrodeposition of TiO_2 nanorods, which involved a low deposition voltage of -0.1 V (vs. 1 M Ag/AgCl) that would facilitate the deposition of TiO_2 on noble metals such as Pt. This protocol allows both the flexibility of preparing $TiCl_3$ precursor solution and the electrodeposition of TiO_2 nanorods to be carried out at ambient conditions.

In the presence of TiO_2/Pt nanorods, RhB degradation studies reveal several pertinent characteristics of the photoactivities of the TiO_2/Pt nanostructures, where nanostructural morphology, addition of Pt metal and TiO_2/Pt interfaces were found to enhance TiO_2 photoactivity. The effects of varying TiO_2 length segments of Pt-TiO_2 nanorods on the photoactivities of TiO_2/Pt nanorods reveal an interesting trend, demonstrating an interplay between light absorption and the amount of light reaching the TiO_2/Pt interface. Lastly, differences in the orientation of bi-segmented TiO_2/Pt nanorods to the light source are presented, which may be useful in any future work on the investigation of the photoactivities of nanostructure arrays.

Table of Contents

Abstract 3
Table of Contents 5
Glossary 9
List of Figures 11
List of Publication 18
Appendix 19
Acknowledgement 19

Chapter 1: Introduction 21

1.1. Motivation 21
1.2. Hydrogen economy 22
1.3. Photocatalytic hydrogen production 24
1.3.1. Semiconductor TiO_2 for hydrogen production 24
1.3.2. Mechanisms of TiO_2 photocatalytic hydrogen production 25
1.3.3. Surface modification of TiO_2 to enhance hydrogen production 27
1.3.4. Nanostructural effects on photoelectrodes 27
1.4. Templated electrodeposition of multi-segmented materials 28
1.5. Thesis Outline 30
1.6. References 31

Chapter 2: Instrumentation and Characterization Techniques 35

2.1. Introduction 35
2.2. Morphology 35
2.2.1. Scanning Electron Microscopy (SEM) 35
2.2.1.1. Uses and Instrumentation of SEM
2.2.1.2. Imaging Modes of SEM
2.2.1.3. Treatment of Charging Samples
2.2.2. Transmission Electron Microscopy (TEM) 36
2.2.2.1. Uses and Instrumentation of TEM
2.2.2.2. Image Contrast in TEM
2.3. Chemical Analysis 37
2.3.1. Energy-dispersive X-ray Spectroscopy (EDS)-TEM 37
2.3.1.1. Operation and Instrumentation of EDS
2.3.1.2. Qualitative EDS Analysis
2.3.1.3. Quantitative EDS Analysis
2.3.1.4. Elemental Mapping
2.3.2. X-Ray Diffraction (XRD) 39
2.3.2.1. Operation and Instrumentation of XRD
2.3.2.2. Sample preparation and XRD measurements
2.3.2.3. High Temperature X-Ray Diffraction (HTXRD)
2.4. Electrochemical Deposition and Photoelectrochemical Studies 42

2.4.1. Potentiostat 43
2.4.2. Setup of Three-Electrode Electrochemical Cell 44
2.4.3. Electrochemical Cell Technical Drawing 46
2.5. Electrochemical Studies 47
2.5.1. Cyclic Voltammetry- the Instrumentation 47
2.5.2. Cyclic Voltammogram- the Theory 47
2.5.3. Cyclic Voltammetry Measurements 50
2.6. Optical Absorption Studies 50
2.6.1. Ultra-violet –visible Spectroscopy 50
2.6.2. Design Setup for Rhodamine Degradation Studies 51
2.6.2.1. Lightbox and Box Lid Technical Drawings
2.6.2.2. Sample Holder/ Cap Illustration
2.6.2.3. Cuvette Holder Illustration 53
2.6.3. Integrating Sphere
2.6.3.1. Operation and Instrumentation of Integrating Sphere
2.6.3.2. Reflectance and Transmittance of Materials
2.7. References 55

Chapter 3: Synthesis of Pt Nanorods and Experimental Procedures 56

3.1. Introduction 56
3.1.1. Nano-sized Pt catalysts 56
3.1.2. Pt as Hydrogen Evolution Catalysts 57
3.1.3. Electrochemical deposition of Pt 58
3.2. Literature Review 59
3.2.4. Templated Electrodeposition of One-Dimensional Pt Nanostructures
3.3. Electro-deposition of Pt from Sodium Hexachloroplatinate (IV) ($NaPtCl_6.6H_2O$) 62
3.3.1. Materials 62
3.3.2. General Experimental Practice 63
3.3.2.1. Bath Solution Preparation of $NaPtCl_6.6H_2O$
3.3.2.2. Method of Templated Electrodeposition of Pt Nanorods
3.3.2.3. Method of Releasing Pt Nanorods From Aluminium Oxide Membrane (AAM)
3.3.3. Results and Discussion 64
3.3.3.1. Optimization of Pt Nanorods Synthesis
3.3.3.1.1. Effect of Species Concentration
3.3.3.1.2. Effect of Deposition Voltage
3.3.3.2. 'Life-time' of Pt Precursor Solution
3.3.3.3. Structural and Chemical Analysis of Pt Nanorods
3.4. Conclusion 73
3.5. References 73

Chapter 4: Synthesis of TiO_2 Nanostructures and Experimental Procedures 77

4.1. Introduction 77

4.2. Literature Review: Electrodeposition of One-Dimensional (1-D) TiO_2 Nanostructures from Ti (IV) and Ti (III) Precursors 77
4.2.1. Electrodeposition of 1-D TiO_2 Nanostructures from $TiOSO_4$ 77
4.2.2. Templated Electrodeposition of 1-D TiO_2 Nanostructures from $TiCl_3$ 78
4.3. Templated Electrodeposition of TiO_2 from $TiOSO_4$ 80
4.3.1. Materials 80
4.3.2. General Experiment Practice 81
4.3.2.1. Bath Solution Preparation of $TiOSO_4$
4.3.2.2. Electrodeposition of TiO_2 Films
4.3.2.3. Templated Electrodeposition of TiO_2 Nanorods from $TiOSO_4$
4.3.2.4. Method of Releasing TiO_2 Nanorods From Template
4.3.3. Results and Discussion 82
4.3.3.1. Electrodeposition of TiO_2 Film from $TiOSO_4$ precursor
4.3.3.2. Characterisation of TiO2 Nanorods Electrodeposited from $TiOSO_4$ Precursor
4.3.3.3. Effect of Varying Deposition Voltages on TiO_2 Nanostructures
4.3.3.4. Problems encountered with TiO_2 deposition on Pt using $TiOSO_4$ precursor
4.4. Templated Electrodeposition of TiO_2 from $TiCl_3$ 96
4.4.1. Materials 96
4.4.2. General Experiment Practice 97
4.4.2.1 Bath Solution Preparation of $TiCl_3$
4.4.2.2 Templated Electrodeposition of TiO_2 Nanorods from $TiCl_3$
4.4.2.3 Method of Releasing TiO_2 Nanorods From Template
4.4.3. Results and Discussion 99
4.4.3.1 Suitable Reagents of $TiCl_3$ precursor
4.4.3.2 Electrodeposition of TiO_2 Nanorods from $TiCl_3$ precursor
4.4.3.3 Effect of pH on TiO_2 Nanostructures
4.4.3.4 Effect of Applied Voltage on TiO_2 Nanostructures
4.5. Conclusion 111
4.6. References 112

Chapter 5: Templated Electro-deposition of Segmented Nanostructures of TiO_2 and Pt 115

5.1. Introduction 115
5.2. Literature Review 116
5.3. Synthesis of Multi-segmented TiO_2/Pt Nanorods 118
5.3.1.Materials 118
5.3.2.General Experiment Practice 118
5.3.3.Results and Discussion 119
5.3.3.1. Structural, Surface and Interfacial Characteristic Studies of Segmented Nanorods
5.3.3.1.1. Structural Characterisation of Segmented TiO_2/Pt

nanorods
5.3.3.1.2. Interfacial Characterisation of Segmented TiO_2/Pt Nanorods
5.3.3.1.3. Chemical Analysis on Segmented TiO_2/Pt Nanorods
5.3.3.1.4. Effect of Order of TiO_2/Pt Deposition on TiO_2/Pt Segmented Nanostructures
5.3.3.1.5. Electrodeposition of Pt on amorphous TiO_2
5.3.3.1.6. Electrodeposition of Amorphous TiO_2 on Pt
5.4. Conclusion 134
5.5. References 135

Chapter 6: Absorption Studies of TiO_2-Pt Nanostructures 138

6.1 Introduction 138
6.1.1 Photocatalysis on Semiconductor TiO_2 Surfaces
6.1.1.1 Intrinsic TiO_2 Band-Gap Photoexcitation
6.1.1.2 Band Energy Positions of TiO_2
6.1.1.3 Surface States in Extrinsic TiO_2
6.1.1.4 Crystallinity and Particle Size Effects on TiO_2 Photocatalysts
6.1.1.5 Photocatalytic Enhancement through Noble Metal Loading of TiO_2
6.1.1.5.1 Schottky Contact between n-type TiO_2 and Pt
6.1.1.5.2 Particle Size Effect on Schottky Barrier Formation between Semiconductor and Metal
6.1.1.5.3 Effect of Intrinsic Dopant Levels in TiO_2 on TiO_2-Pt Barrier Type
6.2 Literature Review 148
6.3 Material Preparation and Experimental Setup 150
6.3.1 Materials
6.3.2 General Experiment Practice 151
6.4 Results and Discussion 151
6.4.1 Photoactivity of Amorphous and Crystalline TiO_2 nanorods 153
6.4.2 Structural Modification and Noble Metal Loading on TiO_2 photoactivity 156
6.4.3 Effects of TiO_2 Length Segment in Bi-segment Pt-TiO_2 Nanorods 156
6.4.4 Enhancement of RhB Degradation With Increased TiO_2-Pt Interfaces
6.4.5 Effects of Orientation of 2 Segmented TiO_2-Pt Nanorods
6.5 Conclusion 164
6.6 References 165

Chapter 7: Conclusion 171

7.1. Thesis Conclusion 171
7.2. Future Direction 172

Glossary

1-D: One-dimensional

AAM: anodic aluminium oxide membrane

BSE: backscattered electrons

CB: conduction band

CE: counter electrode

CO: carbon monoxide

CO_2: carbon dioxide

CdS: cadmium sulphide

DI: deionised

EDS: Energy-dispersive X-ray Spectroscopy

ESR: Electron Spin Resonance

H_2: hydrogen

HCl: hydrochloric acid

H_2O: water

H_2PtCl_6: hydrogen hexachloroplatinate (IV)

$HSCH_2COOH$: mercaptoacetic acid

H_2O_2: Hydrogen peroxide

HTXRD: High Temperature X-Ray Diffraction

IrO_2: iridium oxide

k: rate constant

KCl: potassium chloride

KNO_3: potassium nitrate

MB: methylene blue

MO: methyl orange

Na_2PtCl_6: sodium hexachloroplatinate (IV) hexahydrate

$NaHCO_3$: sodium hydrogen carbonate

NH_4OH: ammonia solution

NO_x: nitrogen oxides

O_2: oxygen

ORR: oxygen reduction reaction

Pt: platinum

PEC: photoelectrochemical

PV: photovoltaic

QDs: quantum dots

RE: reference electrode

RhB: Rhodamine B

RPM: revolutions per minute

RuO_2: ruthenium oxide

SCE: standard calomel electrode

SE: secondary electrons

SEM: scanning electron microscope

SiC: silicon carbide

NaOH: sodium hydroxide

TEM: transmission electron microscope

$TiCl_3$: Titanium chloride

$TiOSO_4.H_2O$: Titanium (IV) oxysulfate hydrate

TiO_2: titanium dioxide

UV: ultra-violet

UV-vis: ultra-violet visible

VB: valence band

WE: working electrode

XRD: x-ray diffraction

List of Figures

Chapter 1. Introduction

Figure 1-1. Electrochemical cell in which the TiO_2 electrode is connected with a platinum electrode through an external load

Chapter 2: Instrumentation and Characterization Techniques

Figure 2-1. Schematic representation of a basic $\theta/2\theta$ measurement geometry in a x-ray diffraction instrument

Figure 2-2. Schematic diagram of Bragg diffraction where two beams with identical wavelength and phase are incident on a crystalline material and are scattered off two different atoms within. Constructive interferences of the waves result in waves with a path difference of $2d \sin\theta$.

Figure 2-3. Schematic diagram representing potentiostatic mode where a potential step is applied and the response is an observed *i*-t curve.

Figure 2-4. Basic circuit of a potentiostat/galvonostat (PGSTAT)

Figure 2-5. Setup of electrochemical cell and electrodes

Figure 2-6. SEM images of aluminium oxide membrane (AAM) A) cross-section, B) top, C) bottom used as a working electrode in the templated electrodeposition of 1D nanostructures.

Figure 2-7. Technical drawings of the electrochemical cell representing the whole cell, side and bottom views

Figure 2-8. Potential-time behavior at the working electrode by imposition of a triangular waveform

Figure 2-9. A general cyclic voltammogram of a single electron oxidation-reduction reaction

Figure 2-10. A cyclic voltammetry scan showing an irreversible redox reaction occurring at aluminium oxide membrane (area=0.8 cm^2) in pH 3 aqueous solution of KNO_3+H_2O_2

Figure 2-11. Schematic diagram of a UV-Vis spectrometer

Figure 2-12. A schematic setup consisting of a light supply and light box housing the samples and filter lens used for absorption studies

Figure 2-13. Technical drawings of the light box and box lid representing their side and top views

Figure 2-14. Diagram showing various perspective of the sample holder/cap

Figure 2-13. Diagram of the cuvette holder

Figure 2-15. Simplified illustration of the use of an integrating sphere for A) transmittance and B) reflectance measurements

Chapter 3: Synthesis of Pt Nanorods and Experimental Procedures

Figure 3-1. Schematic diagram illustrating the electrodeposition of Pt in A) 50% blocked and B) 80-100% blocked AAM membrane

Figure 3-2. Backscattered SEM images of Pt nanorods grown in the pores of AAM at a two step voltage of [-0.4 V/20 s, -0.2 V/3580 s] and employing a $[PtCl_6]^{2-}$ precursor solution, HCl and KCl in their respective concentration ratios of A) [25:1:84], B) [25:5:84] and C) [25:1:0], (i) inset shows free-standing Pt nanorods released from AAM

Figure 3-3. Plot of approximate % charge efficiencies of Pt nanorods deposition (N=50) as a function of applied voltages (vs. Ag/AgCl, 1 M KCl at 25 ^{o}C). Backscattered SEM images A-F corresponds to respective points labeled on the plot. Point F on the plot was omitted due to faults occurring within Pt nanorods

Figure 3-4. Current-time plots for deposition of Pt nanorods in porous AAM at deposition voltages of a) –0.1 V, b) -0.2 V, c) -0.3 V, d) -0.4 V, e) -0.5 V and f) -0.6 V with a corresponding total charge passed of 1.49 C, 1.85 C, 1.88 C, 2.13 C, 2.64 C, 2.54 C respectively

Figure 3-5. A) XRD plot of Pt nanorods dispersed on Si substrate B) HAADF TEM image of a Pt nanorod segment, inset shows a larger section of the Pt nanorod segment

Figure 3-6. Backscattered SEM images of A) free-standing Pt nanorods on Ag conductive substrate achieved by etching AAM in 3 M NaOH; B) free Pt nanorods achieved by etching AAM and Ag conductive layer respectively in conc. NaOH and NH_4OH-based silver etchant

Chapter 4: Synthesis of TiO_2 Nanostructures and Experimental Procedures

Figure 4-1. SEM images of 100 K magnification of annealed TiO_2 films deposited on Au/glass at applied step voltages of [-1.4 V/ 20 s, -1.2 V/ 17980 s] using a $TiOSO_4$ precursor bath solution consisting of $TiOSO_4$ precursor and A) 0.2 ml H_2O_2 and B) 0.3 ml H_2O_2 where TiO_2 films appear to consist of TiO_2 "particles" sizes (averaged over 100 "particles") of 33 ± 9.1 nm and 78 ± 25.1 nm respectively

Figure 4-2. Schematic illustration of A) A non-homogeneous TiO_2 film deposition observed using 0.1 ml H_2O_2/$TiOSO_4$ precursor bath solution and B) Homogeneous TiO_2 film deposition observed using 0.3 ml H_2O_2/$TiOSO_4$ precursor bath solution. The resultant homogeneities in the TiO_2 films in A and B approximate the results of TiO_2 deposition in the porous AAM under the respective conditions.

Figure 4-3. (i) Plot of TiO_2 nanorods with varying experimental lengths (N=100) electrodeposited from pH 3 aqueous solution of $TiOSO_4$ under varying deposition times of a) 1 h, b) 2 h, c) 3h, and d) 5 h; insets (a), (b), (c), (d) showing corresponding SEM images of TiO_2 nanorods at 1 h, 2 h, 3 h and 5 h respectively; (ii) plot derived from current-time plots

Figure 4-4. Current-time plots of TiO_2 nanorod deposition into AAM from $TiOSO_4$ precursor at -1.2 V for A) 1 h, B) 2 h, c) 3 h, and d) 5 h (inclusive of an overvoltage of -1.4 V/20 s), with a total charge passed of 3.14 C, 5.39 C, 8.02 C and 11.99 C respectively

Figure 4-5. A) High Temperature XRD (HTXRD) patterns of TiO_2 nanorods electrodeposited from $TiOSO_4$ annealed *in-situ* from 25 to 600 ^oC, B) XRD pattern of TiO_2 nanorods deposited on Si substrate after annealing in air at 600 ^oC ("A" , ★ and Si indicate peaks of TiO_2 anatase, Au and Si substrate respectively)

Figure 4-6. CV curves (v=20 mV s^{-1}) at (A) Ag flat electrode and AAM (Area=0.80 cm^2) in aqueous KNO_3 solutions of pH 3; (B) at AAM (Area=0.80 cm^2) in pH 3 aqueous solution of KNO_3+H_2O_2 and $TiOSO_4$+

KNO_3+H_2O_2. Regimes of potentials within -1.4 V to -1.0 V and -1.0 V to -0.3 V as indicated above represent possible formation of TiO_2 nanorods and nanotubes respectively.

Figure 4-7. Schematic diagram illustrating nucleation of TiO_2 sites along pore walls of AAM (step 1 to 3); growth of TiO_2 nanorods *via* route (i) steps 4 to 6 from regeneration of NO_3^- from re-oxidation of reduced NO_2^- and TiO_2 nanotubes *via* (ii) steps 4 to 5 confined around the pore walls from limited reduction rates NO_3^-

Figure 4-8. SEM images of TiO_2 nanotubes deposited nanotubes deposited from a voltage step of (A) [-0.9 V/20s, -0.7 V/10800 s] and (B) [-0.5 V/20s, -0.3 V/10800s] where corresponding inset shows varying average wall thickness (N_x=20) denoted by $X_{ave,0.7}$ and $X_{ave,0.3}$ respectively.

Figure 4-9. SEM images of TiO_2 nanostructures deposited from a voltage step of A) [-1.4 V/ 20s, -0.7 V/3580 s] with average wall thickness (N_x=20) denoted by X_{ave1}) and B) [-0.9 V/ 20s, -1.2 V/3580 s]; corresponding insets show magnified TiO_2 nanostructures

Figure 4-10. Schematic illustration of A) formation of thick-walled TiO_2 nanotubes at deposition voltages of [-1.4 V/ 20s, -0.7 V/3580 s], and B) irregular TiO_2 nanostructures at deposition voltages of [-0.9 V/ 20s, -1.2 V/3580 s]

Figure 4-11. (a) SEM image showing gaps between segments of TiO_2 electrodeposited from $TiOSO_4$ and Pt in AAM illustrated by schematic diagrams (b) and (c)

Figure 4-12. SEM images A) 5 k and B) 15 k magnification of free-standing TiO_2 nanorods electrodeposited on Pt nanorods using powder $TiCl_3$ powder as a starting material. TiO_2 nanorods were deposited at -0.1 V for 2 h.

Figure 4-13. (i) Plot of experimental lengths TiO_2 nanorods electrodeposited from aqueous solution of $TiCl_3$ against total charge passed; (ii) plot derived from current-time plots

Figure 4-14. Deposition transients showing varying total charge passed A) 0.93 C, B) 2.77 C, C) 3.31 C, D) 6.36 C under constant deposition voltage of -0.2 V from $TiCl_3$ precursor, to achieve varying amounts of TiO_2 deposition within porous AAM

Figure 4-15. A top view SEM image of free-standing TiO_2 nanorods electrodeposited at -0.2 V from a $TiCl_3$ precursor bath solution prepared from $TiCl_3$ solution reagent. Inset shows a magnified side-view SEM image of the corresponding TiO_2 nanorods.

Figure 4-16. Multiple plots of XRD patterns of TiO_2 films electrodeposited from $TiCl_3$ obtained at various temperatures from 25 to 600 ^oC ("A" and "R" indicates TiO_2 anatase and rutile peaks respectively)

Figure 4-17. SEM images of TiO_2/Pt nanostructures consisting of TiO_2 electrodeposited from $TiCl_3$ electrolyte obtained at pH range of (a) 1.3-1.8 (b) 1.9-2.5

Figure 4-18. Schematic illustration of the (i) formation of dense TiO_2 nanostructures from Ti^{3+} precursor solution of pH 1.9 to 2.5; (ii) formation of highly porous TiO_2 nanostructures from Ti^{3+} precursor solution of pH 1.2 to 1.8

Figure 4-19. CV curves (*v*=20 m/s) at AAM (Area=0.8 cm^2) in aqueous $TiCl_3$ precursor solutions of A) pH 2, B) pH 1.5 and C) pH 1.3 at 20 ^oC

Figure 4-20. Backscattered SEM images of morphology of TiO_2-Pt nanostructures deposited at (A) -0.1 V (B) -0.2 V (C) -0.3 V (D) -0.4 V from $TiCl_3$ precursor at pH 2; inset in D shows a high magnification of Pt-TiO_2-core-shell structure

Figure 4-21. Schematic diagram relating the rate of the $TiOH^{2+}$ oxidation and anodic current densities to the growth of TiO_2 in the AAM at deposition potentials of (a) -0.2 V, (b) -0.3 V, (c) -0.4 V and the respective TiO_2 nanostructures achieved

Figure 4-22. Schematic diagram illustrating (A) dense TiO_2 nanorod consisting of uniform particles as a result of smooth and moderate TiO_2 grain growth at deposition potentials of -0.2 V, (B) highly porous TiO_2 nanorod consisting of particles with large size distribution resulting from rapid and coarse TiO_2 "particle" growth at -0.1 V (high current densities); Pt provides a contrast in the porosity of TiO_2 nanorods in (A) and (B)

Chapter 5: Templated Electro-deposition of Segmented Nanostructures of TiO_2 and Pt

Figure 5-1. General scheme for the fabrication of multi-segmented 1-D nanostructures by templated sequential electrodeposition

Figure 5-2. Backscattered SEM images of a) TiO_2-Pt, b) TiO_2-Pt-TiO_2, c) Pt-TiO_2-Pt-TiO_2 nanorod arrays on a 150 nm thick layer of Ag

Figure 5-3. Top-view SEM image of 'islands' of free-standing 3-segment Pt-TiO_2-Pt nanorods on 3 μm thick Ag film; inset shows 10X magnification of a single 'island'

Figure 5-4. SEM images of a TiO_2-Pt nanorod at magnification of (a) 55K (b) 170 K and TEM images showing (c) TiO_2-Pt nanorod; (d) diffused junction between TiO_2 and Pt segments

Figure 5-5. A) TEM image of a three-segmented Pt-TiO_2-Pt nanorod indicating the multiple point scans (1 to 9) along its length. Pt(i) indicates Pt segment that was deposited as a first layer, and Pt(ii) as the second Pt segment. Inset shows elemental mapping of Pt, Ti and O of the Pt-TiO_2-Pt nanorod. B) Plot showing the variation of % volume of Pt and TiO_2 and % volume ratio of TiO_2/Pt across the length of the Pt-TiO_2-Pt nanorod

Figure 5-6. Schematic representation of the difference between the interfaces of Pt(i)/TiO_2 and TiO_2/Pt(ii) as observed from the TEM image of a Pt-TiO_2-Pt nanarod

Figure 5-7. (a) Backscattered SEM images of (a) Pt-TiO_2-Pt nanorods (b) current density-time plot of (i) first and (ii) second Pt electrodeposition; inset schematic diagram illustrating Pt deposition on (i) Ag and (ii) TiO_2

Figure 5-8. Backscattered SEM Images of A) 3-segment TiO_2-Pt- TiO_2 nanorods showing a clear contrast between the first TiO_2 segment with some diffused Pt (denoted by *TiO_2) and third TiO_2 segment with no diffused Pt (denoted by TiO_2); B) 3-segment unannealed Pt-TiO_2-Pt nanorods with some Pt diffusion into second TiO_2 segment; C) increased Pt diffusion into second TiO_2 segment after thermal treatment at 600 ^{o}C in air

Figure 5-9. Schematic illustration demonstrating the growth of Pt within the porous nanostructure of TiO_2 and the possibility of electrodepositing Pt onto amorphous TiO_2

Figure 5-10. Schematic illustration of the cross-section view of A) unannealed AAM, B) contortion of the AAM resulting from annealing at 600 ^{o}C, and C) possible damage to the AAM as it is being placed under the cell prior to electrodeposition

Figure 5-11. SEM images of free-standing A) unannealed TiO_2 nanorods and B) annealed TiO_2 nanorods at 600 ^oC in air for 5 h; respective insets show higher magnification of the corresponding TiO_2 nanostructures

Figure 5-12. SEM image of free-standing Pt-TiO_2 nanorods obtained by electroless deposition of TiO_2 on Pt from 0.28 M TiCl3 solution for 12 h in AAM. Inset shows a higher magnification of Pt-TiO_2 nanorods

Figure 5-13. Schematic diagram comparing TiO_2 deposition on Pt nanorods by (i) electroless method and (ii) electrodeposition occurring in porous AAM

Chapter 6: Absorption Studies of TiO_2-Pt Nanostructures

Figure 6-1. Band gaps and band edge positions of TiO_2 anatase and TiO_2 rutile photocatalysts depicting correlations with the potential levels of an acceptor and donor species in pH 7 electrolyte

Figure 6-2. Energy correlation between band edges of TiO_2 and Fermi energies of electrode reactions in aqueous electrolyte of pH 7

Figure 6-3. Energy level diagrams of n-type TiO_2 semiconductor (consisting of lattice imperfections) and Pt metal at electrical and thermal equilibrium illustrating A) equilibrating of Fermi levels as TiO_2 and Pt are brought in contact with each other, and B) formation of a space-charge layer resulting from a potential difference across TiO_2 and Pt contact surfaces, and a schottky barrier between n-type TiO_2 and Pt which creates resistance for electrons to travel from TiO_2 semiconductor to Pt metal

Figure 6-4. Energy level diagrams of n-type TiO_2 semiconductor consisting of high concentration of surface defects, resulting an Ohmic flow of electrons from TiO_2 to Pt metal

Figure 6-5. Structural diagram of Rhodamine B ($C_{28}H_{31}ClN_2O_3$, Mr=479.02, λ_{max}~543 nm)

Figure 6-6. Plot comparing the photodegradation of RhB on (i) TiO_2-unannealed and (iii) TiO_2- annealed under UV irradiation; (ii) TiO_2-unannealed and (iv) TiO_2-annealed under irradiation of UV and visible light (λ > 300 nm). All 4 samples consist of arrays of TiO_2 nanorods of approximately 3 μm in length.

Figure 6-7. Photocatalytic activity comparison under visible and UV irradiation (wavelength >300 nm) of (a) TiO_2 film (b) TiO_2 nanorods and (c) bi-segmented Pt-TiO_2 nanorods based on the normalized RhB concentration ratio C/C_o as a function of irradiation time. Insets (a), (b) and (c) show the corresponding SEM images of the respective samples.

Figure 6-8. Schematic diagram illustrating the difference in the aspect ratio of A) bulk TiO_2 and B) an array of TiO_2 nanorods for adsorption of molecules and charge carrier migration lengths.

Figure 6-9. Schematic diagram of RhB degradation on A) TiO_2 nanorods and (B) bi-segmented Pt-TiO_2 nanorods under irradiation of λ > 300 nm. Enhanced RhB photodegradation on Pt-TiO_2 nanorods through electron-hole separation and surface electron excitation by visible light excitation of surface Plasmon resonance of Pt metals on TiO_2

Figure 6-10. A) Plot showing the relationship between the length of TiO_2 segment in bi-segmented Pt-TiO_2 nanorods and its photocatalytic activity on RhB degradation indicated by the rate constant, k. The dotted curve serves as a guide to the eye. B) Schematic diagram illustrating the difference in light absorption and interface reactions in corresponding regions I, II and III

Figure 6-11. Plot reflecting the effect of a) TiO_2, b) Pt-TiO_2, and c) TiO2-Pt-TiO_2 nanorods on RhB degradation rate under 6 h of continuous UV irradiation; SEM images (a), (b) and (c) shows corresponding nanostructures where the total length of TiO_2 segment are kept approximately constant

Figure 6-12. Schematic diagram of a) TiO_2, b) Pt-TiO_2, and c) TiO_2-Pt-TiO_2 nanorods illustrating the effect of increasing number of TiO_2/Pt interfaces on its photoactivity in RhB degradation

Figure 6-13. Rhodamine degradation on Pt-TiO_2 and TiO_2-Pt bi-segmented nanorods under UV irradiation at A) 180 ^{o} light incidence and B) 90 ^{o} light incidence. Insets show schematic illustration of nanorod orientation to light source.

Figure 6-14. Mounted samples consisting of an array of TiO_2-Pt and Pt-TiO_2 freestanding nanorods used for integrating sphere measurements. Angle of light is incident on the nanorods at 180 ^{o}, similar to that in absorption studies.

Figure 6-15. Integrating sphere measurements of A) % reflectance and B) % transmittance of samples consisting of TiO_2-Pt and Pt-TiO_2 bi-segmented nanorods. % Transmittance measurements taken against a standard consisting of only epoxy (used as a support for TiO_2/Pt bi-segmented nanorods)

Appendix

Appendix 3-1: Derivation of graph and error bars in figure 3-3

Appendix 3-2: 'Life-time' calculation of [$PtCl_6^{2-}$] precursor solution

Appendix 4-1: Derivation of plot and error bars in figure 4-3

Appendix 4-2: Derivation of plot and error bars in figure 4-3

Appendix 5-1: Estimation of % Pt in TiO_2 segment of Pt-TiO_2-Pt nanorod system

Appendix 6-1: Derivation of rate constant, k

List of Publications

Gladys Y. Teo, D. Jason Riley, Mary P. Ryan, "A Mechanistic Study on Templated Electrodeposition of One-Dimensional TiO_2 Nanorods and Nanotubes using $TiOSO_4$ as a Precursor", *Electrochemistry Communications, 2014, 47, 13-16*

Acknowledgements

The completion of this thesis has been made possible because of those whose help and support I am deeply grateful for. Firstly, I would like to thank Professor Jason Riley and Professor Mary Ryan for the opportunity given to embark on this PhD, and for all their valuable insights, continuous guidance, support, and encouragement throughout this PhD journey.

Also within the Department of Materials, I would like to thank Dr. Mahmoud Ardakani for his patience and kindness in assisting with the electron microscopy measurements; Richard Sweeney for his help in XRD measurements; Russell Stacey and Mike Lennon for their technical expertise in constructing the setups for my experiments.

My PhD experience had been enriched with everyone that I have met during my time in London. In particular, I want to thank Christina for being the most thoughtful and caring person that you are; Alice, Laurie and Ning for all your genuine friendship and memorable times together; Taek, Ched, Kristina and Sophia for the fun and laughter; and the Riley group for spicing up lab sessions.

Finally and most importantly, I would also like to express my gratitude towards the people whom I am closest to: my family and Mae Mae for their unconditional love, care and moral support throughout life; Charm, Jo and Min for long lasting friendships that transcend time and distance; and Alex for believing in me and supporting my ambitions, and also whose patience, love and care run across miles.

This thesis is dedicated to you all, who have contributed in helping me reach this milestone.

Above all- from whom all blessings flow, to God be the glory.

Gladys
July 2014

Chapter 1: Introduction

1.1. Motivation

Solar energy is the most abundant and permanent energy resource on earth. The ability to harness and utilize solar energy directly through solar technologies can make a substantial contribution to reducing the world's reliance on fossil fuels. At present fossil fuels constitute 80% of the worldwide energy use [1]. The demand for fossil fuels is expected to exceed annual production within the next two decades [2], which poses a challenge to the world's energy sustainability.

The world's dependence on fossil fuels also imposes several environmental risks [3]. The burning of fossil fuels releases carbon dioxide, nitrogen oxides and aerosols, which affect the local, regional and global environment. Energy infrastructures such as power plants, gas and oil pipelines are potentially vulnerable to adverse weather conditions. Owing to the lack of water to cool the condensers, the operations of nuclear and oil plants are potentially at risk during hot and dry weather conditions; fossil and nuclear plants that are destroyed by hurricanes and typhoons pose severe environment and health threats.

To address the impending issue of energy sustainability and the growing environmental and health risks related to the present energy systems, the world is urgently seeking a transformation into a more sustainable energy supply. Currently photovoltaic (PV) modules are a major contribution to this transformation [4]. Coupled with an electrolyzer, this energy system is able to efficiently convert energy harvested from the sun into electrical power. As the demand for a sustainable energy supply increases, researchers are seeking on an efficient and cost effective approach to improve the technology of harnessing solar energy. Mimicking the idea of how nature collects and stores solar energy in chemicals bonds through photosynthesis, an economically viable water splitting cell capable of splitting water directly at the semiconductor surface is developing [5]. The catalytic semiconductor is required to be both a light absorber and an energy converter to store solar energy in the simplest chemical bond, H_2 [6], thereby eradicating significant fabrication and system costs involved with the use of separate electrolyzers wired to photovoltaic cells [7].

Photoelectrochemical cells consisting of TiO_2 semiconductor and Pt metal have been considered to be effective photocatalysts for hydrogen evolution [8]. By employing various types of TiO_2/Pt systems, several attempts have been made to produce H_2 and O_2 through the process of water splitting [9-13]. To date, TiO_2/Pt photocatalytic systems for photocatalysis consist mostly of Pt nanoparticles dispersed on

TiO_2 nanostructures and films [13-16]; or Pt embedded in TiO_2 [17, 18]. These TiO_2/Pt photocatalytic systems present limitations in the functionality of TiO_2 or Pt , as the exposed surface of TiO_2 will be block by the coverage of Pt and vice versa.

In this research, we aim to prepare water-splitting materials consisting of multi-component nanorods of TiO_2 and Pt with well-defined nanostructures. Each individual TiO_2-Pt nanorod functions as photocatalysts for hydrogen production. As the TiO_2-Pt nanorods are irradiated with light in the presence of a water source, oxygen and hydrogen are evolved at the TiO_2 anode and Pt cathode segments of the nanorods respectively. Compared to bulk photocatalysts, the higher surface area of nanostructured photocatalysts favours the adsorption of solute molecules; and the use of multi-component nanorods for photocatalytic water splitting enables the control of the direction of charge movement and light absorption pathways in the material [19], thereby presenting a solution to improving the overall efficiency of photocatalytic hydrogen production.

Amongst a myriad of possibilities in synthesizing TiO_2 and Pt nanorods, the electrodeposition of TiO_2 and Pt using anodic aluminium oxide membrane (AAM) is the preferred method. This method permits an easier control of the position and composition of the materials growth along the length of the nanorods, which allows a customizable and highly reproducible method of obtaining multi-segmented rods with uniformly distributed active sites for efficient catalytic activity.

In order to achieve effective conversion, storage and utilization of renewable energy sources, technological breakthroughs and revolutionary developments are needed. The efforts toward engineering nanostructures offer a new paradigm for developing an efficient photoelectrolysis device to achieve an affordable and environmentally benign method for energy conversion and storage.

1.2. Hydrogen economy

Relating to a proposed system of delivering energy using hydrogen, the well-known term 'Hydrogen Economy' was created by John Bockris, a physical chemist who saw the future of the world's energy economy based on the use of hydrogen [20]. The production of hydrogen is a large and global industry. Its importance stems from its pertinent roles in the production of ammonia via the Haber process and in the conversion of heavy petroleum components into lighter fractions via hydrocracking. As the world faces challenges to energy sustainability, the demand for hydrogen has risen as it is potentially an alternative fuel to the increasingly depleted and yet increasingly employed fossil fuels.

The transformation from the present fossil fuel economy to a hydrogen economy involves numerous scientific and technological advances which will require several decades to be accomplished [21]. There are several methods of producing hydrogen, however if the process is to be carbon neutral and renewable, solar-driven reactions would be the best method. The use of solar energy to drive chemical reactions involves water as the key component. Though water represents a virtually limitless source of hydrogen, it is highly stable and therefore requires a large energy input to release the elements. This energy can be supplied in the form of heat (thermochemical), light (photochemical), or electricity (electrolysis) [22].

Solar thermal is potentially the most efficient path for producing hydrogen from water since it does not involve inefficiencies associated with photochemical transformations or the conversion of solar energy to electricity followed by electrolysis [23]. However, water requires temperatures of more than 2500 K to be thermally decomposed at a significant extent into elemental hydrogen and oxygen [24], which implies the added need for nuclear reactors to supply high temperatures through the process of nuclear fission. A hydrogen economy which requires nuclear electricity is not only energy-intensive but it also imposes safety and environmental constraints such as safe radioactive waste disposal, nuclear proliferation, plant decommissioning and uranium shortage will be magnified [21].

Compared to the solar-thermal approach to water splitting, photoelectrochemical (electrolysis) and photochemical methods present a more desirable method of producing hydrogen using stable, sunlight-harvesting semiconductors. Through electrolysis, energy is supplied in the form of electricity to cleave water into gaseous hydrogen and oxygen. This electricity is generated by solar radiation absorbed in photovoltaic devices, which is coupled to a water electrolyzer. Recently, photochemical water splitting cells composing of stable semiconductors have been designed to enable water splitting directly at the semiconductor surface [25]. Compared to the use of electrolyzers, water splitting cells which enable direct contact between the semiconductor and the liquid are more economically viable because significant fabrication and systems costs which are involved with the use of separate electrolyzers wired to solar cells are avoided [7]. Besides this, water splitting via the photochemical pathway is also more attractive due to the ease at which an electric field can be created at the semiconductor/liquid junction [26].

The discovery of the photoelectrochemical system has brought about significant technological advances in harnessing sunlight for renewable hydrogen production and is becoming more competitive as it promises a more cost effective, clean and environmentally friendly method of producing renewable hydrogen [27].

1.3. Photocatalytic hydrogen production

1.3.1. Semiconductor TiO_2 for hydrogen production

The discovery of photocatalytic water splitting using a semiconductor, titanium dioxide (TiO_2) was reported by Fujishima and Honda [8]. An electrochemical cell was constructed in which a TiO_2 electrode was connected to a platinum (Pt) electrode through an external load as shown in figure 1-1. As the surface of the TiO_2 electrode was irradiated using visible light, a current flow was observed, which consequently produced oxygen (O_2) and hydrogen (H_2) at the TiO_2 and Pt electrodes respectively. This work suggested the feasibility of using TiO_2 for water decomposition by visible light without applying an external voltage and hence marked the beginning of extensive research efforts in synthesizing and understanding TiO_2 materials for the enhancement of photocatalytic efficiency.

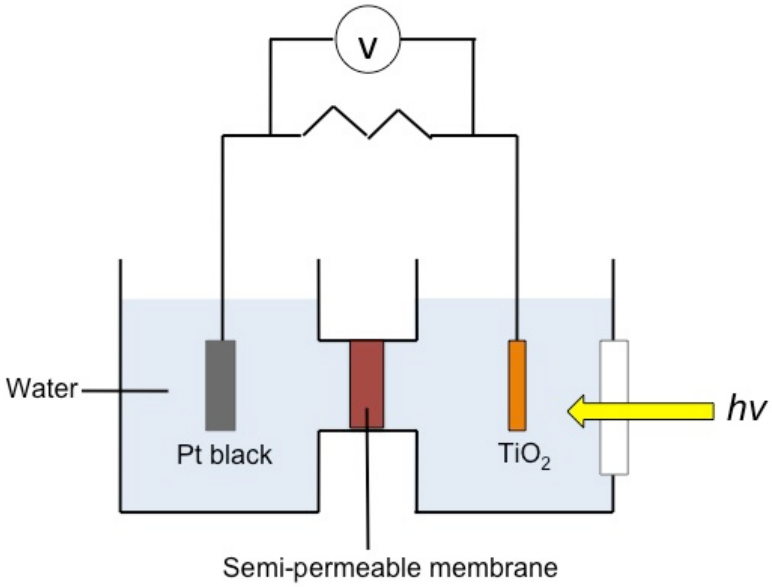

Figure 1-1. Electrochemical cell in which the TiO_2 electrode is connected with a platinum electrode through an external load.

In general, semiconductors which possess a band gap of greater than 1.23 eV and are able to utilise the energy of absorbed photons to convert water into hydrogen and oxygen can function as photocatalysts for hydrogen production [28]. However, many of these semiconductors such as cadmium sulphide (CdS) and silicon carbide (SiC) are unsuitable as photocatalysts for water splitting as they undergo anodic dissolution and photocorrosion [29]. Conductive metal oxide semiconductors such as ruthenium oxide (RuO_2) and iridium oxide (IrO_2) which readily react

with bases and any oxygen produced at the anode are also chemically unstable for water splitting [30]. Due to its strong catalytic activity and high chemical stability in acidic and oxidative environments, TiO_2 is the widely preferred photocatalyst for hydrogen production [29].

Throughout the progress of TiO_2 photocatalytic research, the photocatalytic activities of the two major TiO_2 phases were compared and it has been concluded that the activity of the anatase TiO_2 for autooxidation is much higher than that of rutile. This can be attributed to the influence of the crystal structure and morphology of the exposed lattice planes on the process of charge transfer at the TiO_2/electrolyte interface [31]. Xiao and co-workers [32] evaluated the photocatalytic activity of the synthesized anatase TiO_2 nanosheets of approximately 82% dominant (001) facets loaded with 1 wt% Pt by measuring the efficiency of H_2 evolution from water splitting. The results exhibited a high H_2 production rate of 7381 µmol h^{-1} g^{-1} under ultra-violet visible (UV-vis) light irradiation using a 300 W Xe lamp with a wavelength of 220 -770 nm which can be attributed to the exposed reactive (001) facets and high crystallinity of anatase TiO_2.

Additionally, the electrochemical and photoelectrochemical investigation of single-crystal anatase TiO_2 compared to rutile TiO_2 was carried out by Kavan and co-workers [31]. From the comparison of the flat band potential which represents one of the fundamental properties of any semiconductor-electrolyte system, coupled with the energy band gap, it was found that anatase TiO_2 (101) and rutile TiO_2 (001) electrodes differ mainly in the position of the conduction band edge. While the flat-band potential of rutile TiO_2 is slightly more positive than that of the standard hydrogen electrode that of anatase TiO_2 was shown to be negative of this value. The higher reduction potential of the photogenerated electrons in anatase TiO_2 than in rutile TiO_2 hence suggests that the complete photoelectrolysis of water to H_2 and O_2 by photogenerated conduction band electrons occurs spontaneously with anatase TiO_2 rather than with rutile TiO_2.

1.3.2. Mechanisms of TiO_2 photocatalytic hydrogen production

The electronic structure of a semiconductor plays a key role in the water splitting reaction. Unlike conductors, which possess a continuum of electronic states, intrinsic semiconductors such as TiO_2 consists of a valence and a conduction band between which is a region void of energy levels. This void region, which extends from the top of the valence band to the bottom

of the conduction band is known as the band gap. When a semiconductor is excited by photons with energy equal to or higher than the band gap energy level, electrons from the filled valence band are promoted to the empty conduction band, leaving behind positively charged holes in the valence band.

There are several pathways, which the separated electron and hole follow. As the direct contact between the semiconductor and water allows water species to be pre-adsorbed on the semiconductor surface, electrons and holes at the surface of the semiconductor are able to respectively participate in reduction and oxidation of the water. The reduction and oxidation reactions by the photo-generated holes and electrons on the surface of TiO_2 present the fundamental reaction mechanisms of photocatalytic hydrogen production.

The Gibbs free energy change under standard conditions indicates 237.2 KJ mol^{-1} is required to convert one mole of H_2O molecules to H_2 and ½ O_2, which corresponds to a change in the standard electrochemical potential of 1.23 V per electron transferred, as defined by the Nernst equation. Ideally, a single semiconductor material with a band gap energy large enough to split water, and a conduction and valence band-edge energy that straddle the electrochemical potentials E^o (H^+/H_2) and $E^o(O_2/H_2O)$ will have the ability to drive the hydrogen evolution reaction and oxygen evolution using electrons and holes generated under illumination. Possessing a band gap energy of about 3.2 eV, TiO_2 is able to decompose water into oxygen and hydrogen in an electrochemical cell under irradiation according to equations 1A-1D below [28]:

Excitation of TiO_2 by light: $TiO_2 + 2\ h\nu \rightarrow 2\ e^- + 2\ p^+$ (Equation 1A)

Oxidation reaction at TiO_2 electrode: $2\ p^+ + H_2O \rightarrow ½\ O_2 + 2\ H^+$ (Equation 1B)

Reduction reaction at Pt electrode: $2\ e^- + 2\ H^+ \rightarrow H_2$ (Equation 1C)

The overall reaction is: $H_2O + 2\ h\nu \rightarrow ½\ O_2 + H_2$ (Equation 1D)

Presently, the energy conversion efficiency from solar to hydrogen by TiO_2 via this mechanism remains low, largely due to the recombination of the photo-generated electron-hole pairs. This happens when the excited electrons in the conduction band rapidly recombine with the valence band holes of the semiconductor and releases energy in the form of unproductive heat or photons. To resolve this problem and increase the feasibility of solar photocatalytic hydrogen production, methods such as noble metal loading were investigated which proved to be useful in enhancing hydrogen production.

1.3.3. Platinization of TiO_2 to enhance hydrogen production

In order to enhance photocatalytic activity, noble metals such as Pt particles are often used as electron scavengers. By acting as an electron sink, photo-excited electrons and holes are efficiently separated to result in an increase in TiO_2 photocatalytic activity through decreasing the rate of electron-hole recombination and prolonging the lifetime of electron-hole pairs [33, 34]. Tang and co-workers investigated the quantum yield of oxygen production using Pt as an electron scavenger on TiO_2 film and observed the dynamics of long-lived photoholes, thereby suggesting Pt as a reasonable electron scavenger [35]. Consequently, there has been increasing reports on the effective coupling of TiO_2 and Pt as effective catalysts for hydrogen production [36, 37].

Based on Electron Spin Resonance (ESR) signals, Anpo and Takeuchi [38] reported the significant enhancement of photocatalytic reactivity of TiO_2 powder in the presence of small amounts of Pt loading. By investigating the relationship of ESR signals with Ti^{3+} generated on Pt-loaded TiO_2 and unloaded TiO_2 under UV light irradiation, it was discovered that the Ti^{3+} signal intensity of the unloaded TiO_2 was found to increase linearly with the UV irradiation time while few changes were detected from the Pt-loaded TiO_2. Since Ti^{3+} sites arise from Ti^{4+} sites where photogenerated electrons are trapped, these results clearly indicate that rapid transfer of photogenerated electrons from TiO_2 to Pt had occurred in the Pt-loaded TiO_2. As the charges distribute between TiO_2 and Pt, the Fermi levels of the semiconductor and metal nanoparticle equilibrate and shift closer to the conduction band of TiO_2 [39]. The resulting shift of the Fermi level to a more negative potential improves the efficiency of the photocatalytic reaction of TiO_2 and hence the efficiency for the water-splitting hydrogen production.

1.3.4. Nanostructural effects on photoelectrodes

Recently much interest has been directed towards the use of TiO_2 nanostructures for hydrogen production due to their unique properties. The primary advantage of a structured electrode compared to a planar system is the decoupling of the directions of light absorption and charge-carrier collection [19]. In a traditional planar semiconductor material, the direction of light absorption is similar to that of charge-carrier collection. Since the distance that a minority carrier can diffuse before recombining, L_D is directly related to the minority-carrier mobility, μ ($m^2V^{-1}S^{-1}$) by the following equations 1E and 1F:

$$L = \sqrt{D\tau}$$ (Equation 1E)

where τ is the minority-carrier lifetime and D is the minority carrier diffusion coefficient

The diffusion coefficient is then related to the μ by the Einstein equation:

$$D = \frac{\mu k_B T}{q}$$ (Equation 1F)

This results in the material having a carrier collection limited by minority-carrier diffusion located at the base region. Although increasing the thickness of the material increases the amount of light absorbed, the efficiency of a solar device fitted with a planar semiconductor system is unlikely to increase.

A solution to the device design and optimization issue may be provided by employing arrays of semiconductor nanorods. Because of their significantly smaller size, TiO_2 nanostructures possess a large surface-to-volume ratio and hence specific surface area for photocatalytic activity. As a semiconductor, the movement of the electrons and holes of TiO_2 are not only largely affected by its size, but also by its geometry [40]. This effect can be best exemplified by examining and comparing the structure of a solar cell nanorod array to that of a planar structure of the same material. Each individual nanorod in the cell can be built long in the axial direction to allow for optimal light absorption, while thin in the radial direction to allow excited minority charge carriers residing deep within the semiconductor nanorod array to easily migrate to the semiconductor surface [28]. Overall, the small aspect ratio inherent in the geometry of a nanorod structure is able to result in an increase in the charge collection efficiency despite short minority carrier diffusion lengths.

1.4. Templated Electrodeposition of Multi-Segmented Nanostructures

One-dimensional nanostructures such as rods and wires are becoming important nanomaterials due to their relatively large specific surface area and extremely high aspect ratios, offering the potential to build striped nanostructures with multiple chemical components aligned along the longitudinal axis of the structure. Several methods such as pulsed-laser ablation/ chemical vapour deposition (PLA-CVD), nanolithography and deposition using various techniques into hard templates have been employed to synthesize these multi-component materials. Amongst these, template synthesis is becoming the

preferred method as increased emphasis is placed on low cost, high throughput, high volume and ease of production of multi-segmented nanorods.

Micro- and nanoporous hard templates are commonly used to fabricate one-dimensional multisegmented rods because their pores are uniform and dense, providing an effective approach to synthesize monodisperse nanomaterials in high yield. The use of hard templates also allows the control of the placement and dimensions of different material components of the nanorods during synthesis. Amongst materials such as zeolite, glass and nanoporous solids which are used as templates for the fabrication of nanorods, track-etched polycarbonate and anodic aluminium oxide membrane (AAM) are the most commonly used as they can be produced in a wide range of uniform pore sizes and densities, offering the possibility of synthesizing monodispersed nanomaterials in high yield of 10^9 to 10^{11} nanostructures/cm^2 of template [41]. As compared to polycarbonate templates which often consist of a large number of intersecting pores due to the random pore formation [42], AAM possess uniform pores and parallel channels of large domains, thereby allowing the diameters and lengths of their pores to be easily controlled and finely tailored. Additionally, not only do AAM have high thermal and mechanical stability, they are also chemically and thermally inert during the deposition of metals in the pores [43].

By electrodepositing the target materials into AAM, cylindrical rods with uniform diameters are obtained. The electrochemical deposition method has attracted much attention owing to its low cost and operational simplicity whereby it eradicates the need for expensive instrumentation, high synthesis temperatures or low- vacuum pressures. The most notable advantage of electrodeposition is its capability in precisely controlling the position and composition of the nanorods along the lengths of the membrane [44]. The multi-segmented nanorods can be synthesized by either using an electrolyte containing two or more metal ions in a solution in conjunction with a varying applied potential, or by changing the plating solution and varying the potential of the deposition accordingly until a predetermined number of segments is met [42].

A general technique applies for the fabrication of nanorods through electrochemical deposition regardless of the type of materials to be deposited. Prior to electrodeposition, a thin conductive metal layer such as silver or gold is evaporated onto one side of the template to seal the pores and make the desired side conducting. This metal film is used as a working electrode to enable the electrodeposition of materials in the pores of the template. A layer of sacrificial metal is then deposited before the electroplating of any active nanorod segment to fill up any gaps between the evaporated conductive layer and the AAM and to planarize any irregular area that may exist in the template. The desired components are then deposited sequentially and the nanorods are released by chemically dissolving the

conductive and sacrificial metal layer followed by the template. This technique of synthesizing 1D multi-segmented nanostructures will be revisited again in chapter 5.

To date, multi-segmented nanorods and nanowires synthesized via template electrodeposition have been employed as multiplexed biosensors [45, 46], magnetic composites [47-49], electronic building blocks [50, 51] and optical tags [52, 53], and is beginning to find potential applications in catalysis [54-56]. Based on the linear relationship between the average nanorod length and the amount of charge passed according to Faraday's law, the nanorods can be grown to the desired length. An example was demonstrated through the fabrication of multisegmented nanorods composed of gold, copper and nickel whereby the lengths of the metal segments in a striped rod as well as the total length of the rod were easily tuned by controlling the electrodeposition time [43]. The high degree of control over the particle length, width and composition enables the preparation of large numbers of distinct nanostructure varieties in which the particle aspect ratio, catalytic, optical and electrical properties are tailored for a desired application [52].

Overall, the ability to develop one-dimensional nanostructures with different striping, compositional or shape patterns using templated electrodeposition has so far led to rapid advancements in the area of magnetic and electronic building blocks, and bio-sensing applications. As much as these particles have been practically employed for nano-scale electronics and photonics, an equally compelling opportunity lies in the use of multi-segmented nanostructures for the enhancement of catalytic activities in which its future development holds great promises.

1.5. Thesis Outline

The work in this thesis focuses primarily on the design, fabrication and characterization of TiO_2/Pt striped nanorods; as well as the evaluation of its photocatalytic function through the use of a classical absorption study on Rhodamine B degradation. Result chapters 3 to 6 in this thesis are built largely from the development of separate protocols on the synthesis of Pt nanorods and TiO_2 nanorods via templated electrodeposition, as described respectively in chapter 3 and 4. These protocols are essential in ultimately achieving 1D TiO_2/Pt striped nanostructures. Based on the established synthesis procedures of Pt and TiO_2 nanostructures, a detailed account of the successful fabrication of 1D TiO_2/Pt striped nanostructures are reported in chapter 5. Lastly in chapter 6, the photocatalytic functions of the as-prepared TiO_2/Pt striped nanostructures are demonstrated; and the effects of its physical and chemical properties on TiO_2/Pt photocatalytic activities are examined. The opening of each result

chapter comprises an introduction and a literature survey on the current-state-of-art of the respective subjects.

1.6. References

[1] World Energy Council, 2010 Survey of Energy Resources, in, London, 2010.

[2] S. Shafiee, and E. Topal When will fossil fuel reserves be diminished?, Energy Policy, 37 (2009) 181–189.

[3] World Energy Council, World Energy Resources: Solar, in, London, 2013.

[4] J. M. Pearce, Photovoltaics — a path to sustainable futures, Futures, 34 (2002) 663–674.

[5] A. Credi. and M. Venturi . V. Balzani, Photochemical Conversion of Solar Energy, Chem. Sus. Chem., 1 (2008) 26–58.

[6] A. J. Bard, and M. A. Fox, Artificial Photosynthesis: Solar Splitting of Water to Hydrogen and Oxygen, Acc. Chem. Res, 28 (1995) 141–145.

[7] J. A. Turner, A realizable renewable energy future, Science, 285 (1999) 1493-1493.

[8] A. Fujishima and K. Honda, Electrochemical photolysis of water at a semiconductor electrode, Nature, 238 (1972) 37-38.

[9] C.-W.Huang, C.-H. Liao and J. C. S. Wu, Photocatalytic Separate Evolution of Hydrogen and Oxygen over Highly Ordered Nanorods and Bulk TiO_2 Thin Films, JOCET, 1 (2013) 1-5.

[10] J. Yu, L. Qi and M. Jaroniec, Hydrogen Production by Photocatalytic Water Splitting over Pt/TiO_2 Nanosheets with Exposed (001) Facets, J. Phys. Chem. C 114 (2010) 13118–13125.

[11] S. Tabata, H. Nishida, Y. Masaki and K. Tabata, Stoichiometric photocatalytic decomposition of pure water in Pt/TiO_2 aqueous suspension system, Catal. Lett., 34 (1995) 245-249.

[12] A. Galinska and J. Walendziewski, Photocatalytic Water Splitting over $Pt\text{-}TiO_2$ in the Presence of Sacrificial Reagents, Energy & Fuels, 19 (2005) 1143-1147.

[13] M. Kitano, M. Takeuchi, M. Matsuoka, J. M. Thomas, M. Anpo, Photocatalytic water splitting using Pt-loaded visible light-responsive TiO_2 thin film photocatalysts, Catal. Today, 120 (2007) 133–138.

[14] W.-N. Wang, W.-J. An, B. Ramalingam, S. Mukherjee, D. M. Niedzwiedzki, S. Gangopadhyay, and P. Biswas, Size and Structure Matter: Enhanced CO2 Photoreduction Efficiency by Size-Resolved Ultrafine Pt Nanoparticles on TiO_2 Single Crystals, J. Am. Chem. Soc. , 134 (2012) 11276−11281.

[15] S.-Y. Huang, P. Ganesan, S. Park, and B. N. Popov, Development of a Titanium Dioxide-Supported Platinum Catalyst with Ultrahigh Stability for Polymer Electrolyte Membrane Fuel Cell Applications, J. Am. Chem. Soc 131 (2009) 13898–13899.

[16] A.A. Ismail and D.W. Bahnemann, One-step synthesis of mesoporous platinum/titania nanocomposites as photocatalyst with enhanced photocatalytic activity for methanol oxidation, Green Chem., 13 (2011) 428.

[17] S. J. Yoo, T.-Y. Jeon, K.-S. Lee, K.-W. Park and Y.-E. Sung, Effects of particle size on surface electronic and electrocatalytic properties of Pt/TiO_2 nanocatalysts, Chem. Commun., 46 (2010) 794–796.

[18] S. J. Yoo, T.-Y. Jeon Y.-H. Cho, K.-S. Lee, Y.-E. Sung, Particle size effects of PtRu nanoparticles embedded in TiO_f on methanol electrooxidation, Electrochim. Acta, 55 (2010) 7939–7944.

[19] B. M. Kayes , N. S. Lewis and H. A. Atwater, Comparison of the device physics principles of planar and radial p-n junction nanorod solar cells, J. Appl. Phys., 97 (2005) 114302.

[20] K. Kurokawa, Energy from the Desert, in: K. Komoto K. Kurokawa, P. van der Vleuten, D.Faiman (Ed.), vol. 1, Earthscan, London, 2007.

[21] N. Armaroli and V. Balzani, The Hydrogen Issue Chem. Sus. Chem, 4 (2011) 21-36.

[22] B. Kroposki, J. Levene K. Harrison, PK. Sen and F. Novachek, Electrolysis: Information and Opportunities for Electric Power Utilities., National Renewable Energy Laboratory: Golden, CO., (2006) TP-581-40605.

[23] J. Turner, G. Sverdrup, M. K. Mann, P.-C. Maness, B. Kroposki, M. Ghirardi, R. J. Evans and D. Blake, Renewable hydrogen production, Int. J. of Energ. Res. I, 32 (2008) 379–407.

[24] T. Ohta, Solar-Hydrogen Energy Systems: An Authoritative Review of Water-Splitting Systems by Solar Beam and Solar Heat: Hydrogen Production, Storage, and Utilization, in: Pergamon Press: New York, NY, 1979.

[25] N.S Lewis, Light work with water, Nature, 414 (2001) 589-590

[26] A. Heller, Conversion of sunlight into electrical power and photoassisted electrolysis of water in photoelectrochemical cells, Acc. Chem. Res, 14 (1981) 154-162.

[27] M. Ni, M.K.H Leung, K. Sumathy, D.Y.C Leung, Water electrolysis- a bridge between renewable resources and hydrogen., in: Proceedings of the International Hydrogen Energy Forum, Beijing, PRC, 2004, pp. 475-480.

[28] M. G. Walter, E. L. Warren, J. R. McKone, S. W. Boettcher, Q.i Mi, E. A. Santori and N. S. Lewis, Solar Water Splitting Cells, Chem. Rev, 110 (2010) 6446-6473.

[29] M. Ni, M.K.H. Leung, D. Y. C. Leung, and K. Sumathy, A review and recent developments in photocatalytic water-splitting using TiO_2 for hydrogen production Renew. and sust. energ. rev., 11 (2007) 401-425.

[30] R. Kotz and S. Stucki, In-situ identification of RuO_4 as the corrosion product during oxygen evolution on ruthenium in acid media J. Electroanal. Chem. and Interfacial Electrochem., 172 (1984) 211-219.

[31] L. Kavan, M. Gratzel, S. E. Gilbert, C. Klemenz, and H. J. Scheel, Electrochemical and Photoelectrochemical Investigation of Single-Crystal Anatase, J. Am. Chem. Soc., 118 (1996) 6716-6723.

[32] X. H. Yang, Z. Li, G. Liu, J. Xing, C. Sun, H. G.Yang and C. Li Ultra-thin anatase TiO_2 nanosheets dominated with {001} facets: thickness-controlled synthesis, growth mechanism and water-splitting properties Cryst. Eng. Comm, 13 (2011) 1378-1383.

[33] A.Yamakata, T. Ishibashi and H. Onishi, Water- and Oxygen-Induced Decay Kinetics of Photogenerated Electrons in TiO_2 and Time-Resolved Infrared Absorption Study, J. Phys. Chem. B, 105 (2001) 7258-7262.

[34] K. Iwata, T. Takaya H.-o. Hamaguchi, A. Yamakata, T.-a. Ishibashi, H. Onishi, and H. Kuroda, Carrier Dynamics in TiO_2 and Pt/TiO_2 Powders Observed by Femtosecond Time-Resolved Near-Infrared Spectroscopy at a Spectral Region of 0.9-1.5 μm with the Direct Absorption Method, J. Phys. Chem. B, 108 (2004) 20233-20239.

[35] J. Tang, J. R. Durrant, D. R. Klug, Mechanism of Photocatalytic Water Splitting in TiO_2. Reaction of Water with Photoholes, Importance of Charge Carrier Dynamics, and Evidence for Four-Hole Chemistry, J. Am. Chem. Soc., 130 (2008) 13885-13891.

[36] Sheng-Yang Huang, P. Ganesan, S. Park, and B. N. Popov, Development of a Titanium Dioxide-Supported Platinum Catalyst with Ultrahigh Stability for Polymer Electrolyte Membrane Fuel Cell Applications, Journal of American Chemical Society, 131 (2009) 13898–13899.

[37] G. R. Bamwenda, S. Tsubota, T. Nakamura and M. Haruta, Assisted hydrogen production from a water-ethanol solution: a comparison of activities of Au---TiO_2 and Pt---TiO_2 J. Photochem. Photobiol. A, 89 (1995) 177-189.

[38] M. Anpo and M. Takeuchi, The design and development of highly reactive titanium oxide photocatalysts operating under visible light irradiation, J. Catal., 216 (2002) 505-516.

[39] M. Jakob, H. Levanon, P. V. Kamat, Charge Distribution between UV-Irradiated TiO_2 and Gold Nanoparticles: Determination of Shift in the Fermi Level, Nanoletters, 3 (2003) 353-358.

[40] A. P. Alivisatos, Perspectives on the Physical Chemistry of Semiconductor Nanocrystals, J. Phys. Chem., 100 (1996) 13226-13239.

[41] V. Callegari, and S. D.-Champagne, Using the Hard Templating Method for the Synthesis of Metal-Conducting Polymer Multi-Segmented Nanowires, Macromol. Rapid Commun., 32 (2011) 25-34.

[42] S. J. Hurst, E. K. Payne L. Qin, and C. A. Mirkin, Multisegmented One-Dimensional Nanorods Prepared by Hard-Template Synthetic Methods, Angew. Chem. Int. Ed., 45 (2006) 2672 –2692.

[43] M. R. Kim, D. K. Lee and D.-J. Jang, Template-based electrochemically controlled growth of segmented multimetal nanorods, J. Nano Mat., 2010 (2010) 1-7.

[44] F. Liu, J.Y. Lee, and W. Zhou, Multisegment PtRu Nanorods: Electrocatalysts with Adjustable Bimetallic Pair Sites Adv. Funct. Mater., 15 (2005) 1459-1464.

[45] J. Wang, Barcoded metal nanowires, J. Mat. Chem, 18 (2008) 4017–4020.

[46] J. A. Sioss, R. L. Stoermer, M. Y. Sha, and C. D. Keating, Silica-Coated, Au/Ag Striped Nanowires for Bioanalysis, Langmuir, 23 (2007) 11334–11341.

[47] C. M. Hangarter and N. V. Myung, Magnetic Alignment of Nanowires, Chem. Mater., 17 (2005) 1320-1324.

[48] Y.-G. Guo, L. J. Wan C.-F. Zhu, D.-L.Yang, D.-M. Chen, and C.-L. Bai, Ordered Ni-Cu Nanowire Array with Enhanced Coercivity, Chem. Mater. , 15 (2003) 664-667.

[49] L. Piraux, K. Renard, R. Guillemet, S. M.-Tempfli, M. M.-Tempfli, V. A. Antohe, S. Fusil, K. Bouzehouane, and V. Cros, Template-Grown NiFe/Cu/NiFe Nanowires for Spin Transfer Devices, Nanolett., 7 (2007) 2563-2567.

[50] J. S. Tresback, A. L. Vasiliev, N. P. Padture, S.-Y. Park, and P. R. Berger, Characterization and Electrical Properties of Individual Au–NiO–Au Heterojunction Nanowires, TNANO, 6 (2007) 676-681.

[51] V. Callegari, L. K. Gence, S. Melinte, and S. D.-Champagne, Electrochemically Template-Grown Multi-Segmented Gold-Conducting Polymer Nanowires with Tunable Electronic Behavior, Chem. Mater., 21 (2009) 4241–4247.

[52] C. D. Keating and M. J. Natan, Striped Metal Nanowires as Building Blocks and Optical Tags, Adv. Mater., 15 (2003) 451-454.

[53] S. R. N.-Pena, A. J. Carado, K. E. Shale, and C. D. Keating, Barcoded Metal Nanowires: Optical Reflectivity and Patterned Fluorescence, J. Phys. Chem. B, 107 (2003) 7360-7367.

[54] F. Liu, J. Y. Lee and W. J. Zhou, Segmented Pt/Ru, Pt/Ni, and Pt/RuNi Nanorods as Model Bifunctional Catalysts for Methanol Oxidation, Small 2(2006) 121 – 128.

[55] H.-M. Zhang, Y.-G. Guo, L.-J. Wan and C.-L. Bai, Novel electrocatalytic activity in layered Ni–Cu nanowire arrays, Chem. commun., (2003) 3022–3023.

[56] F. Liu, J. Y. Lee, W. Zhou, Template Preparation of Multisegment PtNi Nanorods as Methanol Electro-Oxidation Catalysts with Adjustable Bimetallic Pair Sites, J. Phys. Chem. B, 108 (2004) 17959-17963.

Chapter 2: Instrumentation and Characterization Technique

2.1. Introduction

A large part of the work in this thesis is concerned with the analysis and characterization of TiO_2/Pt nanostructures synthesized using templated electrodeposition through the use of various instruments. These involved structural, chemical and electrochemical analysis and optical absorption studies. The results of the studies are described in chapter 3 to 6. In this chapter, all of the characterization techniques and synthesis methods used in this study are introduced, and the background on the instrumentation, operation, and theory of each technique provided.

2.2 Morphology

2.2.1 Scanning Electron Microscopy (SEM)

2.2.1.1 Operation and Instrumentation of SEM

Scanning electron microscopy (SEM) is a technique used for the observation of sample surfaces. Free electrons, produced by the thermionic emission gun, are focused into a fine beam using a series of condenser lenses. The electron beam scans and interacts with the sample to yield secondary electrons and backscattered electrons which are collected by the respective detectors and amplified to produce an image.

In this thesis, the FIB-SEM (Carl Zeiss Auriga 40) and the high resolution field emission gun scanning electron microscope (FEG-SEM) (LEO Gemini 1525) were used in the imaging of the morphology of the as-prepared single-segment TiO_2/Pt and multi-segmented TiO_2-Pt nanostructures.

2.2.1.2 Imaging Modes of SEM

There are three imaging modes available in the SEM: the secondary electrons (SE) mode, backscattered electrons (BSE) mode and In Lens. The energy of secondary electrons is small (< 50 eV), hence the SE detector only collects those emitted from the top surface. This means images collected in the SE mode are very sensitive to the surface. The In-Lens detector complements the SE detector for the imaging of samples at higher resolution using shorter working distances (between the objective lens and the sample).

Backscattered electrons arise as a result of the back scattering of the electrons from the incident electron beam. Possessing higher energy than secondary electrons, backscattered electrons interact deeper in the sample and the reflected electrons are sensitive to the sample composition. A sample area, which consists of heavier elements will produce a brighter image due to the higher intensity of the back scattered electrons. The BSE mode hence shows large contrast between regions of Pt and TiO_2 owing to the large difference in the atomic numbers of the elements.

2.2.1.3 Sample Preparation

When imaging charging occurs in non-conductive or in samples with low conductivity where the electrons are unable to flow through the material. Under continuous irradiation by the electron beam, the sample surface accumulates electrons and becomes negatively charged. This causes an image distortion as the position of the electron probe shifts because of the repulsion between the electron probe and the negatively charged surface.

To minimise the effect of charging, non- or low- conductive samples are coated with a thin film of highly conductive elements such as Au or Cr. A thin film of a few nm is coated on the sample in order to maintain the original surface of the sample. For all SEM imaging of samples consisting of TiO_2, Cr is sputtered at 75 mA for 2 minutes using the Emitech K575X turbo sputter coater. The nominal thickness of the Cr layer is 300 nm.

2.2.2 Transmission Electron Microscopy (TEM)

2.2.2.1 Operation and Instrumentation of TEM

The transmission electron microscopy (TEM) is a more sophisticated electron microscope compared to the SEM. It possesses a higher magnification level of up to 50 million and a higher resolution of 0.5 angstroms, hence allowing closer examination of samples down to the atomic scale.

The TEM sample is prepared by depositing the specimen of interest on a thin copper mesh grid transparent to the electron beam and placed in front of the objective lens. Electrons

pass through the sample and a series of lenses, and are scattered and recombined to produce diffraction patterns or images.

The FEI TEM Titan 80/300 and JEOL 2010 TEM were used in the analysis of the interfaces between segments of multi-segmented TiO_2-Pt nanorods.

2.2.2.2 Image Contrast in TEM

Imaging contrasts in TEM uses techniques of mass-thickness, phase and diffraction contrast. In mass-thickness contrasts, thinner regions (consisting of lower mass atomic elements) appear brighter in the image. Phase contrast provides information about crystal order and defects, while diffraction contrast can be used for the study of crystal defects.

2.3 Chemical Analysis

2.3.1 Energy-dispersive X-ray Spectroscopy (EDS)-TEM

2.3.1.1 Operation and Instrumentation of EDS

Energy-dispersive X-ray spectroscopy (EDS) is a non-destructive analytical technique employed to identify specific elements present in the sample and their relative proportions. With an x-ray spectrometer added to the SEM and TEM, EDS element mapping and point analysis can be performed on a chosen scanned area or point image of a sample produced by electron microscopy. X-ray analysis in the TEM provides qualitative and quantitative analysis of samples with a spatial resolution down to the nanometer scale.

The four primary components in an EDS setup are the excitation source from electron or x-ray beam, the x-ray detector, the pulse processor and the analyzer. Images of the sample are provided by the electron beam excitation in the SEM and TEM. Characteristic x-rays of the material are emitted as a result of electron transitions between inner orbits of the element and the x-rays are collected by the detector, which convert the x-ray energies into voltage signals. These voltage signals are then read by the pulse processor and analyzed by the pulse analyzer to produce output pulses proportional in height to the x-ray photon intensity at a specific wavelength.

2.3.1.2 Qualitative EDS Analysis

An EDS spectrum is commonly presented as a plot of the number of counts against the x-ray energy. Unknown elements in the sample can be easily identified by matching the corresponding line energies in the x-ray spectrum with those from the energy table.

2.3.1.3 Quantitative EDS Analysis

A quantitative EDS analysis can be carried out with or without a standard by using EDS analysis software (in this case, INCA). In a standard analysis, the software first performs a Gaussian fit of the elements, from which the area-under-the-peak calculates the respective elemental concentrations of the sample. The areas for each element are then compared to the same elements in the calibration standards of known composition. Standardless quantification is performed in a similar manner, except that instead of measuring against a calibration standard, the software performs ZAF (atomic number-absorption-fluorescence) corrections on the areas under the peaks.

In general, EDS analysis software runs on an approximation where the primary generated characteristic x-ray intensities, I_i are proportional to the respective mass fraction of the elements, C_i (equation 2A). This originated from the theory proposed by Castaing [1], which postulated a directly proportional relationship between the relative intensity of a x-ray line to the mass concentration of its respective element. This is based on an assumption that the number of electrons ejected per atom due to electron excitation equals the atomic number, which is in turn proportional to its atomic weight.

$$C_i \propto I_i \qquad \text{(Equation 2A)}$$

The intensity and concentration of element i are then compared against a standard of the same element with a generated intensity, $I_{(i)}$ and a known concentration, $C_{(i)}$ (equation 2B). The ratio of the intensities of the sample and standard is frequently known as the k-ratio (equation 2C).

$$C_i / C_{(i)} \propto I_i / I_{(i)} \qquad \text{(Equation 2B)}$$

where $I_i/I_{i)} = k_i$ (Equation 2C)

To account for the energy lost through scattering of x-rays and propagation through the sample, a matrix correction factor for element i, $[ZAF]_i$ is added to equation 2D. ZAF consists of the atomic number correction, Z, the absorption correction, A, and the florescence correction F. Given that ZAF is unknown and is dependent on the composition of the sample (which is also an unknown before analysis), the analytical software therefore performs an iteration to calculate the value of C_i.

$C_i / C_{(i)} = k_i [ZAF]_I$ (Equation 2D)

2.3.1.4 Elemental Mapping

An image produced by elemental mapping in the EDS shows the spatial distrubution of elements present in a sample. It is particularly useful in displaying elemental distributions in a sample consisting of varying elemental bulk compositions.

By specifying the elements and the area of interest, the sample is scanned to produce a digital image of each chosen element present. The map of each element is produced by rastering the electron beam point by point over the area, and dots are progressively formed as emitted x-rays are detected. The resolution of the elemental map depends on factors such as the beam size, how long the beam dwells on each point and the concentration of the element in the sample. Compared to a simple line scan, element maps are more informative as they provide a more accurate two-dimensional image of the chemical zones within the sample.

2.3.2 X-Ray Powder Diffraction (XRD)

2.3.2.1 Operation and Instrumentation of XRD

The most commonly used XRD diffraction instrument has measurement geometry as shown in figure 2-1. Both the incoming and exiting beam has an angle of θ with respect to the planar or flattened sample surface. By varying the angle of incidence of the incoming x-ray

beam by θ and the scattering angle by θ, a diffraction pattern is collected. Concurrently, the scattered intensity is measured as a function of 2θ.

As indicated in figure 2-1, a goniometer comprises of at least two axes of rotation. The sample is placed on the rotational axis while the x-ray source and detector rotates along the peripheral axis, with axes of rotation aligned with each other.

Generally, there are two types of x-ray instruments. One involves a fixed x-ray source and the rotation of the sample around θ, while the detector moves by 2θ. Another requires the sample to be fixed while both the x-ray source and detector rotate by θ simultaneously in opposite directions. These rotations are carried out by a goniometer. The D2 phaser (Bruker) XRD used predominantly in this study operates with the latter configuration.

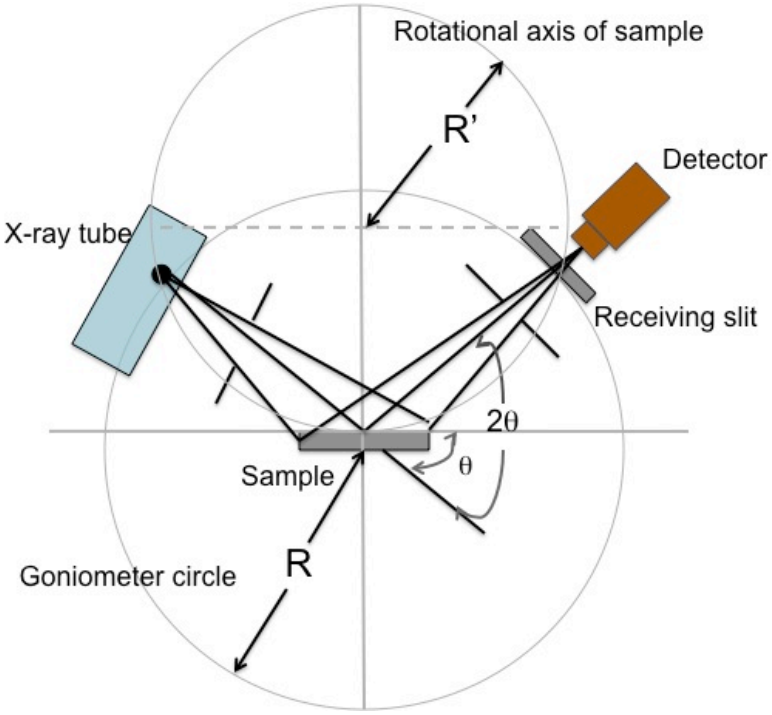

Figure 2-1. Schematic representation of a basic θ/2θ measurement geometry in a x-ray diffraction instrument

The interaction of x-rays with the sample produces secondary diffracted x-ray beams, which relate to the interplanar spacings in the material according to Bragg's Law, equation 2E.

$2d \sin\theta = n\lambda$ (Equation 2E)

where n is an integer

λ is the x-rays wavelength

d is the interplanar spacings resulting in diffraction

θ is the diffracting angle

Bragg diffraction occurs when x-rays comparable to the atomic spacings of a crystalline material scatter and undergo constructive interference as described in Bragg's law. The waves are scattered from the lattice planes at an angle θ, which are separated by interplanar spacing, *d*. Since for constructive interference the difference in path length of two waves is an integer multiple of the wavelength, n, constructive interference occurs when $n\lambda = 2d \sin\theta$, as shown in figure 2-2.

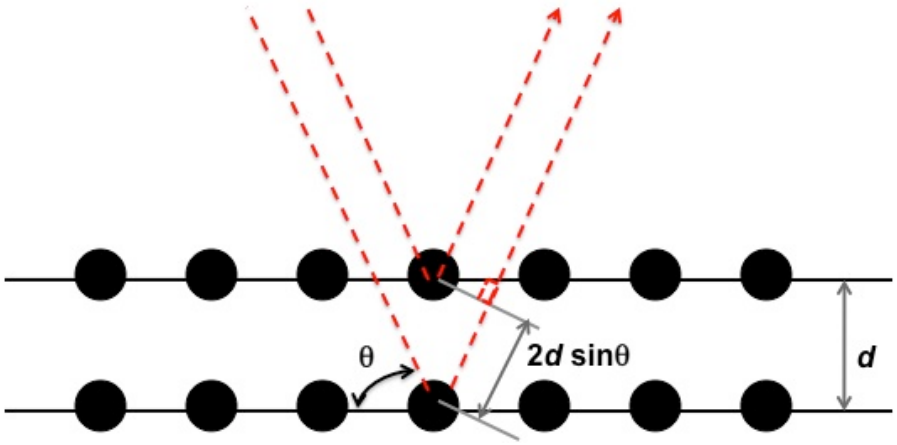

Figure 2-2. Schematic diagram of Bragg diffraction where two beams with identical wavelength and phase are incident on a crystalline material and are scattered off two different atoms within. Constructive interferences of the waves result in waves with a path difference of $2d \sin\theta$.

2.3.2.2 Sample preparation and XRD measurements

X-ray diffraction (XRD) was used in the identification of TiO_2 and Pt present in the synthesized compounds; calculation of crystallite sizes from respective line profile widths;

and quantification of the relative amounts of different phases present in the TiO_2 nanostructures by use of peak-ratio calculations.

The D2 Phaser (Bruker) was used for all XRD measurements of synthesized TiO_2 and Pt compounds. The sample was prepared by grinding down the material to obtain homogeneous, randomly distributed crystallites. It was then pressed onto a sample holder into a smooth flat plane so as to ensure uniform distribution of crystallites contributing to a given set of h, k, l planes.

2.3.2.3 High Temperature X-Ray Diffraction (HTXRD)

High temperature X-ray diffraction (HTXRD) is often employed to study the *in-situ* phase transformations of a compound and crystallite size changes that occur with annealing temperatures. Powder XRD data of TiO_2 samples were obtained on a Philips X'pert diffractometer. The TiO_2 sample (consisting of TiO_2 nanostructures dispersed on Au/glass substrate) was mounted on a platinum-heating strip connected to a thermocouple and the data was collected in continuous mode.

2.4 Electrochemical Deposition

Electrochemical deposition is a technique used to deposit materials from their ions present in an electrolyte and is based on three general principles, ion transport, electron transfer and incorporation [2]. In this thesis, electrodeposition is employed in the fabrication of all one-dimensional (1D) single segment TiO_2/Pt and multi-segmented TiO_2-Pt nanostructures in the pores of anodic aluminium oxide membrane (AAM) templates using a potentiostat. The technique of electrodeposition using templates such as AAM is more specifically known as templated electrodeposition.

Industrially, electrodeposition may consist of a two-electrode electrochemical cell system with a cathode and an anode. The flow of electrons from the anode to the cathode results in a potential difference across the electrochemical cell, otherwise known as the cell potential. The cell potential is determined by the ability of the anode to be oxidized and the cathode to be reduced, which represents the overall potential energy that drives the redox reactions. In this work, a three-electrode electrochemical cell system is employed for the electrodeposition of TiO_2 and Pt. The three-electrode cell system comprises of a working electrode (WE), counter electrode (CE) and reference electrode (RE)

connected to the potentiostat, which allows for the reaction of interest to be focused at a single interface.

2.4.1 Potentiostat

A potentiostat is an electronic instrument with two main functions. The first function is to measure and control the voltage difference between the WE and RE; and the second function is to measure the current flow between the WE and CE. This is achieved through an electronic circuit, where the measurement resistance is altered to allow the current to be measured over several orders of magnitude according to Ohm's law (Equation 2F).

$E_o = I_o R_v$ (Equation 2F)

Where E_o is an output voltage of the potentiostat which is proportional to the current

I_o is the electrochemical current of the potentiostat

R_v is the variable resistance of system

In this study, electrodeposition is performed with the potentiostat/galvonostat instrument, PGSTAT12 using Autolab software. The most common modes of electrochemical cell measurements that can be controlled using the potentiostat/galvonostat (PGSTAT) are potentiostatic and galvonostatic. In the potentiostatic mode (figure 2-3), the PGSTAT controls the potential of the counter electrode (CE) against the working electrode (WE), so as to achieve the specified value of potential difference between the working electrode (WE) and the reference electrode (RE). The corresponding output is current. In the galvonostatic mode, current flow between the WE and CE is controlled, and the potential difference between the WE and RE is continuously monitored.

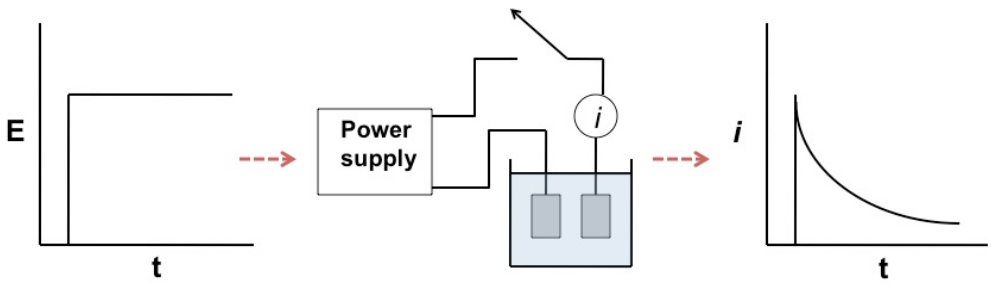

Figure 2-3. Schematic diagram representing potentiostatic mode where a potential step is applied and the response is an observed *i*-t curve.

The basic circuit of the PGSTAT is shown in figure 2-4 [3]. The PGSTAT has three inputs from the cell (WE, CE, RE) and works on a negative feedback mechanism. The flow of current through the cell is directed and regulated by the control amplifier (CA) connected to the CE. Low currents are measured by the Current Follower (LowCF), while high currents are measured by the Shunt (highCR). A voltage follower employs the differential amplifier (Diffamp), which regulates the output voltage, Eout, proportional to the potential difference between WE and RE. The feedback of the PGSTAT switches from cell voltage signal or cell current signal according to the mode (potentiostatic or galvonostatic) chosen. Together with the waveform set at E_{in}, the chosen signal type is then fed into the Summation Point ($\sum$), which is an input into the CA.

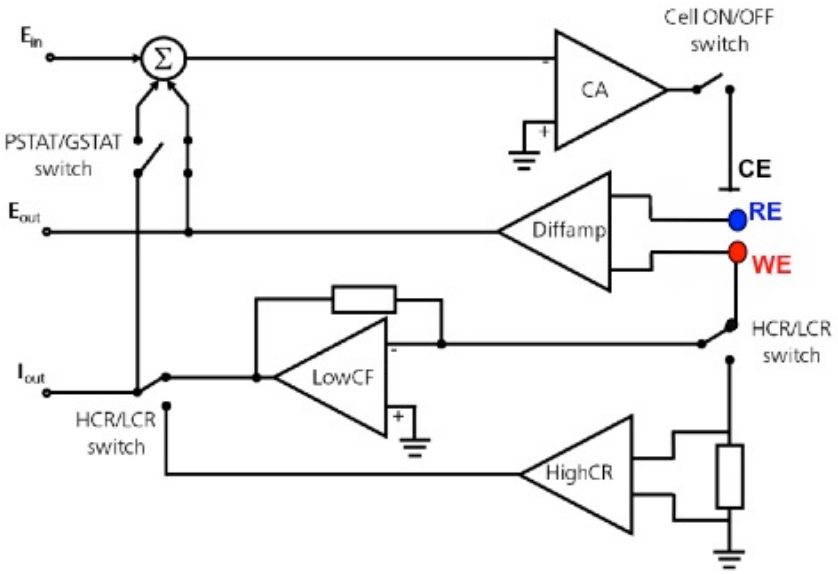

Figure 2-4. Basic circuit of a potentiostat/galvonostat (PGSTAT)

2.4.2 Setup of Electrochemical Cell

Figure 2-5 shows the setup of the three-electrode electrochemical cell used in this study. It consists of a counter, reference and working electrode used in conjunction with the potentiostat. The counter electrode is an electrode, which is used to complete the current circuit in the electrochemical cell. It is usually made of an inert conductor, in this case a platinum mesh, which does not participate in the electrochemical reactions. The silver/silver chloride Ag/AgCl (1 M KCl) electrode with a well-known electrode potential of +0.235 V vs. standard hydrogen electrode (SHE) is used as a reference electrode for potential control and measurement. It possesses a high stability, which is reached by employing the Ag/AgCl redox system consisting of species with constant concentrations. The electrochemical potential of the

Ag/AgCl (1 M KCl) reference electrode is kept constant by restricting current flow through the electrode. The working electrode, typically a metal-coated porous aluminium oxide membrane (AAM) (figure 2-6) is the electrode in which the reaction of interest (e.g. deposition of TiO_2 and Pt) occurs. It is coated with silver on one side to cover the pores and to make it conductive as a working electrode. The silver-coated side of the AAM is then placed on an extended metal plate connected to the potentiostat.

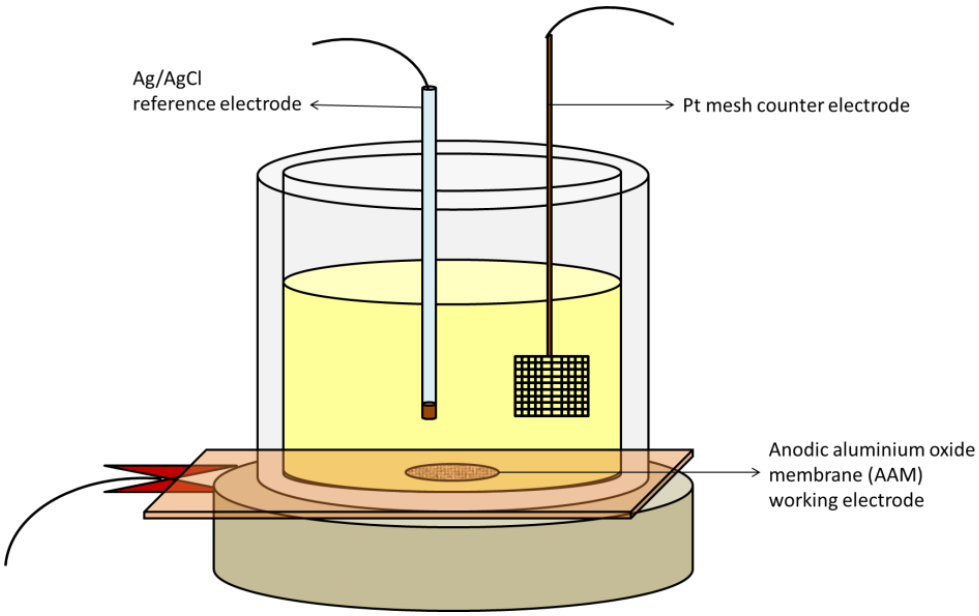

Figure 2-5. Setup of electrochemical cell and electrodes

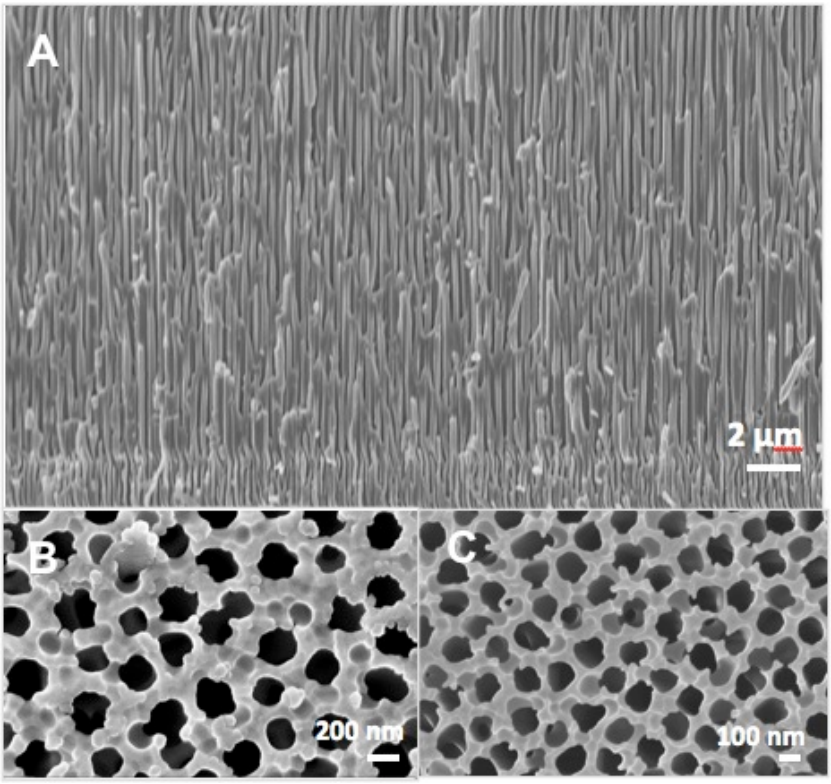

Figure 2-6. SEM images of a blank aluminium oxide membrane (AAM) showing A) cross-section, B) top and C) bottom used as a working electrode in the templated electrodeposition of 1D nanostructures.

2.4.3 Electrochemical Cell Technical Drawing

The technical drawings of the electrochemical cell used are shown in figure 2-7 and the represented views are as labeled. The bottom views represent three individual cell bodies with varying electrode exposure diameters of 10 mm, 15 mm and 25 mm, providing a deposition area size of 0.79 cm^2, 1.77 cm^2 and 7 cm^2 respectively. The technical drawings are provided by Simon Teow Geck Heng using AutoCAD and the cell was constructed by Russell J. Stracey.

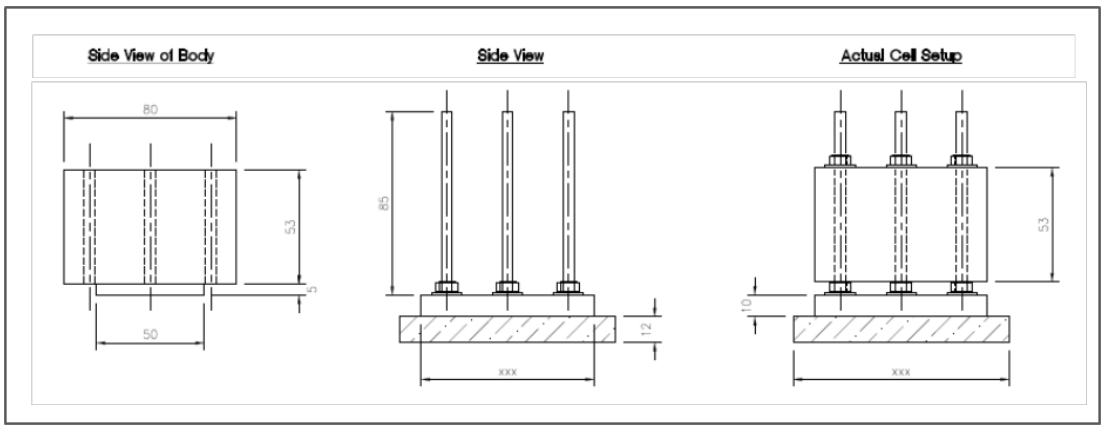

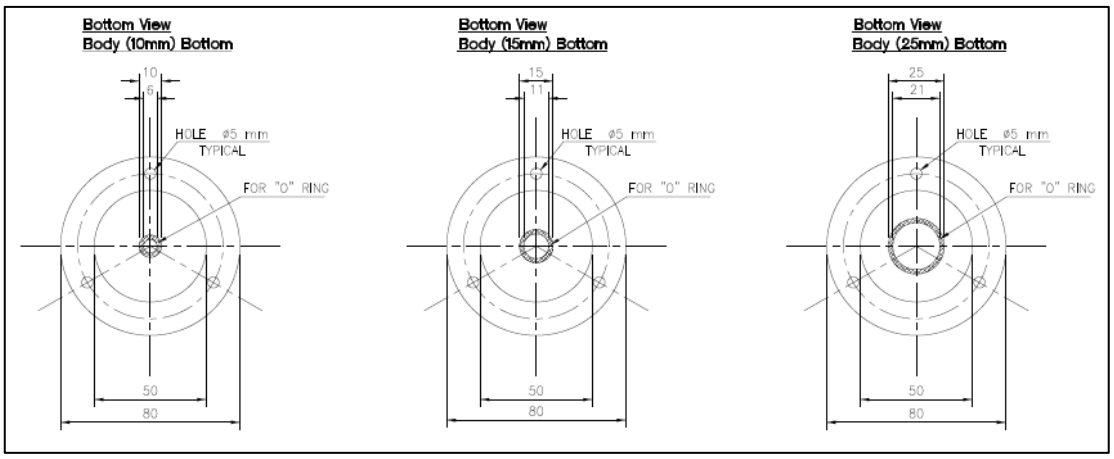

Figure 2-7. Technical drawings of the electrochemical cell representing the whole cell, side and bottom views

2.5 Electrochemical Studies

2.5.1 Cyclic Voltammetry – the Instrumentation

Cyclic voltammetry (CV) is an electrochemical technique, which measures the current that develops in an electrochemical cell, as a triangular waveform potential is being applied to the working electrode, as shown in figure 2-8. In a forward scan according to figure 2-8, the potential first scans negatively from a higher potential (a) to a lower potential (b). The switching potential occurs at (d), where the voltage is sufficient to oxidize or reduce an analyte. This is followed by a reverse scan from (d) to (g) to indicate a positive potential scan. In CV, a general convention is adopted, where positive currents are *anodic*, while negative-going currents are *cathodic*. In general, the reproducibility of cyclic voltammetry depends on several factors such as electrolyte purity, type of electrode material, choice of potential limits and the rate of change of potential. The potential scan rate is commonly chosen to be greater than 10 mV s^{-1}, as slower scan rates may cause perceptible de-activation of the electrode surface [4]. The scan rate is defined by the slope of the potential-time plot in figure 2-8. By measuring the current at the working electrode during potential scans, a cyclic voltammogram is obtained.

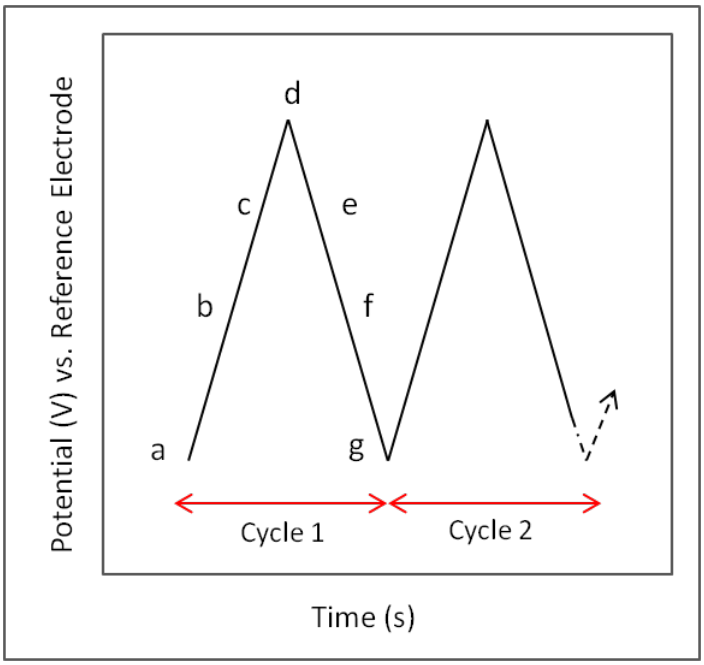

Figure 2-8. Potential-time behavior at the working electrode by imposition of a triangular waveform

2.5.2 Cyclic Voltammogram – the Theory

Figure 2-9 displays a general cyclic voltammogram characteristic of a reversible reduction and oxidation reaction of a single electrode according to equation 2G.

$$M^{+} + e^{-} \leftrightarrow M \quad \text{(Equation 2G)}$$

In figure 2-9, the potential is scanned negatively to cause a reduction to occur from the initial potential (a) to the switching potential (d). Point (c) represents the cathodic peak potential (E_{pc}), where all of the substrate at the surface of the working electrode has been reduced; and results in a cathodic current I_{pc}. A positive scan occurs after the switching potential at (d), where an oxidation reaction occurs from (d) to (g). The cycle can be repeated and the scan rate varied as required.

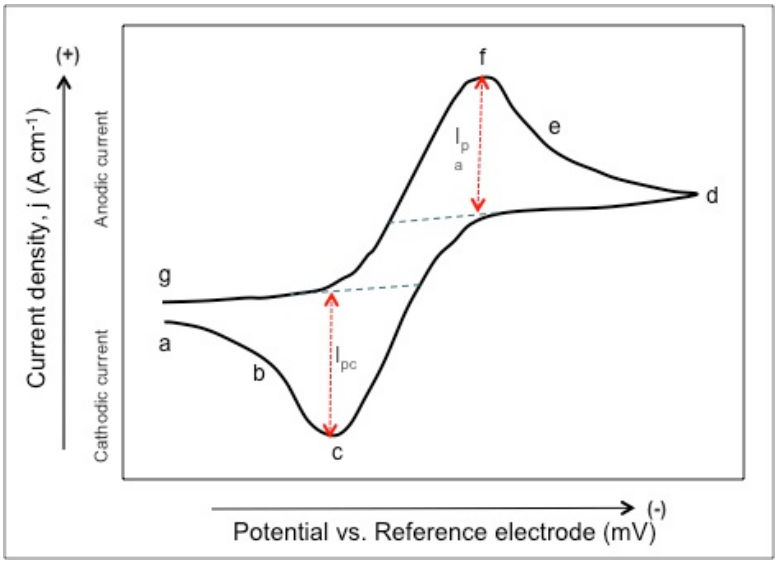

Figure 2-9. A general cyclic voltammogram of a reversible, single electron oxidation-reduction reaction

Unlike in a reversible cyclic voltammetry, an irreversible cyclic voltammetry as shown in figure 2-10 reflects an asymmetrical between the oxidation and reduction peak. This asymmetry in the CV wave may occur when an analyte, which is being reduced or oxidized on the forward scan does not reoxidized or re-reduced in a predicted way on the backward scan. The irreversibility of the redox reactions is typically reflected in the CV scans shown in chapter 4.

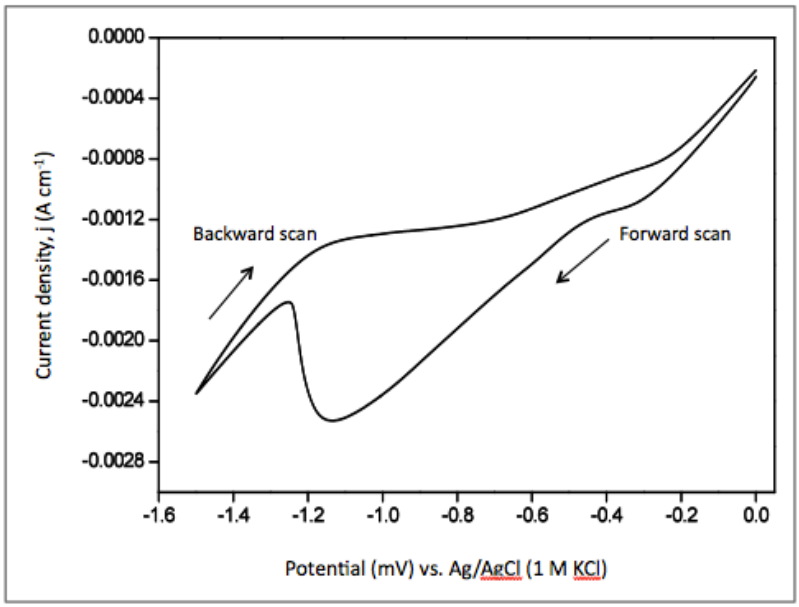

Figure 2-10. A cyclic voltammetry scan (20 mV s^{-1}) showing an irreversible redox reaction occurring at aluminium oxide membrane (area=0.79 cm^2) in pH 3 aqueous solution of KNO_3+H_2O_2

2.5.3 Cyclic Voltammetry Measurements

Cyclic voltammetry studies were carried out using an AUTOLAB PGSTAT12 instrument in a three-electrode cell consisting of Ag flat and silver-coated AAM as the working electrodes, Pt mesh as the counter electrode, and Ag/AgCl (1 M KCl) as the reference electrode. All CV scans were carried out at a scan rate of 20 mV s^{-1}.

2.6 Optical Absorption Studies

2.6.1. Ultra-violet-visible (UV-Vis) Spectroscopy

UV measurements were taken using the UV-Vis spectrometer (Perkin Elmer, Lamda Bio 10). Figure 2-11 illustrates the general component parts of a UV-Vis spectrometer. The UV-Vis spectrometer operates by providing a beam of monochromatic light to illuminate the sample. By measuring the intensity of light, which passes through the sample (I) against the intensity of light before it passes through the sample (I_O), the ratio I/I_O is the transmittance expressed as a percentage (%T). Based on the transmittance, the absorbance (A) is related to the %T by the expression, A= -log (%T/100%) and the absorbance of the sample is directly proportional to the concentration of the absorbing species in the solution and the path length according to the Beer-Lambert law. The output signal of the spectrometer is represented by a plot of the absorbance on the vertical axis plotted against the wavelength.

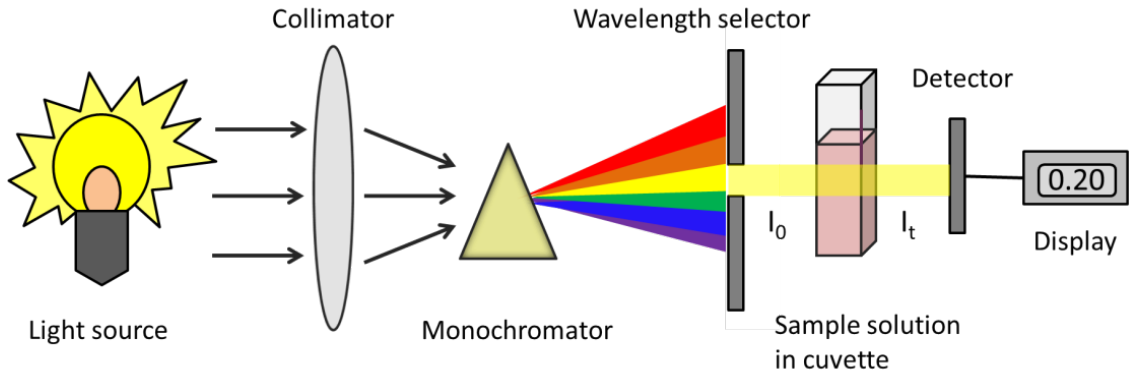

Figure 2-11. Schematic diagram of a UV-Vis spectrometer

2.6.2. Design Setup for Rhodamine Degradation Studies

The photoactivity of as-prepared TiO_2 and TiO_2/Pt nanorods were studied by measuring the rate of decomposition of Rhodamine B (RhB) in solution using the UV-vis spectrometer. The photocatalytic reaction of each sample was carried out using the setup, designed in-house, shown in figure 2-12. The samples were immersed in RhB solution in a cuvette held in a fixed position by the cuvette holder from a solar simulator irradiation source, a xenon lamp (LPS-220, Photon Technology International) providing a constant illumination of 26.5 µW cm^{-2}. IR filters were placed in front of the light source to reduce the heat intensity passing through and to prevent the sample from rapid heating.

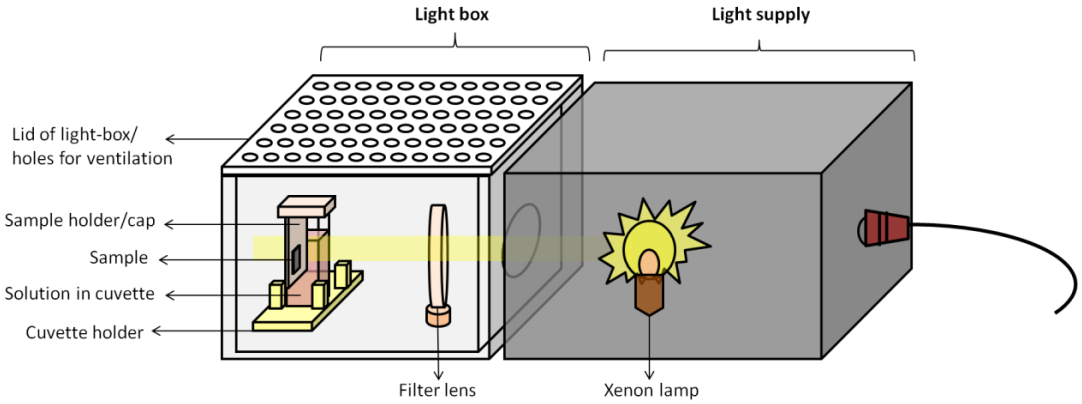

Figure 2-12. A schematic setup consisting of a light supply and light box housing the samples and filter lens used for absorption studies

2.6.2.1. Light box and Box Lid Technical Drawings

The technical drawings of the light box and box lid are shown in figure 2-13, where their respective sides are as indicated. Both the light box and lid are made of steel. Holes of diameter 1 mm were designed at the side of the light box and the top of the lid to prevent heat from building up in the lightbox. The technical drawings are provided by Simon Teow Geck Heng using AutoCAD and the light box was constructed by Mike Lennon.

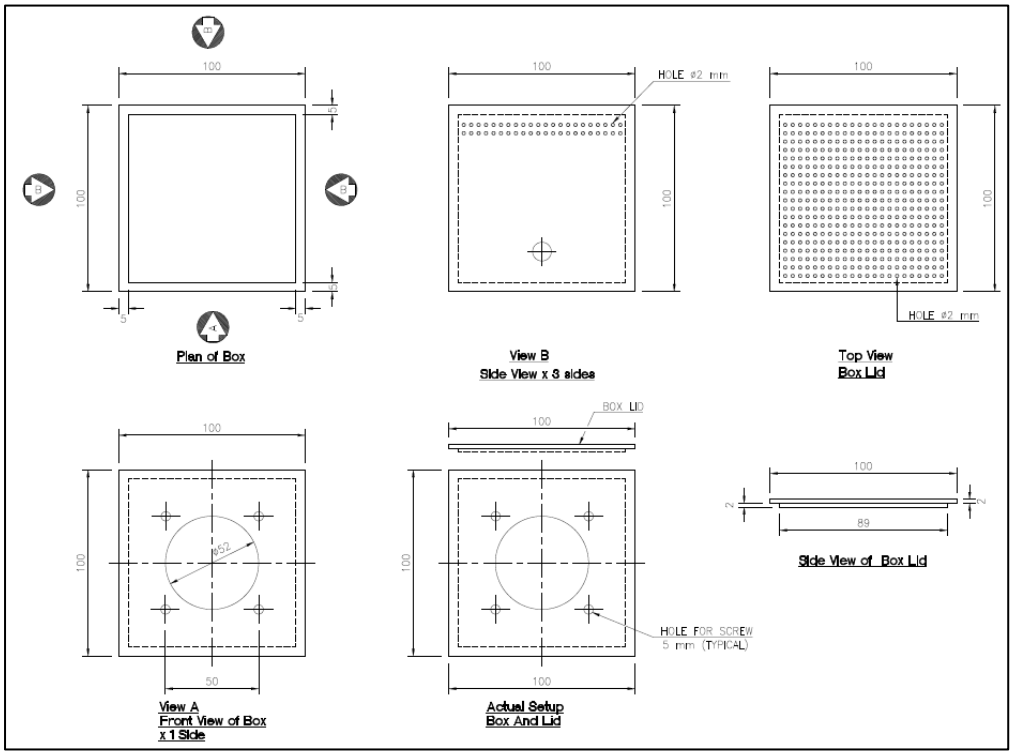

Figure 2-13. Technical drawings of the light box and box lid representing their side and top views

2.6.2.2. Sample Holder/Cap Illustration

A diagram showing the various perspectives of the sample holder/cap is illustrated in figure 2-14 and the position of the sample placement has been outlined. The sample holder/caps were 3-D printed with the help of Reva Vaze and Gareth D M Morris.

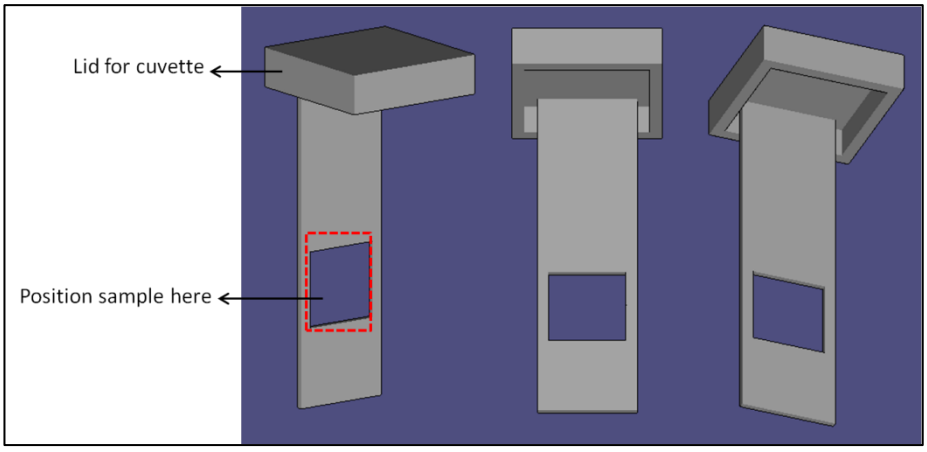

Figure 2-14. Diagram showing various perspective of the sample holder/cap

2.6.2.3. Cuvette Holder Illustration

A diagram of the cuvette holder is shown in figure 2-15. It functions to position 2 cuvettes in fixed locations from the light source. The cuvette holder was 3-D printed with the help of Reva Vaze.

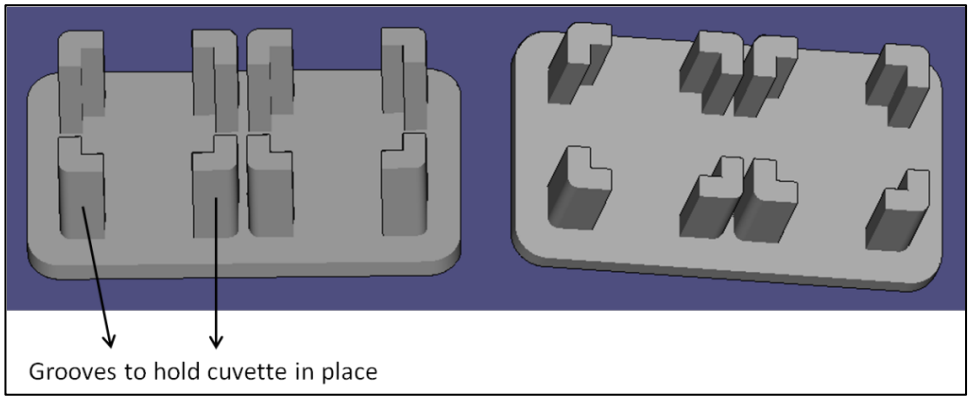

Figure 2-15. Diagram of the cuvette holder

2.6.3. Integrating Sphere

2.6.3.1. Operation and Instrumentation of Integrating Sphere

An integrating sphere is an optical device consisting of a hollow spherical cavity covered with a highly diffusing and highly reflective interior coating. It has port openings to allow for light to enter and exit, and it is also where detectors and light sources are located. The total area of the port openings are small and usually take up no more than 5% of the sphere surface area. Integrating sphere is commonly employed for optical, photometric and radiometric measurements.

Originating from the theory of radiation exchange within a spherical enclosure, light that is incident on any point on the inner spherical surface are distributed equally to all other points by multiple scattering reflections. This allows the accurate measure of the total light intensity radiated in all angles and directions from the light source, through average diffuse reflectance of the interior surface. The sum of all light intensity incident on the small aperture of the input port is then collected and measured by a detector connected to the integrating sphere. Spectroradiometers consisting of a detector coupled to a

spectral separation device such as a diffraction grating monochromator provide measurements of light as a function of wavelength.

2.6.3.2. Reflectance and Transmittance of Materials

The largest application for the integrating sphere is the reflectance and transmittance measurements of diffuse or scattering materials. These measurements are commonly performed spectrally, as a function of wavelength. To measure the transmittance of a material, the sample is placed at the entrance port to the sphere as shown in figure 2-16 (A); while in reflectance measurements, the sample is placed at the port opening located opposite the entrance port where the incident flux is reflected by the sample (figure 2-16 (B)). The detector then collects the total hemispherical reflectance consisting of both the diffuse and specular reflections.

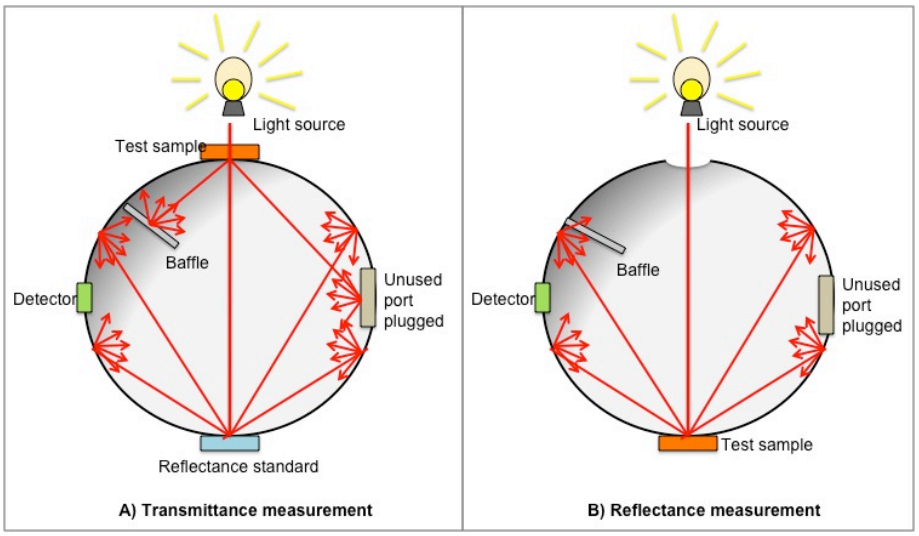

Figure 2-16. Simplified illustration of the use of an integrating sphere for A) transmittance and B) reflectance measurements

In this study, integrating sphere measurements were performed on freestanding arrays of bi-segment TiO_2/Pt nanorods using an in-built integrating sphere of the Cary 5000 series UV-vis-NIR (Agilent Technologies). The sample area for analysis is approximately 0.17 cm^2, which is confined by the characteristic port opening diameter size of 0.4 cm.

2.7. References

[1] R. Castaing, Application des Sondes Electro- niques a une Methode d'Analyse Ponctuelle Chimique et Crystal-lographique, in, Univ. Paris, 1951.

[2] M. Paunovic, and M. Schlesinger, Fundamentals Of Electrochemical Deposition in: The Electrochemical Society Series, John Wiley & Sons, Inc., Hoboken, New Jersey, 2006.

[3] Metrohm Autolab, Basic overview of the working principle of a potentiostat/galvanostat (PGSTAT) – Electrochemical cell setup, in: Autolab Application Note EC08, Ecochemie, 2011.

[4] H. Hamann, A. Hamnett, and C. W. Vielstich, Electrochemistry, Wiley-VCH Verlag GmbH & Co. kGaA, Germany, 2007.

Chapter 3: Synthesis of Pt Nanorods and Experimental Procedures

3.1. Introduction

3.1.1. Nano-sized Pt catalysts

For many years, platinum has played a key role as a noble metal catalyst for specific reactions and in industrial applications. It has received considerable attention as an excellent catalyst in areas such as the oxidation of harmful nitrogen oxides (NO_x) and carbon monoxide (CO) in diesel and gasoline engine exhausts [1, 2]; in the processes of hydrogenation [3] and production of nitric acid [4]; and as a critical electro-catalyst for the oxygen reduction reaction (ORR) and fuel oxidation reactions of hydrogen, methanol, ethanol and formic acid in the fuel cell technology [5, 6].

As supply decreases and the gross demand for platinum grows, the price for platinum continues to remain high at an average of US$ 1435 per oz in 2014 [7]. The high cost of platinum presents an impediment to the commercialization of Pt catalysts, fuelling interests in increasing its catalytic efficiency in order to reduce the amount of Pt required. One way of meeting this challenge is to develop Pt catalysts of finer sizes such as nanoparticles and nanostructures of Pt. By increasing the active surface area of Pt, the amount of noble metal required decreases, thereby lowering the overall costs of applications involving Pt [8].

The enhancement of the catalytic properties of Pt nanocrystals in catalytic and electrocatalytic reactions can be evaluated in terms of its reactivity, selectivity and stability [9]. Studies have suggested that the shape of a Pt nanocrystal affects both its catalytic reactivity and selectivity. Through studies of benzene hydrogenation on surface shape-controlled cubic and cuboctahedral Pt nanoparticles, Bratlie and co-workers [10] noted that in contrast to the single crystal Pt (100) in cubic particles, cuboctahedral particles with additional Pt (111) surfaces promoted the production of cyclohexene. The surface activation energies and higher turnover rates obtained from kinetic data and Arrhenius plots showed that a larger presence of edge and corner atoms holds the key to the augmentation of benzene hydrogenation on Pt (111) surfaces. Lim and co-workers [8] tested multi-octahedral Pt nanocrystals as electrocatalysts for the oxygen reduction reaction in a proton exchange membrane fuel cell and found that the multi-octahedral Pt nanocrystals with preferential Pt (111) facets exposed exhibited enhanced specific activity of 2.7 times that of the commercial Pt/C catalyst. Additionally, it was also found

that its unique morphology enabled the multi-octahedral Pt nanocrystals to retain its branched structure without significant particle coarsening, thereby exhibiting greater durability.

Besides Pt nanoparticles, one-dimensional (1D) nanostructures of Pt have shown increased catalytic activity and durability for fuel cell applications. As-prepared platinum/platinum-alloy nanotubes by Chen and co-workers [11] showed a higher mass activity and a significantly higher specific activity than Pt/C catalysts, both of which are good indicators of an electrocatalyst's quality. Similarly, Pt nanorods comprising of high-index Pt (311) facets also exhibited better catalytic properties for a methanol selective oxidation reaction at low temperature compared to 3 nm-sized Pt nanoparticles [12]. Not only does a rods anisotropic morphology allow for preferential exposure of certain crystals facets for improved activity, but also eliminates the need for a catalyst support and hence the loss of electrical contact between the Pt catalysts and the support. By tuning their dimensions at multiple length scales and its nanometer-sized wall thickness, 1D Pt nanostructures possess the potential to achieve an even greater surface area, utilization, activity, stability and mass transport for enhanced catalytic performance.

3.1.2. Pt as Hydrogen Evolution Catalysts

In the formation of hydrogen via a reduction process according to equation 3A below, the reduction of the stable oxidizing agent H^+ requires two electrons before a stable form of the product, H_2 is achieved.

$2H^+ + 2e^- \rightarrow H_2$ (Equation 3A)

This can be further represented in two steps:

$H^+ + e^- \rightarrow H\cdot$ (Equation 3B)

$2H\cdot \rightarrow H_2$ (Equation 3C)

The intermediate radical H· represented in equation 3B is highly unstable, its formation is highly endothermic, resulting in a very low overall rate of reaction.

According to the Volmer reaction, the catalytic role of Pt in H_2 production can be seen in its ability to decrease the energy barrier of the H^+/H_2 reduction reaction by formation of the Pt-H

complex in equation 3D. This formation of Pt-H complex is far more stable and less endothermic than the formation of H· radical.

$Pt + H^+ + e^- \rightarrow Pt\text{-}H$ (Equation 3D)

The hydrogen in equation 3D is strongly adsorbed to the surface of Pt. As $H_{(ads)}$ coverage of Pt increases, H_2 formation may proceed by the following two proposed mechanisms: the Tafel reaction (equation 3E) or the Heyrovsky reaction (equation 3F).

Whether the Volmer-Tafel mechanism or the Volmer-Heyrovsky mechanism occurs depends on factors such as the Pt-H bond strength, pH conditions and the surface structure of the Pt catalyst. In studying the H adsorption states on Pt (100) in sulphuric acid, Armand and Clavilier [13] found weakly bonded H to participate in the hydrogen reactions at high potentials, while strongly-bonded H was presumed inert. Using infrared (IR) [14] and Raman spectroscopy [15], Pt-H vibration was identified on polycrystalline Pt in H_2SO_4, and it was proposed that this weakly bonded H was used in the H_2 evolution. Conversely, there were no vibrational signals from the strongly bonded H at high potentials, and it was thus proposed that this H was located in or below the surface atom layer. Based on Tafel plots (electrode potential vs. log of current density) for H_2, a basic environment was found to facilitate the Volmer-Tafel mechanism [16, 17], while Volmer-Heyrovsky mechanism proceeded under acidic conditions [18]. Further, it was also revealed that different crystal faces of Pt differ in their activation energies, which contributed overall to their difference in the sensitivity of H adsorption. Pt (110) had the lowest activation energy on and facilitates the Volmer-Tafel mechanism, while Pt (100) has a higher activation energy resulting in the Volmer-Heyrovsky mechanism [19] being dominant.

$H\text{-}Pt\text{-}Pt + H^+ + e^- \rightarrow H\text{-}Pt\text{-}Pt\text{-}H \rightarrow 2Pt + H_2$ (Equation 3E)

$Pt\text{-}H + H^+ + e^- \rightarrow Pt + H_2$ (Equation 3F)

3.1.3. Electrochemical deposition of Pt

Platinum being one of the longest known and most studied of the six platinum group metals is known to possess a high stability in its +4 oxidation state. Compared to the simple Pt salts such as $PtCl_4$, less labile platinum complexes such as those of consisting of chlorides $[PtCl_6]^{2-}$ and ammines $[Pt(NH_3)_2]^{2+}$ undergo smaller degree of hydrolysis, facilitating easy electrodeposition of Pt from these simple coordination complexes [20]. In the electrodeposition of Pt, a high

current density is generally not used, as it is likely to lead to high hydrogen evolution because of the good catalytic activity of freshly deposited Pt.

The versatility of being able to control operating parameters such as temperature, pH and current density, as well as, the advantage of achieving Pt deposition down to a fraction of a micron, enable Pt catalytic surfaces with a range of particle sizes and surface to be achieved via electrodeposition [21]. This is of prime importance, since Pt is a good catalyst for various chemical and electrochemical reactions.

As a widely used hydrogen evolution catalysts, the electrodeposition of Pt as a photocathode to various semiconductors has been widely studied in designing photoelectrochemical (PEC) cells for photocatalytic water splitting. Parachinno and co-workers [22] investigated a highly active oxide photocathode consisting of cuprous oxide/Al-doped zinc oxide/TiO_2, activated for hydrogen evolution using electrodeposited Pt nanoparticles from an aqueous solution of hydrogen hexachloroplatinate (IV), H_2PtCl_6. Also using a similar precursor, Pt metal islets were electrochemically deposited on p-SiC surface and were used in the study of water-splitting [23].

3.2. Literature Review

3.2.1. Templated Electrodeposition of One-Dimensional Pt and Pt-Based Nanorods

One-dimensional (1-D) nanostructures of Pt and Pt-based materials have been the focus of intense research and development due to their large surface area, unique electronic and catalytic properties [24-27]. Compared to Pt nanoparticles, 1-D Pt nanostructures were reported to exhibit higher electrocatalytic activities, and an increased stability to dissolution and aggregation [28, 29].

A versatile method of fabricating 1-D Pt nanostructures is by templated electrodeposition using anodic aluminium oxide membranes (AAM). Besides its low-cost and convenient operation, templated electrodeposition has the ability to control and confine the dimensions of the Pt nanostructures. Through templated electrodeposition, a variety of Pt and Pt-based 1-D nanostructures, such as nanotubes, nanowires and nanorods with high uniformity and aspect ratio have been reported [30-32].

In the preparation of arrays of Pt nanowires and nanotubes, Ponrouch and co-workers [33] have provided a detailed analysis on the effects of varying electrodeposition conditions such as the Pt precursor concentration, the deposition potential, and the conductivity of the electrolyte

on the resultant nanostructure. Drawing from the presence of hydrogen evolution limiting the diffusion of Pt^{IV} species to the electrode occurring at -0.3 V (vs. SCE), Pt nanotubes were observed at $V_{dep} \leq$ -0.3 V. It was also suggested that limited diffusion of Pt^{IV} species and hence number of Pt nucleation sites from a low Na_2PtCl_6 precursor concentration of 0.5 mM and 1.0 mM also resulted in the formation of Pt nanotubes. Also, a KCl-free precursor solution was found to be conducive to the growth of Pt nanotubes.

Besides conventional factors such as the current density, operating mode and electrolyte composition, the extent of pore coverage on the metalized side of the AAM was also found to influence the structural outcome of templated Pt electrodeposition. In a growth model proposed by Fu and co-workers [31], Pt nanowires and nanotubes were electroplated using 0.01 M platinum-p-salt ($Pt(NH_3)_2(NO_2)_2$) solution, and the formation of Pt nanotubes were suggested to be the mediate state in the growth process of Pt nanowires. It was determined that the growth of Pt nanowires or nanotubes largely depended on the overage of the Au metal layer at the bottom of the AAM template (figure 3-1). A 50% blocked-AAM confined Pt electroplating to the Au particles attached on the AAM inner walls (figure 3-1 A), which subsequently built up to form a nanotube structure. This was based on the assumption that the Au particles had attached on the inner walls of the AAM during the sputtering process and acted as an initial site for Pt deposition. In contrast, employment of 80-100% blocked-AAM through deposition of a thicker gold layer encouraged the growth of Pt nanowires (figure 3-1 B).

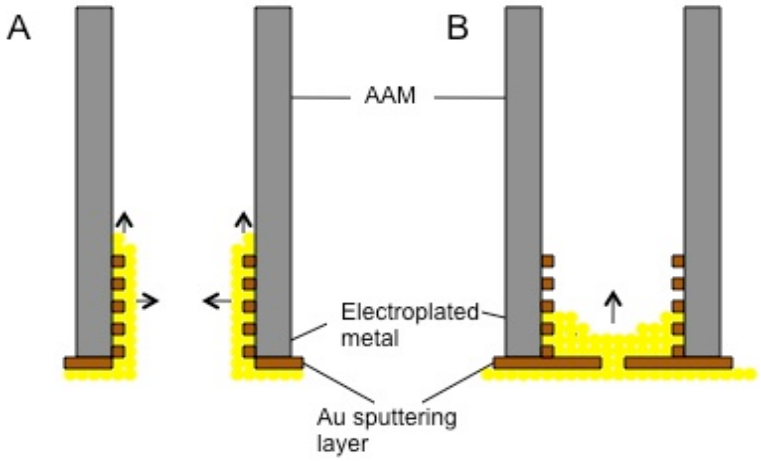

Figure 3-1. Schematic diagram illustrating the electrodeposition of Pt in A) 50% blocked and B) 80-100% blocked AAM membrane

At present, Pt-metal alloy nanostructures are starting to generate interest because such material enhances electrocatalytic activity and offer long-term resistance. This is shown in Pt-based alloys such as Pt-Rh and Pt-Ru which prevent Pt from CO poisoning during oxygen reduction; and in the marked improvement in the catalytic activities reported for Pt alloys consisting of Rh and Au [34, 35]. There are a few reports on the synthesis of 1-D segmented Pt/metal nanostructures via sequential electrodeposition into porous AAM and the advantages of employing such unique structures has been discussed. According to Liu and co-workers [36], 1-D nanostructures of segmented Pt/metal is able to provide a more accurate and direct comparison between the intrinsic activities of different Pt/metal pair sites. A comparison was made between five-segment nanorods consisting of a combination of Pt, Ru and Ni in a methanol oxidation study, and results showed Pt-RuNi pair sites to be the most catalytically active and sustainable, followed by Pt-Ru and Pt-Ni sites. In another study, prior to this, the same group had also demonstrated that the extent of the catalytic activity of multi-segmented PtNi nanorods is linearly related to the number of Pt-Ni interfaces [37]. In addition to possess enhanced catalytic properties, 1-D segmented Pt-metal nanostructures consisting of other materials such as the Pt-Ni [38, 39] and Co-Pt [39] segmented nanowires had also shown to have better magnetic and magneto-optic properties.

Presently, there is limited work on the templated electrodeposition of 1-D Pt and Pt-based nanostructures using electrolytes consisting of chloride-based Pt compound precursor, $[PtCl_6]^{2-}$ mostly in the form of hexachloroplatinic acid (H_2PtCl_6) [30, 32, 40, 41] and sodium hexachloroplatinate (Na_2PtCl_6) [42-44]. Pt precursor electrolytes of H_2PtCl_6 are formed either by the addition of $HClO_4$ as a supporting electrolyte, or the use of relatively high concentrations of 100 mM HCl or 1 M boric acid for pH adjustment. Currently, reports on the templated electrodeposition of Pt using Na_2PtCl_6 are limited. In both works by Ponrouch and co-workers [33, 42], 1-D Pt nanostructures were achieved from a precursor solution consisting of a relatively low concentration of 0.25 mM to 2.5 mM Na_2PtCl_6, and a relatively high amount of 10 mM HCl and 100 mM KCl. Except for the absence of KCl, Pt precursor solution were prepared in a similar manner by Napolskii and co-workers [44] by using a low concentration of 10 mM Na_2PtCl_6 and a high concentration of HCl.

Current works on the electrodeposition procedures, characterization and application of 1-D Pt and Pt-based nanostructures provide us with the insight and understanding into fabricating 1-D Pt nanorods. Initial preparation of the Pt precursor solution was adapted from two works [42, 44], both of which had employed Na_2PtCl_6 as the Pt precursor, and the deposition potentials

stated were also taken as points of reference. The composition of the Pt precursor solution was then modified to consist of a much higher concentration of Na_2PtCl_6 and a lower concentration of HCl, which results in higher rate of Pt deposition and facilitates Pt deposition on semiconductor (i.e. TiO_2) respectively. For the first time, the successful templated electrodeposition of 1-D Pt nanorods from a highly concentrated Pt precursor solution has been reported. The Na_2PtCl_6 stock solution is highly stable and lasts for multiple electrodeposition cycles.

In this chapter, we focus largely on the fabrication of Pt nanorods via electrodeposition into porous AAM, and the structural and chemical analysis of these Pt nanorods, all of which are necessary prior to building 1-D multi-segmented Pt-TiO_2 nanostructures. The established synthesis procedures and characterization of the electrodeposited Pt nanorods in this work contribute to the overall electrodeposition aim of achieving 1-D multi-segmented Pt-TiO_2 nanostructures.

3.3. Electro-deposition of Pt from Sodium Hexachloroplatinate (IV) ($NaPtCl_6.6H_2O$)

3.3.1. Materials

Sodium hexachloroplatinate (IV) hexahydrate ($Na_2PtCl_6 \cdot 6H_2O$, Mr=561.87 g/mol) was purchased from Sigma-Aldrich. Hydrogen peroxide (6% w/v H_2O_2), hydrochloric acid (HCl, 12% v/v) and nitric acid (69% HNO_3) were obtained from BDH Laboratory Supplies. Methanol (Chromasolv® Plus for HPLC ≥ 99.9 %), hydrochloric acid (37% HCl) and sodium hydroxide (40 % w/v NaOH) were purchased from VWR and ammonia solution (35 %, FW=17.05 NH_4OH) was purchased from Fischer Scientific. Commercial Anopore® aluminium oxide hydrophilic membranes (AAM) of diameters 25 and 47 mm with 200 nm nominal pore size were commercially available from Whatman International Ltd. and were used directly for electrodeposition without prior cleaning or pretreatment. Nanopure deionised water was used in all the experiments. All chemicals were of analytical reagent grade and were used without further purification.

3.3.2. General Experimental Practice

3.3.2.1. Bath Solution Preparation of $NaPtCl_6.6H_2O$

The composition of Na_2PtCl_6, HCl and KCl were varied in concentration ratios of [25:1:84], [25:5:84] and [25:1:0] in order to study its effects on Pt electrodeposition. A typical Pt electrolyte was prepared by mixing 25 mM of aqueous $Na_2PtCl_6 \cdot 6H_2O$ with 1 mM aqueous HCl and left to stir for approximately 1 hour before use. The solution has a resultant pH of approximately 3 to 4, which is non-corrosive and hence will not cause etching of the AAM during electrodeposition. This Pt electrolyte was used for all depositions of Pt unless otherwise specified. The side of AAM with smaller pores was sputtered with silver of approximately 200 nm using a silver target 57 mm x 1 mm thick (Quorum Technologies Ltd) and Emitech K575X turbo-pumped sputter coater.

3.3.2.2. Method of Templated Electrodeposition of Pt Nanorods

Pt is electrodeposited into the AAM using the Pt bath solution by applying two potentiostatic steps of -0.4 V (vs. Ag/AgCl, 1 M KCl) for 20 s followed by -0.2 V (vs. Ag/AgCl, 1 M KCl) for the remaining deposition time as required, using a potentiostat (Autolab, PGSTAT12). A standard three electrode single compartment cell was used with the silver sputtered side of AAM serving as a working electrode, a Pt wire mesh as a counter-electrode and an Ag/AgCl (1 M KCl) as a reference electrode.

3.3.2.3. Method of Releasing Pt Nanorods From Aluminium Oxide Membrane (AAM)

To obtain free-standing films of Pt nanorods on silver, Pt-filled AAM is suspended on the solution surface of 3 M NaOH for 1 h to etch off the AAM and then rinsed gently with DI water. The suspension procedure of the Pt-filled AAM on 3 M NaOH consists of firstly sealing the metal-sputtered side of the AAM with epoxy and attaching a string (approx. length of 1-2 cm), followed by floating the sample on NaOH solution with the metal-sputtered side of the AAM facing upwards. Attachment of the string to the sample enables easy removal of the sample from NaOH solution after etching. Free Pt nanorods are released by first etching off the silver sputtered layer by treating the AAM with an etching solution consisting of methanol, 30% ammonium hydroxide and 30% hydrogen peroxide (5:1:1 v/v/v) until all the silver has been completely removed, followed by

dissolving the aluminium oxide in 3 M NaOH solution [45]. The obtained Pt nanorods are centrifuged at 2000 RPM for 15 min and finally dispersed in deionised water by sonication repeatedly for 3 cycles.

3.3.3. Results and Discussion

3.3.3.1. Optimization of Pt nanorods synthesis

3.3.3.1.1. Effect of Species Concentration

The deposition conditions and Pt precursor concentrations of previous works [42, 44] were developed and modified in an attempt to fabricate homogeneous Pt nanorods in the AAM. As aqueous electrolytes of Pt complex compounds are more stable than Pt simple salts due to their smaller degree of hydrolysis, Na_2PtCl_6 was chosen as a Pt precursor in all the experiments [46]. The Na_2PtCl_6 concentration of 25 mM used in this study is approximately 2.5 times more concentrated than the maximum concentration of 10 mM used in existing literatures, and it is the highest concentration reported so far for the templated electrodeposition of Pt.

A Pt precursor stock solution consisting of Na_2PtCl_6, 1-5 mM HCl and 84 mM KCl was found to be unstable as precipitation was observed after approximately 24 h. Conversely, a highly stable Pt precursor stock solution was prepared in the absence of KCl. To investigate the contribution of KCl and HCl towards the electrodeposition of Pt, the amount of HCl and KCl were varied. It was found that Pt precursor solutions consisting of Na_2PtCl_6, HCl and KCl in concentration ratios of [25:1:84] and [25:5:84] resulted in Pt nanorod growth with high variation in lengths as seen in figure 3-2 A and 3-2 B respectively.

A more detailed comparison between the Pt nanorods in figure 3-2 A and 3-2 B suggests that an increased HCl concentration in the presence of KCl produced relatively less uniform Pt nanorods in the AAM. However in the absence of KCl at [25:1:0], the growth of Pt nanorods in the AAM had smaller length variation, evident from the uniformity of the free-standing Pt nanorods in figure 3-2 C and 3-2 D. Considering all these factors, a Pt precursor solution of [25:1:0] was

found to provide the best electrolyte conditions for the homogeneous growth of Pt nanorods in the AAM.

Here, it is concluded that the electrodeposition of Pt does not necessarily require KCl as a supporting electrolyte, and that a Pt precursor solution consisting of solely Na_2PtCl_6 and a lower concentration of HCl (than previously reported) provide sufficient conductivity for Pt electrodeposition. Moreover, more uniform Pt deposits and a stable stock solution were achieved without KCl. While Pt nanotubes were observed by Ponrouch and co-workers [42] in the absence of KCl, in this study highly dense Pt nanorods were successfully achieved under similar conditions.

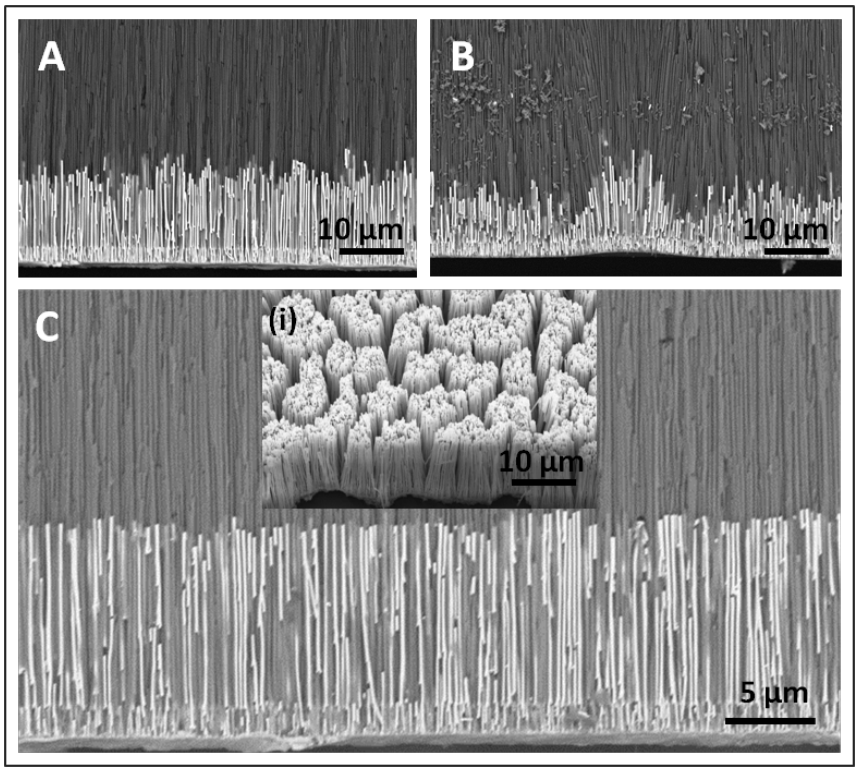

Figure 3-2. Backscattered SEM images of Pt nanorods grown in the pores of AAM at a two step voltage of [-0.4 V/20 s, -0.2 V/3580 s] (vs. Ag/AgCl, 1 M KCl at 25 ^{o}C) and employing a $[PtCl_6]^{2-}$ precursor solution, HCl and KCl in their respective concentration ratios of A) [25:1:84], B) [25:5:84] and C) [25:1:0], (i) inset shows free-standing Pt nanorods released from AAM

In order to qualitatively explain the effect of species concentration in the preparation of the $[PtCl_6]^{2-}$ solution, as well as, in the optimum concentration of

[25:1:0], the equilibrium equations involving the electrochemical deposition of Pt are considered [47]. At lower HCl concentrations, the overall equilibrium shifts strongly to the right as seen in equations 3G and 3H. The equilibrium is further shifted right by a sufficiently high concentration of $[PtCl_6]^{2-}$ precursor, overall favouring uniform Pt deposition across the pores of the AAM.

$[PtCl_6]^{2-}+2e^- \leftrightarrow [PtCl_4]^{2-}+2Cl^-$ E^o=0.485V vs. SCE (Equation 3G)

$[PtCl_4]^{2-}+2e^- \leftrightarrow Pt+4Cl^-$ E^o=0.517V vs. SCE (Equation 3H)

3.3.3.1.2. Effect of Deposition Voltage

A comparison of the charge efficiencies of Pt deposition at varying deposition voltages, as plotted in figure 3-3, suggests that there exists an optimum operating voltage for the deposition of Pt inside the pores of the AAM. An estimated % charge efficiencies were calculated using ratios of the average experimental lengths of the Pt nanorods (averaged over 50 Pt nanorods measured from figure 3-3) electrodeposited at applied voltages of -0.1 V, -0.2 V, -0.3 V and -0.5 V for a total of 0.5 h; and theoretical lengths calculated from the modified Faraday's law (equation 3I) based on the measured current densities at each voltage. It is assumed that at 100% charge efficiency, all the input charges are used in the reduction of $[PtCl_6]^{2-}$ to Pt metal in the pores of the AAM.

Modified Faraday law of electrolysis relating nanorod length to charge:

$L= 4QM/Fz\rho\pi d^2$ (Equation 3I)

Where Q= Total charge passed

M= Molar mass of substance

F= Faraday's constant, 96486 C mol^{-1}

z= Number of e^- transferred per mole of substance produced

A comparison between the actual length of Pt nanorods (averaged over 50 Pt nanorods measured from its respective SEM images in figure 3-3 A-F) and the theoretical Pt length derived from deposition transients (figure 3-4) suggest the existence of a Faraday charge efficiency in the deposition of Pt (figure 3-3). Derivations of the plot and error bars in figure 3-3 are shown in appendix 3-1. A

less than 100% charge efficiencies of Pt deposition at operating voltages of -0.1 V to -0.5 indicates charge losses, which may be attributed to H_2 evolution from the surface of the freshly deposited Pt metal in each AAM pore. The highest charge efficiency of 33% was achieved at an operating voltage of -0.2 V. From the backscattered SEM images of the Pt nanorods/AAM deposited at the respective voltages in figure 3-3, Pt nanorods deposited at -0.1 V and -0.2 V showed the most uniform growth (figure 3-3B); which is in good agreement with their standard deviation values of 7 % and 9 %.

From the analysis, both -0.1 V and -0.2 V would seem the optimal voltages for the deposition of the Pt nanorods. However a deposition of -0.2 V was chosen for subsequent growth of Pt nanorods in this study because of its higher charge efficiency. It should be noted that the % charge efficiency at -0.6 V was not taken into account. This is because of faults that had developed within segments of the Pt nanostructures in the AAM pores (figure 3-3F) as a result of an increased rate of H_2 evolution on the Pt surfaces at this more negative voltage, thereby making quantification of the nanorod lengths difficult. This is shown evidently from its corresponding deposition transient in figure 3-4F, where unlike currents at deposition voltages less negative than -0.6 V, increasing currents observed at -0.6 V (figure 3-4F) may be characterized by an increased reaction of H_2 evolution.

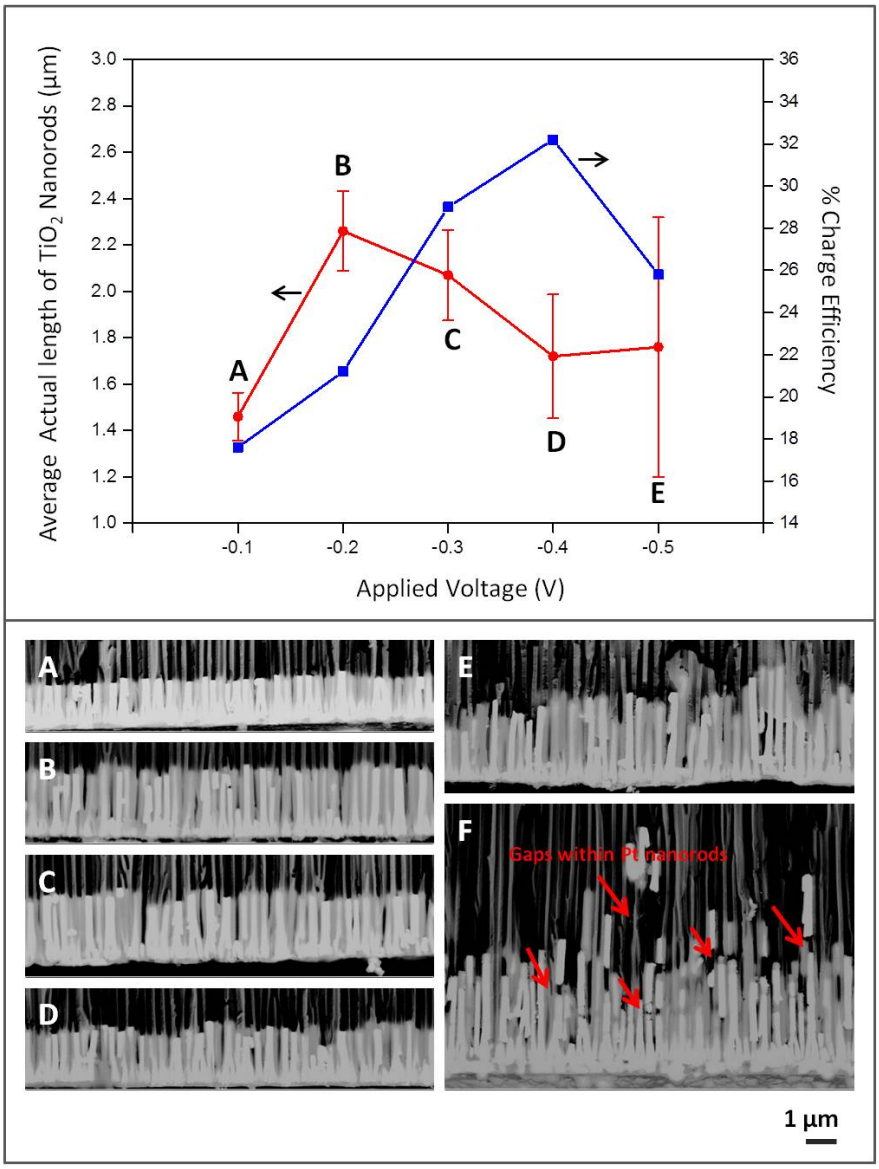

Figure 3-3. Plot of approximate % charge efficiencies of Pt nanorods deposition (averaged over 50 Pt nanorods) as a function of applied voltages (vs. Ag/AgCl, 1 M KCl at 25 ^{o}C). Backscattered SEM images A-F corresponds to respective points labeled on the plot. Point F on the plot was omitted due to faults occurring within Pt nanorods. (Derivation of plot and error bars shown in appendix 3-1)

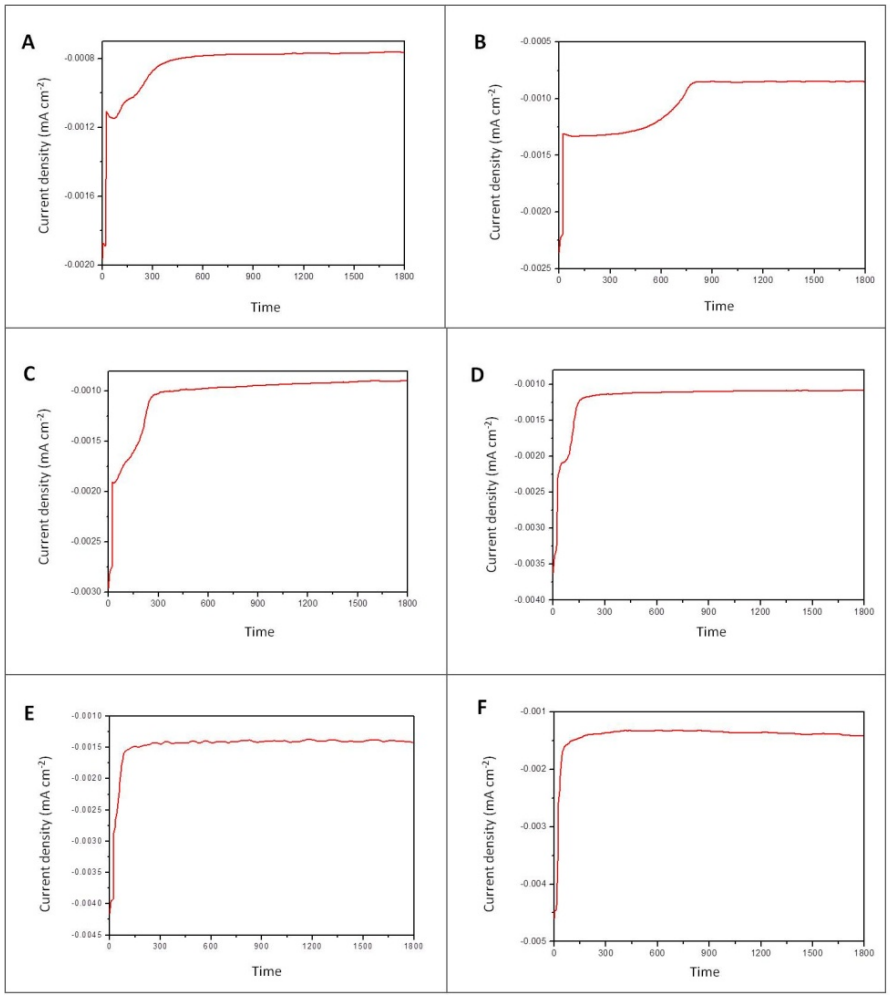

Figure 3-4. Current-time plots for deposition of Pt nanorods in porous AAM at deposition voltages of a) –0.1 V, b) -0.2 V, c) -0.3 V, d) -0.4 V, e) -0.5 V and f) -0.6 V (vs. Ag/AgCl, 1 M KCl at 25 ^{o}C) indicating total charge passed of 1.49 C, 1.85 C, 1.88 C, 2.13 C, 2.64 C, 2.54 C, with expected Pt nanorod lengths of 5.64 µm, 7.02 µm, 7.13 µm, 8.03 µm and 10.02 µm respectively

3.3.3.2. 'Lifetime' of Pt Precursor Solution

As with solutions consisting of transition compound metals such as $[PtCl_6]^{2-}$, such solutions are unstable due to the spontaneous hydrolysis of Pt-Cl bonds occurring at pH > 2.0-2.2 [46, 48]. A recent and commonly cited hydrolysis pathway of $[PtCl_6]^{2-}$ had been proposed by Sillen and Martell [49], where at low pH, chloride may be replaced by water in two hydrolysis steps according to equations 3J and 3K:

$[PtCl_6]^{2-}+H_2O \leftrightarrow [PtCl_5(H_2O)]^{1-}+Cl^-$ (Equation 3J)

$[PtCl_5(H_2O)]^{1-} + H_2O \leftrightarrow [PtCl_4(H2O)_2]^{0}+Cl^-$ (Equation 3K)

In contrast, a clear and stable $[PtCl_6]^{2-}$ precursor stock solution of [25:1:0] was successfully prepared in this study. The concentration of $[PtCl_6]^{2-}$ used in this study is approximately 14 000 ppm, in which at such high concentration, hydrolysis is greatly reduced. Here, the concentration used is much higher than those in the current literatures of 200 to 2000 ppm, in which it was found that the chlorine coordination number in $[PtCl_6]^{2-}$ varies linearly from approximately 3 to 6 over a $[PtCl_6]^{2-}$ concentration of 200 to 2000 ppm [48].

Additionally, the presence of a high concentration **of** $Na_2PtCl_6{\cdot}6H_2O$ enabled the Pt electrolyte stock solution to be reused**.** Iteration was performed to estimate the number of times a precursor solution of $Na_2PtCl_6{\cdot}6H_2O$ can be reused before the initial concentration starts to fall below 100 %, which is denoted by *x*. The calculations (in appendix 3-1) revealed a large theoretical value of 10^9, ideally suggesting that the $PtCl_6^{2-}$ solution can be reused for almost infinite number of times without a significant drop in the $PtCl_6^{2-}$ concentration.

Unfortunately, this was not possible as a fraction of $PtCl_6^{2-}$ solution would be lost each time it was being transferred from the electrodeposition cell back to the stock bottle. This resulted in the substantial loss of $PtCl_6^{2-}$ solution over time, in which it became insufficient in fully submerging the Pt mesh of the counter electrode and the tip of the reference electrode present in the electrodeposition cell. From experimental observation, the actual 'lifetime' of the solution was found to be approximately 50 cycles, thereafter, a fresh $PtCl_6^{2-}$ solution had to be prepared in order to maintain the solution level to the desired level in the electrodeposition cell.

3.3.3.3 Structural and Chemical Analysis of Pt nanorods

The structure of the Pt nanorods was investigated by XRD and TEM. Figure 3-5A shows the XRD patterns of the as-produced Pt nanorods dispersed on a Si substrate suggesting that the Pt crystal growth via electrodeposition has a random orientation and is polycrystalline in nature. More specifically, the main crystal orientations of Pt are found in the directions of (111), (200), (220) and (011) and their respective grain sizes were estimated from Scherrer's equation (equation 3L) to be 9.19 nm, 7.78 nm, 6.94 nm and 4.95 nm respectively. The multiple orientation of Pt crystal growth can also be seen

from the TEM image in figure 3-5B where at least four main crystal orientations had been identified.

$$D = K\lambda / \beta \cos\Theta \qquad \text{(Equation 3L)}$$

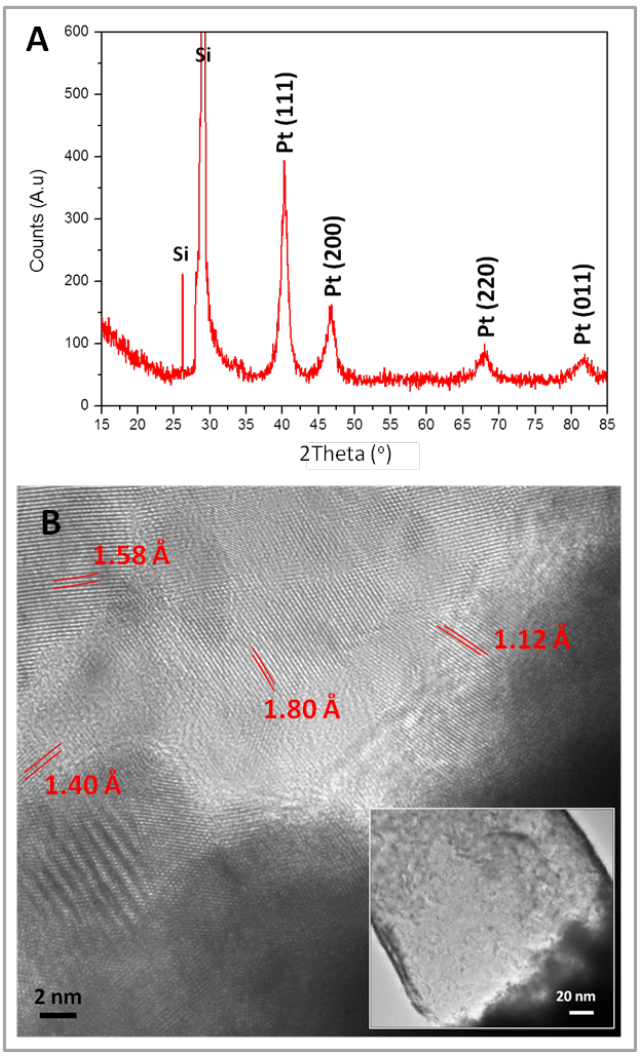

Figure 3-5. A) XRD plot of Pt nanorods dispersed on Si substrate B) HAADF TEM image of a Pt nanorod segment, inset shows a larger section of the Pt nanorod segment

In order to successfully free Pt nanorods from the AAM, the appropriate etchant is chosen based on its ability to dissolve the Ag conductive layer, yet at the same time preserving the integrity of the Pt nanorods. Though highly concentrated acidic solutions such as *aqua regia* and concentrated nitric acid (commonly used to dissolve metal conductive layers) were good etchants for the Ag conductive layer, they also reacted with the Pt nanorods. It was found that the methanol, ammonium hydroxide and hydrogen peroxide (5:1:1) solution effectively removed the Ag conductive layer and

protected the Pt nanorods. The successful release of the Pt nanorods from the AAM and Ag conductive layer using this ammonium-based etchant is shown in figure 3-6. These Pt nanorods have a diameter of 200 nm, similar to those of the AAM pores, demonstrating that the structural integrity of the Pt nanorods was retained despite the washing procedures.

The effectiveness of this ammonium hydroxide based silver etchant is important in the production of the photocatalytic nanorods as it enables the maximum yield of nanorods from the AAM. Using conc. NaOH to remove the AAM alone produces nanorods that are low in quality and yield, because the conductive layers are still attached to the nanorods. This limits further processing.

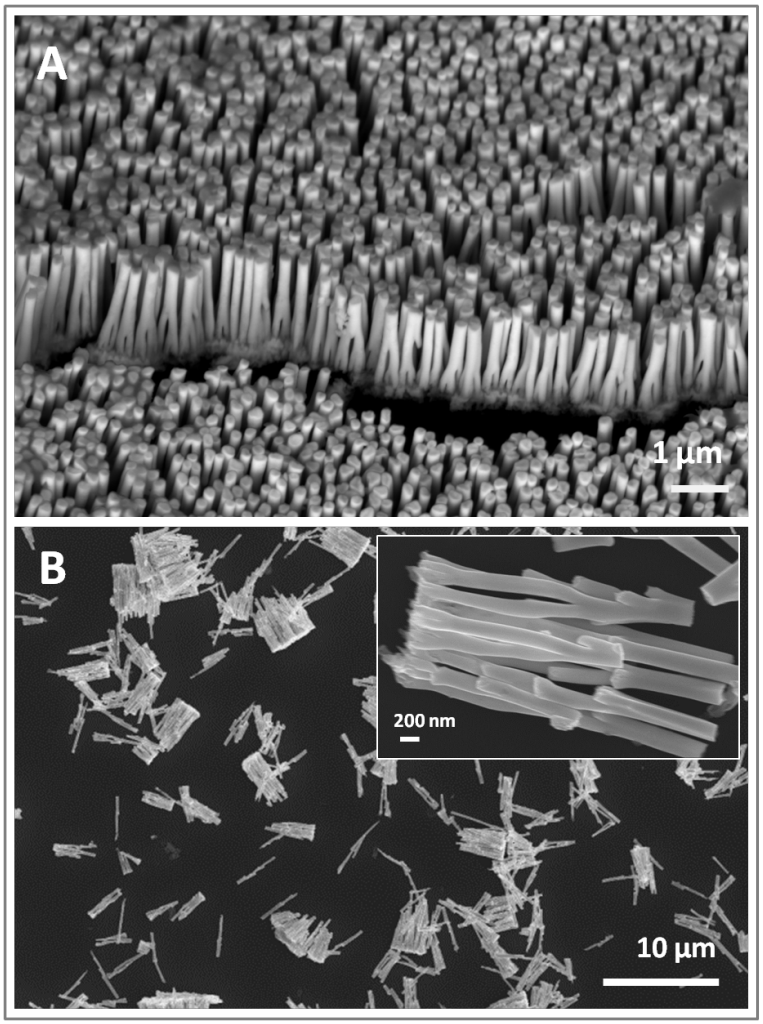

Figure 3-6. Backscattered SEM images of A) free-standing Pt nanorods on Ag conductive substrate achieved by etching AAM in 3 M NaOH; B) free Pt nanorods achieved by etching AAM and Ag conductive layer respectively in conc. NaOH and NH_4OH-based silver etchant

3.4. Conclusion

Highly ordered 1D Pt nanorods have been successfully fabricated via templated electrodeposition into AAM. Electrochemical conditions such as the species concentration of the Pt precursor electrolyte and deposition voltages were optimized to achieve highly uniform and homogeneous array of Pt nanorods. By employing a high concentration of 25 mM Na_2PtCl_6 and 1 mM HCl, a clear and stable Pt precursor electrolyte has been prepared, in which the 'lifetime' of the bath solution was found to be approximately 50 cycles. Overall, the established synthesis procedures and characterization of the electrodeposited Pt nanorods contribute to the overall electrodeposition aim in this study of achieving 1D multi-segmented Pt-TiO_2 nanostructures; and will also be useful in designing highly structured novel materials and nanocomposite structures for prospective applications in photocatalysis, opto-electronics, chemical and bio-analysis.

3.5. References

[1] A. Obuchi, A. Ohi, M. Nakamura, A. Ogata, K. Mizuno, H. Ohuchi, Performance of platinum-group metal catalysts for the selective reduction of nitrogen oxides by hydrocarbons, Appl. Catal. B, 2 (1993) 71-80.

[2] S. E. Voltz, C. R. Morgan, D. Liederman, and S. M. Jacob, Kinetic Study of Carbon Monoxide and Propylene Oxidation on Platinum Catalysts, Ind. Eng. Chem. Prod. Res. Develop., 12 (1973) 294-301.

[3] R. M. D. Nunes, B. F. Machado, M. M. Pereira, M. J. S.M. Moreno and J. L. Faria, Platinum supported on TiO_2 as a new selective catalyst on heterogeneous hydrogenation of α, β-unsaturated oxosteroids J. Mol. Catal. A: Chem., 333 (2010) 1-5.

[4] J. P.-Ramırez, F. Kapteijn, K. Schöffel, J. A. Moulijn, Formation and control of N_2O in nitric acid production: Where do we stand today?, Appl. Catal., B, 44 (2003) 117-151.

[5] Holmes S. Liao, K.-A. H. Tsaprailis, and V. I. Birss, High Performance PtRuIr Catalysts Supported on Carbon Nanotubes for the Anodic Oxidation of Methanol, J. Am. Chem. Soc., 128 (2006) 3504-3505.

[6] H. A. Gasteiger, S. S. Kocha, B. Sompalli, F. T. Wagner, Activity benchmarks and requirements for Pt, Pt-alloy, and non-Pt oxygen reduction catalysts for PEMFCs, Appl. Catal., B, 56 (2005) 9-35.

[7] J. Matthey PLC, Platinum Today, in United Kingdom, 2014.

[8] B. Lim, X. Lu, M. Jiang, P.H. C. Camargo, E. C. Cho, E. P. Lee, and Y. Xia, Facile Synthesis of Highly Faceted Multioctahedral Pt Nanocrystals through Controlled Overgrowth, Nano Lett, 8 (2008) 4043-4047.

[9] J. Chen, B. Lim, E. P. Lee, and Y. Xia, Shape-controlled synthesis of platinum nanocrystals for catalytic and electrocatalytic applications, Nano Today, 4 (2009) 81-95.

[10] M. Bratlie, H. Lee, K. K. Komvopoulos, P. Yang, and G. A. Somorjai Platinum Nanoparticle Shape Effects on Benzene Hydrogenation Selectivity, Nano Lett, 7 (2007) 3097–3101.

[11] Z. Chen, M. Waje, W. Li, and Y.Yan, Supportless Pt and PtPd Nanotubes as Electrocatalysts for Oxygen-Reduction Reactions, Angew. Chem. Int. Ed., 46 (2007) 4060-4063.

[12] L. Yang, X. Song, M. Qi, L. Xia and M. Jin, Templated high-yield synthesis of Pt nanorods enclosed by high-index {311} facets for methanol selective oxidation, J. Mater. Chem. A, 1 (2013) 7316.

[13] D. Armand and J. Clavilier, Qualitative Analysis Of The Dwibibution Of The Hydrogen Adsorption States At Platinum Surfaces (Art I. Application to Pt(100) in sulfuric acid medium), J. Electroanal. Chem, 225 (1987) 205-214.

[14] R. J. Nichols, and A. Bewick, Spectroscopic identification of the adsorbed intermediate in hydrogen evolution on platinum, J. Electroanal. Chem, 243 (1988) 445–453.

[15] B. Ren, X. Xu, X. Q. Li, W. B. Cai, Z. Q. Tian, Extending surface Raman spectroscopic studies to transition metals for practical applications: II. Hydrogen adsorption at platinum electrodes, Surf. Sci., 427-28 (1999) 157–161.

[16] B. E. Conway, and G. Jerkiewicz, Relation of energies and coverages of underpotential and overpotential deposited H at Pt and other metals to the 'volcano curve' for cathodic H2 evolution kinetics, Electrochim. Acta, 45 (2000) 4075–4083.

[17] J. Barber, S. Morin, and B. E. Conway, Specificity of the kinetics of H_2 evolution to the structure of single-crystal Pt surfaces, and the relation between opd and upd H, J. Electroanal. Chem, 446 (1997) 125–138.

[18] M.C. Tavares, S.A.S. Machado, and L.H. Mazo, Study of hydrogen evolution reaction in acid medium on Pt microelectrodes, Electrochim. Acta, 46 (2001) 4359–4369.

[19] N. M. Markovic, B. N. Grgur and P. N. Ross, Temperature-Dependent Hydrogen Electrochemistry on Platinum Low-Index Single-Crystal Surfaces in Acid Solutions, J. Phys. Chem. B, 101 (1997) 5405-5413.

[20] M. E. Baumgärtner, and C. J. Raub, The Electrodeposition of Platinum and Platinum Alloys, Platinum Metals Rev., 32 (1988) 188-197.

[21] C. R. K. Rao, and D. C. Trivedi, Chemical and electrochemical depositions of platinum group metals and their applications, Coord. Chem. Rev., 249 (2005) 613–631.

[22] A. Paracchino, V. Laporte, K. Sivula, M. Grätzel and E. Thimsen, Highly active oxide photocathode for photoelectrochemical water reduction, Nat. Mater., 10 (2011).

[23] J. Akikusa, and S. U. M. Khan, Photoelectrolysis of water to hydrogen in p-SiC/Pt and p-SiC/n-TiO_2 cells, Int. J. Hydrogen Energy, 27 (2002) 863-870.

[24] Penate-Quesada, J. Mitra and P. Dawson L. Non-linear electronic transport in Pt nanowires deposited by focused ion beam, Nanotech., 18 (2007) 215203-215208.

[25] X. Teng, M. Feygenson, Q. Wang, J. He, W. Du, A. I. Frenkel, W. Han, and M. Aronson, Electronic and Magnetic Properties of Ultrathin Au/Pt Nanowires, Nano Lett, 9 (2009) 3177-3184.

[26] S. Sun, F. Jaouen and J.-P. Dodelet, Controlled Growth of Pt Nanowires on Carbon Nanospheres and Their Enhanced Performance as Electrocatalysts in PEM Fuel Cells, Adv. Mater., 20 (2008) 3900–3904.

[27] S. M. Choi, J. H. Kim, J. Y. Jung, E. Y. Yoon, and W. Bae Kim, Pt nanowires prepared via a polymer template method: Its promise toward high Pt-loaded electrocatalysts for methanol oxidation, Electrochim. Acta, 53 (2008) 5804–5811.

[28] C. Koenigsmann, A. C. Santulli, K. Gong, M. B. Vukmirovic, W.-P. Zhou, E. Sutter, S. S. Wong, and R. R. Adzic, Enhanced Electrocatalytic Performance of Processed, Ultrathin, Supported Pd Pt Core Shell Nanowire Catalysts for the Oxygen Reduction Reaction, J. Am. Chem. Soc., 133 (2011) 9783–9795.

[29] Zhongwei Chen, Mahesh Waje, Wenzhen Li, and Yushan Yan, Supportless Pt and PtPd Nanotubes as Electrocatalysts for Oxygen-Reduction Reactions, Angew. Chem. Int. Ed, 46 (2007) 4060-4063.

[30] Y. Lu, M. Yang, F. Qu, G. Shen and R. Yu Amperometric Biosensors Based on Platinum Nanowires, Anal. Lett., 40 (2007) 875–886.

[31] J. Fu, S. Cherevko, C.-H. Chung, Electroplating of metal nanotubes and nanowires in a high aspect-ratio nanotemplate, Electrochem. Commun., 10 (2008) 514-518.

[32] H.-P. Liang, Y.-G. Guo, J.-S. Hu, C.-F. Zhu, L.-J. Wan, and C.-L. Bai, Ni−Pt Multilayered Nanowire Arrays with Enhanced Coercivity and High Remanence Ratio, Inorg. Chem., 44 (2005) 3013-3015.

[33] A. Ponrouch, S. Garbarino, S. Pronovost, P.-L. Taberna, P. Simon, and D. Guay, Electrodeposition of Arrays of Ru, Pt, and PtRu Alloy 1D Metallic Nanostructures, J. Electrochem. Soc., 157 (2010) K59-K65.

[34] E. Antolini, T. Lopes, E. R. Gonzalez An overview of platinum-based catalysts as methanol-resistant oxygen reduction materials for direct methanol fuel cells, J. Alloy Compd., 461 (2008) 253–262.

[35] S. Zhou, G. S. Jackson and B. Eichhorn, AuPt Alloy Nanoparticles for CO-Tolerant Hydrogen Activation: Architectural Effects in Au-Pt Bimetallic Nanocatalysts, Adv. Funct. Mater., 17 (2007) 3099–3104.

[36] F. Liu, J. Y. Lee and W. J. Zhou, Segmented Pt/Ru, Pt/Ni, and Pt/RuNi Nanorods as Model Bifunctional Catalysts for Methanol Oxidation, Small, 2 (2006) 121-128.

[37] F. Liu, J. Y. Lee and W. Zhou, Template Preparation of Multisegment PtNi Nanorods as Methanol Electro-Oxidation Catalysts with Adjustable Bimetallic Pair Sites, J. Phys. Chem. B, 108 (2004) 17959-17963.

[38] Han-Pu Liang, Yu-Guo Guo, Jin-Song Hu, Chuan-Feng Zhu, Li-Jun Wan, and Chun-Li Bai, Ni−Pt Multilayered Nanowire Arrays with Enhanced Coercivity and High Remanence Ratio, Inorg. Chem. , 44 (2005) 3013−3015.

[39] W. Chen, Z. Li, G. B. Ji, S. L. Tang, M. Lu, Y. W. Du, Magnetic coupling in $Co_{1-x}Pt_x$ (x>0.5) nanowires electrodeposited on an AAO template, Solid State Commun., 133 (2005) 235–239.

[40] O.G Drago, H. Chiriac, C. Gherasim, Synthesis and characterization of nobles metals nanowires, J. Optoelectron Adv Mater., 12 (2010) 1739 - 1742.

[41] L. B Kong, L. Mei, M.-K. Li , X.-Y. Guo , H.-L. Li Morphology of Platinum Nanowire Array Electrodeposited Within Anodic Aluminium Oxide Template Characterized by Atomic Force Microscopy, Chinese Phys. Lett., 20 (2003) 763-766.

[42] A. Ponrouch, S. Garbarino, E. Bertin , C. Andrei , G. A. Botton and D. Guay Highly Porous and Preferentially Oriented {100} Platinum Nanowires and Thin Films, Adv. Funct. Mater., 22 (2012) 4172–4181.

[43] Alexandre Ponrouch, Sébastien Garbarino, Stéphanie Pronovost, Pierre-Louis Taberna, Patrice Simon and Daniel Guaya, Electrodeposition of Arrays of Ru, Pt, and PtRu Alloy 1D Metallic Nanostructures, ournal of The Electrochemical Society, 153 (2010) K59-K65.

[44] K. S. Napolskii, P. J. Barczuk, S. Yu. Vassiliev, A. G. Veresov, G. A. Tsirlina, P. J. Kulesza, Templating of electrodeposited platinum group metals as a tool to control catalytic activity, Electrochim. Acta, 52 (2007) 7910–7919.

[45] S. Mukherjee, X. Li, F. Gao, and Z. Gu, An Efficient Silver Etchant for the Fabrication of Active Nanowires Using Anodized Aluminum Oxide Templates, Electrochem. Solid-State Lett., 13 (2010) D50-D52.

[46] M. E. Baumgärtner, and Ch. J. Raub, The Electrodeposition of Platinum and Platinum Alloys, Platinum Metals Rev., 32 (1988) 188-197.

[47] M. Dekker, Standard Potentials In Aqueous Solutions in: R. Parsons A.J. Bard, J. Jordan (Ed.), New York, 1985.

[48] W. A. Spieker, J. Liu, J. T. Miller, A. J. Kropf, J. R. Regalbuto, An EXAFS study of the co-ordination chemistry of hydrogen hexachloroplatinate(IV) 1. Speciation in aqueous solution, Appl. Catal., A, 232 (2002) 219–235.

[49] L. G. Sillen, and A. E. Martell, The Stability Constants of Metal Ion Complexes, The Chemical Society, Burlington House, London, 1971.

Chapter 4: Synthesis of TiO_2 Nanostructures and Experimental Procedures

4.1. Introduction

The multi-functionality of semiconductor titanium dioxide (TiO_2) has seen its utilization in numerous industrial applications. Known largely for its strong photocatalytic activity, robust chemical stability under acidic and oxidative environments, low production cost and non-toxicity, TiO_2 has found uses in areas such as photocatalysis [1, 2], dye-sensitized solar cells [3-5] and biomedical devices [6, 7]. Amongst a myriad of existing TiO_2 structures, highly ordered one-dimensional (1D) nanostructures have been found to be particularly important in achieving scaled-up functional devices [8]. A preferred method to fabricate 1D nanostructures of TiO_2 is by templated electrodeposition. This is due mainly to its low cost, high volume and the ability to accurately control the amount of material deposited. Amongst the Ti precursors, $TiOSO_4$ and $TiCl_3$ are more commonly used for the electrodeposition of TiO_2 because of the relative ease of employing an aqueous solvent.

There are differences between the electrodeposition mechanisms of TiO_2 from $TiOSO_4$ and $TiCl_3$ precursors. Briefly, TiO_2 is electrodeposited from $TiOSO_4$ precursor solution as a result of from the cathodic production of OH^-, marked by an increase in the local pH at the AAM (working electrode) and the overall oxidation state of Ti^{+4} remains unchanged. In contrast, TiO_2 electrodeposited from $TiCl_3$ precursor solution is an anodic process, which involves the anodic oxidation of Ti^{3+} to Ti^{4+} via a hydrolytic formation of Ti^{3+} intermediate.

Proceeding from this point onwards, the chapter is divided into two main sections. The first section describes the templated electrodeposition of TiO_2 using $TiOSO_4$ precursor and the second section describes the templated electrodeposition of TiO_2 using $TiCl_3$. Each of the two sections comprises of sub-sections on the materials, general experiment practice, and results and discussion.

4.2. Literature Review

4.2.1. Electrodeposition of TiO_2 Nanostructures from Aqueous $TiOSO_4$

Methods of electrodepositing nanocrystalline TiO_2 thin films from an aqueous $TiOSO_4$ precursor solution were developed by Natarajan and Nogami [9]. The Ti-precursor solution was prepared first by dissolving Ti powder in a solution of H_2O_2 and ammonia, followed by dissolving the obtained yellow gel in H_2SO_4 or HNO_3 to obtain a red coloured solution, $TiOSO_4$. By adding KNO_3 to $TiOSO_4$ and adjusting the solution pH to 1 to 3, the Ti precursor electrolyte was employed for

the electrochemical deposition of TiO_2 films on an ITO electrode. In their study, Natarajan and Nogami also reported on the important role of KNO_3 in driving the electrochemical deposition of TiO_2 to achieve nanoporous amorphous TiO_2 films, which crystallises after thermal treatment. Depositions of the TiO_2 films were performed in the potential range of -0.9 V to -1.4 V (vs. SCE).

Deeming Natarajan and Nogami's preparation method of Ti bath solution tedious, Karuppuchamy and co-workers [10] simplified the process by adding KNO_3 and H_2O_2 to commercial $TiOSO_4$ powder, resulting in a red coloured solution similar to that obtained by Natarajan and Nogami. It was also reported that cooling of the Ti precursor solution to 10 ^oC during the electrodeposition process was essential in obtaining transparent and homogeneous TiO_2 films. Additionally, Blanco and co-workers [11] deposited TiO_2 films on ITO at -1.2 V (vs. Ag/AgCl) from a bath solution consisting of $TiOSO_4$, H_2O_2 and NH_4NO_3 and reported the temperature of the bath solution to affect TiO_2 crystallinity, where a higher proportion of TiO_2 anatase phase was found in the TiO_2 films deposited at 63 ^oC. Thermal effect on the kinetic of the ions during the electrodeposition process was suggested to be the cause of this effect.

Continuing from the establishment of the process of TiO_2 electrodeposition, similar works on mainly TiO_2 films [5, 9, 10] and three-dimensional nanoframes had followed [12]. To date, reports on the templated electrodeposition of TiO_2 nanotubes using aqueous $TiOSO_4$ are very limited [13]. Also, there has yet to be a report on the electrodeposition of TiO_2 nanorods in AAM using $TiOSO_4$ precursor. Despite a number of reports on the templated synthesis of 1D metal oxide nanorods [14], nanowires [15] and nanotubes [16-18], the growth mechanism of metal oxide nanostructures in AAMs is yet to be fully rationalised.

In the first portion of this chapter, we focus on the synthesis and characterization of highly ordered one-dimensional TiO_2 nanorods and nanotubes by template electrodeposition using $TiOSO_4$ precursor; and by studying the effect of deposition voltages on the nanostructural growth of TiO_2 in the AAM, we elucidate the growth mechanisms of TiO_2 nanorods and nanotubes.

4.2.2. Templated Electrodeposition of TiO_2 from Aqueous $TiCl_3$

Fabricating TiO_2 from the oxidative hydrolysis of $TiCl_3$ precursor has been performed using electrochemical deposition [8, 19, 20] and electro-less deposition [21-24] methods. As compared to the electro-less deposition methods such as the sol-gel method, electrodeposition of TiO_2 offers a faster and controllable way of preparing TiO_2. Kavan and co-workers [19]

pioneered the method of electrochemically depositing TiO_2 films at 0 V (vs. SCE) from aqueous $TiCl_3$ precursor by anodic oxidative hydrolysis. In the report, Kavan and co-workers [19] postulated that the anodic Ti^{3+}(aq.) oxidation is analogous to the chemical oxidation of O_2 by a rapid hydrolytic pre-equilibrium (equation 4A), followed by an oxidation of the formed $TiOH^{2+}$ monohydroxy intermediate to Ti(IV) oxo-species which can be subsequently converted to TiO_2 after thermal treatment (equation 4B).

$$Ti^{3+}(aq) + H_2O \underset{\leftarrow}{\overset{fast}{\rightleftharpoons}} TiOH_2^+ + H^+ \qquad \text{(Equation 4A)}$$

$$TiOH_2^+ \underset{-e^-}{\overset{slow}{\rightleftharpoons}} Ti(IV)\ polymers \xrightarrow[-H_2O]{450°C,\,1\,h} TiO_2 \qquad \text{(Equation 4B)}$$

Following this, there were a few interesting points that had been mentioned about the nature of fabricating TiO_2 from aqueous $TiCl_3$. Firstly, it was suggested that a practical working pH range of the $TiCl_3$ precursor solution should be between 2 to 2.5 in order to reduce the sensitivity of the $TiCl_3$ solution to O_2 and hence minimise precipitation. This could also serve as a reason as to why the preparation and electrodeposition process was carried out under anaerobic conditions. Secondly, the steady-state anodic current density during electrodeposition of $TiCl_3$ precursor solution was found to depend on pH where the faradaic efficiency was reported to be 100 % above pH 3 and 0 % below pH 1.5. The rate of the anodic reaction was however found to be independent of the potential, which was demonstrated by an almost constant anodic current in a broad potential range.

Besides electrodeposition of TiO_2 films, 1-D TiO_2 nanowire arrays [8, 20, 25] and 1-D TiO_2 segments [26, 27] have also been electrochemically fabricated from $TiCl_3$ precursor. Arrays of highly-order 1-D TiO_2 nanostructures have been of great interest mainly because of its ideal architecture in increasing efficiency for charge-transport devices; and the most versatile method for the replication of 1-D TiO_2 nanostructure patterns is by template electrodeposition. Musselman and co-workers [20] reported a general method of producing high-quality arrays of TiO_2 nanorods by templated electrodeposition onto transparent conducting substrates. A similar study was also carried out by Liu and co-workers [25], in which arrays of TiO_2 nanowires were fabricated by pulse electrodeposition from $TiCl_3$ precursor. In both works, there was however no mention of the atmospheric conditions under which the $TiCl_3$ precursor preparation and electrodeposition procedures were carried out. In another study, fabrication of single-crystalline TiO_2 nanorod arrays were performed under an Ar atmosphere [8]. Also, taking into account the high resistance of the solution in the AAM pores, a higher $TiCl_3$ solution concentration of 0.25 M

was reported to be used, compared to a lower concentration of 0.05 M which had been employed in preparing TiO_2 films [19].

There are two similar studies involving the template electrodeposition of small segments TiO_2 (approx. 50 nm length) from a bath solution consisting of $TiCl_3$ and carboxymethetyl-cellulose (CMC) saturated with nitrogen. As it was observed from TEM images of PPy/TiO_2/PPy fibers, the deposited porous TiO_2 segments were described to consist of loosely deposited TiO_2 nanoparticles, which function as separators between conducting polymers of polypyrrole (PPy) and polyaniline (PAn) for application as nano-batteries [27]; and polymers of polypyrrole (PPy) for use as super-capacitors [26].

In the second portion of this chapter (following the templated electrodeposition of TiO_2 from $TiOSO_4$), we describe detailed experimental procedures of preparing a stable $TiCl_3$ bath solution under ambient conditions, as well as, the successful electrodeposition 1-D TiO_2 nanostructures at conditions of room temperature and an uncontrolled atmosphere. The conditions and procedures of the electrodeposition of TiO_2 nanorods from $TiCl_3$ that have been established here are used in the subsequent fabrication of the TiO_2 segments of the TiO_2-Pt striped nanorods in chapter 5.

4.3. Templated Electrodeposition of TiO_2 from $TiOSO_4$

4.3.1. Materials

Titanium (IV) oxysulfate hydrate ($TiOSO_4.H_2O$, Mr=159.93 g/mol)) was purchased from Sigma-Aldrich. Hydrogen peroxide (6% w/v H_2O_2), hydrochloric acid (HCl, 12% v/v), nitric acid (69% HNO_3) and potassium nitrate (KNO_3) were obtained from BDH Laboratory Supplies. Methanol (Chromasolv® Plus for HPLC ≥ 99.9 %), hydrochloric acid (37% HCl) and sodium hydroxide (40 % w/v NaOH) were purchased from VWR and ammonia solution (35 %, FW=17.05 NH_4OH) was purchased from Fischer Scientific. Commercial Anopore® aluminium oxide hydrophilic membranes (AAM) of diameters 25 and 47 mm with 200 nm nominal pore size and 0.2 μm filter pore size were commercially available from Whatman International Ltd. and were used directly for electrodeposition without prior cleaning or pretreatment. Nanopure deionised water was used in all the experiments. All chemicals were of analytical reagent grade and were used without further purification.

4.3.2. General Experiment Practice

4.3.2.1. Bath Solution Preparation of $TiOSO_4$

A bath solution consisting of $TiOSO_4$ was prepared by first cooling 55 ml of deionised water to 10 °C in an ice bath, followed by addition of 50 mM of H_2O_2. 10 mM $TiOSO_4.H_2O$ was then dissolved into the mixture and stirred vigorously until the solution turned clear orange-red after which 50 mM KNO_3 was added. To minimize the bulk hydrolysis of $TiOSO_4$ in water, the bath solution was maintained at approximately pH 3 and at 10 °C throughout the electrodeposition process.

4.3.2.2. Electrodeposition of TiO_2 Films

Electrodeposition of TiO_2 films on a gold-on-glass working electrode was performed under a two-step potentiostatic control of [-1.4 V (vs. 1 M Ag/AgCl) /20 s, -1.2 V (vs. 1 M Ag/AgCl)/ *x* s] using an AUTOLAB PGSTAT12 potentiostat, where *x* represents the desired time for electrodeposition. An initial overvoltage of 200 mV was applied to all the deposition voltages.

4.3.2.3. Templated Electrodeposition of TiO_2 Nanostructures from $TiOSO_4$

TiO_2 nanorods and nanotubes were electrodeposited in the AAMs from the $TiOSO_4$ precursor bath solution under a range of potentiostatic conditions of -1.2 V to -0.3 V (vs. 1 M Ag/AgCl) using an AUTOLAB PGSTAT12 instrument. An initial overvoltage of 200 mV was applied to all the deposition voltages. The respective defined potentiostatic conditions of TiO_2 nanorods and nanotubes electrodeposition are found under the results section.

4.3.2.4. Method of Releasing TiO_2 Nanorods From Template

To release the TiO_2 nanostructures from the AAM, the silver sputter layer was removed by applying a freshly prepared solution of *aqua regia* until all the silver has been completely removed, followed by etching the AAM in 3 M NaOH solution. The samples were then collected by repeated centrifuging at 2000 RPM for 15 minutes, washed with DI water and redispersed in DI water.

4.3.3. Results and Discussion

4.3.3.1. Electrodeposition of TiO_2 Film from $TiOSO_4$ precursor

Prior to the electrodeposition of TiO_2 nanorods in the AAM, the conditions for such a process were examined by an initial preparation of TiO_2 films on Au/glass electrodes. The SEM images in figure 4-1 represents the successful growth of TiO_2 films on Au/glass electrodes via electrodeposition at applied step voltages of -1.4 V/ 20 s, -1.2 V/ 17980 s (vs. Ag/AgCl, 1 M KCl at 25 ^{o}C) using a $TiOSO_4$ precursor bath solution consisting of H_2O_2 in amounts of either 0.2 ml or 0.3 ml, respectively resulting in TiO_2 films that appear to be made of TiO_2 "particles" of different sizes. Based on an average count of 100 TiO_2 "particles" and assuming TiO_2 particles to be spherical, diameters of TiO_2 "particles" of TiO_2 films that were grown from a 0.3 ml H_2O_2 /$TiOSO_4$ precursor bath solution (Figure 4-1A) were calculated to be approximately 33 ± 9.1 nm, while those of 0.2 ml H_2O_2/$TiOSO_4$ precursor bath solution (Figure 4-1B) were of approximately 78 ± 25.1 nm. Comparison of these figures evidently shows that TiO_2 films resulting from 0.3 ml H_2O_2 /$TiOSO_4$ precursor bath solution consisted of smaller and more uniform TiO_2. From the SEM images in figure 4-1, the as-prepared TiO_2 films obtained from both these conditions appears to be nanoporous, similar to that observed by Karuppuchamy and co-workers [10] where in their study the TiO_2 film was described from obtained SEM images to consist of an aggregate of very small crystallites sizes of a few tens of nanometers.

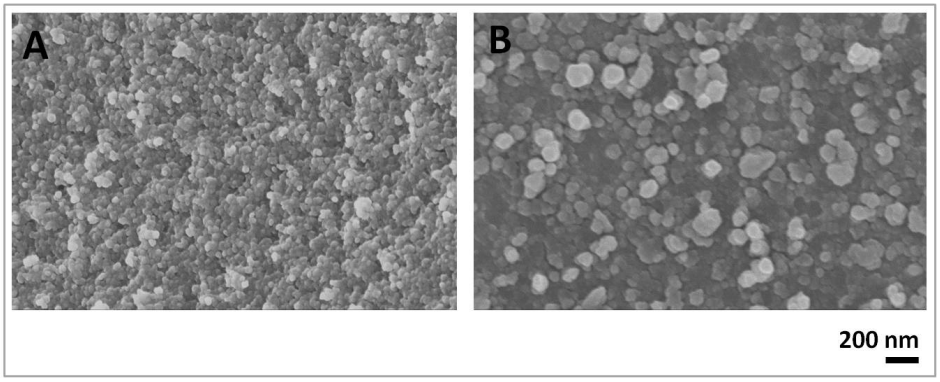

Figure 4-1. SEM images of 100 K magnification of annealed TiO_2 films deposited on Au/glass at applied step voltages of [-1.4 V/ 20 s, -1.2 V/ 17980 s] (vs. Ag/AgCl, 1 M KCl at 25 ^{o}C) using a $TiOSO_4$ precursor bath solution consisting of $TiOSO_4$ precursor and A) 0.3 ml H_2O_2 and B) 0.2 ml H_2O_2 where TiO_2 films appear to consist of TiO_2 "particles" sizes (averaged over 100 "particles") of 33 ± 9.1 nm and 78 ± 25.1 nm respectively

The formation of smaller and more homogeneous TiO_2 particles can be expected with the use of a higher concentration of 0.3 ml H_2O_2. According to equation 4C, H_2O_2 complexes with $TiOSO_4$ to form $Ti(O_2)SO_4$, which plays an essential role in the formation of TiO_2 through the process of hydrolysis. It is observed that when H_2O_2 concentrations lower than 0.2 ml was used, the mixture remained turbid from the unreacted $TiOSO_4$ despite hours of mixing. A clear red solution is therefore obtained by increasing the concentration of H_2O_2 in the bath solution, which allows for the complete complexation of $TiOSO_4$. This increases the initial concentration of the solute $Ti(O_2)SO_4$ to favour the formation of larger number of TiO_2 nucleation sites and hence larger number of TiO_2 nuclei during hydrolysis. Generally, for a given concentration of $Ti(O_2)SO_4$ solute, a larger number TiO_2 nuclei will result in smaller sized "particles". Additionally, the smaller size distribution of TiO_2 "particles" resulting from 0.3 ml H_2O_2 /$TiOSO_4$ precursor bath solution may be indicative of a more constant growth rate of TiO_2 nuclei compared to that occurring in a 0.2 ml H_2O_2 /$TiOSO_4$ precursor bath solution which yield TiO_2 "particles" with larger size distribution.

$TiOSO_4 + H_2O_2 \leftrightarrow Ti(O_2)SO_4 + H_2O$ (red solution) (Equation 4C)

As discussed earlier, it is well observed that by using 0.3 ml H_2O_2/$TiOSO_4$ precursor bath solution, a more uniform deposition of TiO_2 film is electrodeposited on the Au/glass electrode. Figure 4-2A represents the non-homogeneous TiO_2 film deposition observed using 0.1 ml H_2O_2/$TiOSO_4$ precursor bath solution. In contrast by using 0.3 ml H_2O_2 /$TiOSO_4$ precursor bath solution, a homogeneous TiO_2 film deposition was seen. The importance of achieving homogeneity in TiO_2 film deposition on the Au/glass electrode can be seen in its parallel application of the electrodepositing TiO_2 in a porous template such as the AAM.

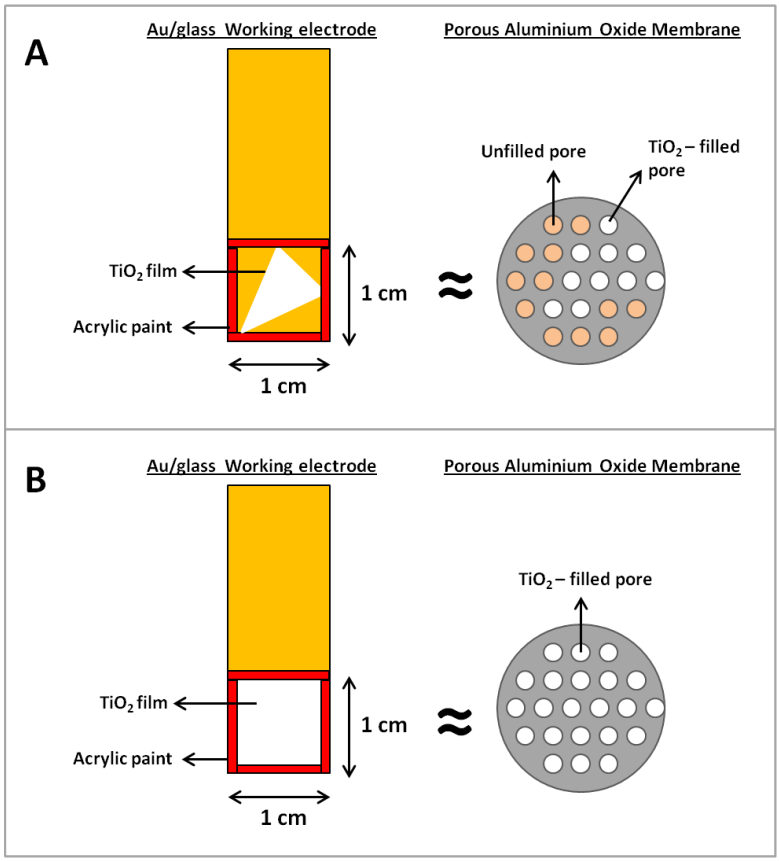

Figure 4-2. Schematic illustration of A) A non-homogeneous TiO_2 film deposition observed using 0.1 ml $H_2O_2/TiOSO_4$ precursor bath solution and B) Homogeneous TiO_2 film deposition observed using 0.3 ml $H_2O_2/TiOSO_4$ precursor bath solution. The resultant homogeneities in the TiO_2 films in A and B approximate the results of TiO_2 deposition in the porous AAM under the respective conditions.

4.3.3.2. Characterisation of TiO_2 Nanorods Electrodeposited from $TiOSO_4$ precursor

The SEM images in figure 4-3 (a), (b), (c) and (d) show highly uniform TiO_2 nanorods that were achieved from $TiOSO_4$ precursor at applied step voltages of -1.4 V (vs. Ag/AgCl, 1 M KCl at 25 ^{o}C) for the first 20 s followed by -1.2 V (vs. Ag/AgCl, 1 M KCl at 25 ^{o}C) for a total of 1, 2, 3 and 5 hours respectively. An initial overvoltage of 200 mV was applied to all the deposition voltages. Under the same deposition voltage conditions, Plots (i) (derived from respective length measurements of TiO_2 nanorods in figure 4-3 and averaged over 100 nanorods) and plot (ii) (derived from the current density time plots) indicates a deviation from the expected linear relationship between the Faradaic charge and deposition time as the extent of deposition time increases. At longer deposition times, a decreasing conductivity through an increased TiO_2 length at longer deposition times may have occurred, resulting in decreasing deposition currents as shown in figure 4-4. The

derivations of the plot and error bars in figure 4-3 are shown in appendix 4-1. Treatment of the samples using concentrated acid ([*aqua* regia]=1 HNO_3: 3 HCl) and strong base (3 M NaOH) revealed that the as-prepared TiO_2 nanorods exhibited strong chemical stability as they were found to retain their structural integrity thereafter (Figure 4-3).

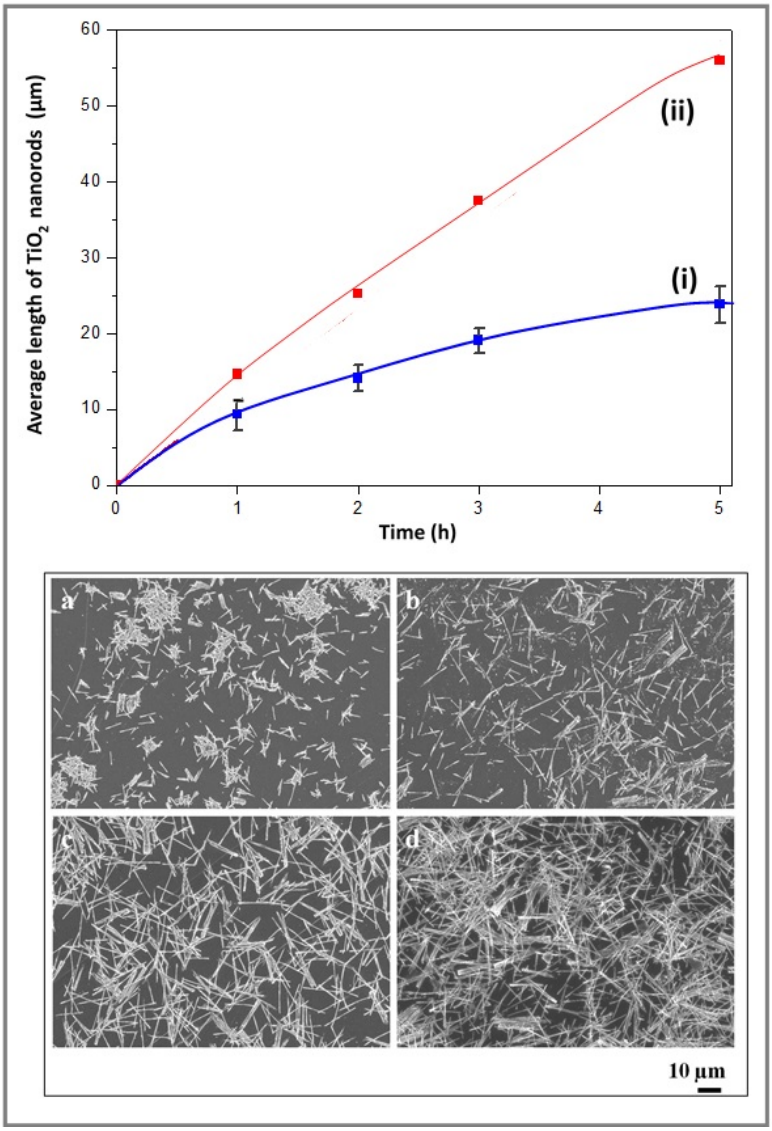

Figure 4-3. (i) Plot of TiO_2 nanorods with varying experimental lengths (averaged over 100 nanorods) electrodeposited from pH 3 aqueous solution of $TiOSO_4$ at -1.2 V (inclusive of overvoltage of 200 mV/20 s) under varying deposition times of a) 1 h, b) 2 h, c) 3h, and d) 5 h; insets (a), (b), (c), (d) showing corresponding SEM images of TiO_2 nanorods at 1 h, 2 h, 3 h and 5 h respectively; (ii) plot derived from current-time plots (derivations of the plot and error bars shown in appendix 4-1)

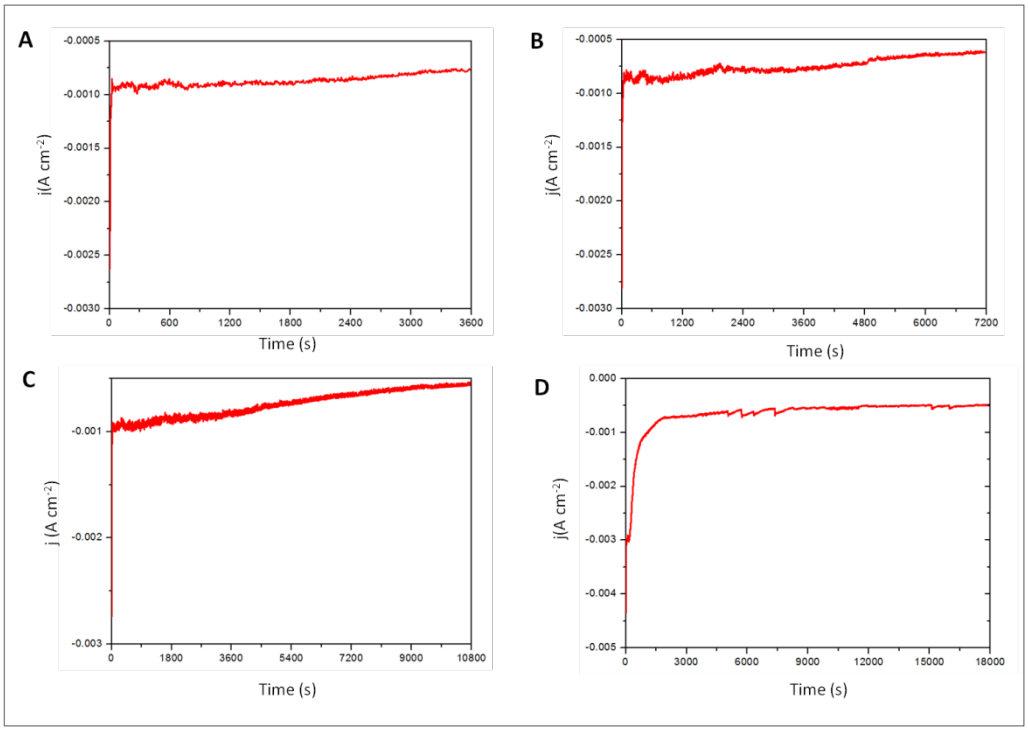

Figure 4-4. Current-time plots of TiO_2 nanorod deposition into AAM from $TiOSO_4$ precursor at -1.2 V for A) 1 h, B) 2 h, c) 3 h, and d) 5 h (inclusive of an overvoltage of -1.4 V for 20 s), with a total charge passed of 3.14 C, 5.39 C, 8.02 C and 11.99 C respectively

To investigate the phase transformation behaviour of the as-prepared TiO_2 nanorods, High temperature X-ray diffraction (HTXRD) measurements were conducted. TiO_2 nanorods were dispersed on gold/glass substrates and annealed *in-situ* from approximately 30 °C to 600 °C. It should be noted that the annealing temperatures here are taken as approximates because a substrate of Au/glass was used instead of the usual Pt strip on which the temperatures were calibrated for. Nonetheless, this method can still be used to track the gradual phase transformation of TiO_2. The HTXRD phase transformation-temperature profile of TiO_2 nanorods on gold/glass substrates in figure 4-5A confirms that the as-prepared TiO_2 nanorods are amorphous at room temperature; and upon thermal treatment gradually crystallise to produce a diffraction pattern that matches well with that of anatase TiO_2 (JPCDS 00-002-0406). It is also observed that the onset temperature for which phase transformation from TiO_2 amorphous to TiO_2 anatase occurs is 450 °C. Additionally, similar as-prepared TiO_2 nanorods (deposited on Si substrate) that had been annealed in air at 600 ^{o}C prior to XRD measurement confirms that anatase TiO_2 is achieved (figure 4-5B).

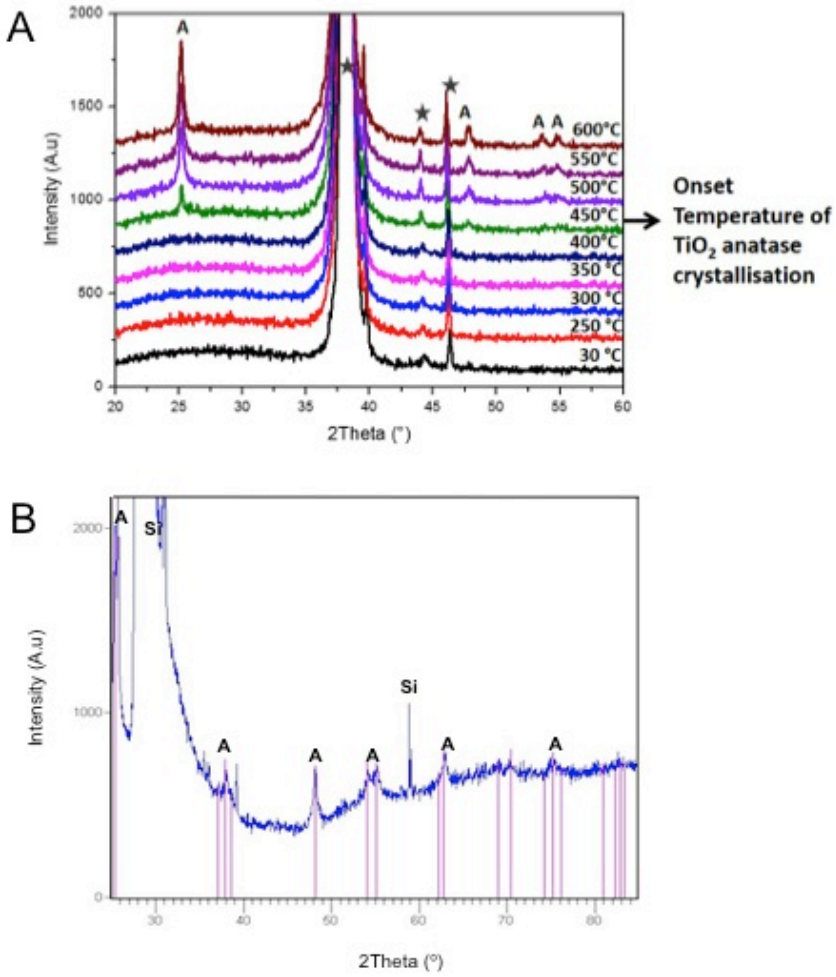

Figure 4-5. A) High Temperature XRD (HTXRD) patterns of TiO_2 nanorods electrodeposited from $TiOSO_4$ annealed *in-situ* from 25 to 600 ^{o}C, B) XRD pattern of TiO_2 nanorod deposited on Si substrate after annealing in air at 600 ^{o}C ("A", ★ and Si indicate peaks of TiO_2 anatase, Au and Si substrate respectively)

4.3.3.3. Effect of varying deposition voltages on TiO_2 Nanostructures

In addition to the TiO_2 nanorod growth at -1.4 V/-1.2 V, it was also found that TiO_2 nanotubes were achieved at lower deposition step voltages of -0.9 V/-0.7 V and -0.5 V/-0.3 V. For formation of both TiO_2 nanorods and nanotubes, the electrodeposition of TiO_2 from $TiOSO_4$ proceeds from the cathode in an aqueous acidic solution containing NO_3^- ions, which when reduced according to equation 4D leads to an increase in the local pH by generation of OH^-. This results in the hydrolysis of $Ti(O_2)SO_4$, a Ti intermediate complex formed prior to electrodeposition (equation 4E) to produce a hydroxide precipitate that subsequently, via condensation and heat treatment, yields TiO_2 (equation 4F) [9].

In a study to confirm the species responsible for the increase in local pH, Natarajan and Nogami [9] found that there was no film formation in the absence of NO_3^- ions, concluding that the cathodic production of OH^- was essential for the electrodeposition of TiO_2 from $TiOSO_4$. In our study, it was observed that there were there was no TiO_2 deposition in the AAM pores in the absence of KNO_3 at deposition voltages in the range of -1.4 V to 0 V, establishing that nitrate reduction was not only required in the formation of TiO_2 nanorods but also in TiO_2 nanotube formation.

NO_3^- (ads) + H_2O + 2 e^- → NO_2^- (ads) + 2 OH^- (Equation 4D)

$TiOSO_4 + H_2O_2 \leftrightarrow Ti(O_2)SO_4 + H_2O$ (red solution) (Equation 4E)

$Ti(O_2)SO_4 + 2OH^- + (\chi+1)H_2O \rightarrow TiO(OH)_2.\chi H_2O + H_2O_2 + SO_4^{2-} \rightarrow TiO_2$ (Equation 4F)

To investigate the role of nitrate reduction in the deposition of TiO_2 nanorods (-1.4 V to -1.0 V) and nanotubes (-1.0 V to -0.3 V), CV scans were carried out using a Ag flat electrode and AAM electrode in a pH 3 bath solution consisting of only NO_3^-. The resultant current voltage curves are shown in figure 4-6. There is a maxima match of the reduction peak at -1.0 V to the reduction of NO_3^-. A significant difference between the CV scans on an Ag flat electrode and AAM is the presence of a reduction peak at -0.25 V belonging to that of deposition in a silver-coated AAM, which is not seen for that on the Ag flat electrode.

According to a study conducted by Bowen and Hughes [28], polyvalent anions such as PO_4^{3-} and $(COO)_2^{2-}$ from anodizing electrolytes of phosphoric and oxalic acid are incorporated within the matrix of an AAM, whose surface consists of amphoteric sites which are able to become positively or negatively charged depending on the pH represented by equation 4G and 4H [29]. At pH of 4 and lower, the concentration of PO_4^{3-} and $(COO)_2^{2-}$ anions are reduced according to equation 4I and 4J. At the same time, the surface of the pore walls becomes positive-charged, overall facilitating the adsorption and reduction of negatively charged NO_3^- ions around the pore walls of AAM. From this, it is reasonable to attribute the peak at -0.25 V to NO_3^- (ads) reduction to NO_2^- (ads) along the pore walls of AAM according to equation 4D. As the local pH increases, $Ti(O_2)SO_4$ is hydrolysed to form TiO_2 nucleation sites along the pore walls as illustrated in figure 4-6 steps 1 to 3.

$MOH_2^+ \leftrightarrow MOH + H^+$ (Equation 4G)

$MOH \leftrightarrow MO^- + H^+$ (Equation 4H)

where M represents a metal ion of +2 charge adsorbed onto Al_2O_3 surface of AAM.

$PH^- \leftrightarrow P^{2-} + H^+$ (Equation 4I)

$COOH \leftrightarrow COO^- + H^+$ (Equation 4J)

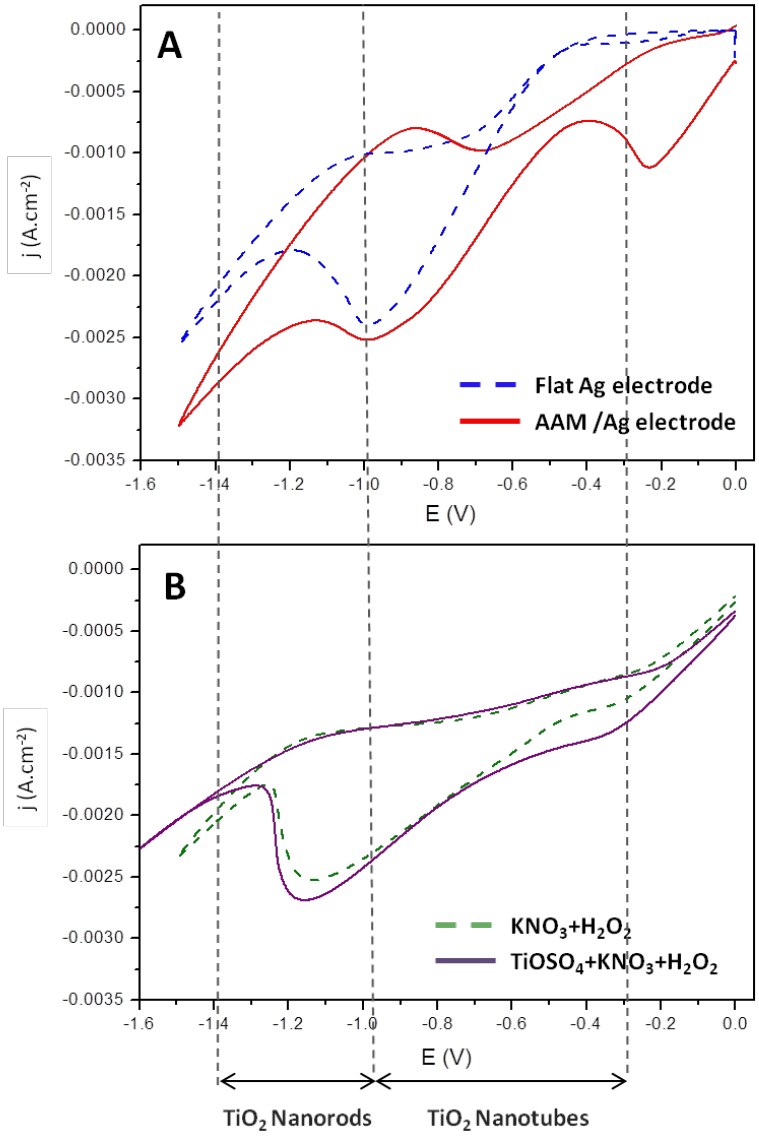

Figure 4-6. CV curves (v=20 mV s^{-1}) at (A) Ag flat electrode and AAM (Area=0.80 cm^2) in aqueous KNO_3 solutions of pH 3; (B) at AAM (Area=0.80 cm^2) in pH 3 aqueous solution of $KNO_3+H_2O_2$ and $TiOSO_4$+ $KNO_3+H_2O_2$. Regimes of potentials within -1.4 V to -1.0 V and -1.0 V to -0.3 V as indicated above represent possible formation of TiO_2 nanorods and nanotubes respectively

Preceding the nucleation of TiO_2 along the pore walls, figure 4-7 routes (i) and (ii) illustrate the proposed deposition mechanisms of TiO_2 nanorods and nanotubes formation respectively. The regeneration of NO_3^- species in route (i) step 4 distinguishes the mechanism of TiO_2 nanorods formation from that of TiO_2 nanotubes. This regeneration of NO_3^- may occur as a result of the re-oxidation of reduced NO_2^- species with the uncomplexed H_2O_2 present in the electrolyte according to reaction 4K. To test the reaction of NO_2^- with H_2O_2, a highly selective reagent, mercaptoacetic acid, $HSCH_2COOH$ was employed as an indicator for nitrite ions, which caused a solution of nitrite to develop a characteristic salmon colour owing to the production of S-nitroso compound [30]. In the test, 3 drops of $HSCH_2COOH$ were added to an aqueous solution of 50 mM $NaNO_2$, expectedly turning the mixture salmon pink. Upon adding 10 mM of H_2O_2, a colourless solution was observed after 5 min of continuous stirring, indicating the consumption of NO_2^- ions by reaction with H_2O_2. Two control tests involving the addition of $HSCH_2COOH$ to H_2O_2 and $HSCH_2COOH$ in $NaNO_2$ were carried out prior to the above test which further confirms that under continuous stirring, the mixture containing both H_2O_2 and $HSCH_2COOH$ remained colourless, and that containing $HSCH_2COOH$ and $NaNO_2$ kept its characteristic salmon colour throughout.

$NO_2^- + H_2O_2 \rightarrow NO_3^- + H_2O$ (Equation 4K)

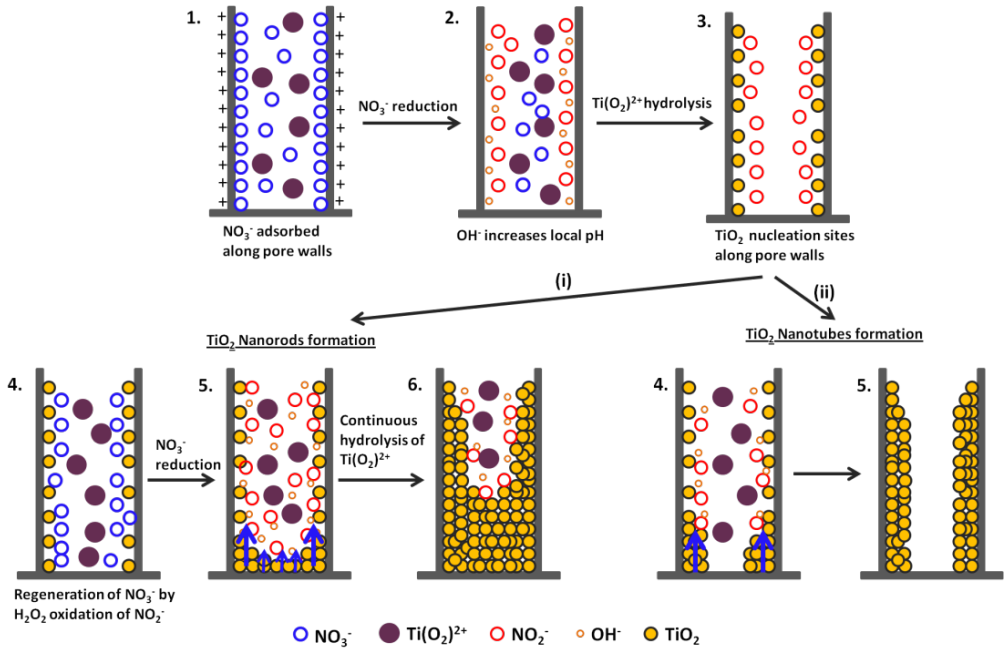

Figure 4-7. Schematic diagram illustrating nucleation of TiO_2 sites along pore walls of AAM (step 1 to 3); growth of TiO_2 nanorods *via* route (i) steps 4 to 6 from regeneration of NO_3^- from re-oxidation of reduced NO_2^- and TiO_2 nanotubes *via* (ii) steps 4 to 5 confined around the pore walls from limited reduction rates NO_3^-

The reduction rate of NO_3^- ions increases due to an abundant supply of NO_3- in the pores generated by the continuous reoxidation of the NO_2^- to NO_3^-, as well as the diffusion of NO_3- ions down the AAM according to route (i) step 5. This is shown in Figure 4-6B where both CV curves of KNO_3/H_2O_2 and $KNO_3/H_2O_2/TiOSO_4$ electrolytes produce an increased cathodic current towards the potential range of -1.4 V to -1.0 V for formation of TiO_2 nanorods. At this potential, NO_3^- ions are saturated and distributed homogeneously within the pores of AAM, where it is preferentially reduced to OH^- nearest the conducting surfaces defined by the bottom conductive surface and pore walls of the AAM. Hydrolysis of $Ti(O_2)SO_4$ to TiO_2 then takes place on pre-existing TiO_2 nucleation sites along the pore walls of AAM and subsequently on existing TiO_2 particles as illustrated in step 6, finally resulting in a bottom up deposition of TiO_2 to form nanorods characterised by higher rates of TiO_2 deposition around the pore walls.

As deposition potentials move from -1.2 V to a less negative potential of -0.3 V, the nanostructural growth of TiO_2 in the pores of AAM shifts from that of nanorods to nanotubes. At deposition voltages of less negative than -1.0 V, the rate of nitrate reduction starts to decrease, limiting the local amount of OH- ions produced in the pores

to result only in $Ti(O_2)SO_4$ hydrolysis around the pore walls where initial TiO_2 nucleation sites are located (figure 4-6 route (ii) steps 4 and 5). The SEM images in figure 4-8A and 4-8B show TiO_2 nanotubes of different wall thickness (each averaged over 20 nanotubes). TiO_2 nanotubes which are deposited from a voltage step of [-0.9 V/20s, -0.7 V/10800 s] (figure 4-xA) were observed to have an average wall thickness (denoted by $X_{ave,0.7}$ and $X_{ave,0.3}$ in inset of figure 4-7A and 4-7B respectively) larger than that deposited at [-0.5 V/20s, -0.3 V/10800s] (figure 4-8B), hence suggesting that there exists a proportional relationship between the rate of nitrate reduction and wall thickness of TiO_2 nanotubes within the potential range of -1.0 V to -0.3 V.

The morphologies of TiO_2 nanostructures that can be achieved from the two deposition regimes of [-1.4 V to -1.0 V] and [-1.0 V to -0.3 V] are not only limited to TiO_2 nanorods and thin-walled TiO_2 nanotubes. Additionally, TiO_2 nanostructures resulting from deposition voltages of [-1.4 V/ 20s, -0.7 V/3580 s] (figure 4-9A) and [-0.9 V/ 20s, -1.2 V/3580 s] (figure 4-9B) display morphologies that vary from those as seen earlier in figure 4-8.

Tubular nanostructures of TiO_2 were obtained from deposition voltages of [-1.4 V/ 20s, -0.7 V/3580 s] (figure 4-9A), in which its wall thickness of 69.3 ± 8.9 nm is approximately three times that of TiO_2 nanotubes deposited at [-0.9 V/20s, -0.7 V/10800 s] (figure 4-7A). According to the proposed scheme in figure 4-9A, an overpotential of -1.4 V in the first 20 s produces homogeneous TiO_2 sites on the AAM pore walls, arising from a high NO_3^- reduction rate in the deposition regime of "TiO_2 nanorods" (refer to figure 4-6). As the deposition potential is made less negative at -0.7 V after 20 s, reduction rates of NO_3^- becomes limited, resulting in the decrease in deposition rates of TiO_2 (refer to figure 4-6). Since most of the electrodeposition occurs in this deposition regime, the formation of tubular nanostructures is as expected. Additionally, the homogeneous TiO_2 sites formed around the AAM pore walls at -1.4 V in the first 20 s provides a high concentration of pre-existing sites from which subsequent TiO_2 growth occurs at -0.7 V, thereby accounting for the thicker wall structures observed in figure 4-9A.

At deposition voltages of [-0.9 V/20s, -1.2 V/3580 s], irregular TiO_2 nanostructures with morphologies resembling that between nanotubes and nanorods is achieved (figure 4-9B). At an initial applied overpotential of -0.9 V for the first 20 s, reduction rate of NO_3^- is limited, and a low rate of $Ti(O_2)SO_4$ hydrolysis results in a low concentration of

inhomogeneous TiO_2 sites on the pore walls of AAM (figure 4-10B). However, when the deposition voltage is made more negative at -1.2 V after 20 s, electrodeposition shifts to the regime of "TiO_2 nanorods" (figure 4-6) where the rate of NO_3^- reduction increases to favour the hydrolysis of $Ti(O_2)SO_4$ to TiO_2. Based on the low availability and inhomogeneous distribution of pre-existing TiO_2 sites around the pore walls of the AAM, it is postulated that the high rate of TiO_2 growth occurs in random orientations from pre-existing TiO_2 sites, which eventually results in irregular TiO_2 nanostructures (figure 4-9B).

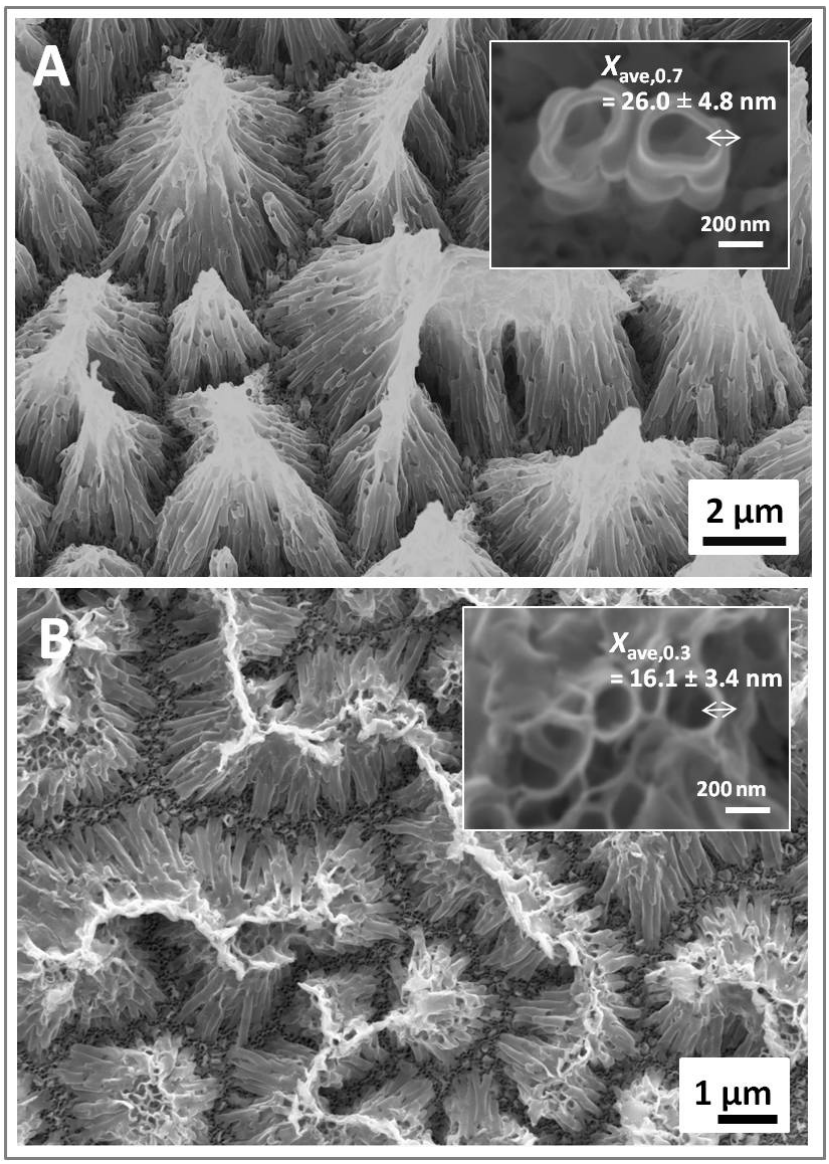

Figure 4-8. SEM images of TiO_2 nanotubes deposited nanotubes deposited from a voltage step of (A) [-0.9 V/20s, -0.7 V/10800 s] and (B) [-0.5 V/20s, -0.3 V/10800s] where corresponding inset shows varying average wall thickness (N_x=20) denoted by $X_{ave,0.7}$ and $X_{ave,0.3}$ respectively.

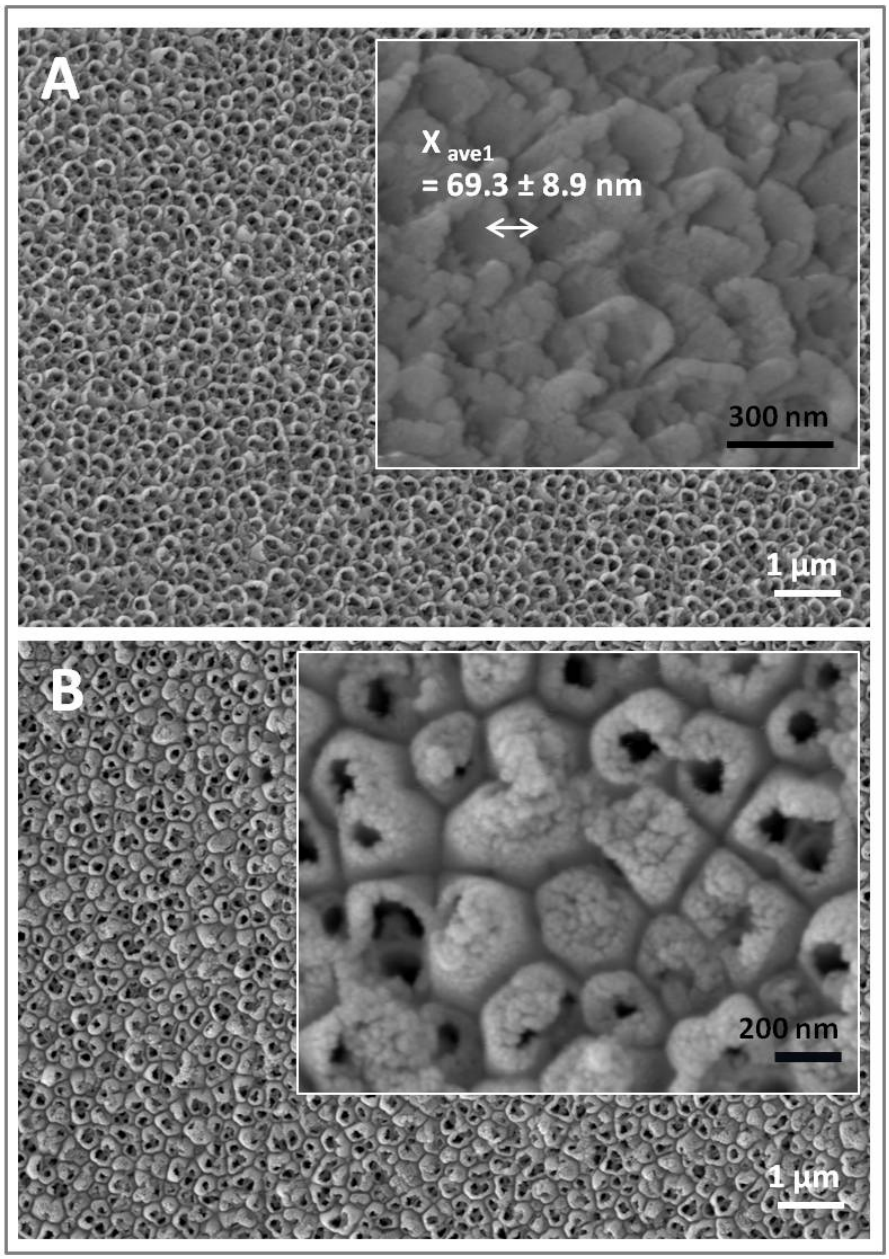

Figure 4-9. SEM images of TiO_2 nanostructures deposited from a voltage step of A) [-1.4 V/ 20s, -0.7 V/3580 s] with average wall thickness (N_X=20) denoted by X_{ave1}) and B) [-0.9 V/ 20s, -1.2 V/3580 s]; corresponding insets show magnified TiO_2 nanostructures

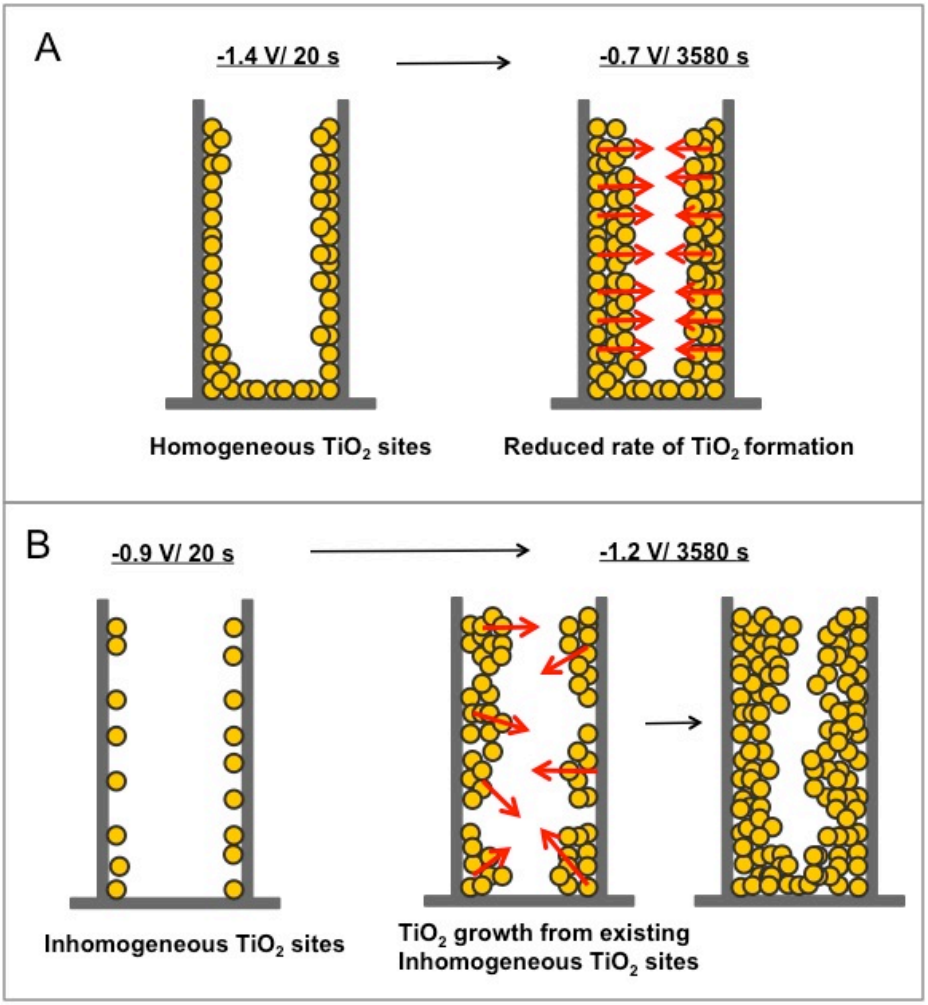

Figure 4-10. Schematic illustration of A) formation of thick-walled TiO_2 nanotubes at deposition voltages of [-1.4 V/ 20s, -0.7 V/3580 s], and B) irregular TiO_2 nanostructures at deposition voltages of [-0.9 V/ 20s, -1.2 V/3580 s]

4.3.3.4. Problems encountered with TiO_2 deposition on Pt using $TiOSO_4$ precursor

The effects of a range of TiO_2 deposition voltages from Ti (IV) particularly on highly catalytic surfaces such as Pt were investigated by depositing Pt nanorods prior to TiO_2 in the pores of AAM. Despite success in the electrodeposition of TiO_2 at -1.2 V, there were significant defects in the material. In particular the presence of gaps between segments of TiO_2 and Pt seen in Figure 4-11(a) indicates poor attachment of TiO_2 to Pt within the pores of AAM. Two scenarios in Figure 4-11(b) and 4-11(c) have been proposed to further illustrate this. According to Figure 411-b, broken segments of TiO_2 seen along the pores of AAM suggest that the preceded growth of TiO_2 nanorods from Pt surface were later broken up by the generation of hydrogen bubbles occurring at a high operating voltage of -1.4 V and -1.2 V. This may originate from tiny H_2 bubbles trapped within the TiO_2

nanostructures near the Pt surface, which eventually expand to create a propulsive force upwards through the pores of the TiO_2 nanostructure within the AAM. In the second scenario, the gaps between TiO_2 and Pt segments in Figure 4-11c depicts the possibility of hydrogen gas evolved at the surface of Pt which would likely hinder the effective nucleation and subsequent growth of TiO_2 from the surface of Pt. Lowering the applied voltages to between -0.1 V to -0.9 V resulted in the formation of TiO_2 nanotubes instead as discussed earlier 4.6.3.3, which did not contribute towards a favourable growth method for the fabrication of TiO_2 nanorod segments.

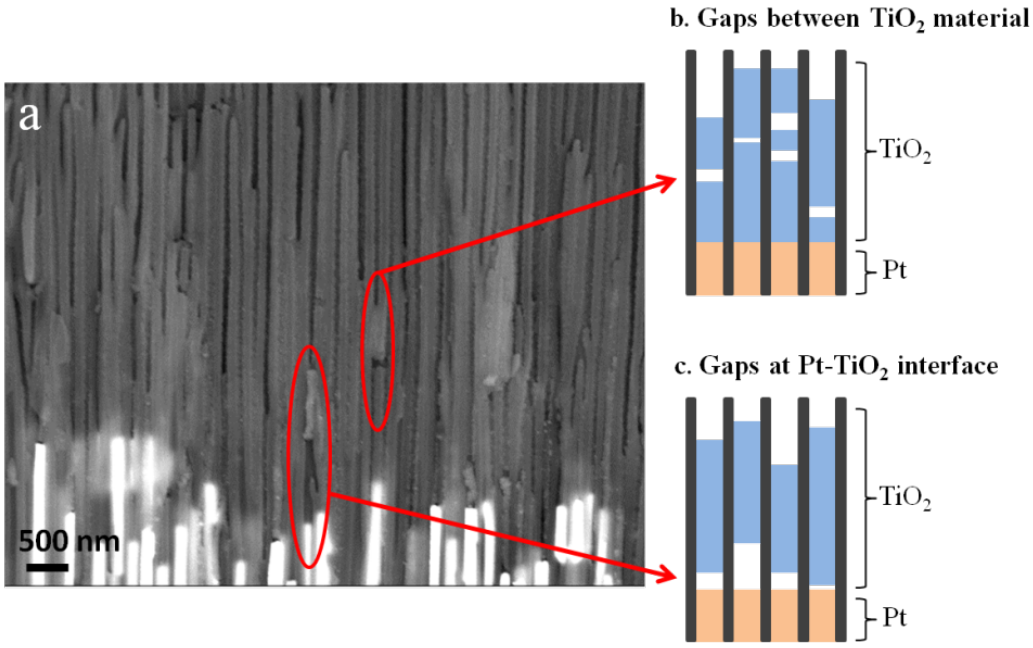

Figure 4-11. (a) SEM image showing gaps between segments of TiO_2 electrodeposited from $TiOSO_4$ and Pt in AAM illustrated by schematic diagrams (b) and (c)

4.4. Templated Electrodeposition of TiO_2 from $TiCl_3$

4.4.1. Materials

Titanium chloride ($TiCl_3$, Mr= 154.230 g/mol), titanium chloride solution ($TiCl_3$ ~10 wt. % in 20-30 wt. % hydrochloric acid) and sodium hydrogen carbonate ($NaHCO_3$, Mr=84 g/mol) were purchased from Sigma-Aldrich. Hydrogen peroxide (6% w/v H_2O_2), hydrochloric acid (HCl, 12% v/v), nitric acid (69% HNO_3) and potassium nitrate (KNO_3) were obtained from BDH Laboratory Supplies. Methanol (Chromasolv® Plus for HPLC ≥ 99.9 %), hydrochloric acid (37% HCl) and

sodium hydroxide (40 % w/v NaOH) were purchased from VWR and ammonia solution (35 %, FW=17.05 NH_4OH) was purchased from Fischer Scientific. Commercial Anopore® aluminium oxide hydrophilic membranes (AAM) of diameters 25 and 47 mm with 200 nm nominal pore size and 0.1 μm filter pore size were commercially available from Whatman International Ltd. and were used directly for electrodeposition without prior cleaning or pretreatment. Carbon film supported copper TEM grids (300 mesh) were purchased from Agar Scientific. Nanopure deionised water was used in all the experiments. All chemicals were of analytical reagent grade and were used without further purification.

4.4.2. General Experiment Practice

4.4.2.1. Bath Solution Preparation of $TiCl_3$

The preparation of $TiCl_3$ precursor solution has been designed for normal ambient conditions, eliminating the need to create an argon or nitrogen environment. This simplifies the procedure and increases the ease of $TiCl_3$ precursor preparation. The step procedures of successfully preparing a stable $TiCl_3$ precursor solution, as well as, the respective reaction characteristics are described below.

$TiCl_3$ in 10-20 % aqueous HCl was preferred over powdered $TiCl_3$ as the precursor material because the former was found to be more stable and thus easier to handle. A typical $TiCl_3$ electrolyte was prepared by adding 12.3 g of $NaHCO_3$ (3 M) in small batches of approximately 0.5 g to 0.35 M $TiCl_3$ (~10 wt. % in 20-30 wt. % hydrochloric acid) in 30 ml of DI water to tune the pH of solution to pH 2-2.5. The mixture is then swirled vigorously to ensure that the violet solution turns clear before adding the next batch of 0.5 g $NaHCO_3$. As $NaHCO_3$ reacts with HCl to produce CO_2, continuous vigorous swirling of the $TiCl_3$ mixture dispels the gaseous CO_2 to ensure a resultant deep violet solution, which does not precipitate and will remain stable during for up to 5 h of electrodeposition. The resultant pH of the solution ranges between values of 2 to 2.5.

The known sensitivity of Ti^{3+} salt and its aqueous solutions to traces of atmospheric O_2 has led to the importance in controlling the atmospheric conditions for the preparation of $TiCl_3$ aqueous electrolyte for the fabrication of TiO_2 nanostructures [19]. Under normal ambient conditions, oxidation of Ti^{3+} proceeds via equation 4L and 4M by influence of molecular oxygen present [31]. This is simply represented by the rapid acidic hydrolysis of

Ti^{3+}, followed by a rate-determining reaction of the reactive species, $TiOH^{2+}$, with oxygen. Therefore in order to limit reaction 4M, many experiments involving $TiCl_3$ were carried out under controlled atmospheric conditions to prevent interaction of $TiCl_3$ with oxygen and moisture [8, 19, 24]. Despite this, the preparation of $TiCl_3$ electrolyte and electrodeposition of TiO_2 in our study as stated earlier are designed to perform well under normal ambient conditions.

$Ti^{3+}(aq) + H_2O \Leftrightarrow TiOH^{2+} + H^+$ (Equation 4L)

$TiOH^{2+} + O_2 \rightarrow$ products (Equation 4M)

According to the buffering system of bicarbonate in equation 4N, the addition of a large amount of $NaHCO_3$ is likely to shift the equilibrium to the far left to produce CO_2, which was observed from the fizzing of $TiCl_3$ solution as an increased amount of $NaHCO_3$ is added. The vigorous and continuous swirling of the $TiCl_3$ mixture thus helps to quickly force CO_2 out of the solution, allowing the reaction to continually proceed to the left to neutralize H^+ and thereby preventing the mixture from precipitating as soon as all sodium hydrogen carbonate has been added.

$CO_2+H_2O \leftrightarrow H_2CO_3 \leftrightarrow HCO_3^-+H^+$ (Equation 4N)

By varying the amount of $NaHCO_3$ added, the pH of $TiCl_3$ precursor solution can be tuned. This is characterised by changes in the colour of the resultant solution and is associated with the different Ti species present in the solution. Pecsok and Fletcher [32] reported that monohydroxylated compound $Ti(OH)(OH_2)_5^{2+}$ is the primary specie present in the $TiCl_3$ bath solution of pH 1 to 3. However as the pH is increased to 3, Ti (III) hydroxylation occurs and a black-coloured dimer of $Ti_2O(OH_2)_{10}^{4+}$ is formed, turning the solution from bright violet to a very deep blue. This black appearance was then concluded by Cassaignon and co-workers [33] to be the polycationic species with mixed valence arising from an intervalence transfer between Ti(III) and Ti(IV). Despite reports in the slight variations in both reports, there is a similar observation that the type of Ti active species formed is sensitive to the pH of the $TiCl_3$ bath solution. This has been observed to affect the quality of the deposited TiO_2 nanostructures will be further discussed in section 4.8.3.3.

4.4.2.2. Templated Electrodeposition of TiO_2 Nanorods from $TiCl_3$

TiO_2 nanorods were grown inside the pores of the AAM by applying a potentiostatic control of -0.2 V (vs. Ag/AgCl)/ *x* s using an AUTOLAB PGSTAT12 potentiostat, where *x* represents the desired time for electrodeposition.

4.4.2.3. Method of Releasing TiO_2 Nanorods From Template

After deposition, TiO_2-filled AAM is removed from the solution, gently rinsed with DI water and annealed in air at 600 °C for 2 h to obtain anatase TiO_2. To obtain freestanding TiO_2 nanorods, TiO_2-filled AAM is suspended on the surface of 3 M NaOH for 1 h to etch off the AAM and then rinsed gently with DI water. The suspension procedure of the TiO_2-filled AAM on 3 M NaOH consists of firstly sealing the metal-sputtered side of the AAM with epoxy and attaching a string (approx. length of 1-2 cm), followed by floating the sample on NaOH solution with the metal-sputtered side of the AAM facing upwards. Attachment of the string to the sample enables easy removal of the sample from NaOH solution after etching. Free TiO_2 nanorods are released by first etching off silver sputtered layer by treating the AAM with an etching solution consisting of methanol, 30% ammonium hydroxide and 30% hydrogen peroxide (5:1:1 v/v/v) until all the silver has been completely removed, followed by dissolving the AAM in 3 M NaOH solution. The obtained TiO_2 nanorods are then centrifuged at 2000 RPM for 15 min and washed repeatedly and finally dispersed in DI water or ethanol by sonication.

4.4.3. Results and Discussion

4.4.3.1. Selection of $TiCl_3$ Reagent for Electrodeposition of TiO_2 Nanorods

$TiCl_3$ has become an important precursor in the electrodeposition of TiO_2 due to the possibility of electrodepositing TiO_2 on Pt at lower voltages, thus overcoming the challenges faced when $TiOSO_4$ has been employed as the precursor (details provided in section 4.6.3.4). Commercial $TiCl_3$ reagent, which is present in two forms: powder $TiCl_3$ and $TiCl_3$ solution (10 wt. % in 20-30 wt % HCl) have been used in this study for the template electrodeposition of TiO_2.

In this study, the advantage of using $TiCl_3$ was first discovered through the use of powder $TiCl_3$. The anodic oxidative hydrolysis reaction of Ti^{3+} to produce TiO_2 occurs at a less

negative potential of -0.2 V, minimising the evolution of H_2 from the Pt surface, which does not hinder the continuous upward growth of TiO_2 in the AAM from the Pt surface. The successful electrodeposition of the TiO_2 nanorod segment on Pt nanorods is shown in figure 4-12. Additionally, this method facilitates the deposition of TiO_2 above Pt segments where there are no observable structural defects from broken segments of TiO_2 due to H_2 evolution, which had otherwise occurred via electrodeposition from $TiOSO_4$ precursor as it was previously observed in figure 4-11.

The preparation of the $TiCl_3$ electrolyte using powder $TiCl_3$ was however found to be cumbersome as powder $TiCl_3$ itself is highly hygroscopic and is highly reactive when exposed to air (fumes were immediately observed as soon as $TiCl_3$ contacts air). An alternative form of commercially available $TiCl_3$ is the $TiCl_3$ solution (10 wt. % in 20-30 wt % HCl), which is used for all the subsequent synthesis of TiO_2. Diluted $TiCl_3$ in HCl solution is a more benign reagent compared to powder $TiCl_3$, hence overall easing the preparation of the $TiCl_3$ electrolyte and allow for $TiCl_3$ precursor solution to be prepared under ambient conditions. Overall, highly-ordered TiO_2 nanorods could be successfully achieved using both powder $TiCl_3$ and $TiCl_3$ solution (10 wt. % in 20-30 wt % HCl), with the latter being the preferred choice due to the ease of handling.

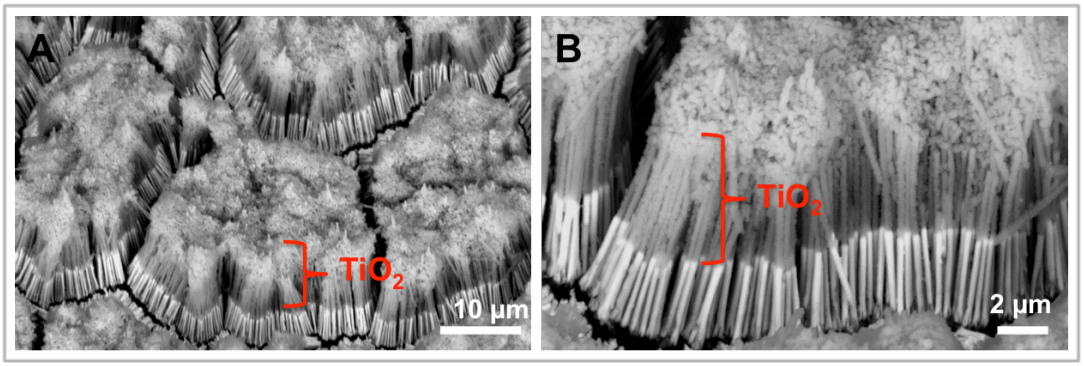

Figure 4-12. SEM images A) 5 k and B) 15 k magnification of free-standing TiO_2 nanorods electrodeposited on Pt nanorods using powder $TiCl_3$ powder as a starting material. TiO_2 nanorods were deposited at -0.1 V (vs. Ag/AgCl, 1 M KCl at 25 ^{o}C) for 2 h.

4.4.3.2. Characterisation of TiO_2 Nanorods Electrodeposited from $TiCl_3$ Precursor

Figure 4-13 (i) shows a linear relationship between the lengths of the TiO_2 nanorods (averaged over 100 nanorods) and the total amount of charge passed during electrodeposition. Increasing lengths of the TiO_2 nanorods were prepared with a total

charge of 0.93 C, 2.77 C, 3.31 C and 6.36 C respectively, using a membrane surface area of approximately 0.79 cm^2. The knowledge of the linear dependence of the length of TiO_2 on the total deposition charge enables a realistic control over the desire length of TiO_2 segment and the amount of material. Similar to the deposition transients resulting from TiO_2 deposition using $TiOSO_4$ precursor, slightly decreasing deposition currents of TiO_2 deposition from $TiCl_3$ precursor was also observed (figure 4-14). Likewise, this may be caused by a decrease in the surface conductivity of TiO_2 with increasing deposition time. Comparison between plot (i) and plot (ii) (derived from the current density time plots) indicates an approximate 56 % Faradaic efficiency for the reaction. Using a $TiCl_3$ precursor bath solution prepared from $TiCl_3$ solution reagent and a constant deposition potential of -0.2 V, highly ordered and dense TiO_2 nanorods are achieved (figure 4-15).

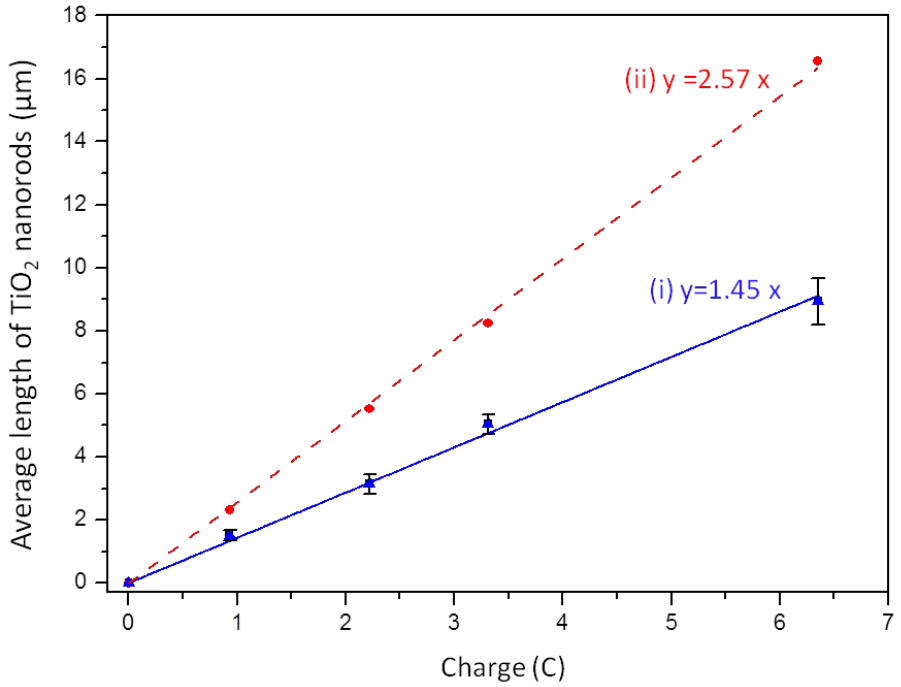

Figure 4-13. (i) Plot of experimental lengths TiO_2 nanorods electrodeposited from aqueous solution of $TiCl_3$ against total charge passed; (ii) plot derived from current-time plots

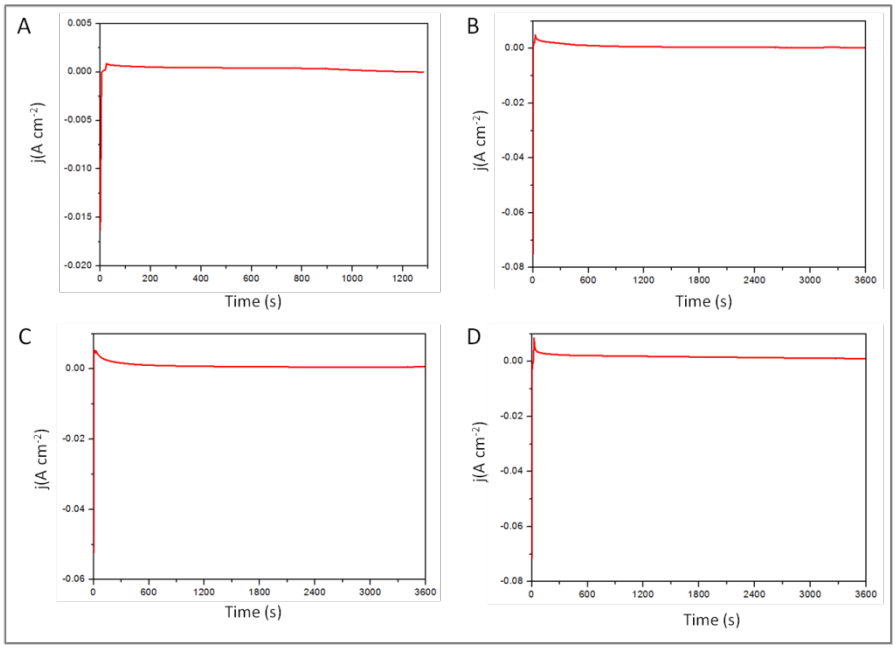

Figure 4-14. Deposition transients showing varying total charge passed A) 0.93 C, B) 2.77 C, C) 3.31 C, D) 6.36 C under constant deposition voltage of -0.2 V (vs. Ag/AgCl, 1 M KCl at 25 ^{o}C) from $TiCl_3$ precursor, to achieve varying amounts of TiO_2 deposition within porous AAM

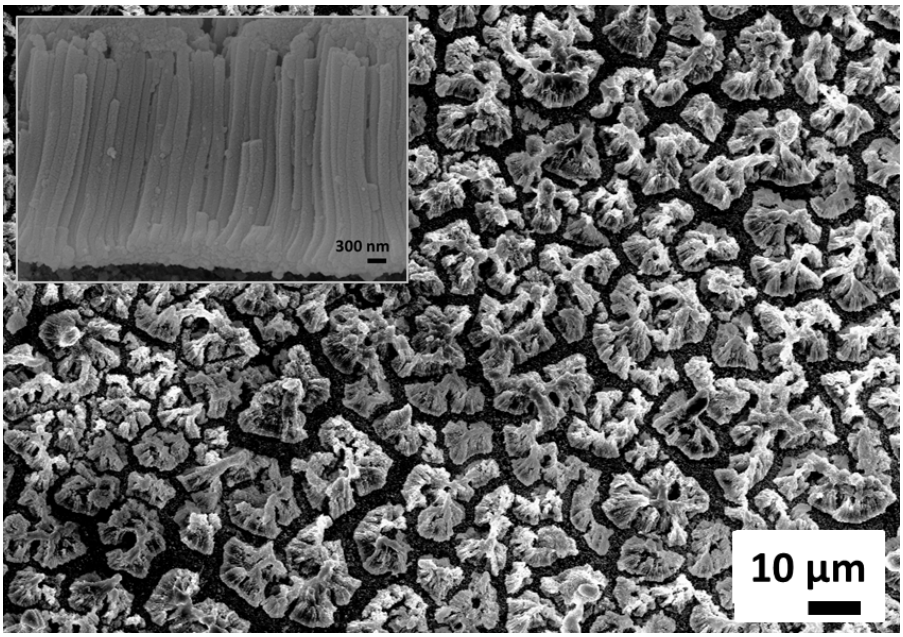

Figure 4-15. A top view SEM image of free-standing TiO_2 nanorods electrodeposited at -0.2 V (vs. Ag/AgCl, 1 M KCl) from a $TiCl_3$ precursor bath solution prepared from $TiCl_3$ solution reagent. Inset shows a magnified side-view SEM image of the corresponding TiO_2 nanorods.

The phase transformation-temperature profile of TiO_2 samples obtained from $TiCl_3$ were analysed by the XRD diffraction performed on separately prepared TiO_2 films before annealing and after annealing at 400 ^oC, 450 ^oC, 500 ^oC, 600 ^oC and 700 ^oC for 5 h in air. The relatively small counts of TiO_2 peaks with respect to that of the Ag peaks is a result of a much higher electron density of high purity silver foil substrate on which TiO_2 was deposited. The XRD diffractogram in Figure 4-16 confirms that the TiO_2 samples are amorphous before thermal treatment and begins to crystallise at 400 ^oC with diffraction peaks of anatase and rutile corresponding to JPCDS 00-002-0406 and 01-088-1175 respectively. Based on the peak intensities, proportions of the different TiO_2 polymorphs were evaluated using equation 4O [34] where the main peaks (101) of TiO_2 anatase and (110) of TiO_2 rutile were chosen for the analysis. The first appearance of the TiO_2 anatase and rutile polymorph blend at 500 ^oC consists of approximately 36 % anatase and 64 % rutile and as the sample is treated at a higher temperature of 600 ^oC, the proportion of anatase increased to 41 %.

$X_A = [1+1.26(I_R/I_A)]^{-1}$ (Equation 4O)

The co-mixture of anatase and rutile phase present in TiO_2 nanorods from $TiCl_3$ (Ti^{3+}) precursor is in contrast to that of TiO_2 nanorods from $TiOSO_4$ (Ti^{4+}) precursor (figure 4-4B), where only TiO_2 anatase was achieved under the same annealing condition of 600 ^oC.

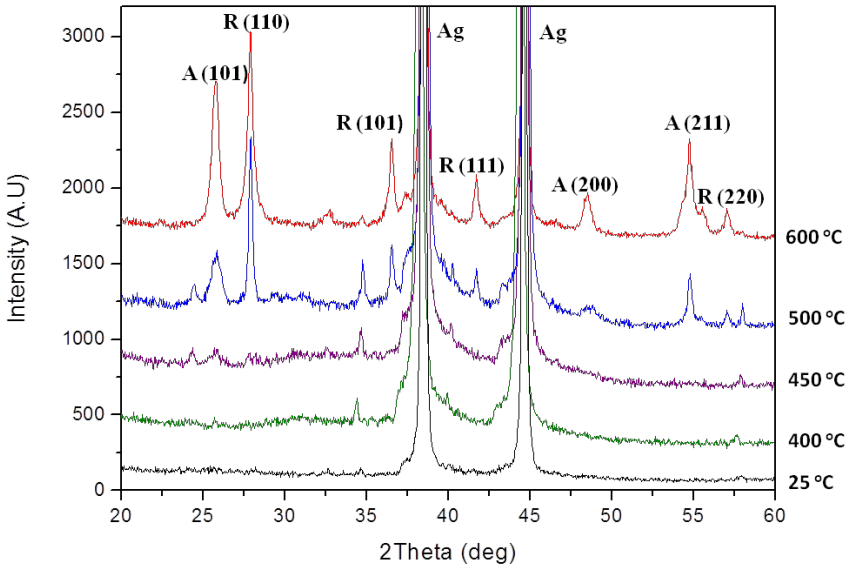

Figure 4-16. Multiple plots of XRD patterns of TiO_2 films electrodeposited from $TiCl_3$ obtained at various temperatures from 25 to 600 ^oC ("A" and "R" indicates TiO_2 anatase and rutile peaks respectively

4.4.3.3. Effect of pH on TiO_2 Nanostructures

It has been reported that the desired pH range of $TiCl_3$ electrolyte for the electrochemical deposition of TiO_2 lies between 1.5 to 3.1 [19]. This is because at a lower pH, the deposition of TiO_2 is prevented by an increase in the solubility of TiO_2, while at a high pH an uncontrolled deposition of TiO_2 will result [24]. The pH effects of the $TiCl_3$ precursor solution on the TiO_2 nanostructures were investigated at pH 1.5 and 2.5. Figure 4-17 shows that TiO_2 nanorods that were electrodeposited from an electrolyte of pH 1.5 had high porosity. This is evident by the fact that Pt had infiltrated into the pores of TiO_2 structures as shown in Figure 4-17, where the use of the backscattered SEM imaging enhances the imaging contrast proportional to the material's mean atomic number, thereby resulting in Pt to appear brighter in the region of TiO_2. In comparison, denser TiO_2 nanorods were achieved by adjusting pH to 2 using $NaHCO_3$. The formation of a clear junction between the TiO_2 and Pt segments as seen in Figure 4-16B is the result of an increased in density of TiO_2 nanorods at pH 2 where there are evidently fewer Pt particles inside the TiO_2 matrix. A series of experiment carried out suggested that a pH range of 1.9 to 2.5 favours the growth of denser TiO_2 nanostructures while highly porous TiO_2 nanostructures are produced at a lower pH range of 1.2 to 1.8.

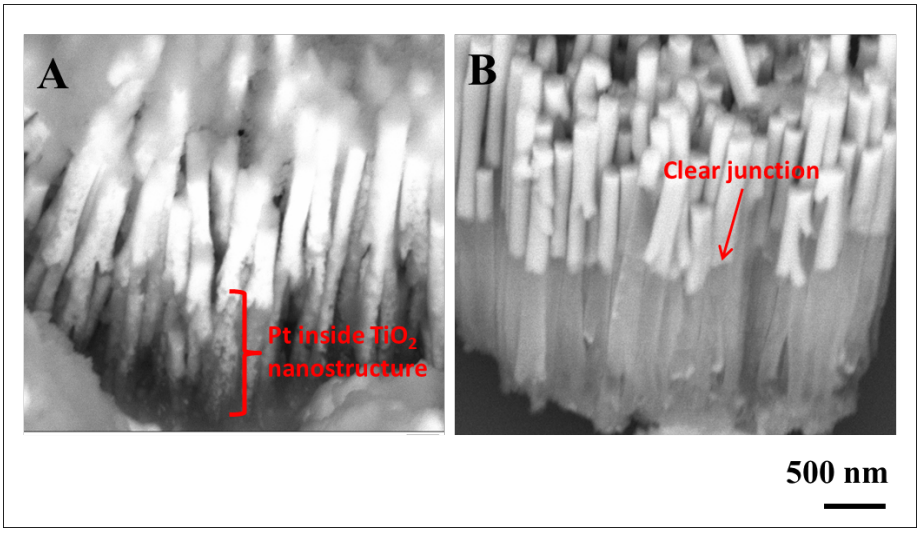

Figure 4-17. SEM images of TiO_2/Pt nanostructures consisting of TiO_2 electrodeposited electrodeposited at -0.2 V (vs. Ag/AgCl, 1 M KCl) from a $TiCl_3$ precursor bath solution obtained at pH range of (a) 1.3-1.8 (b) 1.9-2.5

The schematic diagram in figure 4-18 illustrates the proposed mechanisms for the formation of different TiO_2 nanostructures at a pH 1.3-1.8 and pH 1.9-2.5 and may offer an explanation to why there is a contrast in the density of TiO_2 nanostructures at pH range of 1.9-2.5 compared to pH 1.3-1.8 as shown in figure 4-17. In a study of amphoteric properties of hydrous Al_2O_3 using alkalimetric and acidimetric titration, Huang and Stumm [29] determined the pH at zero net adsorption of H^+ and OH^- to be 8.50 and had described the extent of adsorption of cations on hydrous Al_2O_3 to increase with increasing pH. Other studies have also demonstrated similar properties of hydrous Al_2O_3 and have characterized the interaction of hydrous oxide with cations as an ion exchange process, in which the adsorbed cations replace bound protons [35, 36]. Accordingly this has been illustrated in figure 4-18, showing some bound protons are replaced by hydrolysed $TiOH^{2+}$ reactive species. Since the extent of cation exchanges increases with pH, similarly it is proposed that the extent of proton replacement with $TiOH^{2+}$ will be higher at pH range of 1.9-2.5 compared to that at pH 1.3-1.8, hence suggesting a higher number of active $TiOH^{2+}$ nucleation sites at pH 2 which increases the rate of subsequent oxidation to TiO_2.

A CV study that had been performed in AAM using $TiCl_3$ precursor solution at pH 1.3, 1.5 and 2 (figure 4-19) indicates the dependence of $TiOH^{2+}$ oxidation rate on the pH of $TiCl_3$ precursor solution. At a potential of -0.2 V, the steady-state anodic current density of $TiOH^{2+}$ oxidation is higher at pH of 2 compared to pH 1.5 and further decreases at pH is dropped to

1.3. A similar trend was also observed by Kavan and co-workers [19] on a Pt rotating disc electrode. This further supports the proposed mechanism where the rate of $TiOH^{2+}$ oxidation increases with the higher number of $TiOH^{2+}$ reactive sites present within the AAM pores, arising from a greater extent of ion exchange at a higher pH.

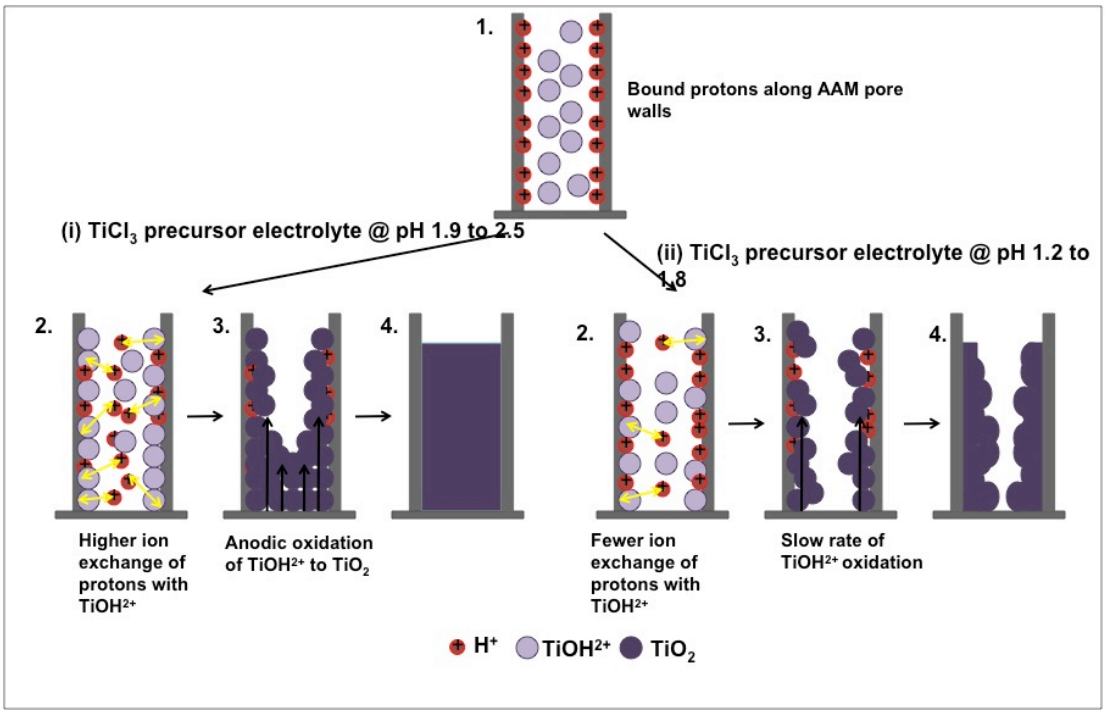

Figure 4-18. Schematic illustration of the (i) formation of dense TiO_2 nanostructures from Ti^{3+} precursor solution of pH 1.9 to 2.5; (ii) formation of highly porous TiO_2 nanostructures from Ti^{3+} precursor solution of pH 1.2 to 1.8

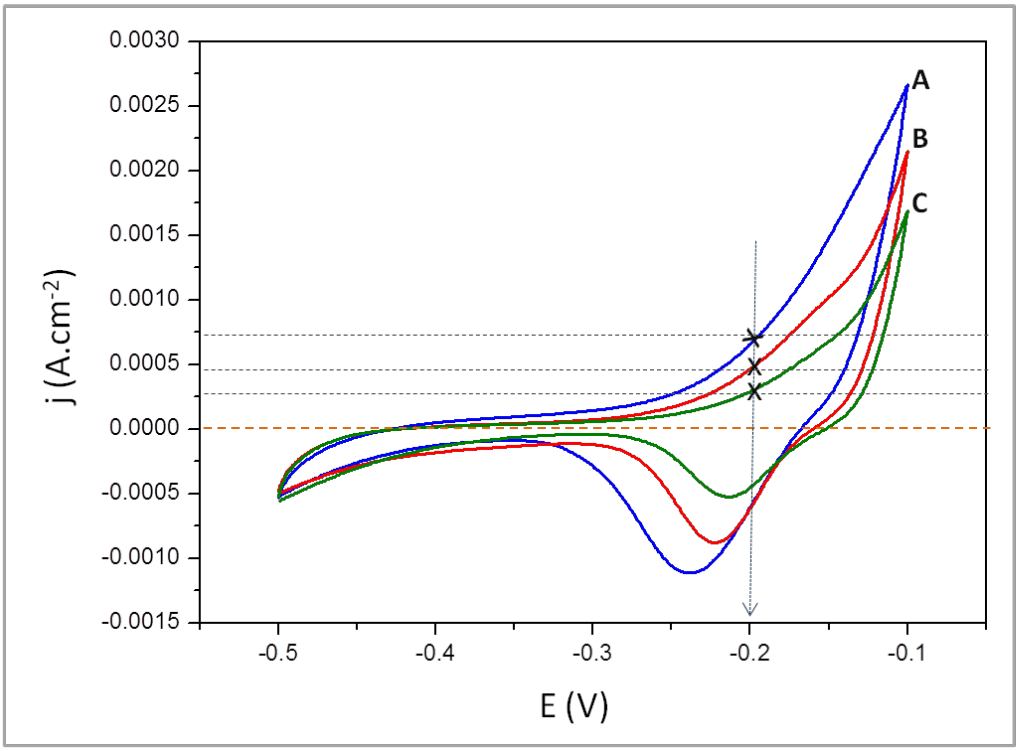

Figure 4-19. CV curves (v=20 m/s) at AAM (Area=0.8 cm^2) in aqueous $TiCl_3$ precursor solutions of A) pH 2, B) pH 1.5 and C) pH 1.3 at 20 ^oC

4.4.3.4. Effect of Applied Voltage on TiO_2 Nanostructures

Figure 4-20 shows changes in the nanostructures of TiO_2 electrodeposited from a $TiCl_3$ precursor solution resulting from different deposition potentials of -0.1 V, -0.2 V, -0.3 V and -0.4 V. The pH of the $TiCl_3$ precursor solution was kept at approximately pH 2 for all electrodeposition performed at -0.1 V, -0.2 V, -0.3 V and -0.4 V. The reason for Pt deposition as a second layer on TiO_2 is to elucidate the nanostructures of TiO_2 through enhanced contrast between Pt and TiO_2 in the SEM backscattered mode. As seen in figure 4-20B, arrays of well-defined TiO_2 nanorod segments with an average length (over 10 nanorods) of 606 ± 40 nm were achieved at -0.2 V. At more negative potentials of -0.3 V (figure 4-19C), shorter TiO_2 length segments of approximately 213 ± 14 nm (over 10 nanorods) were achieved; and a further decrease in the deposition potential at -0.4 V resulted in the disappearance of TiO_2 nanorod segments where instead tubular nanostructures of TiO_2 are formed (figure 4-19D).

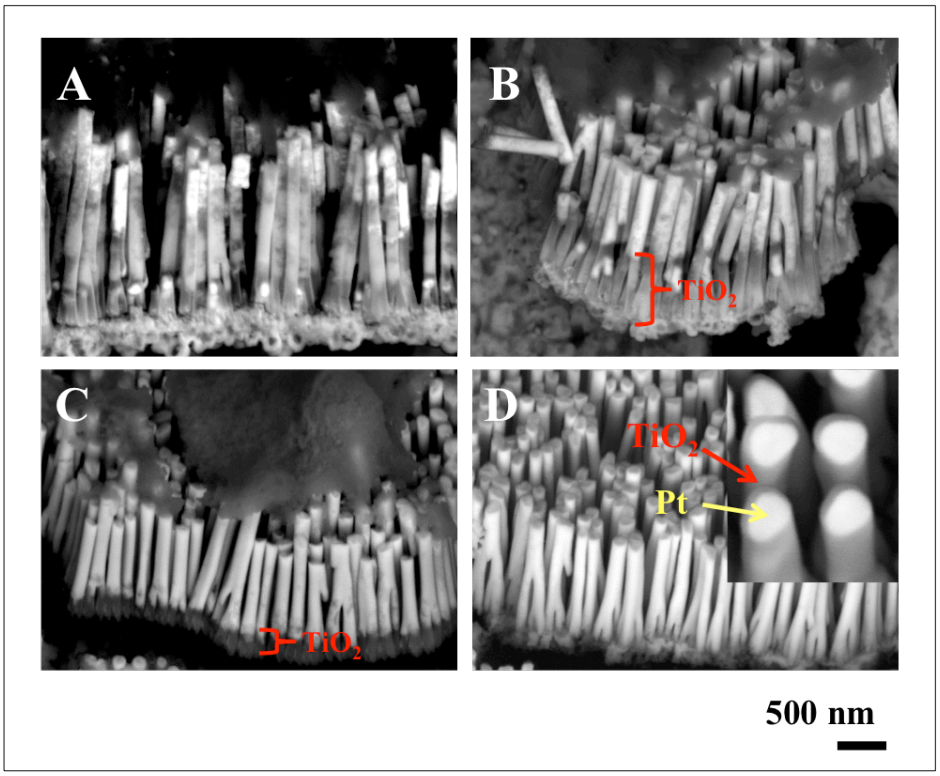

Figure 4-20. Backscattered SEM images of morphology of TiO_2-Pt nanostructures deposited at (A) -0.1 V (B) -0.2 V (C) -0.3 V (D) -0.4 V (vs. Ag/AgCl, 1 M KCl) from $TiCl_3$ precursor at pH 2; inset in D shows a high magnification of Pt-TiO_2-core-shell structure

A proposed schematic diagram in Figure 4-21 relates the rate of the $TiOH^{2+}$ oxidation and anodic current densities to the growth of TiO_2 in the AAM and hence explains the TiO_2 nanostructures obtained in figure 4-20. As established earlier, it can be assumed that the extent of $TiOH^{2+}$ active sites adsorbed on the pore walls of the AAM are the same for 3 different samples (a), (b) and (c) before voltage is applied. Referring back to the CV scan-pH 2 in figure 4-19, a moderately higher anodic current density is achieved at -0.2 V compared to significantly lower current densities at potentials of -0.3 V and -0.4 V. From this, a higher TiO_2 growth rate can be expected from an increased reaction of $TiOH^{2+}$ oxidation, resulting in denser TiO_2 nanostructures. The variations in TiO_2 growth rates are represented by the length and number of the arrows indicated in the 2nd step of figure 4-22, where longer arrows suggest higher rates of TiO_2 growth.

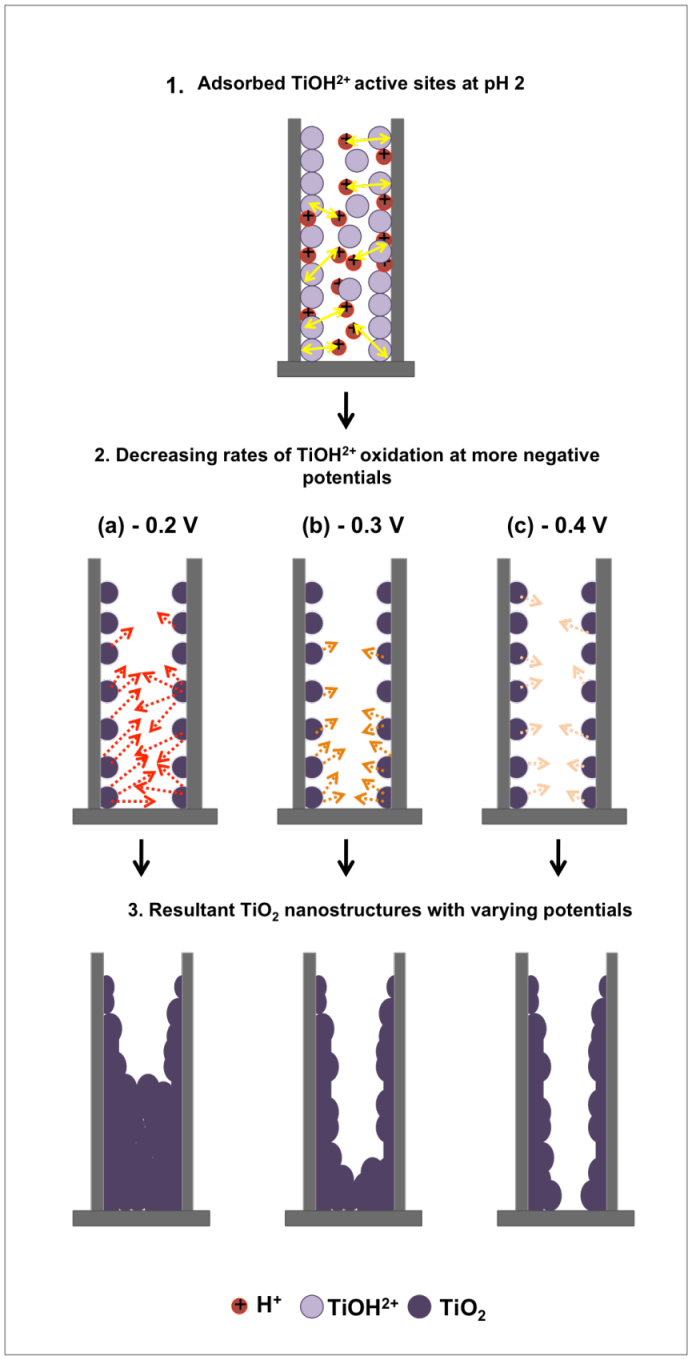

Figure 4-21. Schematic diagram relating the rate of the $TiOH^{2+}$ oxidation and anodic current densities to the growth of TiO_2 in the AAM at deposition potentials of (a) -0.2 V, (b) -0.3 V, (c) -0.4 V (vs. Ag/AgCl, 1 M KCl) and the respective TiO_2 nanostructures achieved

Next, a comparison is made between TiO_2 nanorod structures electrodeposited at pH 2 $TiCl_3$ solution at deposition potentials of -0.1 V and -0.2 V. As seen in figure 4-20, the TiO_2 nanorods deposited at -0.1 V are more porous than that at -0.2 V, as there is a higher amount of bright region (Pt) observed within the TiO_2 segments grown at -0.1 V. Referring back to the CV scan-pH 2 in figure 4-19 reveals that the steady-state anodic current density (2.8 mA cm^{-2}) at -0.1 V is

significantly higher than that at -0.2 V (0.75 mA cm^{-2}), thereby suggesting a higher deposition rate occurring at -0.1 V.

Based on varying deposition rates occurring between conditions at -0.1 V and -0.2 V, a schematic illustration has been postulated in figure 4-22. As rapid rate of $TiOH^{2+}$ oxidation occurs initially at -0.1 V (high anodic current densities), the concentration of $TiOH^{2+}$ active species at the vicinity of the existing TiO_2 nuclei in the AAM becomes depleted, causing reaction rate to become diffusion-controlled. This causes a non-uniform grain growth arising from the non-homogeneous availability of $TiOH^{2+}$ reactive species at existing TiO_2 nuclei sites, overall producing a highly porous TiO_2 nanorod consisting of TiO_2 particles with broader size distributions within the AAM (figure 4-21B). In contrast, figure 4-22A shows a more compact TiO_2 nanorod structure consisting of TiO_2 particles of narrower size distribution, as a result of moderate and smooth grain growth at lower current densities. In a study of diffusion-controlled processes in Ag electrodeposition, Globa and co-workers [37] had observed significant non-uniformity in Ag deposited in the AAM, resulting from limiting concentrations at sufficiently high current densities. Although several other studies have reported on coarse-grain growth at elevated temperatures [38, 39], this phenomenon may be analogous to high current densities, since both effects suggest increase in reaction rates.

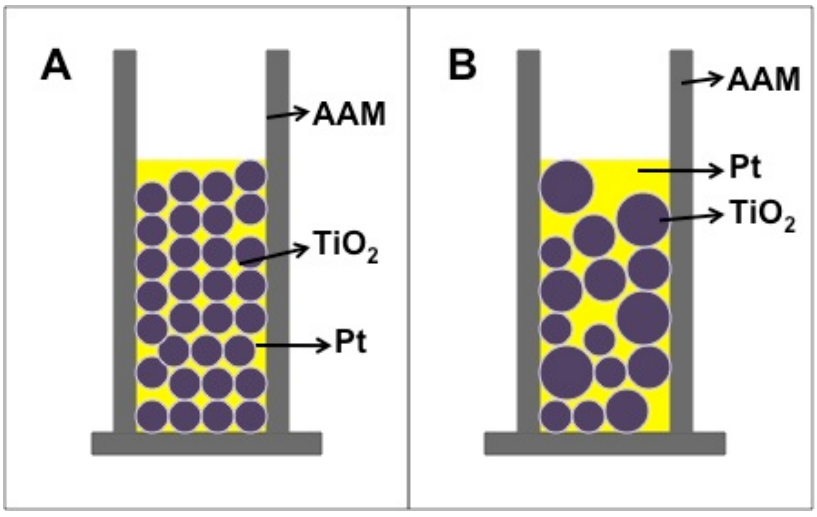

Figure 4-22. Schematic diagram illustrating (A) dense TiO_2 nanorod consisting of uniform particles as a result of smooth and moderate TiO_2 grain growth at deposition potentials of -0.2 V (vs. Ag/AgCl, 1 M KCl), (B) highly porous TiO_2 nanorod consisting of particles with large size distribution resulting from rapid and coarse TiO_2 "particle" growth at -0.1 V (high current densities) (vs. Ag/AgCl, 1 M KCl); Pt provides a contrast in the porosity of TiO_2 nanorods in (A) and (B)

4.5. Conclusion

Highly ordered 1D nanostructures of TiO_2 were successfully prepared from the templated electrodeposition of two different precursors: $TiOSO_4$ (Ti^{4+}) and $TiCl_3$ (Ti^{3+}). High potentiostatic conditions of -1.2 V (vs. Ag/AgCl, 1 M KCl at 25 ^{o}C) using TiOSO4 precursor resulted in TiO2 nanorods, but at the same time had promoted hydrogen evolution, which made it challenging for TiO_2 nanorods to be deposited onto noble metal surfaces such as Pt; while lowering the potentiostatic voltages resulted in the growth of TiO_2 nanotubes. Supported by a series of cyclic voltammetry study and chemical tests, detailed mechanisms of their respective growth were determined; and the differentiating factor to the formation of TiO_2 nanorods and nanotubes was understood to be the regeneration of high amounts of NO_3- species occurring at more negative deposition voltages.

A protocol for the electrodeposition of TiO_2 nanorods from $TiCl_3$ precursor was established, which involves a low deposition voltage of -0.2 V (vs. 1 M Ag/AgCl) that would facilitate the deposition of TiO_2 on noble metals such as Pt. The ability to synthesize TiO_2 nanostructures from a stable $TiCl_3$ solution prepared under normal ambient conditions will provide the flexibility and ease at which $TiCl_3$, a compound that is highly sensitive to moisture and air, can be handled even in the absence of an argon or nitrogen environment. Additionally, changes in potentiostatic conditions such as pH and deposition potentials revealed changes in TiO_2 morphology, in which are explained through a series of proposed mechanisms.

Overall, the proposed mechanisms here may offer an explanation to the electrodeposition of other metal oxide nanotubes and additionally provide us insight to tailoring metal oxide nanotubes and nanorods in the future. It is no doubt that these highly ordered 1D TiO_2 nanostructures will find a wide variety of uses. The robust structure of TiO_2 nanorods can be incorporated into designing nanostructural metal-semiconductor striped nanorods for catalysts, biosensors and nanoelectronics; while the presence of open-ends and hollow cores of TiO_2 nanotubes open up possibilities in creating 1D composites of TiO_2 by the direct encapsulation of other materials into its core nanostructure.

4.6. References

[1] A. Fujishima, Electrochemical photolysis of water at a semiconductor electrode, Nature, 238 (1972) 37-38.

[2] K. Hashimoto, H. Irie and A. Fujishma, TiO_2 Photocatalysis: A Historical Overview and Future Prospects, Jpn. J. Appl. Phys., 44 (2005) 8269–8285.

[3] G. K. Mor, K. Shankar, M. Paulose, O. K. Varghese, and C. A. Grimes, Use of Highly-Ordered TiO_2 Nanotube Arrays in Dye-Sensitized Solar Cells, Nano lett., 6 (2005) 215-218.

[4] K. Zhu, N. R. Neale, A. Miedaner, and A. J. Frank, Enhanced Charge-Collection Efficiencies and Light Scattering in Dye-Sensitized Solar Cells Using Oriented TiO_2 Nanotubes Arrays, Nano Lett. , 7 (2007) 69-74.

[5] T. Kuwabara, H. Sugiyama T. Yamaguchi, K. Takahashi, Inverted type bulk-heterojunction organic solar cell using electrodeposited titanium oxide thin films as electron collector electrode, Thin Solid Films, 517 (2009) 3766–3769.

[6] E. Topoglidis, A. E. G. Cass, G. Gilardi, S. Sadeghi, N. Beaumont, and J. R. Durrant, Protein Adsorption on Nanocrystalline TiO_2 Films: An Immobilization Strategy for Bioanalytical Devices, Anal. Chem., 70 (1998) 5111-5113.

[7] K.-S. Mun, S. D. Alvarez W.-Y. Choi and M. J. Sailor, A Stable, Label-free Optical Interferometric Biosensor Based on TiO_2 Nanotube Arrays, ACS Nano, 4 (2010) 2070–2076.

[8] X. Zhang, B. Yao L. Zhao, C. Liang, L. Zhang, and Y. Mao, Electrochemical Fabrication of Single-Crystalline Anatase TiO_2 Nanowire Arrays, J. Electrochem. Soc., 148 (2001) G398-G400.

[9] C. Natarajan and G. Nogami, Cathodic Electrodeposition of Nanocrystalline Titanium Dioxide Thin Films, J. Electrochem. Soc., 143 (1996) 1547-1550.

[10] S. Karuppuchamy, K. Nonomura T. Yoshida, T. Sugiura, H. Minoura, Cathodic electrodeposition of oxide semiconductor thin films and their application to dye-sensitized solar cells, Solid State Ionics, 151 (2002) 19-27.

[11] C. F. C. Blancoa, C. Palb, J. J. Ojedab, A. K. Rayb,z and A. K. Sharmac, Morphological and Elemental Studies on Titania Thin Films Electrodeposited at Different Bath Temperatures, J. Electrochem. Soc., 159 (2012) E30-E36.

[12] Y. Chen, H.-C. Kim, J. McVittie, C. Ting and Y. Nishi, Synthesis of TiO_2 nanoframe and the prototype of a nanoframe solar cell, Nanotechnol., 21 (2010) 185303-185310.

[13] A. W. Maijenburg, J. Veerbeek, R. d. Putter, S. A. Veldhuis, M. G. C. Zoontjes, G. Mul, J. M. Montero-Moreno, K. Nielsch, H. Schäfer, M. Steinhartd and J. E. t. Elshofa, Electrochemical synthesis of coaxial TiO_2-Ag nanowires and their application in photocatalytic water splitting, J. Mater. Chem. A, 2 (2014) 2648-2656.

[14] M. Lai and D. J. Riley, Templated Electrosynthesis of Zinc Oxide Nanorods, Chem. Mater., 18 (2006) 2233-2237.

[15] M. J. Zheng, L. D. Zhang, G. H. Li, W. Z. Shen, Fabrication and optical properties of large-scale uniform zinc oxide nanowire arrays by one-step electrochemical deposition technique, Chem. Phys. Lett., 363 (2002) 123–128.

[16] L.Li, S. Pan X. Dou, Y. Zhu, X. Huang, Y. Yang, G. Li, and L. Zhang, Direct Electrodeposition of ZnO Nanotube Arrays in Anodic Alumina Membranes, J. Phys. Chem. C, 111 (2008) 7288-7291.

[17] P. Bocchetta, M. Santamaria and F. D. Quarto, Electrosynthesis of Ce–Co Mixed Oxide Nanotubes with High Aspect Ratio and Tunable Composition, Electrochem. Solid-State Lett., 11 (2008) K27-K30.

[18] M. Lai, J. A. G. Martinez, M. Gratzel and D. J. Riley, Preparation of tin dioxide nanotubes via electrosynthesis in a template, J. Mater. Chem. , 16 (2006) 2843–2845.

[19] L. Kavan, B. O'Regan, A. Kay and M. Gratzel, Preparation of TiO_2 (anatase) films on electrodes by anodic oxidative hydrolysis of TiCl3, J. Electroanal. Chem., 346 (1993) 291-307.

[20] K. P. Musselman, G. J. Mulholland, A. P. Robinson, L. Schmidt-Mende, and J. L. MacManus-Driscoll, Low-Temperature Synthesis of Large-Area, Free-Standing Nanorod Arrays on ITO/Glass and other Conducting Substrate, Adv. Mater., 20 (2008) 4470–4475.

[21] F. Pedrazaa, and A. Vazquez, Obtention of TiO_2 rutile at room temperature through direct oxidation of TiCl3, J. Phys. Chem. Solids, 60 (1999) 445-448.

[22] I. S. Cho, Z. Chen, A. J. Forman, D. R. Kim, P. M. Rao, T. F. Jaramillo, and X. Zheng Branched TiO_2 Nanorods for Photoelectrochemical Hydrogen Production, Nano lett., 11 (2011) 4978–4984.

[23] C. D. Lokhande, E.-H. Lee, K.-D. Jung, O.-S. Joo, Room temperature chemical deposition of amorphous TiO_2 thin films from Ti(III) chloride solution, J. Mater. Sci., 39 (2004) 2915-2918.

[24] R. Liu and A. Sen, Controlled Synthesis of Heterogeneous Metal−Titania Nanostructures and Their Applications, J. Am. Chem. Soc., 134 (2012) 17505−17512.

[25] S. Liu, and K. Huang, Straightforward fabrication of highly ordered TiO_2 nanowire arrays in AAM on aluminum substrate, Sol. Energ. Mat. Sol. , 85 (2005) 125-131.

[26] L. Liu, Y. Zhao, Q. Zhou, H. Xu, C. Zhao, Z. Jiang, Nano-polypyrrole supercapacitor arrays prepared by layer-by-layer assembling method in anodic aluminum oxide templates, J. Solid State Electrochem., 11 (2006) 32-37.

[27] Z. Qiang, C. Xiaoli, C. Ling, L. Ling, S. Zhenkun, and J. Zhiyu, Fabrication of Polymeric Nano-Batteries Array Using Anodic Aluminum Oxide Templates, J. Nanosci. Nanotechnol., 9 (2009) 929-932.

[28] W. R. Bowen and D. T. Hughes, Properties of Microfiltration Membranes: The Surface Electrochemistry of Anodic Film Membranes, J. Colloid Interface Sci., 143 (1990) 252-265.

[29] C.-P. Huang and W. Stumm, Specific Adsorption of Cations on Hydrous gamma-Al_2O_3, J. Colloid Interface Sci., 43 (1972) 409-420.

[30] Jr. R. M. Hawthorne, and M. J. Ruthenberg, A New Single-Solution Confirmatory Test for Nitrite Ion, J. Chem. Educ., 55 (1978) 29.

[31] F. P. Rotzinger and M. Gratzel, Characterization of the Perhydroxytitanyl (2+) Ion in Acidic Aqueous Solution. Products and Kinetics of Its Decomposition, Inorg. Chem., 26 (1987) 3704-3708.

[32] R. L. Pecsok and A. N. Fletcher, Hydrolysis of Titanium(III), Inorg. Chem., 1 (1962) 155–159.

[33] S. Cassaignon and M. Koelsch, J.-P. Jolivet, From $TiCl_3$ to TiO_2 nanoparticles (anatase, brookite and rutile): Thermohydrolysis and oxidation in aqueous medium, J. Phys. Chem. Solids, 68 (2007) 695-700.

[34] R. A. Spurr and H. Myers, Quantitative Analysis of Anatase-Rutile Mixtures with an X-Ray Diffractometer, Anal. Chem., 29 (1957) 760–762.

[35] L. Vordonis, P. G. Koutsoukos, A. Lycourghiotis, Development of carriers with controlled concentration of charged surface groups in aqueous solutions: I. Modification of γ-Al_2O_3 with various amounts of sodium ions, J. Catal., 98 (1986) 296–307.

[36] H. Tamuraa, N.Katayamab, R. Furuichia, CO_2 Adsorption Properties of Al_2O_3, Fe_2O_3, Fe_3O_4, TiO_2 and MnO_2 Evaluated by Modeling with the Frumkin Isotherm, J. Colloid Interface Sci., 195 (1997) 192–202.

[37] P.G. Globa, E. A. Zasavitsky, V. G. Kantser, S. P. Sidelinikova, A. I. Dikusar, Kinectics of Electrodeposition of Silver and Copper at Template Syntehsis of Nanowires, in, Cornell University Library, 2007.

[38] H. Natter, M. Schmelzer, M.-S Löffler, C. E. Krill , A. Fitch, and R. Hempelmann Grain-Growth Kinetics of Nanocrystalline Iron Studied In Situ by Synchrotron Real-Time X-ray Diffraction, J. Phys. Chem. B, 104 (2000) 2467-2476.

[39] S. Mitra, P. Poizot, A. Finke, J.-M. Tarascon, Growth and Electrochemical Characterization versus Lithium of Fe_3O_4 Electrodes Made by Electrodeposition, Adv. Funct. Mater., 16 (2006) 2281–2287.

Chapter 5: Templated Electro-deposition of Segmented Nanostructures of TiO_2 and Pt

5.1. Introduction

Recently much interest has been directed toward the use of one-dimensional multi-segmented nanostructures for a range of functional applications such as catalysis [1, 2]; biodetection and biosensing [3, 4]; and optical applications [5, 6]. The usefulness of one-dimensional multi-segmented nanostructures such as nanorods can be attributed to their highly ordered structure consisting of a controlled, alternating distribution of complementary material segments. Their relatively large specific surface area and extremely high aspect ratios offer the potential to design and build nanostructures with multiple chemical components aligned along the longitudinal axis.

One method of preparing these ordered arrays of multisegmented nanorods with such control in size and composition is by template-assisted electrodeposition where the target material is electrodeposited into cylindrical pores of a suitable template such as anodic aluminium oxide membranes (AAM). The pre-eminence of templated electrodeposition is the ability to precisely control the position and composition of different materials along the lengths of the nanorods to prepare a highly ordered one-dimensional multi-segmented nanostructure. In controlling the distribution of active sites, it offers a unique opportunity to prepare nanorods with highly reproducible interfaces between segments of different materials and hence the possibility to manipulate its functional activity. Additionally, template-assisted electrodeposition is becoming the preferred method as increased emphasis is placed on low cost, high throughput, high volume and ease of production [7].

Regardless of the type and number of materials to be deposited, the same general procedure applies to the fabrication of multi-segmented 1-D nanostructures *via* templated electrodeposition (figure 5-1). The first step requires sputtering of a metal layer on one side of the AAM to cover the pores of the AAM and to make it conductive as a working electrode. A sacrificial layer is then deposited into the AAM to protect the core materials during the etching process of the conductive layer. After electrodeposition of the number of desired segments in the AAM, the multi-segmented nanostructures are released by chemically dissolving the conductive layer, sacrificial material and the AAM.

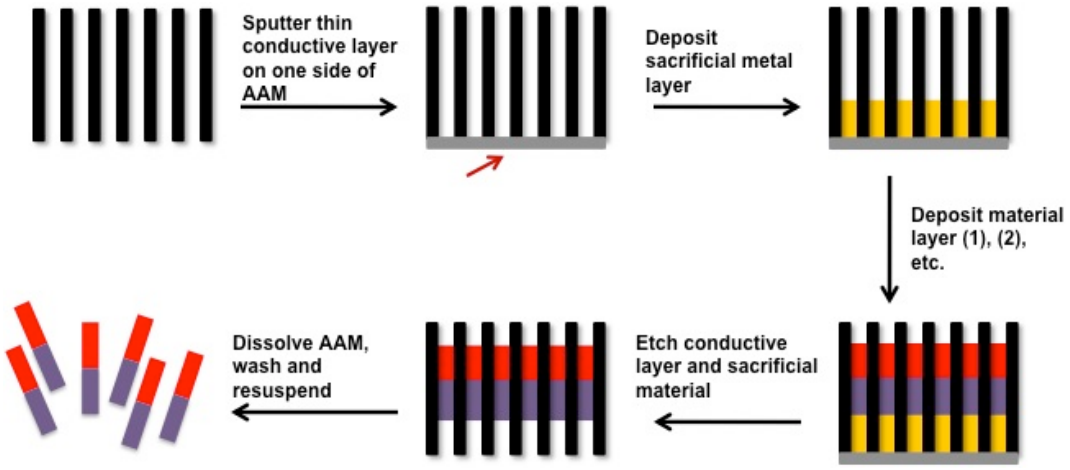

Figure 5-1. General scheme for the fabrication of multi-segmented 1-D nanostructures by templated sequential electrodeposition

In some cases, the electrodeposition of multi-layer 1-D nanostructures can be achieved by employing a single electrolyte bath consisting of multiple metal ions. With well-separated redox potentials between the two metals, the less active metal will be electrodeposited at a lower potential, while applying a higher potential will allow the deposition of the more active metal. Typically, the less active metal is kept at a higher concentration than the more active metal so that the segments deposited at a higher overpotential contains predominantly that metal. By applying pulsed electrochemical deposition, the deposition voltages can be easily modulated.

5.2. Literature review

The first electrochemical metal deposition into a hard template was demonstrated by Possin [8], where Zn, Sn and In nanowires were fabricated by electrodeposition in small pores of track-etched mica. This method was later popularized by Penner and Martin [9] as a fabrication technique for metal nano- and microstructures; by Martin and co-workers [10] and Brumlik and Martin [11] for the fabrication of organic and metallic microtubules. Using nuclear track filters as templates, Chakarvati and Vetter [12] reported for the first time, the electrodeposition of semiconductor-metal (Se-Cu) microstructures.

Since then, the study of the synthesis, properties and applications of multi-segmented 1-D nanostructures has advanced. These include multi-segmented nanostructures consisting mostly of a combination of metals, semiconductors and polymers. Multi-segmented nanostructures consisting of multiple different components possess unique physical and chemical properties, which extend their functionality beyond those of their individual components.

To-date, there have been extensive reports on the templated electrodeposition of multi-segmented 1-D metallic nanostructures, due to advantages from their confinement to nanoscale dimensions. Metallic nanowires synthesized from magnetic and non-magnetic couples such as Co-Cu [13], Ni-Co [14], Fe-Cu [15] and NiFe/Cu/NiFe [16] were studied for their GMR effects. As opposed to their individual metallic components of Fe, Co and Ni, these metallic multi-layer nanostructures were found to exhibit giant magnetoresistance (GMR) due to the resultant electronic structures of the magnetic and non-magnetic layers [17]. Tanase and co-workers [18], and Myung and Hungarter [19] have successfully synthesized Pt/Ni and Ni/Au nanowires and have revealed the function of these metallic nanowires as resistors, owing to their ohmic behaviour. Additionally, the presence of multiple striping patterns of metallic nanorods such as those consisting of Au/Ag find their uses as optical tags and biodetectors, as varying composition and thickness in their striping patterns show distinct contrast in both optical and electron microscopy, and also in the simultaneous identification of multiple species in a solution [3, 20, 21]. With the ability to control the composition, size, distribution, surface area and morphology through template electrodeposition, metallic nanostructures of Ni-Cu [1], Pt-Ni [2], Pt-Ru [22] and Pt-Au also provide a model system for the study of catalytic activity.

In addition to metallic multi-segmented 1-D nanostructures, multi-segmented nanostructures consisting of a combination of metal, semiconductor and polymer have also been successfully achieved by templated electrodeposition and find applications as transistors and switches. Mallouk and co-workers have synthesized multi-segmented Au-CdS nanowires (sheathed in Si) through electroplating in AAM, which showed the behaviour of a field-effect transistor (FET). Nanowires of Au-Ppy-Cd-Au [23] were shown to possess electronic transport properties arising from the Schottky contact between Ppy and Cd, and the electrical contacts provided by Au caps. Similarly, works involving the synthesis of Au-CdSe-Au [24] and $TiO_2/W_{21}O_{41}$ (paratungsate) /PAN (polyaniline)/SWNTs (single-walled carbon nanotubes) [25] multi-layer nanowires were also reported to function as diodes. Non-ohmic response, on the other hand, resulted from nanowires of Au-TiO_2-Au, where it was proposed that the TiO_2 defects could be responsible for this phenomenon [26].

To date, works on the templated electrodeposition of multi-segmented TiO_2/Pt nanostructures are very limited. There is currently only one study reporting bi-segmented TiO_2-Pt and Pt-capped-TiO_2 nanostructures synthesized *via* TiO_2 electro-less deposition on prior electrodeposited Pt [27]. In addition, TiO_2/Pt nano-systems for photocatalysis consist mostly of Pt nanoparticles dispersed on TiO_2 nanostructures and films [28-30]; or Pt nanocatalysts embedded on TiO_2 [31] where the functionality of TiO_2 may be limited due to the exposed surface of TiO_2 being blocked by the coverage of Pt. In this chapter, novel 1-D TiO_2/Pt nanorods consisting of alternating lengths of TiO_2 and Pt segments are

designed to create maximum surface area of exposure for the purpose of photocatalysis. Here, we report on the procedures of fabricating highly ordered segmented TiO_2-Pt, TiO_2-Pt-TiO_2 and Pt-TiO_2-Pt-TiO_2 nanorods by sequential electrodeposition within AAM, based on procedures that had been established earlier in chapters 3 and 4. By employing templated electrodeposition, individual segment of TiO_2 and Pt can be conveniently tuned to study its effect on photocatalytic activity and at the same time, offers the possibility of reproducing multiple TiO_2/Pt interfaces, which play an essential role in enhancing the photoactivity of TiO_2.

5.3. Synthesis of Multi-segmented TiO_2/Pt Nanorods

5.3.1. Materials

Materials employed for the synthesis of multi-segmented TiO_2/Pt nanorods are as listed in chapter 3 and 4. Unless otherwise stated, deposition conditions for all TiO_2 segments from $TiCl_3$ precursor bath solution are -0.2 V (vs. Ag/AgCl, 1 M KCl, 25 ^{o}C) and that of Pt segment from $PtCl_6^{2-}$ precursor bath solution are -0.4 V for 20 s, followed by -0.2 V (vs. Ag/AgCl, 1 M KCl, 25 ^{o}C).

5.3.2. General Experimental Practice

Segmented nanorods consisting of alternating segments of Pt and TiO_2 are synthesized via sequential electrochemical deposition from their precursor electrolytes of $Na_2PtCl_6 \cdot 6H_2O$ and $TiCl_3$ (~10 wt. % in 20-30 wt. % hydrochloric acid) according to the respective procedures described in the previous chapters. The method of sputtering silver on AAM, cell set-up and potentiostat were similar to those used in the synthesis of Pt and TiO_2 nanorods. Between the depositions of each segment, the sample is removed from the deposition solution, rinsed with DI water, and left to dry in air at room temperature. The first solution is then replaced with the appropriate precursor solution for the next desired deposition. This procedure is repeated until the desired number of segments is achieved. After deposition of the final segment, the sample is removed from the solution, gently rinsed with DI water and annealed in air at 600 °C for 2 h to crystallise the TiO_2 segments. To obtain free-standing arrays of segmented nanorods, the sample is immersed in 3 M NaOH for 1 hour to etch off the AAM and then rinsed gently with DI water. Free segmented nanorods are released by first etching off the silver sputtered layer by treating the AAM with an etching solution consisting of methanol, 30% ammonium hydroxide and 30% hydrogen peroxide (5:1:1 v/v/v) until all the silver has been completely removed, followed by dissolving the AAM in 3 M NaOH solution. The obtained segmented nanorods were

then centrifuged at 2000 RPM for 15 min and washed repeatedly and finally dispersed in DI water or ethanol by sonication.

5.3.3. Results and Discussion

5.3.3.1. Structural, Surface and Interfacial Characteristic Studies of Segment Nanorods

5.3.3.1.1. Structural Characterisation of Segmented TiO_2/Pt Nanorods

Highly-ordered two, three and four-segmented TiO_2-Pt nanorods with variable TiO_2 and Pt length segments were successfully fabricated from aqueous precursor solutions of $TiCl_3$ and Na_2PtCl_6 respectively as shown in the backscattered SEM images in figure 5-2. Characterization of these striped nanorods using a backscattered mode provided greater enhancement in distinguishing the TiO_2 segments from the Pt segments, where Pt segments appear brighter due to its higher atomic number. As each TiO_2 and Pt segments shown in figure 5-2 are precisely controlled to achieve a desired length, the versatility of tuning the individual segments of TiO_2 and Pt for a specific activity is clearly demonstrated.

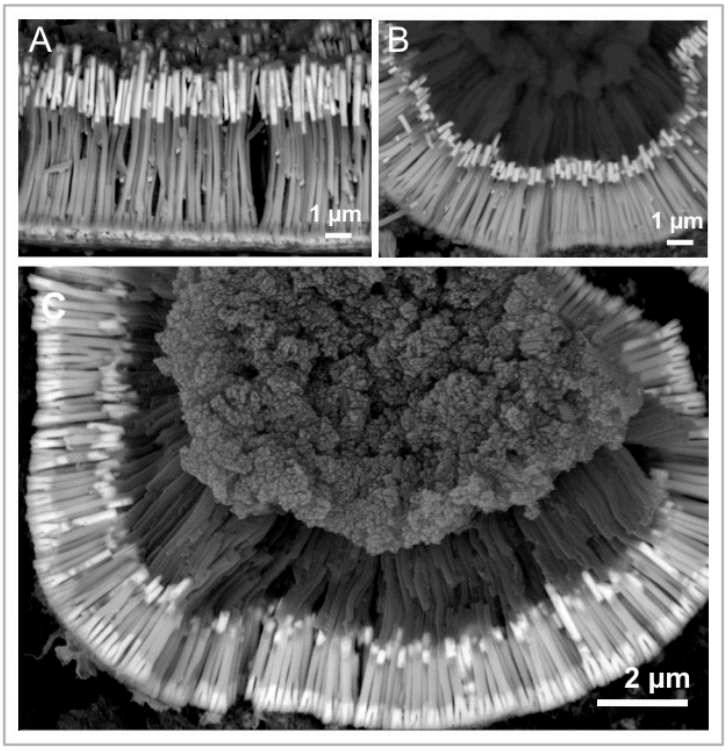

Figure 5-2. Backscattered SEM images of a) TiO_2-Pt, b) TiO_2-Pt-TiO_2, c) Pt-TiO_2-Pt-TiO_2 nanorod arrays on a 150 nm thick layer of Ag

A naturally occurring phenomenon that is frequently observed upon removing the AAM template in an alkaline solution of conc. NaOH is the bending and bundling of the free-standing nanostructures into 'islands', as shown figure 5-3. The tendency to bend and aggregate into bundles is due largely to the capillary forces acting on the nanostructures during evaporation of the solvent after the chemical etching process [32]. From experimental observation, the formation of 'islands' was found to occur more in unannealed samples with nanorods that are grown to a height of more than 1 μm.

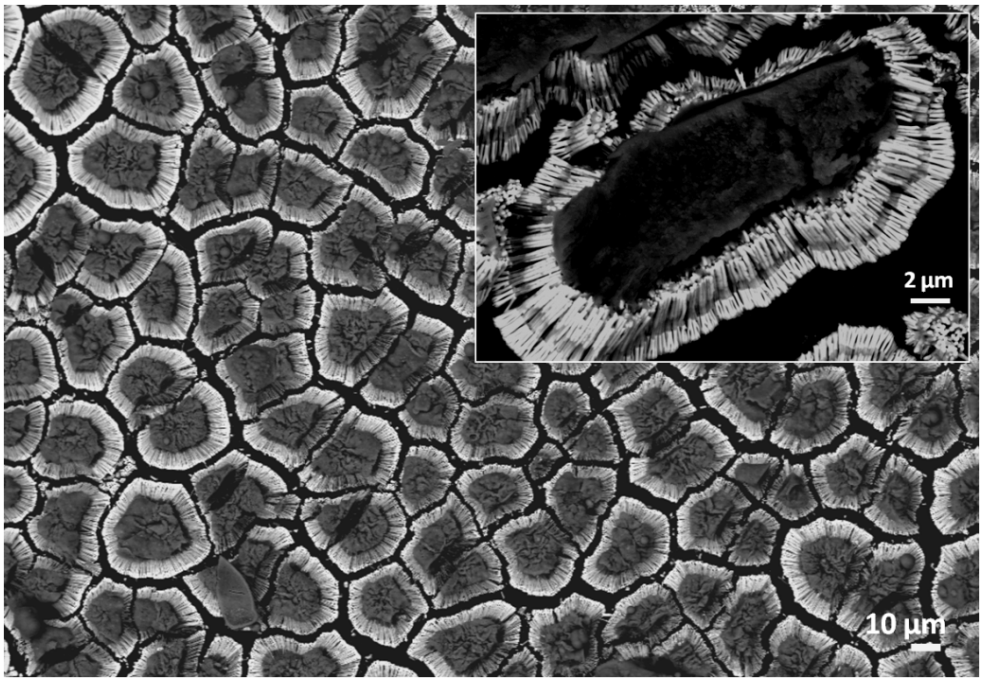

Figure 5-3. Top-view SEM image of 'islands' of free-standing 3-segment Pt-TiO_2-Pt nanorods on 3 μm thick Ag film; inset shows 10X magnification of a single 'island'

5.3.3.1.2. Interfacial Characterisation of Segmented TiO_2/Pt Nanorods

Under TEM imaging, it can be clearly seen that the junction between the two segments of TiO_2 and Pt are of approximately 50 nm in axial length consisting of both TiO_2 and Pt particles (Figure 5-4). This inter-particle diffusion of TiO_2 and Pt with a width of approximately 50 nm helps to create a strong adhesion between the two segments, bonding the metal to the metal oxide with very different properties. At a specific resistivity of 10^9-10^{10} Ohm.cm at 25 ^oC [33], intrinsic amorphous TiO_2 is approximately 10^{14}-10^{15} times less conductive than Pt, this low conductivity was initially thought to pose a challenge in depositing Pt on TiO_2. However, here the as-prepared Pt-TiO_2 bi-

segment nanorods have shown that Pt particles are deposited onto the surface of TiO_2 despite the potential low conductivity of hydrous amorphous TiO_2. Also, the electrodeposition rate of TiO_2 growth on Pt in the template does not decrease even after the metal surface is covered by TiO_2, suggesting that electrodeposition is not limited by the conductivity of the TiO_2 deposit in either of these cases. The deposition of Pt on TiO_2 is discussed further in section 5.3.3.1.5.

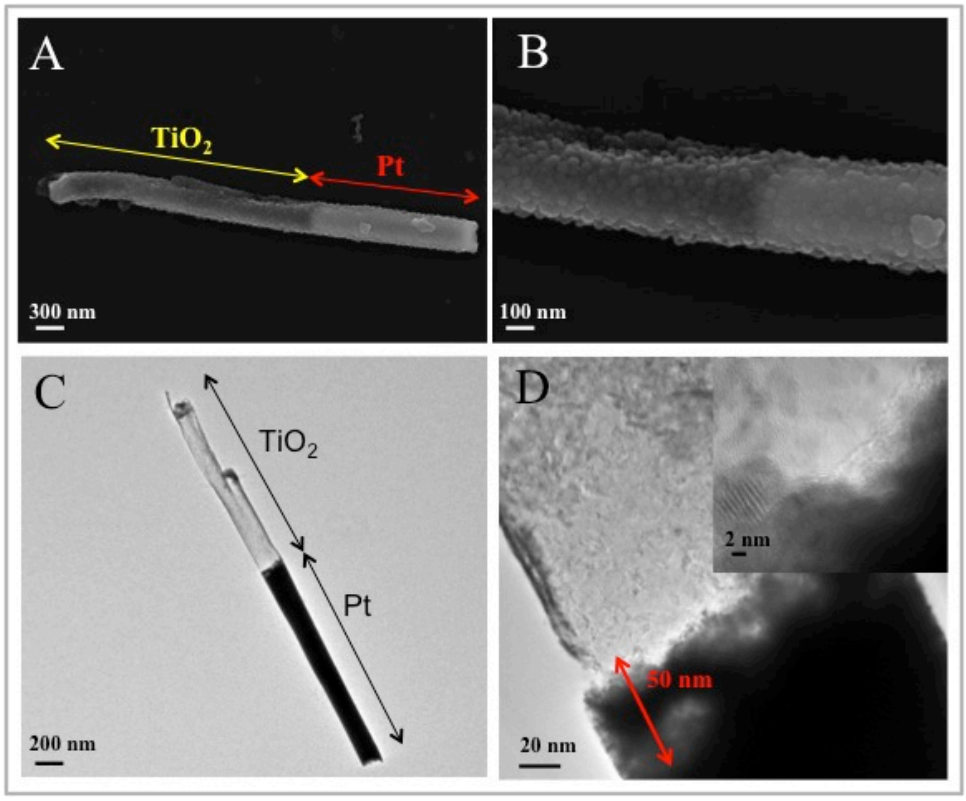

Figure 5-4. SEM images of a TiO_2-Pt nanorod at magnification of (a) 55K (b) 170 K and TEM images showing (c) TiO_2-Pt nanorod; (d) diffused junction between TiO_2 and Pt segments

5.3.3.1.3. Chemical Analysis on Segmented TiO_2/Pt Nanorods

The variation in local chemical composition along the length of a Pt-TiO_2-Pt nanorod was studied using EDX-TEM analysis. Multiple-point scans (points 1 to 9) (using a beam spot size < 50 nm) were performed on a Pt-TiO_2-Pt nanorod as indicated in the TEM image shown in figure 5-5A. Based on the given % weight values of TiO_2 and Pt, the % volume of TiO_2 and Pt at each point were calculated and plotted in figure 5-5B. Variations in the % volume of TiO_2 and Pt along the axis of the Pt-TiO_2-Pt nanorod provide an approximate indication of the location and integrity of the TiO_2/Pt interfaces.

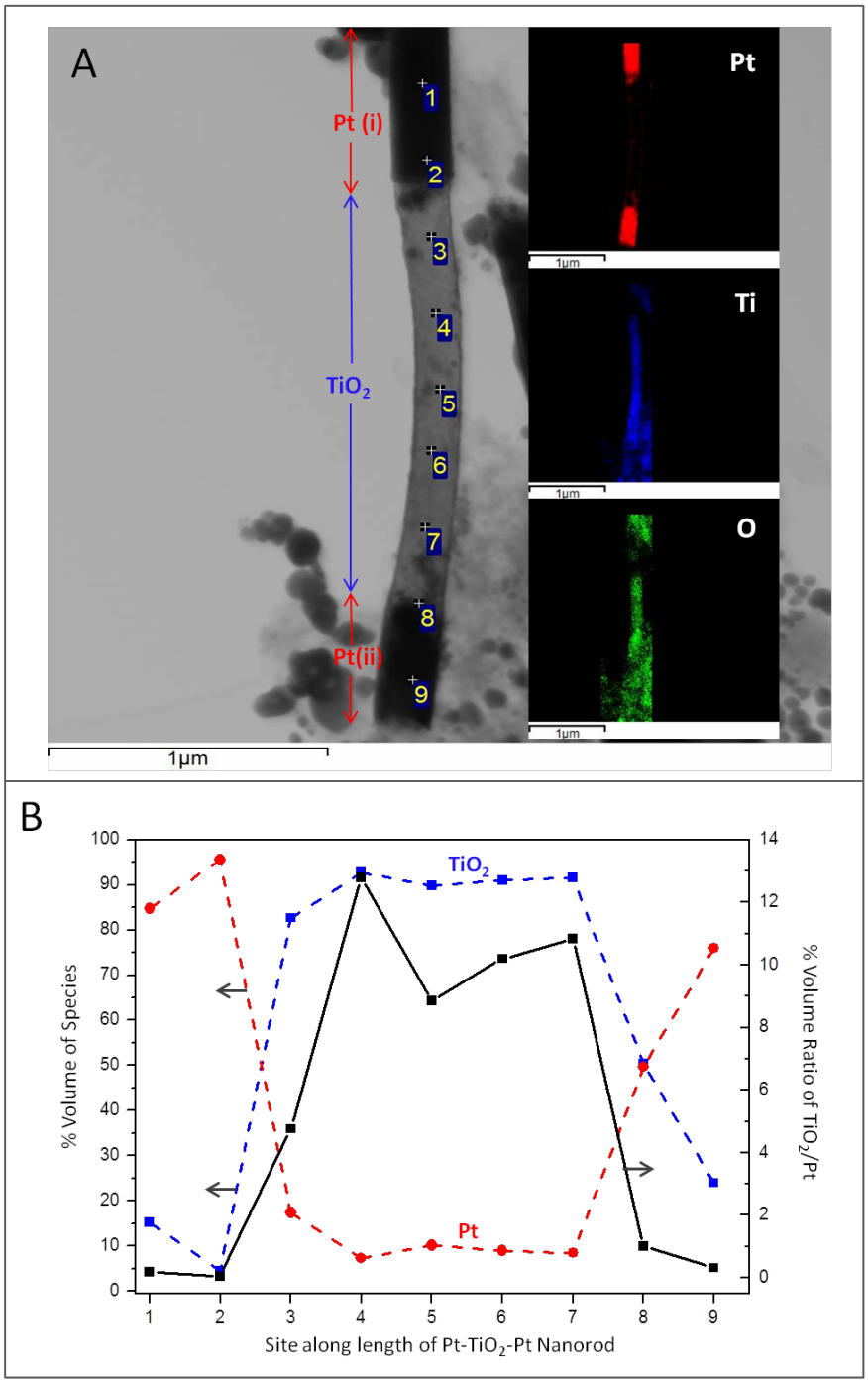

Figure 5-5. A) TEM image of a three-segmented Pt-TiO_2-Pt nanorod indicating the multiple point scans (1 to 9) along its length. Pt(i) indicates Pt segment that was deposited as a first layer, and Pt(ii) as the second Pt segment. Inset shows elemental mapping of Pt, Ti and O of the Pt-TiO_2-Pt nanorod. B) Plot showing the variation of % volume of Pt and TiO2 and % volume ratio of TiO_2/Pt across the length of the Pt-TiO_2-Pt nanorod

It is suggested that the TiO_2/Pt interfaces are located where steep changes in the gradient of the % volume plots of TiO_2 and Pt are observed between points 2-3

(interface 1) and 7-9 (interface 2), where there exist a mixture of both TiO_2 and Pt. By comparing between interface 1 and interface 2, it can be seen that the diffusion zone for interface 2 is greater than that of interface 1 as the gradients of the % volume plots of Tio2 and Pt change over a larger distance at interface 2. From this, the diffusion zone of interface 1 and 2 were estimated to be 0.5 μm and 1 μm respectively. A clearer illustration of the difference between the two interfaces is provided in figure 5-6, where a relatively sharper interface between Pt(i) and TiO_2 segments is represented at interface 1, while a TiO_2 meniscus-like curvature is observed at interface 2 between segments of TiO_2 and Pt(ii). The outline of the TiO_2 meniscus is seen from the elemental mapping images of Pt, and elemental mapping images of Ti evidently shows a higher proportion of Ti within the segment of Pt(ii) compared to Pt(i) segment (figure 5-5 inset). The observable difference between the architecture of interface 1 and interface 2 can be explained by the order in which the segments were grown. In this case, the deposition of TiO_2 on Pt(i) resulted in a sharper interface (interface 1), while a change in the order of deposition with Pt(ii) deposition on TiO2 had given rise to a more diffused Pt/TiO_2 zone.

Additionally, the marked contrast between interfaces of Pt(i)/TiO_2 and TiO_2/Pt(ii) reflects the difference in the growth nature of Pt and TiO_2 in the pores of the AAM during electrodeposition. A more diffused interface between TiO_2 and Pt(ii) segments may suggest that the pore walls of the AAM are preferential sites of growth for TiO_2, which is unlikely to be true for the electrochemical growth of Pt.

Besides information about the TiO_2/Pt interface, the plot of % volume of Pt in figure 5-5 suggests that some Pt is present within the TiO_2 segment, which could be due to a slight porosity inherent to the TiO_2 nanostructures. Despite this, the structure of the TiO_2 segment is that of a dense nanorod comprising of a much higher volume of TiO_2. The average % volume ratio of TiO_2 to Pt is calculated to be approximately 9.5 ± 3. A more detailed discussion on the TiO_2/Pt interfaces and TiO_2 porosity are provided in the following sections.

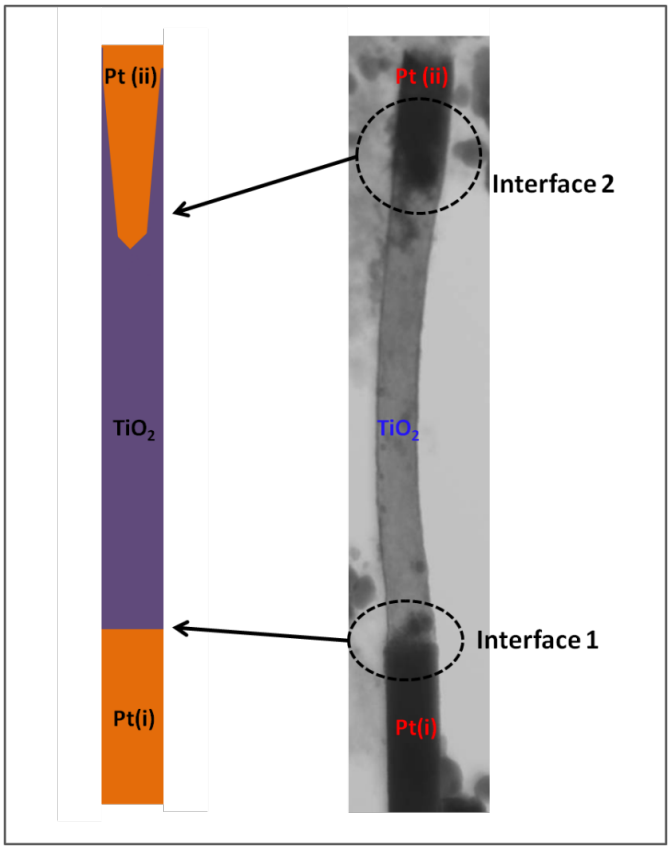

Figure 5-6. Schematic representation of the difference between the interfaces of Pt(i)/TiO_2 and TiO_2/Pt(ii) as observed from the TEM image of a Pt-TiO_2-Pt nanorod

5.3.3.1.4. Effect of Order of TiO_2/Pt Deposition on TiO_2/Pt Segmented Nanostructures

The engineering of multi-segmented nanorods consisting of alternating segments of TiO_2 and Pt has been made possible due to the compatibility of the active surfaces of Pt nanorods and electrically conductive amorphous TiO_2. Figure 5-7A shows the successful synthesis of an unannealed three-segmented Pt-TiO_2-Pt nanorods. Each Pt segment was electrochemically deposited at a constant potential of -0.2 V for 0.5 h. According to the current density-time graph in Figure 5-7B, the total calculated charge that was passed during the deposition of the first and third Pt segments are 1.65 C and 1.43 C which does not differ significantly considering that the surfaces at which both segments were deposited on had very different properties. It can be seen that the main contribution to the difference in the total charges of Pt-(i) and Pt-(iii) comes mostly from the initial deposition phase (0 to 600 s). Unlike the reaction in Pt-(iii) which equilibrated quickly to a constant current density of -7.90 mA cm^{-2}, the current density in Pt-(i) equilibrated only after approximately 10 minutes of the deposition. This observable difference can

be attributed to the different surface type at which each deposition had occurred. The schematic diagram in inset 5-7B (i) illustrates the occurrence of the initial deposition of the first Pt segment on a rougher surface of Ag consisting of 100 nm pores due to pore branching at the bottom (clearly visible in the SEM image), while inset 5-7B (ii) shows the deposition of the second Pt segment on TiO_2 in pores of 200 nm in diameter. In comparing between the expected Pt-(iii) length calculated from Faradaic charge efficiency and the actual Pt-(iii) length measured from Figure 5-7A (averaged over 20 Pt-(iii) nanorods), the % volume of Pt-(iii) that had infiltrated TiO_2-(ii) segment is approximately 5% (see appendix 5-1).

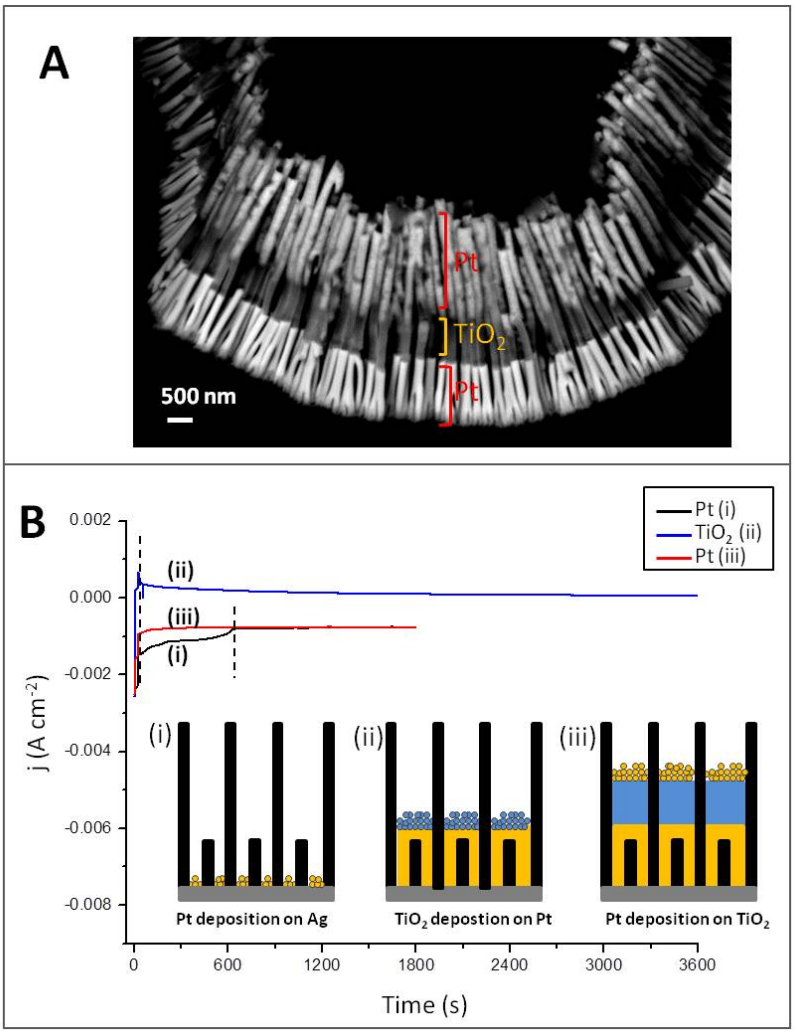

Figure 5-7. (a) Backscattered SEM images of (a) Pt-TiO_2-Pt nanorods (b) current density-time plot of (i) first and (ii) second Pt electrodeposition; inset schematic diagram illustrating Pt deposition on (i) Ag and (ii) TiO_2

Backscattered SEM images in figure 5-8 elucidate the differences in the integrity of the TiO_2/Pt nanostructures depending on the order of material deposition. In figure 5-8A, the 3-segment TiO_2-Pt-TiO_2 nanorods that are grown bottom-up by order of TiO_2, Pt, TiO_2 shows a marked contrast in the brightness intensity between the first TiO_2 segment (denoted by $*TiO_2$) and the third TiO_2 segment (denoted by TiO_2). With Pt segments appearing the brightest followed by segments of $*TiO_2$ and lastly TiO_2, it is suggested that a fraction of the total Pt material that was electrodeposited after $*TiO_2$ had infiltrated into the porous nanostructure of $*TiO_2$ with the Pt resulting in enhanced brightness of this segment; while the third TiO_2 segment does not contain Pt and therefore appears darker due to its low electron density. From this, one can expect the structural properties of bi-segment $*TiO_2$-Pt nanorods to be different from those of Pt-TiO_2 nanorods because TiO_2 segments of TiO_2-Pt nanorods are richer in Pt; which may affect their respective photocatalytic properties.

A comparison was made between an unannealed (figures 5-8B) sample and an annealed sample (in air at 600 ^{o}C) (figure 5-8C) of three-segmented Pt-TiO_2-Pt nanorods, in which differences in the integrity of the nanostructure were observed from the effects of thermal treatment. It was found that the second layer of TiO_2 had decreased by approximately half, possibly arising from an increased diffusion of Pt into porous TiO_2 segment as a result of heat treatment.

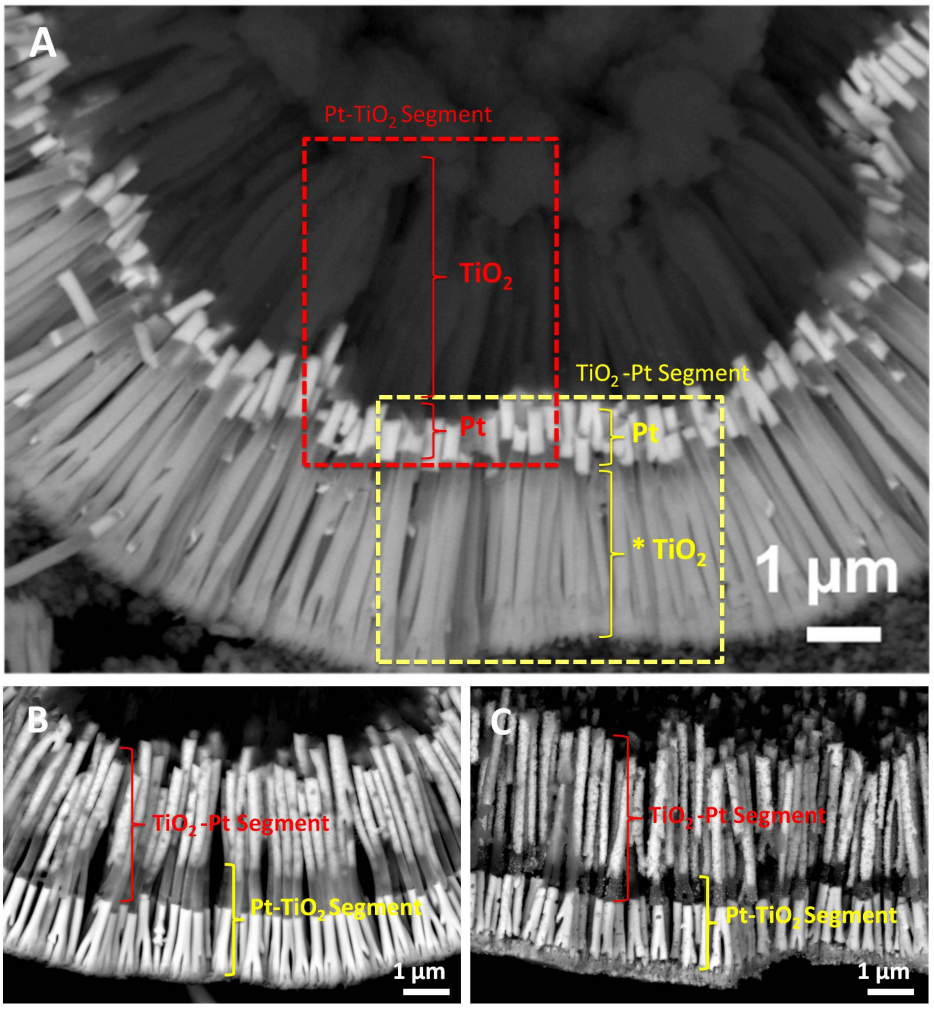

Figure 5-8. Backscattered SEM Images of A) 3-segment TiO_2-Pt- TiO_2 nanorods showing a clear contrast between the first TiO_2 segment with some diffused Pt (denoted by *TiO_2) and third TiO_2 segment with no diffused Pt (denoted by TiO_2); B) 3-segment unannealed Pt-TiO_2-Pt nanorods with some Pt diffusion into second TiO_2 segment; C) increased Pt diffusion into second TiO_2 segment after thermal treatment at 600 ^{o}C in air

5.3.3.1.5. Electrodeposition of Pt on amorphous TiO_2

Works on the electrodeposition of Pt particles on amorphous TiO_2 nanostructures have been reported [34]. It is suggested that the spontaneous deposition of Pt within the TiO_2 nanostructures may be a result of surface defects present in the amorphous TiO_2. Surface oxygen vacancies are found everywhere on the surface of reducible metal oxides such as TiO_2 and may play a role in modifying the electronic properties of the surface of the semiconductor material [35]. In an attempt to study the effect of surface oxygen vacancies on the adsorption of Pt, Han and co-workers [36] found that the

surface oxygen vacancy sites of anatase TiO_2 constitutes the most active sites for the adsorption of a single Pt atom. At the same time, it was also concluded that cluster formation of Pt is energetically favoured upon complete filling of the oxygen vacancy sites by the adsorbed Pt atom.

Based on this knowledge, a parallel conclusion can be drawn on the surface state of amorphous TiO_2, since large amounts, of up to 67 %, is comprised of under- or over-coordinated structural units such as TiO_3, TiO_4, TiO_5 and TiO_7 in amorphous TiO_2 are also assumed to be oxygen deficiency defects similar to those present in crystalline TiO_2 [37]. Moreover, due to the lack of periodic ordered structure, large pores commonly found on the surfaces of amorphous TiO_2 also act as vacancies in the diffusion process [38].

Based on the surface defects and existing porosity present in the TiO_2 nanostructures, a model has been proposed to explain how diffusion of Pt into the TiO_2 nanostructures occurs, this is illustrated in figure 5-9. When the AAM containing the first layer of electrodeposited TiO_2 is immersed in a $[PtCl_6]^{2-}$ precursor solution, $[PtCl_6]^{2-}$ ions migrate downwards through the pores channels of TiO_2 and are adsorbed onto the surface of TiO_2. The presence of pores within the TiO_2 nanostructure provides a large surface area for the adsorption of $[PtCl_6]^{2-}$. Through an applied voltage, $[PtCl_6]^{2-}{}_{ads}$ is reduced to $(Pt)_{ads}$ at the surface of TiO_2, and anchors onto an oxygen vacancy site of the amorphous TiO_2 which serves as a nucleation centre for the growth of Pt clusters. The Pt clusters grow within the porous structure of TiO_2 upon continuous reduction of $[PtCl_6]^{2-}$; and subsequently deposits on top of the TiO_2 segment once the pores has been filled. This schematic illustration is also used to account for the possibility of electrodepositing Pt onto amorphous TiO_2, which is generally known to possess low electrical conductivity.

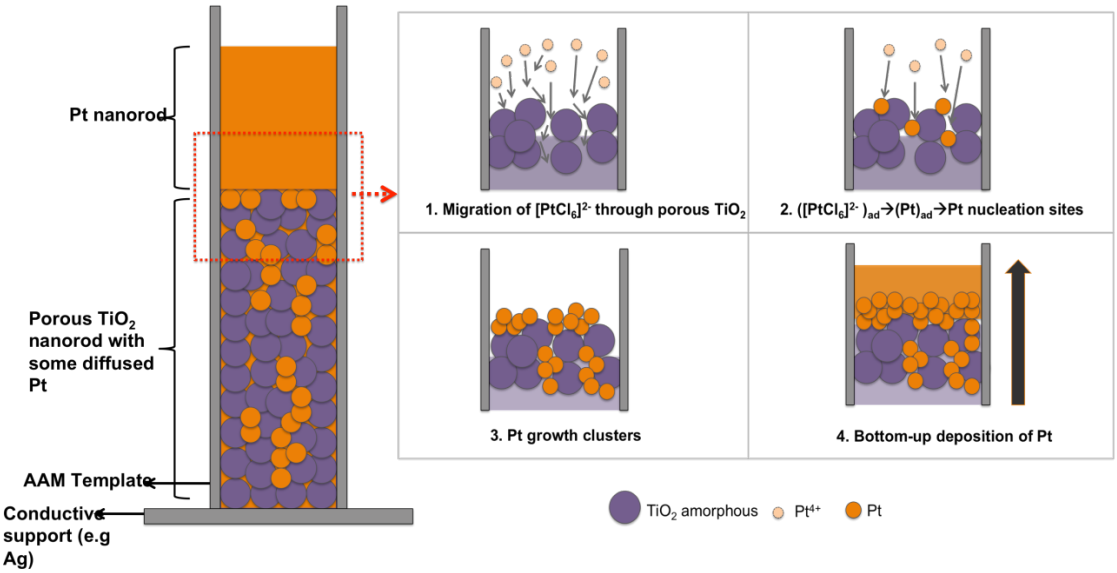

Figure 5-9. Schematic illustration demonstrating the growth of Pt within the porous nanostructure of TiO_2 and the possibility of electrodepositing Pt onto amorphous TiO_2

In this study, the deposition of Pt on amorphous TiO_2 is being employed to fabricate TiO_2-Pt bi-segmented nanostructures. This procedure is preferred over Pt deposition on crystalline TiO_2, mainly because the deposition of Pt on crystalline TiO_2 requires prior annealing of the TiO_2/AAM sample, which would result in the contortion of the AAM after annealing at 600 ^{o}C in air as shown in figure 5-10B. As the AAM is known to be very fragile, the contorted TiO_2/AAM would then crack under the weight of the cell (figure-10C) and hence the damaged sample cannot be used for subsequent material deposition.

Despite this, an attempt is made to compare between the nanostructures of TiO_2-Pt with and without prior annealing of TiO_2, by comparing unannealed and annealed samples of single TiO_2 nanostructures. From figure 5-11A, the unannealed TiO_2 nanorods appears to have a rough texture, comprising of inhomogeneous “particles” as observed from its magnified SEM image in figure 5-11A inset. In contrast, it can be seen from figure 5-11B that when the exact same TiO_2 sample has been annealed in air at 600 ^{o}C, there is a distinct change in the surface morphology. The rough texture of the nanostructures as previously observed in the unannealed TiO_2 material is now smoother, which probably results from coalescence of the inhomogeneous “particles”. In addition, the annealed nanostructures are observed to be more rigid as compared to the unannealed nanostructures where some defects along the nanorods as indicated in

figure 5-11A. At this point, differences in surface morphology of both unannealed and annealed TiO_2 nanostructures provide insight to the structural differences which exist within the TiO_2 segments of the TiO_2-Pt bi-segment nanorods. Unfortunately, a comparison between the exact structures of the TiO_2 segments (consisting of Pt diffusion) cannot be made, since the material distribution (Pt/TiO_2) within the TiO_2 segment is not known.

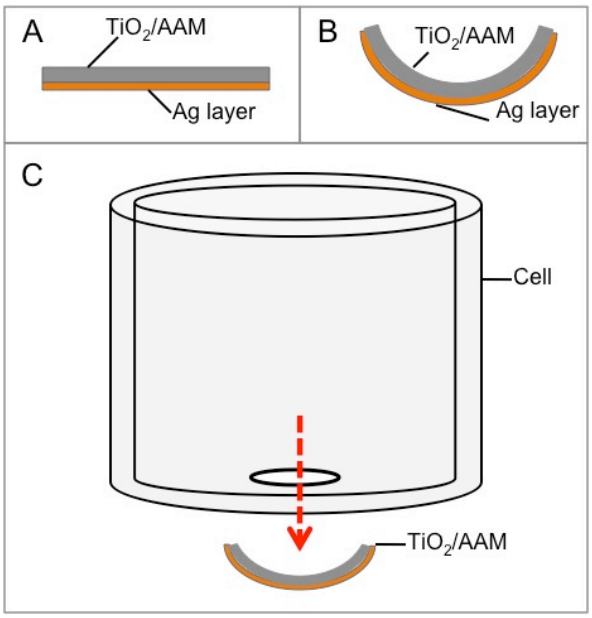

Figure 5-10. Schematic illustration of the cross-section view of A) unannealed AAM, B) contortion of the AAM resulting from annealing at 600 ^{o}C, and C) possible damage to the AAM as it is being placed under the cell prior to electrodeposition

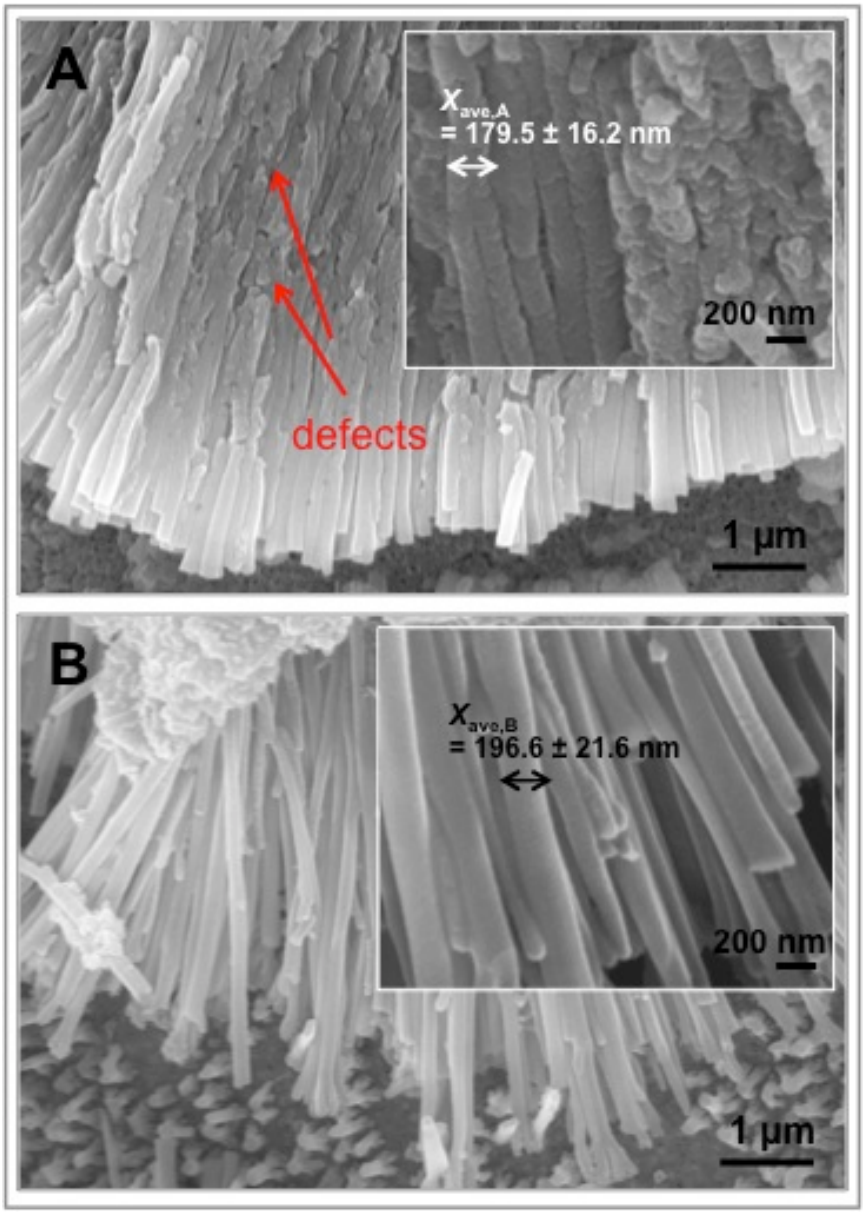

Figure 5-11. SEM images of free-standing A) unannealed TiO_2 nanorods and B) annealed TiO_2 nanorods at 600 ^{o}C in air for 5 h; respective insets show higher magnification of the corresponding TiO_2 nanostructures

5.3.3.1.6. Electrodeposition of amorphous TiO_2 on Pt

In further characterising the growth of TiO_2 on Pt, AAM consisting of electrodeposited Pt was soaked in 0.28 M $TiCl_3$ solution under ambient conditions. After approximately 12 hours, dense TiO_2 segments with an average length of 200 nm were found to grow on Pt as shown in figure 5-12, indicating that the nanorod surface of Pt is able to catalyze TiO_2 deposition. According to Liu and Sen [39], the oxidative conversion of Ti^{3+} to Ti^{4+} occurs

uniquely on nanostructured metallic surfaces such as Pt, Au and Ni nanowires and nanoparticles. A growth mechanism of the electroless deposition of TiO_2 on Pt nanostructure substrate had been proposed to occur via reactions 5A and 5B, leading to an overall reaction shown in reaction 5C. Although the electroless deposition of TiO_2 occurs spontaneously on Pt nanorods, this method results in TiO_2 growth which proceeds much slower than when electrodeposition is employed.

$2H^+ + 2e^- \leftrightarrow H_2$ (Reaction 5A)

$Ti^{3+} + 2H_2O \leftrightarrow TiO_2 + 4H^+ + e^-$ (Reaction 5B)

$2Ti^{3+} + 4H_2O \leftrightarrow 2TiO_2 + 6H^+ + H_2$ (Reaction 5C)

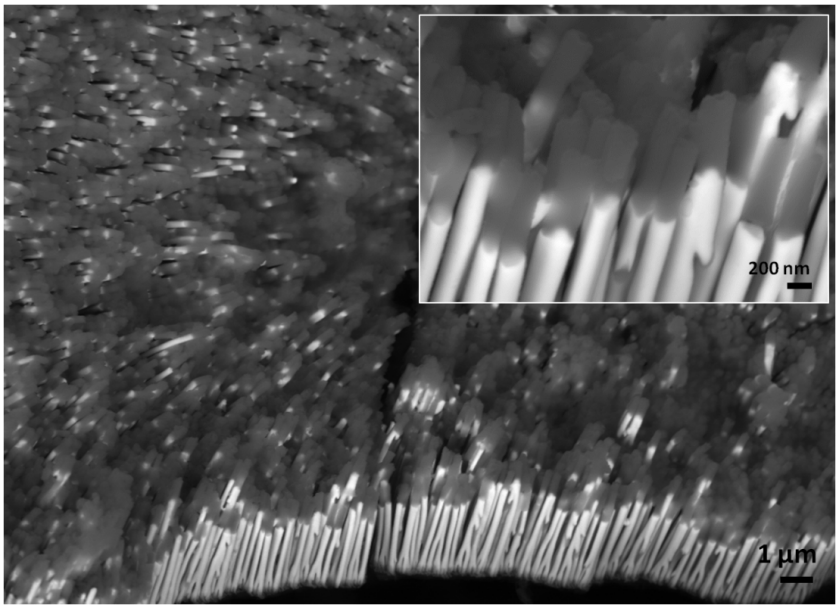

Figure 5-12. SEM image of free-standing Pt-TiO_2 nanorods obtained by electroless deposition of TiO_2 on Pt from 0.28 M $TiCl_3$ solution for 12 h in AAM. Inset shows a higher magnification of Pt-TiO_2 nanorods

The schematic diagram in figure 5-13 compares the growth mechanism of TiO_2 on Pt nanorods *via* electroless method and electrodeposition, where an array of nanostructures is represented by a single nanostructure in the AAM pore for purpose of illustration. According to figure 5-13 (i), the surface of Pt nanostructure helps in mediating the electron transfer between Ti^{3+} and H^+ in the formation of TiO_2 [39]. This reaction occurs spontaneously on surfaces of nanostructured Pt, which favours a lower overpotential for H^+ reduction to H_2 [40]. Accordingly, the deposition of TiO_2 is

characterised by the formation of bubbles, a less concentrated $TiCl_3$ solution as Ti^{3+} is being consumed and a decrease in pH [27]. As illustrated in figure 5-13 (ii), the growth mechanism of TiO_2 occurs in a slightly different manner during the process of electrodeposition, where the oxidation of Ti^{3+} to TiO_2 is being continuously driven at an appropriate applied potential and electrons produced from the reaction reaches the Pt counter electrode where one of the possible reactions may involve protons reduction to produce H_2. In both cases, the growth of TiO_2 does not decrease even when the surface of Pt has already been covered by TiO_2, which suggests that the deposited amorphous TiO_2 is electrically conductive and permeable to the protons (in the case of electroless deposition).

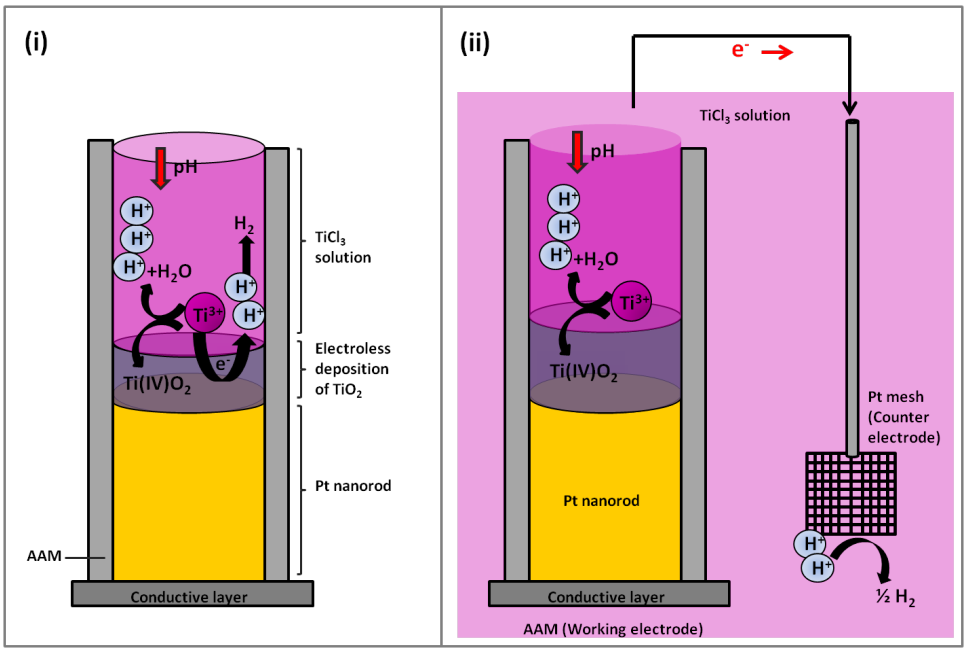

Figure 5-13. Schematic diagram comparing TiO_2 deposition on Pt nanorods by (i) electroless method and (ii) electrodeposition occurring in porous AAM

5.4 Conclusion

Multi-segmented TiO_2-Pt, Pt-TiO_2-Pt, TiO_2-Pt-TiO_2 and Pt-TiO_2-Pt-TiO_2 nanorods were successfully fabricated *via* sequential electrodeposition in AAM according to the procedures established in chapter 3 and 4. Analysis on the structural, surface and interfacial characterization of these TiO_2/Pt striped nanorods reveals the possibility of electrodepositing metallic Pt on a semiconductor material such as TiO_2, and additionally provides insight into the type of junction formed between TiO_2/Pt, noting that the integrity of the interface varies according to the sequence of material deposition.

Overall, the high degree of control in the fabrication of these one-dimensional TiO_2/Pt striped nanostructures enables a variety of TiO_2/Pt nanostructures to be tested and tuned for multifunctional purposes, where they not only find potential to function as photocatalysts for water splitting and pollutant degradation, but also as chemical sensors.

5.4. References

[1] H.-M. Zhang, Y.-G. Guo, L.-J. Wan and C.-L. Bai, Novel electrocatalytic activity in layered Ni–Cu nanowire arrays, Chem. Commun., (2003) 3022–3023.

[2] F. Liu, J. Y. Lee, and W. Zhou, Template Preparation of Multisegment PtNi Nanorods as Methanol Electro-Oxidation Catalysts with Adjustable Bimetallic Pair Sites, J. Phys. Chem. B, 108 (2004) 17959-17963.

[3] S. R. Nicewarner-Peña, R. G. Freeman, B. D. Reiss, L. He, D. J. Peña, I. D. Walton, R. Cromer, C. D. Keating, M. J. Natan, Submicrometer Metallic Barcodes, Science, 294 (2001) 137-141.

[4] R. M. Hernandez, L. Richter, S. Semancik, S. Stranick, and Thomas. E. Mallouk, Template Fabrication of Protein-Functionalized Gold−Polypyrrole−Gold Segmented Nanowires, Chem. Mater., 16 (2004) 3431-3438.

[5] C. D. Keating and M. J. Natan, Striped Metal Nanowires as Building Blocks and Optical Tags Adv. Mater., 15 (2003) 451-454.

[6] J. J. Mock, S. J. Oldenburg, D. R. Smith, D. A. Schultz, and S. Schultz, Composite Plasmon Resonant Nanowires, Nano lett., 2 (2002) 465-469.

[7] S. J Hurst, E. K. Payne, L. Qin, C. A. Mirkin Multisegmented one-dimensional nanorods prepared by hard-template synthetic methods, Angew Chem. Int Ed Engl., 45 (2006) 2672-2692.

[8] G. E Possin, A Method for Forming Very Small Diameter Wires, Rev. Sci. Instrum., 41 (1970) 772 - 774.

[9] R. M. Penner and C. R. Martin, Preparation and Electrochemical Characterization of Ultramicroelectrode Ensembles, Anal. Chem., 59 (1987) 2625-2630.

[10] C. R. Martin, L. S. Van Dyke, Z. Cai, and W. Liang, Template Synthesis of Organic Microtubules, J. Am. Chem. Soc., 112 (1990) 8976-8977.

[11] C. J. Brumlik, and C. R. Martin, Template synthesis of metal microtubules, J. Am. Chem. Soc., 113 (1991) 3174–3175.

[12] S. K. Chakarvarti and J. Vetter, Microfabrication of metal-semiconductor heterostructures and tubules using nuclear track filters, J. Micromeoh. Microeng., 3 (1993) 57-59.

[13] L. Piraux, J. M. George, J. F. Despres, C. Leroy, E. Ferain, R. Legras, K. Ounadjela and A. Fert, Giant magnetoresistance in magnetic multilayered nanowires, Appl. Phys. Lett., 65 (1994) 2484.

[14] R. Ferré, K. Ounadjela, J. M. George, L. Piraux, and S. Dubois, Magnetization processes in nickel and cobalt electrodeposited nanowires, Phys. Rev. B, 56 (1997) 14066.

[15] A. Blondel, J. P. Meier, B. Doudin and J.-Ph. Ansermet, Giant magnetoresistance of nanowires of multilayers, Appl. Phys. Lett., 65 (1994) 3019

[16] L.Piraux, K. Renard, R. Guillemet, S. Matefi-Tempfli, M. Matefi-Tempfli, V. Andrei Antohe, S. Fusil, K. Bouzehouane, and V. Cros, Template-Grown NiFe/Cu/NiFe Nanowires for Spin Transfer Devices, Nano lett., 7 (2007) 2563-2567.

[17] E. Y. Tsymbal and D. G. Pettifo, Perspectives of Giant Magnetoresistance, Solid State Phys., 56 (2001) 113-237.

[18] M. Tanase, D. M. Silevitch, A. Hultgren, L. A. Bauer, P. C. Searson, G. J. Meyer and D. H. Reich, Magnetic trapping and self-assembly of multicomponent nanowires, J. Appl. Phys., 91 (2002) 8549.

[19] C. M. Hangarter and N. V. Myung, Magnetic Alignment of Nanowires, Chem. Mater. , 17 (2005) 1320-1324.

[20] J. A. Sioss, R. L. Stoermer, M. Y. Sha, and C. D. Keating, Silica-Coated, Au/Ag Striped Nanowires for Bioanalysis, Langmuir, 23 (2007) 11334–11341.

[21] S. R. Nicewarner-Peña, A. J. Carado K. E. Shale , and C. D. Keating, Barcoded Metal Nanowires: Optical Reflectivity and Patterned Fluorescence, J. Phys. Chem. B, 107 (2003) 7360-7367.

[22] F. Liu, J. Y. Lee and W. J. Zhou, Segmented Pt/Ru, Pt/Ni, and Pt/RuNi Nanorods as Model Bifunctional Catalysts for Methanol Oxidation, Small 2(2006) 121 – 128.

[23] V. Callegari, L. Gence, S. Melinte, and S. Demoustier-Champagne, Electrochemically Template-Grown Multi-Segmented Gold-Conducting Polymer Nanowires with Tunable Electronic Behavior, Chem. Mater., 21 (2009) 4241–4247.

[24] D. J. Pena, J. K. N. M Bindyo, A. J. Carado, T. E. Mallouk, C. D. Keating, B. Razavi, and T. S. Mayer, Template Growth of Photoconductive Metal-CdSe-Metal Nanowires, J. Phys. Chem. B, 106 (2002) 7458-7462.

[25] N. I. Kovtyukhova and T. E. Mallouk, Nanowire p±n Heterojunction Diodes Made by Templated Assembly of Multilayer Carbon-Nanotube/Polymer/ Semiconductor-Particle Shells around Metal Nanowires, Adv. Mater., 17 (2005) 187-192.

[26] E. D. Herderick, J. S. Tresback, A. L. Vasiliev and N. P. Padture, Template-directed synthesis, characterization and electrical properties of Au–TiO_2–Au heterojunction nanowires, Nanotechnology, 18 (2007) 155204-155210.

[27] R. Liu and A. Sen, Controlled Synthesis of Heterogeneous Metal−Titania Nanostructures and Their Applications, J. Am. Chem. Soc. , 134 (2012) 17505−17512.

[28] W.-N. Wang, W.-J. An, B. Ramalingam, S. Mukherjee, D. M. Niedzwiedzki, S. Gangopadhyay, and P. Biswas, Size and Structure Matter: Enhanced CO_2 Photoreduction Efficiency by Size-Resolved Ultrafine Pt Nanoparticles on TiO_2 Single Crystals, J. Am. Chem. Soc. , 134 (2012) 11276−11281.

[29] S.-Y. Huang, P. Ganesan, S. Park, and B. N. Popov, Development of a Titanium Dioxide-Supported Platinum Catalyst with Ultrahigh Stability for Polymer Electrolyte Membrane Fuel Cell Applications, J. Am. Chem. Soc 131 (2009) 13898–13899.

[30] A. A. Ismail and D. W. Bahnemann, One-step synthesis of mesoporous platinum/titania nanocomposites as photocatalyst with enhanced photocatalytic activity for methanol oxidation, Green Chem., 13 (2011) 428-435.

[31] . J. Yoo, T.-Y. Jeon, S K.-S. Lee, K.-W. Park and Y.-E. Sung, Effects of particle size on surface electronic and electrocatalytic properties of Pt/TiO_2 nanocatalysts, Chem. Commun., 46 (2010) 794–796.

[32] N. Haberkorn and P. Theato, Template-Assisted Fabrication of Well-Ordered p-Type Nanorod Arrays for Photovoltaic Applications, Polymer Preprints, 51 (2010) 246-247.

[33] A. Tighineanu, T. Ruff, S. Albu, R.Hahn, P. Schmuki, Conductivity of TiO_2 nanotubes: Influence of annealing time and temperature, Chem. Phys. Lett., 494 (2010) 260-263.

[34] X. Cui, Z. Li, Y. Yang, W. Zhang, Q. Wang, Low-Potential Sensitive Hydrogen Peroxide Detection Based on Nanotubular TiO_2 and Platinum Composite Electrode, Electroanalysis, 20 (2008) 970 – 975.

[35] V. E. Henrich, and P. A. Cox, The Surface Science of Metal Oxides, Cambridge University Press, 1994.

[36] Y. Han, C.-J. Liu and Q. Ge, Effect of Surface Oxygen Vacancy on Pt Cluster Adsorption and Growth on the Defective Anatase TiO_2(101) Surface, J. Phys. Chem. C, 111 (2007) 16397-16404.

[37] V. V. Hoang, Structural properties of simulated liquid and amorphous TiO_2, Phys. Status Solidi, 244 (2007) 1280 – 1287.

[38] V. V. Hoang, H. Zung and N. H. B. Trong, Structural properties of amorphous TiO_2 nanoparticles, EPJ D, 44 (2007) 515–524.

[39] Ran Liu and Ayusman Sen, Controlled synthesis of heterogeneous metal-titania nanostructures and their applications, J. Am. Chem. Soc., 134 17505-17512.

[40] I. A. Ammar, and S. A. Awad Hydrogen Overpotential at Electrodeposited Nickel Cathodes in Hydrochloric Acid Solutions, J. Phys. Chem., 60 (1956) 837–841.

Chapter 6: Absorption Studies of TiO_2-Pt Nanostructures

6.1 Introduction

6.1.1 Photocatalysis on Semiconductor TiO_2 Surfaces

6.1.1.1 Intrinsic TiO_2 Band-Gap Photoexcitation

The electronic structure of semiconductor TiO_2 plays an important role in its function as a photocatalyst. As opposed to metals in which a continuum of electronic states exists, semiconductors such as intrinsic TiO_2 have a void energy region within which there are no energy levels (this differs slightly for an extrinsic TiO_2 semiconductor which is discussed later in section 6.1.1.2). The void region is termed the band gap and extends from the top of a filled valence band (VB) to the bottom of a vacant conduction band (CB). Typical band gap energies of crystalline TiO_2 anatase and rutile are 3.2 eV and 3.0 eV, respectively, at room temperature [1]. When light of sufficient energy is absorbed by TiO_2 to cause excitation across its band gap, electron and hole pairs are created, which may undergo charge transfer to adsorbed species on the TiO_2 semiconductor surface when the material is immersed in a solution or gaseous phase. The continuous and exothermic transfer of charges from TiO_2 semiconductor to the surface adsorbed species is called a heterogeneous photocatalysis.

In the heterogeneous photocatalysis at TiO_2, the first step involves light absorption of energy greater than or equals to that of its band gap (i.e. $\geq$ 3.2 eV for TiO_2 anatase), which is sufficient to excite electrons from the VB to the CB to generate electron-hole pairs in the TiO_2. Following this, the electrons and holes migrate to the surface of the TiO_2, where they have the ability to respectively reduce electron acceptor species and oxidize donor species which are pre-adsorbed onto the TiO_2 surface. Concurrently, electrons and holes may also recombine on the surface or within the bulk of TiO_2.

The efficiency of a photocatalytic process can be measured by the number of events occurring per photon absorbed, otherwise known as the quantum yield [2]. In determining the quantum yield, it is difficult to accurately measure the total light absorbed due to possible light scattering by the semiconductor surface. Hence an apparent quantum yield is used instead as a measure of efficiency, where an assumption is made that all the light is absorbed. The apparent quantum yield, ϕ, for an ideal system is proportional to the rate of all charge transfer processes (k_{CT}), and inversely proportional to the sum of the charge transfer rate and the bulk and surface

recombination rate of electrons-holes (k_R), as shown in equation 6A. At times, efficiencies are measured in terms of the product yield of the photocatalytic process.

$$\phi \propto \frac{k_{CT}}{k_{CT} + k_R} \quad \text{(Equation 6A)}$$

6.1.1.2 Band Energy Positions of TiO_2

In order for photo-induced CB electrons in semiconductor TiO_2 to transfer to the surface adsorbed species, the band gap energy between the VB and CB of TiO_2, as well as, its VB and CB band energy positions relative to the redox potentials of the adsorbate are important factors to consider. Figure 6-1 shows the band gap positions of TiO_2 anatase and rutile on an electrochemical potential scale (V vs. standard hydrogen electrode (SHE) at pH 7) [3], where TiO_2 anatase and rutile represents the two most used polymorphs of TiO_2 for photocatalysis. The band gap of TiO_2 anatase is 3.2 eV, which is slightly larger than that of rutile (3.0 eV) due to the CB level of TiO_2 anatase being 0.2 eV more negative than that of TiO_2 rutile as shown in figure 6-1.

For reduction to occur, the CB potential of the semiconductor must be positioned above (or more negative than) the reduction potential of the acceptor species, A (A/A^-) (figure 6-1). Similarly, for oxidation processes, the VB potential of the semiconductor must be positioned below (or more positive than) the oxidation potential of the donor species, D (D^+/D) (figure 6-1). The positions of the band edges of oxide materials on the electrochemical potential scale are variable, for which they may shift according to changes in pH (-0.059 V/ pH), solvent type, surface impurities, adsorbed compounds [4].

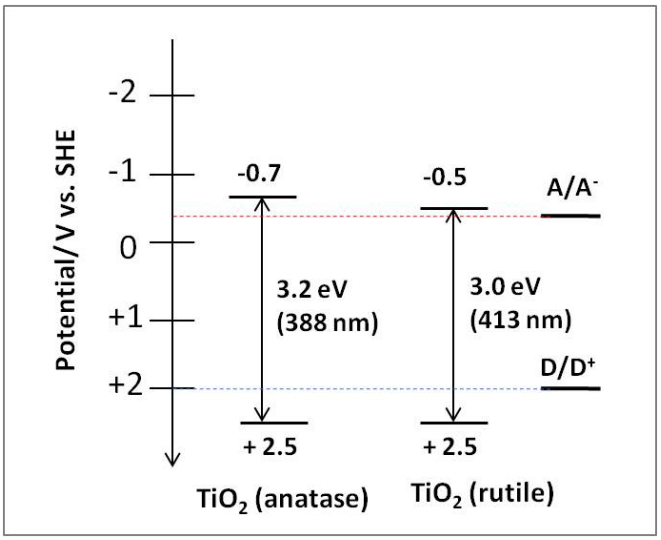

Figure 6-1. Band gaps and band edge positions of TiO_2 anatase and TiO_2 rutile photocatalysts depicting correlations with the potential levels of an acceptor and donor species in pH 7 electrolyte

Another important factor in determining the suitability of a material for photocatalysis is the stability of the semiconductor photocatalysts under photo-illumination. A plot of the characteristic energy levels of a semiconductor and its critical decomposition potentials on a common energy scale is able to immediately show how thermodynamically stable or unstable the semiconductor is [5]. An example of such a plot for TiO_2 is shown in figure 6-2. Ideally, the stability of a material under illumination requires that the Fermi energies for decomposition are located outside the energy bands (VB and CB) of the respective photocatalyst material. The Fermi energy for decomposition defined as the electrochemical potential of the decomposition reaction. However, it is not uncommon to find that that the Fermi level for cathodic decomposition by electrons is located outside the conduction band, while that of anodic decomposition by holes is located inside the band gap. This results in the material being stable against cathodic decomposition, yet prone to the anodic decomposition upon illumination at high intensity. This occurs in TiO_2, as shown in figure 6-2, where the Fermi level for cathodic decomposition, ${}_nE_{decomp.}$ is located more negative than its CB, while the Fermi level for anodic decomposition, ${}_pE_{decomp.}$ is positioned within the CB and VB. The anodic decomposition is prevented by introducing a redox system to the electrolyte, such as H_2O, the Fermi level of which is above that of the ${}_pE_{decomp}$ as indicated in figure 6-2 [5]. Thermodynamically, this method will be effective for a large concentration of electron donors for hole capture at the semiconductor-electrolyte interface; and kinetically, where the transfer of holes proceeds to the sacrificial couple occurs at a fast rate. For TiO_2, its instability against anodic decomposition is

compensated with the rapid and spontaneous oxygen evolution at the TiO_2 surface under photo-illumination. Additionally, Fermi level pinning occurs at the TiO_2/electrolyte interface arising from the presence of electronic surface states of oxygen defects in TiO_2 (discussed in the following section 6.1.1.3), which further enhances the anodic reactions on TiO_2, and thereby contributes to the overall stability of TiO_2 as a photocatalyst [6].

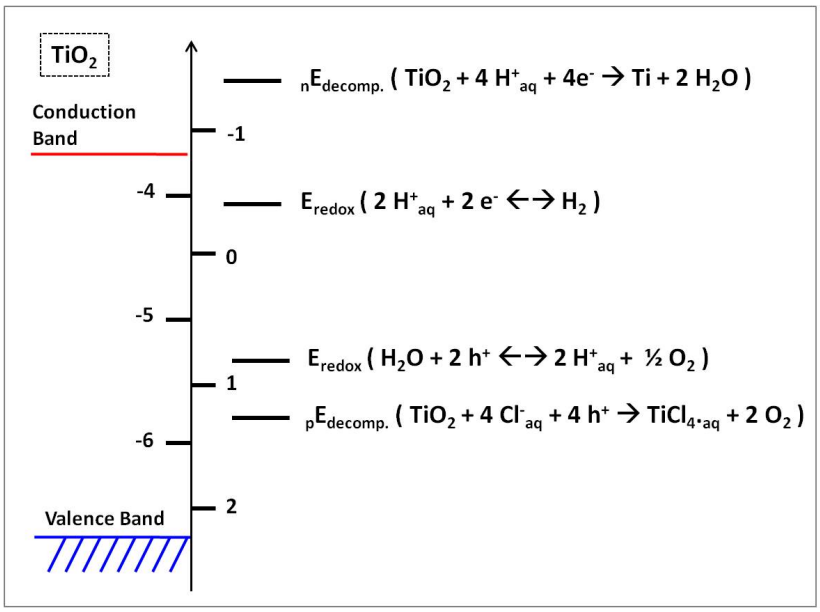

Figure 6-2. Energy correlation between band edges of TiO_2 and Fermi energies of electrode reactions in aqueous electrolyte of pH 7

6.1.1.3 Surface States in Extrinsic TiO_2

Very often in the preparation of colloidal and polycrystalline TiO_2, ideal crystal lattices of the semiconductor are not produced. Instead, surface and bulk irregularities in TiO_2 occur naturally in the preparation process, which creates surface electron states with energies that are different from the existing bands present in bulk TiO_2 semiconductor. In defective TiO_2 crystals, oxygen vacancies and Ti^{3+} states act as intrinsic dopants to cause a shift in the Fermi-level towards the CB of TiO_2, in which the Fermi-level would otherwise be located mid-way between the CB and VB of a defect-free TiO_2 material. Because of this property, TiO_2 semiconductors are commonly known to be extrinsic, n-type semiconductors.

In a basic cell structure of TiO_2, each Ti^{4+} ion is surrounded by an octahedron of six O^{2-} ions [7]. Lattice defects in TiO_2 may arise due to the loss of oxygen atoms, and defect states associated with Ti^{3+} ions appear within the band gap at 0.7 to 0.8 eV below E_F. Other calculations on TiO_2 (110) surfaces have predicted that a gap does not exist between the defect states and the CB

[8], and that the defect states was estimated to lie between 0.7 to 1.8 eV above the VB [9]. So far, it has been generally agreed upon that the defects in TiO_2 (110) are represented as localized states at Ti sites next to the oxygen vacancies and defects formation arises from the redistribution of electrons to previously unoccupied Ti-3d orbitals after oxygen atoms haven been removed [10-12].

6.1.1.4 Crystallinity and Particle Size Effects on TiO_2 Photocatalysts

There are a combination of factors which influences the production and lifetime of electron-hole pairs, surface adsorption and desorption processes and surface redox reactions in semiconductor TiO_2, and in turn, its photocatalytic activity. This includes factors such as crystallinity and crystal structure [13-15], particle size [16, 17], porosity [18], density of surface hydroxy groups [19, 20], and preparation method [21, 22]. Amongst these, the crystal structure and particle size effect of TiO_2 are two factors most widely investigated for improving the photocatalytic efficiency of TiO_2.

A significant parameter of influence on TiO_2 as a photocatalyst is its crystal structure, which is known to be the most primitive but essential property in predicting its photocatalytic activity. TiO_2 exists in three stable phases: amorphous, anatase and rutile, in which TiO_2 anatase and rutile crystal phases possess photocatalytic properties [14, 23]. TiO_2 photocatalysts consisting of TiO_2 polymorphs of anatase and rutile were reported to demonstrate a higher photoactivity than either of its individual phases. It was rationalised that the higher CB edge of TiO_2 anatase of 0.2 eV allows for rapid interfacial electron transfer from TiO_2 anatase to TiO_2 rutile, and the energy barrier between both phases suppresses the back flow of electrons [24-26]. A classic example of a mixed-phase TiO_2 is the commercially available TiO_2 P25 (Degussa), which consists of 80% anatase and 20% rutile and is often employed as a benchmark for photocatalysts.

Particle size is another important factor for photocatalysis because it has a direct impact on the specific surface area of the catalyst. Generally, smaller-sized particles with dimensions in the nanometer range possess higher adsorption rate and an increased in the number of active surface sites for reactions, for which it increases the surface charge carrier transfer rate in photocatalysis [27, 28]. It was, however, revealed that the photocatalytic activity of TiO_2 does not increase monotonically with decreasing particle size, and that there exists an optimal TiO_2 particle size for which further decrease in the particle size does not contribute to a marked improvement in its photoactivity [21, 29].

Presently, the solar energy conversion efficiency by TiO_2 in photocatalytic processes such as water splitting remains low mainly due to the inability of TiO_2 to utilize visible light [30] and fast electron-hole recombination [31]. Crystalline TiO_2 possess a band gap of approximately 3.0 to 3.2 eV, suggesting that it is only able to utilize UV light, which accounts for only approximately 4% of the total solar radiation energy. Since visible light contributes to approximately 50 % of the total solar radiation energy, the solar efficiency of TiO_2 catalysts can be improved by extending its absorption range into visible light region.

There is a direct competition occurring between the recombination of electrons and holes, and the trapping of the electrons and holes for surface reactions. Influenced by factors such as increased defects, size and shape non-uniformities, the transport pathway of charge carriers in TiO_2 becomes longer, which implies that the electrons spend a longer time in the material to undergo more trapping and de-trapping events before being collected at the surface for reactions [32]. An example is seen in the electron transport in mesoporous TiO_2 nanocrystalline films, which was found to be 10^2 to 10^3 times slower than in a single-crystal TiO_2 [33]. Additionally, increasing structural porosity of TiO_2 also contributes to greater electron transport pathway through a smaller number of inter-particle contacts [18]. Therefore in order to achieve high charge-collection efficiencies, the transport rate of the charge carriers should be significantly faster than the process of recombination. To circumvent the limitations associated with photoefficiencies and electron transport, chemical additives (addition of electron donors [34] and carbonate salts [35]) and modification of the TiO_2 catalyst (noble metal loading [36], metal ion doping [37, 38], anion doping [39-41], dye sensitization [32, 42, 43]) have been used to promote TiO_2 photocatalytic activity and enhance visible light response.

6.1.1.5 Photocatalytic Enhancement through Noble Metal Loading of TiO_2

One of modification techniques used in overcoming the limitations of TiO_2 as a photocatalysts is by the addition of noble metals onto the surface of TiO_2. Noble metals such as Pt, Au, Pd, Rh, Ru, Ni, Cu and Ag have been reported to be very effective in enhancing the energetics of TiO_2 photocatalysis and in improving the yield of a product through changes in its surface properties [36, 42, 44-47]. Enhancement in photoreactivity was first observed by Sato and White [48] using Pt/TiO_2 photocatalysts in the photo-assisted decomposition of H_2O. The addition of metals to TiO_2 has also been shown to yield products that are different from those formed by catalysis on bare TiO_2. For example, methane was in high yield in the decomposition of liquid acetic acid

over platinized-TiO_2 photocatalyst under UV light, while on TiO_2, the product was mostly ethane [49].

In achieving marked enhancements in metal-oxide photoactivities through noble metal loading, several reports had attributed the enhancement effect of noble metals to the presence of a Schottky contact between the metal oxide and metal; and at the same time, have also directly correlated it to the role of Pt in acting as an electron sink [2, 50-53]. In some ways, this explanation undermines the concept of employing noble metal to enhance TiO_2 photoactivity. While a Schottky junction may be established at a TiO_2 semiconductor-Pt metal interface characterised by a potential drop from the metal to the semiconductor, this concept based on the Schottky barrier predicts that under irradiation, electron-hole separation is enhanced by photo-generated holes flowing to the Pt metal and the accumulation of photogenerated electrons in TiO_2, instead of a transfer of electrons from the semiconductor to the metal as explained by the reports as mentioned earlier [54]. There is no doubt of the role Pt play as an electron sink to TiO_2 as existing reports have evidently demonstrated the electron transfer from semiconductors to metals and the accumulation of electrons on Pt [55, 56]. Therefore in this section, the concept of the Schottky barrier existing between TiO_2/Pt will be introduced and in particular, an explanation is provided to explain how noble metals may enhance the photoactivity of TiO_2 through the understanding of circumstances under which a Schottky junction may exists and the proposed type of contact that is formed between a n-type semiconductor and a metal nanomaterial on a macroscopic and microscopic scale.

6.1.1.5.1 Schottky Contact between n-type TiO_2 and Pt

When a n-type TiO_2 semiconductor and a metal Pt are brought into contact with each other at thermal equilibrium, redistribution of electric charges occur within both materials as illustrated in figure 6-3A. This happens due to difference in characteristic Fermi levels (E_F) and work function (defined by the minimum energy an electron must attain to become a free electron) of the n-type semiconductor and metal (where Pt metal (~5.6 eV) has a greater work function than that of TiO_2 semiconductor (~4.2 eV)). The difference in Fermi levels between the n-type semiconductor and metal causes electrons from the n-type semiconductor to migrate to the metal, until their Fermi levels align to establish a new Fermi level, E_F', as indicated in figure 6-3A.

Due to induction effects, the charges existing near the surfaces of the n-type TiO_2 semiconductor and Pt metal oppose each other, where positively charged Ti^{3+} surface states of surface-defective TiO_2 are found localized near its surface, and a high density of induced negative charges reside near the surface of Pt. An intimate contact between TiO_2 and Pt at thermal equilibrium produces a space charge region, characterised by a potential difference across the surfaces of TiO_2 and Pt to result in an upward band bending of TiO_2 CB and VB toward the contact surface of Pt. This space charge region exists primarily within the TiO_2 semiconductor and, depending on doping distance can extend up to a depth of 100 μm into the TiO_2 [57]. Represented by a potential drop from the Pt metal surface in contact with TiO_2 semiconductor to the interior of the TiO_2 semiconductor, an electric field is created within the space charge region, setting up a resistance barrier commonly known as the Schottky barrier (figure 6-4B). Due to the presence of an electric field within the depleted region, electrons in the TiO_2 VB are driven away from the TiO_2-Pt interface, while CB holes are transported towards the TiO_2-Pt interface. This mechanism thus demonstrates how electron and hole pairs are efficiently separated, and that the Pt metal does not act as an electron sink to TiO_2 since the Schottky barrier between TiO_2 and Pt presents a high resistance for the transfer of electrons from TiO_2 to Pt.

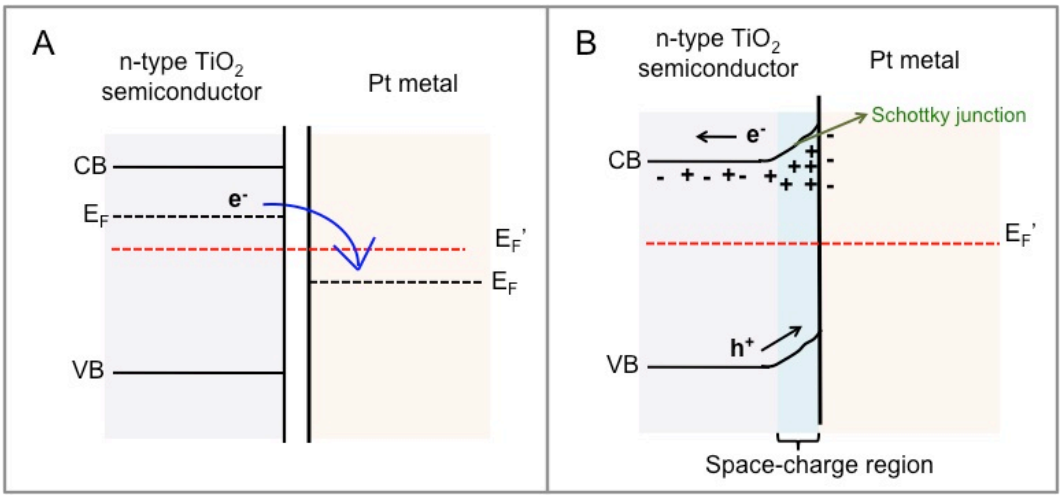

Figure 6-3. Energy level diagrams of n-type TiO_2 semiconductor (consisting of lattice imperfections) and Pt metal at electrical and thermal equilibrium illustrating A) equilibrating of Fermi levels as TiO_2 and Pt are brought in contact with each other, and B) formation of a space-charge layer resulting from a potential difference across TiO_2 and Pt contact surfaces, and a schottky barrier between n-type TiO_2 and Pt which creates resistance for electrons to travel from TiO_2 semiconductor to Pt metal

6.1.1.5.2 Particle Size Effect on Schottky Barrier Formation between Semiconductor and Metal

As discussed earlier, the Schottky junction formation between an n-type semiconductor and metals reduces the kinectics of electron injection from the TiO_2 CB to the Pt metal, which is largely applicable to macroscopic n-type semiconductors and metals. However in microscopic materials, the significantly smaller size of the material as compared to the thickness of the depletion layer may account for the absence of a Schottky barrier. In particular, this was found to exist in small particles such as quantum dots (QDs) with diameters of < 15 nm. Curran and Lamouche [58] suggested that potential drop within very small semiconductor particles of 10 to 15 nm becomes limited by the size of the particles. It was pointed out that that although a space charge layer is formed within the small semiconductor particle, the space charge layer is extended to the entire surface of the semiconductor particle, such that the particle does not experience an appreciable electric field effect [58]. Under this condition, the electric field strength within the particle is assumed to be so small that it will not have an influence on the carrier transport of the semiconductor. Evidently, it was found under UV illumination that a strong driving force exists to facilitate the transfer of electrons from the metal oxide (ZnO) particles of 5 nm to the Pt islands [59]. Since there were no photogenerated electrons found to reside on the QD of ZnO-Pt particle during illumination, a conclusion was made that Pt is an efficient electron sink for ZnO metal oxide nanoparticles.

Additionally, the absence of the Schottky barrier at the semiconductor-metal interface in the nano-scale can also be explained in view of donor densities present in semiconductor QDs. The typical donor densities arising from electron donor states of Ti^{3+} and oxygen vacancies of synthetic macroscopic n-type TiO_2 (e.g. TiO_2 films) are reported to be in the order range of 10^{-18} to 10^{-20} cm^{-3} [60, 61]. Based on a donor density of 10^{20} cm^{-3}, the total number of donors on each QDs with a volume of approximately 10^{-18} cm^3 (QD diameter of 10 to 15 nm) is estimated to be in the order of 1 to 10^2, which is hardly significant.

Furthermore, Bardeen [57] pointed out that the condition for an appreciable space charge layer to exist within the semiconductor requires the density of surface states to be less than 10^{12} states/cm^2, which further supports that the electric field effect within the QDs is negligible. Since the concentration of surface defects present in each n-type TiO_2 QDs is significant compared to those of macroscopic n-type TiO_2, its influence on the TiO_2 CB and VB

band bending is expected to be negligible, which hence explains the absence of a Schottky barrier between TiO_2/Pt at the nano-scale.

6.1.1.5.3 Effect of Intrinsic Dopant Levels in TiO_2 on TiO_2-Pt Barrier Type

The transfer of photogenerated electrons from the metal oxide to the metal in contact with the metal oxide is not just seen in QD particles, but has also been evidently reported for macroscopic metal oxide/metal materials. Turning our attention to how noble metals such as Pt may act as an electron sink for semiconductor TiO_2 may suggest an absence of a resistance barrier at the TiO_2-Pt interface. To simplify calculations, models and studies performed to investigate the Schottky barrier are largely derived based on single-crystalline rutile [62, 63] and anatase TiO_2 [64-66]. However in practice, a large proportion of synthetic TiO_2 materials do not turn out to be perfect single-crystals. Instead, they often consist of greater imperfections in lattice structures and higher concentrations of defect states, which may considerably alter the resistivity at the semiconductor-metal contact [67].

A proposed schematic diagram, figure 6-4, illustrates a model of a contact between a heavily doped n-type TiO_2 semiconductor and Pt metal. The dotted line in figure 6-4 represents the CB and VB bending in TiO_2 with normal doping densities of 10^{20} cm^{-3}. Compared to a normal doped TiO_2-Pt contact (discussed earlier in figure 6-3), the CB and VB in a heavily doped n-type TiO_2 bends steeply towards the contacted Pt metal surface due to the presence of significantly higher densities of oxygen vacancies and Ti^{3+} surface states (>10^{20} cm^{-3}) at the surface of TiO_2 (figure 6-4). Consequently, the space-charge region within TiO_2 is significantly reduced, in which its width is sufficiently thin compared to the mean free path of a photogenerated electron in the CB of TiO_2. In this case, the resistance of a heavily doped layer can be considered negligible, which permits the flow of photogenerated electrons from the CB of TiO_2 to Pt under illumination, characteristic to that of an ohmic contact. Generally, high doping levels in the semiconductor produces ohmic metal-semiconductor contacts, while low doping levels result in Schottky-like contacts [54].

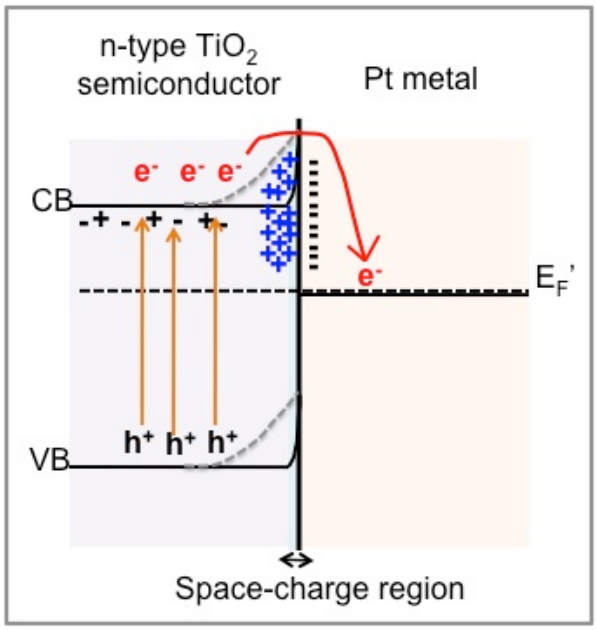

Figure 6-4. Energy level diagrams of n-type TiO_2 semiconductor consisting of high concentration of surface defects, resulting an Ohmic flow of electrons from TiO_2 to Pt metal

6.2 Literature Review

Since its first introduction by Krauetler and Bard [49], the surface platinization of TiO_2 has become a popular TiO_2 modification technique because of it enhances the photocatalytic reactions of TiO_2. By serving as an electron sink, the presence of Pt on TiO_2 is generally believed to retard fast electron-hole recombination and facilitate interfacial electron transfer to electron acceptors.

Amongst several photocatalytic reactions of TiO_2/Pt, the photodegradation of organic pollutants on TiO_2 and TiO_2/Pt systems has been widely studied, as TiO_2 and TiO_2/Pt particulates are known to be successful in degrading dye pollutants under visible light irradiation. Studies so far have shown that platinised TiO_2 exhibit higher photoactivity as compared to bare TiO_2 [50, 68, 69], and that there are on a variety of TiO_2/Pt systems used in enhancing photodecomposition of organic pollutants under visible light and UV light irradiation.

The simplest and most common TiO_2/Pt system used in the photodegradation study of organic pollutants consists of Pt particles deposited on the surface of TiO_2 powdered particles [50, 69-71]. For example, Li and Li [72] prepared Pt-TiO_2 photocatalysts by the method of photoreduction, which were then used for photocatalytic oxidation of aqueous methylene blue (MB) and methyl orange (MO) under UV and visible light irradiation. The results indicated that Pt-TiO_2 could be sensitized by visible light and that the highest rate of photocatalytic degradation of MB and MO was achieved at

an optimal content of 0.75 % Pt-TiO_2. By employing a similar method to prepare Pt/TiO_2 particles, Li and co-workers [73] studied the mechanisms of RhB degradation on Pt/TiO_2 particles in the presence of electron donors, and revealed that the rate of RhB degradation was dependent on the adsorption behaviour of RhB on Pt/TiO_2 particles.

While Pt/TiO_2 powder systems may work as photoocatalysts, there is a major drawback associated with their nanocomposite structure. In most cases, Pt nanoparticles are deposited onto the surface of TiO_2 as isolated 'nano-islands', and increasing the Pt loading often hinders surface reactions on TiO_2, rendering majority of the TiO_2 surface unused. According to Xu and co-workers [74] who employed Pt-TiO_2 core-shell nanocomposites for the photodegradation of RhB, Pt-TiO_2 core-shell structure are better photocatalysts than Pt/TiO_2 powder systems because of the ability to control the chemical and colloidal stability within the shell and provide a three-dimensional interaction between metal Pt and semiconductor TiO_2 for effective charge transfer. In their study, it was revealed that the Pt-TiO_2 core-shell nanocomposites possess tunable photo-reactivity, in which the incorporation of noble metal Pt core into the shell of TiO_2 contributed to the enhancement of TiO_2 photocatalytic activity only under visible light but not UV light.

So far, the study of one-dimensional (1D) Pt/TiO_2 photocatalysts on the photodegradation of organic compounds is very limited. Well-aligned arrays of TiO_2-Pt coaxial nanotube on Ti substrate were tested for its photoactivity on phenol degradation under UV light irradiation and results demonstrated that the TiO_2-Pt coaxial nanotubes exhibited a significantly higher photoactivity than that of TiO_2 nanotubes [75]. It is believed that the marked enhancement in the photocatalytic efficiency can be attributed mainly to its high aspect ratio, which facilitates the transport of photogenerated electrons to the conductive substrate.

In this chapter, we report for the first time, photo-absorption studies on highly ordered 1D striped nanorods of TiO_2/Pt *via* a simple photodegradation system of RhB under visible and UV light. Consisting of alternating segments of TiO_2 and Pt, these 1D TiO_2/Pt nanostructures offers convenience in manipulating photocatalytic activity through its customizable TiO_2/Pt length segments and reproducible TiO_2/Pt interfaces. By being able to control the chemical compositions of each segment and the reproducibility of interfaces, the photoactivities of the 1D TiO_2/Pt striped nanorods can be conveniently evaluated against parameters such as the length segments, structural integrity and number of TiO_2/Pt pair sites. The architecture of the 1D TiO_2/Pt striped nanorods provides a direct demonstration of TiO_2/Pt bifunctional mechanisms, which is not possible by alternate routes.

6.3 Material Preparation and Experimental Setup

6.3.1 Materials

Rhodamine B ($C_{28}H_{31}ClN_2O_3$, Mr=479.02, λ_{max}~543 nm) was purchased from Sigma Aldrich, its structural diagram is in figure 6-5. Materials used for the synthesis of TiO_2 and TiO_2/Pt nanorods are listed in chapters 3 and 4. All reagents are of analytical grade and were used without further purification.

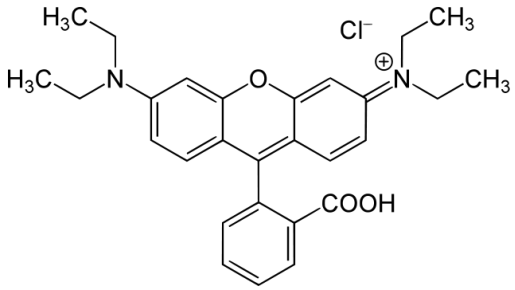

Figure 6-5. Structural diagram of Rhodamine B ($C_{28}H_{31}ClN_2O_3$, Mr=479.02, λ_{max}~543 nm)

6.3.2 General Experiment Practice

The photoactivity of as-prepared TiO_2 and TiO_2/Pt nanorods was studied by measuring the degradation rate of Rhodamine B solution. A test sample consisted of a 4 ml cuvette filled with 2.22 x 10^{-6} M of aqueous RhB and an array of free-standing TiO_2 or TiO_2/Pt nanorods of area 6.4 cm^2 (synthesized according to the procedure indicated in chapters 4 and 5 and AAM etched) immersed in the RhB solution. Further details and illustration of the optical setup are provided in chapter 2, section 2.6.

Photoresponse tests were all performed on crystalline TiO_2 or TiO_2/Pt nanorods, unless otherwise stated. Crystalline samples were achieved by annealing at 600 ^oC to crystallise the TiO_2 segments (crystallinity of TiO_2 shown in chapter 4). No heat treatment was applied to amorphous samples. The test sample is then placed in a fixed position from a solar simulator irradiation source, a xenon lamp (LPS-220, Photon Technology International) providing a constant illumination of 26.5 µW cm^{-2}. Measurements carried out under a combination of visible and UV irradiation (simulating that of the solar light) required an Infrared (IR) Cutoff filter (T >85%, 480nm-680nm, T <10%, 740nm-1200nm, T= 50%, 680nm-740nm) (Edmund Optics Ltd) positioned directly in front of the light source to reduce heating. In photoabsorption studies carried out under solely UV light, the

300 nm Bandpass Interference Filter (Edmund Optics Ltd) was used. All the photoactivities of the samples were evaluated using normalized absorbencies of RhB solutions, which were measured using a UV-VIS spectrophotometer (Perkin Elmer, Lambda Bio 10) at regular irradiation time intervals of 1 h.

Reflectance and transmittance measurements were performed on samples consisting of freestanding arrays of bi-segment TiO_2/Pt nanorods by employing an integrating sphere (Cary 5000 series UV-vis-NIR, Agilent Technologies). The axis lengths of the TiO_2/Pt nanorods were aligned at 180 ^{o} to the light source. Details on the integrating sphere measurements can be found in chapter 2, section 2.6.3.

6.4 Results and Discussion

6.4.1 Photoactivity of Amorphous and Crystalline TiO_2 nanorods

Figure 6-6 shows a comparison in the spectral changes of RhB in the presence of an array of amorphous (plots i, ii) and crystalline (plots iii, iv) TiO_2 nanorods of length 3 μm (with phase composition of 36 % anatase and 64 % rutile as determined in chapter 4, section 4.8.3.2) under irradiation of UV light (plot i, iii), as well as under both visible and UV light (wavelength >300 nm) (plot ii, iv). Characterized by a decrease in the absorbance at approximately 552 nm over a period of 6 h, the degradation of RhB in the presence of TiO_2 photocatalyst provides a measure of the TiO_2 photocatalytic activity.

The slight decrease in RhB absorbance after exposure of solution to amorphous TiO_2 in (i) is attributed to the adsorption of RhB on TiO_2 and its photoactivity to RhB is subsequently considered to be negligible. Compared to amorphous TiO_2 (i), a significant decrease in the concentration of RhB is observed in the presence of crystalline TiO_2 (ii). Similar findings were demonstrated in photocatalytic studies comparing the effect of amorphous and crystalline TiO_2. Under irradiation of wavelength > 300 nm, the photoactivity of amorphous TiO_2 powdered samples suspended in an aqueous 2-propanol solution was found to be negligible, as opposed to that anatase TiO_2, which showed an appreciable photocatalytic activity [14]. Furthermore, it was observed that the photocatalytic effect of TiO_2 material (consisting of TiO_2 particles of the same size), varied linearly with the fraction of anatase present in TiO_2 [14, 76]. Generally, the negligible photocatalytic activity of amorphous TiO_2 is attributed to high concentration of surface and bulk defects which act as trap sites to facilitate recombination of e^- and h^+ [77, 78].

Under irradiation with both UV and visible light, a similar trend is observed for amorphous (ii) and crystalline TiO_2 (iv), where crystalline TiO_2 (iv) shows a greater decrease in RhB absorbance. The extent of RhB degradation in the presence of amorphous TiO_2 (ii) under a combined irradiation of UV and visible light indicates the presence of photoactivity in amorphous TiO_2 (ii), which cannot be assumed to be negligible. This can be explained by the difference in the mechanism of RhB degradation under a combination of UV and visible light illumination compared to that under irradiation of only UV light. Unlike TiO_2, RhB is able to absorb visible light and as a result it injects electrons into the CB of TiO_2. The injected electrons then participate in the reduction of surface chemisorbed oxidants (e.g. O_2) to subsequently produce *OH radicals, which ultimately lead to the degradation of RhB. Therefore, under illumination of UV and visible light, amorphous TiO_2 (ii) plays the role of a mediator to RhB in the separation of injected electrons and dye cation radicals; while in crystalline TiO_2 (iv), the semiconductor act as both photocatalyst and mediator to achieve a higher rate of RhB degradation as shown by a significant decrease in the RhB concentration (iv) in solution.

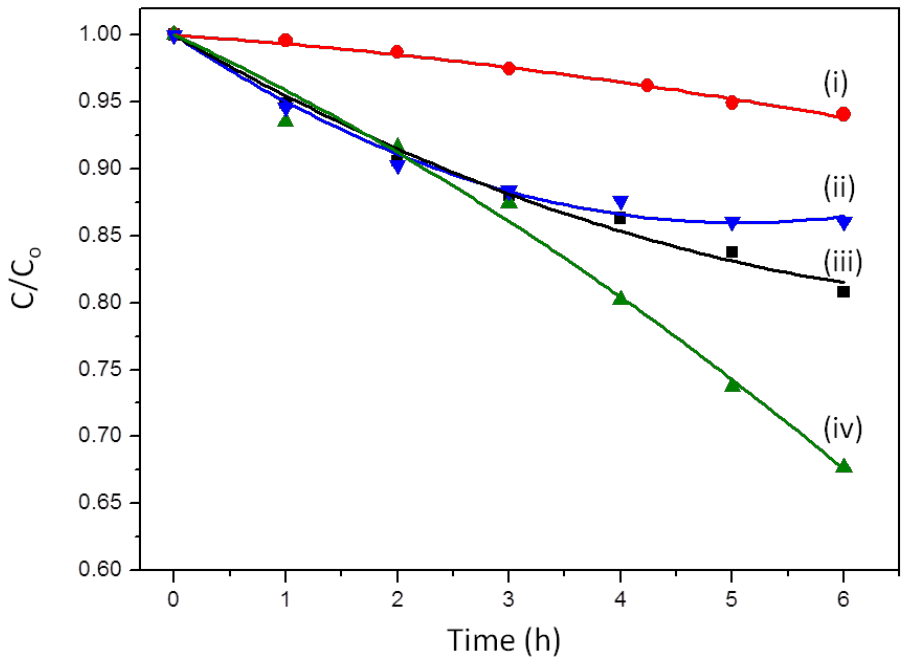

Figure 6-6. Plot comparing the photodegradation of RhB on (i) TiO_2-unannealed and (iii) TiO_2-annealed under UV irradiation; (ii) TiO_2-unannealed and (iv) TiO_2-annealed under irradiation of UV and visible light ($\lambda > 300$ nm). All 4 samples consists of arrays of TiO_2 nanorods of approximately 3 μm in length.

6.4.2 Structural Modification and Noble Metal Loading on TiO_2 Photoactivity

The nanostructural effects of TiO_2 were examined by comparing the rates of RhB degradation in the presence of an as-synthesized TiO_2 film (figure 6-7, inset a) and an array of freestanding TiO_2 nanorods (figure 6-7, inset b) under irradiation at wavelengths >300 nm. The TiO_2 film was prepared *via* electrodeposition onto a flat Ag electrode, while the TiO_2 nanorods were electrodeposited into porous AAM. $TiCl_3$ precursor solution of the same composition was used for both electrodepositions and the charge was controlled so as to achieve the same amount of TiO_2 deposits.

From figure 6-7, it is seen that the TiO_2 nanorods exhibit a higher rate of RhB degradation and hence a higher photocatalytic activity compared to the TiO_2 film. There are two reasons to suggest why this may have occurred. The first reason may be attributed to the higher aspect ratio of TiO_2 nanorods as compared to that of bulk TiO_2, which is able to accommodate higher adsorption of RhB and oxidants such as O_2 to its surface. Under light illumination of λ > 300 nm, RhB and TiO_2 are activated at λ>470 nm and λ<380 nm respectively, resulting in two simultaneous reaction pathways. The first reaction involves the electron injection by activated RhB into the conduction band (CB) of TiO_2, where the photogenerated electron reacts with adsorbed oxidants such as O_2 to produce oxygen radicals for the degradation of RhB. Concurrently, photogenerated electrons in TiO_2 are excited to the CB of TiO_2 and are scavenged by O_2 to produce O_2 radicals, while surface adsorbed OH^- or H_2O molecules are oxidized by the valence holes. Since both reaction pathways require the adsorption of molecules (RhB, O_2, OH^-, H_2O) onto the surface of TiO_2, a higher surface area of TiO_2 nanorods adsorbs a higher concentration of molecules, which enhances the rate of RhB degradation.

The second reason for the enhanced photoactivity of TiO_2 nanorods is proposed in figure 6-5, where the high specific surface area of the TiO_2 nanorods enables decoupling of the directions of light absorption and charge carrier collection [79]. This is in contrast to the planar structure of a TiO_2 film, in which the direction of light absorption is the same direction as that of the charge carrier collection. In order for an excited charge carrier that is photogenerated deep within the TiO_2 film to migrate to the surface of TiO_2 film for reactions, the diffusion length of the charge carrier, L_D should be greater than the absorption length, $1/\alpha$ (scheme A) in a TiO_2 film. This constraint, however, does not apply to TiO_2 nanorods, as its unique geometry provides short diffusion pathways in the radial direction for charge carrier (even with short lifetime), to easily reach the surface of TiO_2 for reactions (scheme B).

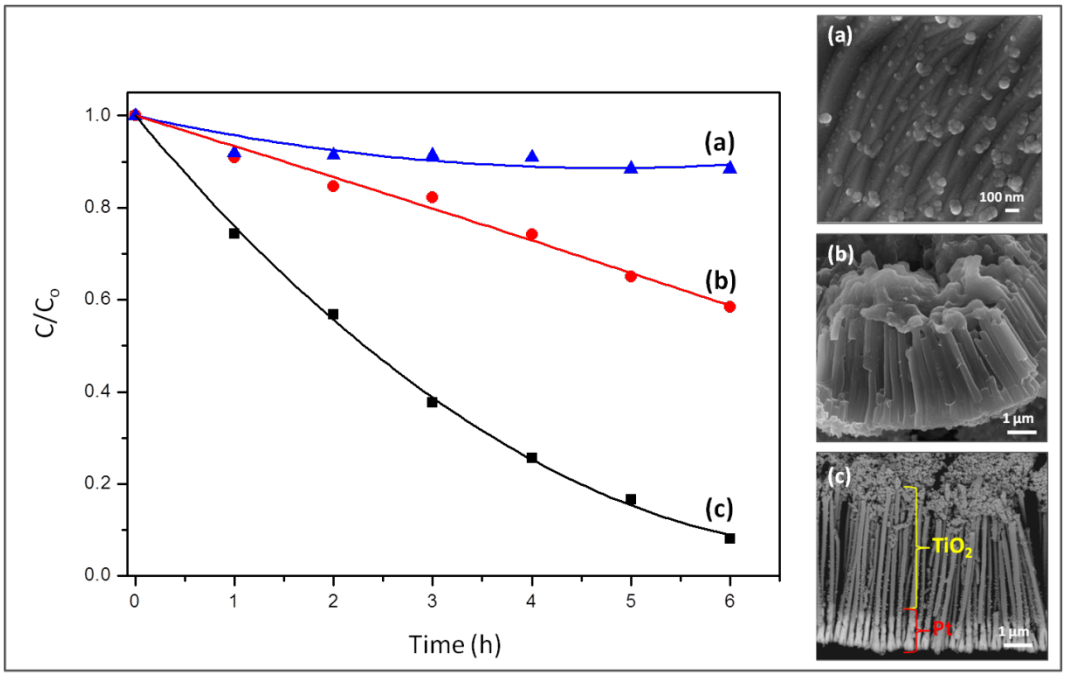

Figure 6-7. Photocatalytic activity comparison under visible and UV irradiation (wavelength >300 nm) of (a) TiO_2 film (b) TiO_2 nanorods and (c) bi-segmented Pt-TiO_2 nanorods based on the normalized RhB concentration ratio C/C_o as a function of irradiation time. Insets (a), (b) and (c) show the corresponding SEM images of the respective samples.

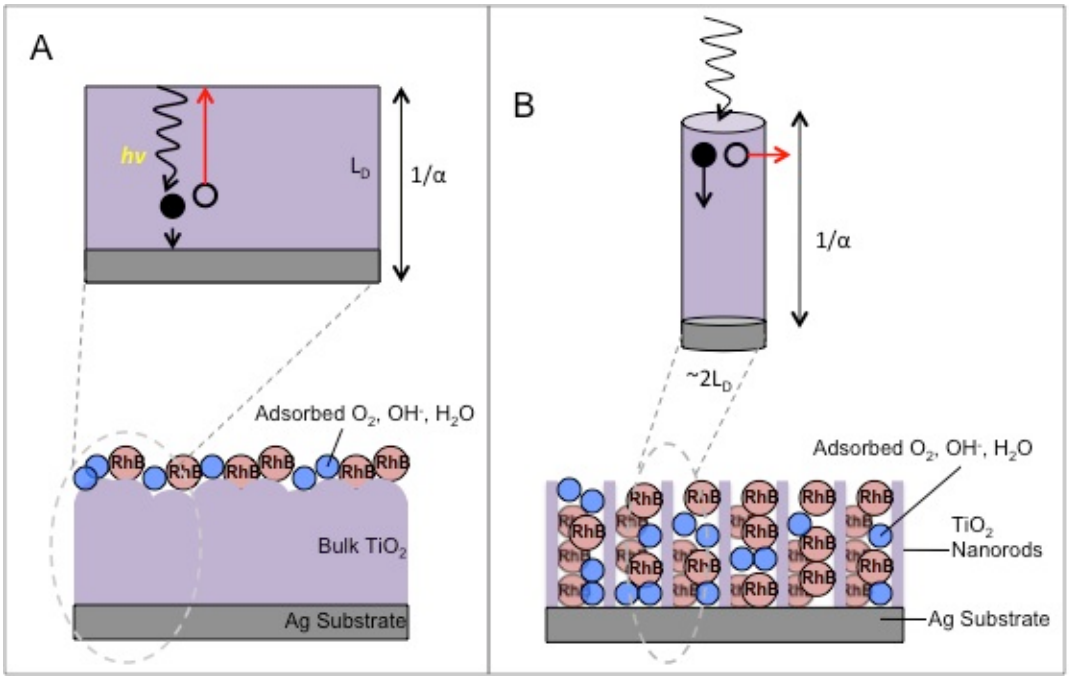

Figure 6-8. Schematic diagram illustrating the difference in the aspect ratio of A) bulk TiO_2 and B) an array of TiO_2 nanorods for adsorption of molecules and charge carrier migration lengths.

Besides surface area, efficient charge separation on TiO_2 was reported to play a crucial role in affecting the efficiency of RhB photodegradation under the irradiation of visible and UV light (λ > 300 nm). In order to demonstrate this effect, Pt was added to TiO_2 through the fabrication of bi-segment Pt-TiO_2 nanocomposite structures, the rate of RhB photodegradation in the presence of Pt-TiO_2 nanocomposite structures were compared to that of TiO_2 nanorods. For each sample, the length of each TiO_2 nanorod was kept approximately constant at 3 μm. After 6 hours of irradiation, a significantly higher rate of RhB degradation was observed for samples of Pt-TiO_2 nanorods compared to bare TiO_2 nanorods. This demonstrates that the bi-segmented Pt-TiO_2 nanorods possessed a significantly higher photocatalytic activity. According to the proposed scheme in figure 6-9, Pt acts as an electron trap to facilitate electron-hole separation and subsequent electron transfer to the adsorbed species on Pt-TiO_2 surface. Additionally, surface electron excitation and electron-hole separation may also be enhanced through visible light excitation of the surface Plasmon resonance of Pt metals on TiO_2 [80]. Overall, it is suggested that these cooperative effects of Pt on TiO_2 contribute to the observed significant enhancement in TiO_2 photocatalytic activity under a combined illumination of visible and UV light.

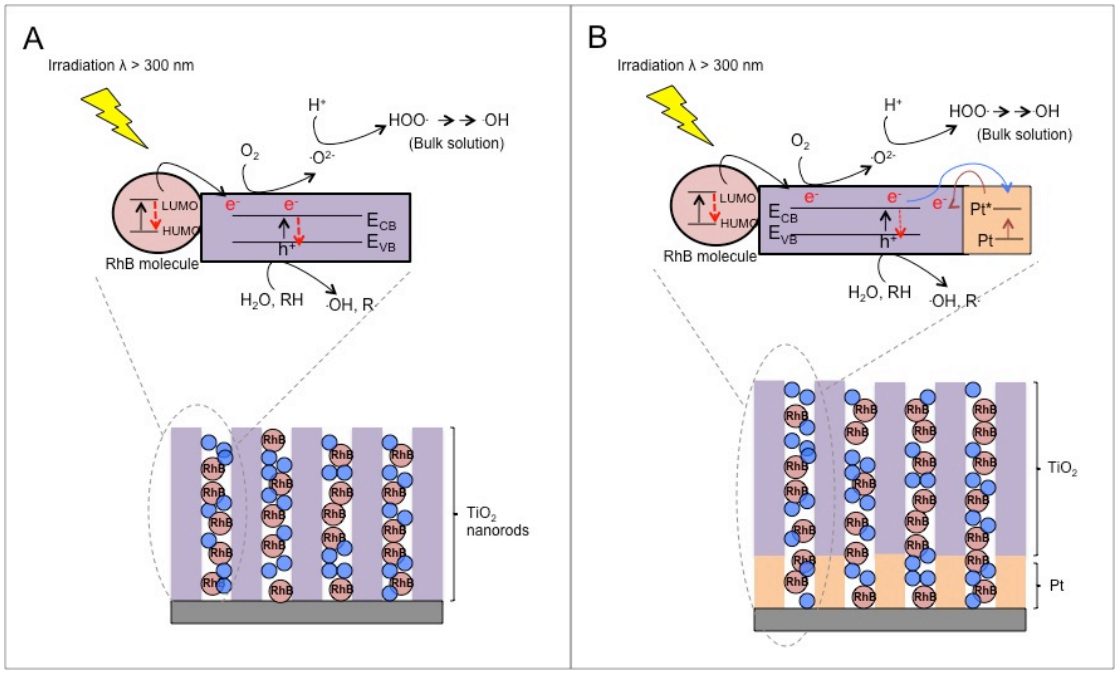

Figure 6-9. Schematic diagram of RhB degradation on A) TiO_2 nanorods and (B) bi-segmented Pt-TiO_2 nanorods under irradiation of λ > 300 nm. Enhanced RhB photodegradation on Pt-TiO_2 nanorods through electron-hole separation and surface electron excitation by visible light excitation of surface Plasmon resonance of Pt metals on TiO_2

6.4.3 Effects of TiO_2 Length Segment in Bi-segment Pt- TiO_2 Nanorods

As was discussed earlier in section 6.4.2, increasing the aspect ratio of TiO_2 photocatalyst through structural modification of bulk TiO_2 to nanostructural TiO_2 has shown advantages in the enhancement of TiO_2 photocatalytic activity. Since the aspect ratio of the TiO_2 photocatalyst plays a role in altering its photocatalytic activity, it is of interest, next, to see how varying the TiO_2 length segment of each bi-segmented Pt-TiO_2 nanorods may affect the photoactivity of the bi-segmented Pt-TiO_2 nanorods. Pt-TiO_2 nanorods were prepared by depositing Pt as the first layer and TiO_2 as the second layer, into the pores of the AAM. Each sample is presented as an array of bi-segmented Pt-TiO_2 nanorods free-standing on a layer of sputtered Ag material. Different samples of Pt-TiO_2 nanorods were produced by varying the TiO_2 length segments in the range of 1 to 31 μm, while keeping the length of the Pt segments constant at approximately 3 μm for all the samples. The rate of photodegradation of RhB on Pt-TiO_2 nanorod samples was carried out under visible and UV irradiation of $\lambda > 300$ nm and it is assumed that the photoactivity of the Pt segments alone are negligible.

Figure 6-10A shows the relationship between the TiO_2 length segment of bi-segmented Pt-TiO_2 nanorods and its effect on RhB degradation represented by the pseudo first-order reaction rate constant, *k* (derivation of k in appendix 6.1). As it is assumed that the concentration of other reactants are large compared to the concentration of RhB present in the sample solution and hence remain constant throughout the duration of experiment, the kinetics follow a pseudo first-order reaction with respect to only the concentration of RhB. The resultant plot in figure 6-10A is divided into three regions, denoted by I, II and III. In region I, the rate constant, *k*, increases as the length of the segment of TiO_2 increases from 0 μm (represented by just Pt nanorods) to approximately 3.5 μm. As the length of the segment of TiO_2 is increased further in region II, *k* starts to decrease, thereafter in region III, *k* plateaus at an approximately constant value for TiO_2 length segments greater than approximately 5.5 μm.

A schematic diagram shown in figure 6-10B proposes how the length of TiO_2 segments may affect the overall photoactivity of the Pt-TiO_2 nanorods. It is proposed that an 'addition effect' of light absorption and Pt/TiO_2 interface reaction contribute to the trend as observed in region I. In this region, a gradual increase in the TiO_2 segment length and hence TiO_2 surface area, is marked by an increase in TiO_2 photoactivity *via* higher photon absorption and higher surface adsorption of species. Additionally, there is sufficient light reaching the Pt/TiO_2 interface to further enhance photoactivity through the movement of photogenerated charge carriers across the TiO_2/Pt interface. The TiO_2 segment length of approximately 3.5 μm hence represents the optimal length

for which highest photoactivity of TiO_2 can be achieved from a combination of photon absorption and interface reactions.

Beyond region I, a further increase in the TiO_2 segment length in region II is characterized by a 'competition effect' which takes place between the light absorbed by TiO_2 and the amount of light reaching the TiO_2/Pt interface. Increasing the TiO_2 segment length within region II may be able to provide higher surface area for species adsorption and photon absorption, yet this also suggests less light reaching the TiO_2/Pt interface due to more light being absorbed by an increased amount of TiO_2 above the interface. Derived from Lambert's law of absorption, equation 6B provides an approximation of the value of TiO_2 absorption coefficient, which is calculated to be 2501 cm^{-1} based on an extinction coefficient value of 0.008 at a wavelength of 402 nm (provided for TiO_2 rutile single crystals) [81].

Derivative of the Lambert's law of absorption or Bouguer's Law:

$\alpha = 4\pi k/\lambda$ (Equation 6B)

where α is the absorption coefficient,

k is the extinction coefficient,

λ is the corresponding wavelength

From this, the reciprocal value of the absorption coefficient is calculated to be 4 μm, which represents the depth (χ) at which the energy of the light at 402 nm reduces exponentially by a factor of $e^{-\alpha}$. This value should only be taken as a reference, since in this work, the TiO_2 nanostructures are a mixed phase of TiO_2 anatase and rutile, and are polycrystalline in nature. It is suggested that the $1/\alpha$ value for the electrodeposited material in this study is approximately 3.5 μm, which is of the same order of magnitude as that reported in the literature for single crystal TiO_2 rutile.

Lastly in region III, it is proposed that the increment in the TiO_2 segment length of the Pt-TiO_2 nanorods beyond 5.5 μm does not result in further change in its photoactivity. This may firstly be due to the fact the same amount of light intensity is attenuated by the different TiO_2 length segments along the length of the nanorod (as absorption coefficient values are independent of the length of TiO_2 segments in the case for length segments of > 5.5 μm). Additionally, as the upper portion of the nanostructure absorbs the majority of the light, a 'shielding effect' arises from the longer length of the TiO_2 segments, resulting in little or no light through to both the

lower section and interface of the nanorods. It is then suggested that these nanorods have approximately the same effective photocatalytic surface area, and that the photoactivities of Pt-TiO_2 nanorods consisting of TiO_2 length segments of > 5.5 μm would be similar to that of a single-segment TiO_2 nanorod of the same length segment. This is evident from the *k* value of 0.029 ± 0.002 h^{-1} of a 6 μm single-segment TiO_2 nanorod, which corresponds well with the expected range of rate constant values of 0.008 to 0.023 h^{-1} obtained in figure 6-10A at TiO_2 length segment of 6 μm.

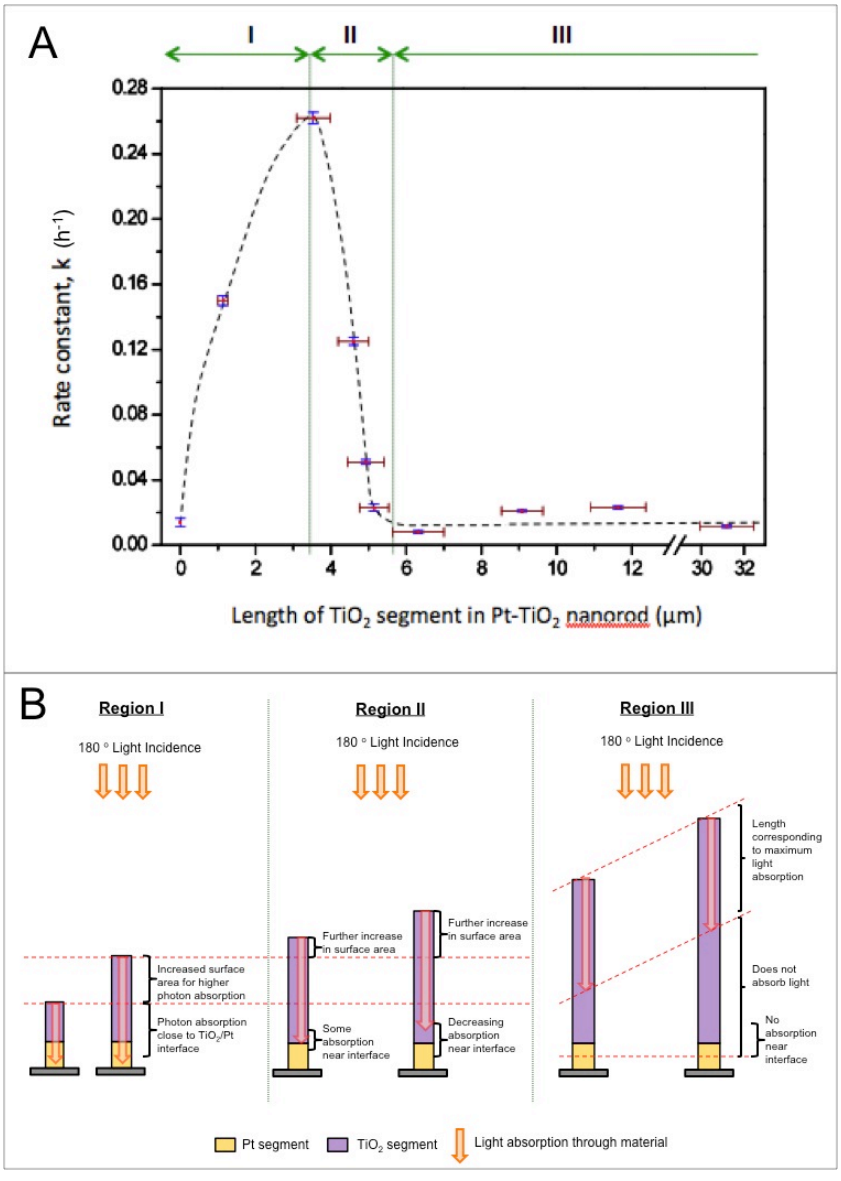

Figure 6-10. A) Plot showing the relationship between the length of TiO_2 segment in bi-segmented Pt-TiO_2 nanorods and its photocatalytic activity on RhB degradation indicated by the rate constant, k. The dotted curve serves as a guide to the eye. B) Schematic diagram illustrating the difference in light absorption and interface reactions in corresponding regions I, II and III

6.4.4 Enhancement of RhB Degradation With Increased Number of TiO_2-Pt Interfaces

Generally, the contact between TiO_2 and Pt segments, defined by the TiO_2/Pt interface, is known to be important in enhancing photocatalysis through the separation of photogenerated electrons and holes, and in prolonging their lifetime. To investigate the effect of the number of interfaces of TiO_2/Pt nanorods on its photoactivity, TiO_2/Pt nanorods with one segment (TiO_2), two segments (Pt-TiO_2) and three segments (TiO_2-Pt-TiO_2) were prepared. The total length of TiO_2 segments in each sample were kept approximately constant at 6 μm, so that any observable differences between photoactivities could be attributed to the number of TiO_2/Pt interfaces. Photocatalytic studies on RhB degradation were conducted under UV irradiation.

A comparison between the photodegradation of RhB in the presence of single TiO_2, two segmented (Pt-TiO_2) and three segmented (TiO_2-Pt-TiO_2) nanorods are as displayed in figure 6-11. Expectedly, the rate of RhB degradation increases in order of increasing number of TiO_2/Pt interfaces. According to the schematic diagram in figure 6-12, the enhancement of RhB degradation with increasing concentration of TiO_2/Pt interfaces may be attributed to a more efficient reduction in electron-hole recombination as electrons are transferred to the reactive sites on metallic Pt. This allows the holes to freely diffuse to the TiO_2 surface for oxidation reactions. Increasing the contact between TiO_2 and Pt thereby results in a higher efficiency of electron-hole separation, which in turn increases the available number of photogenerated electrons and holes for surface reactions.

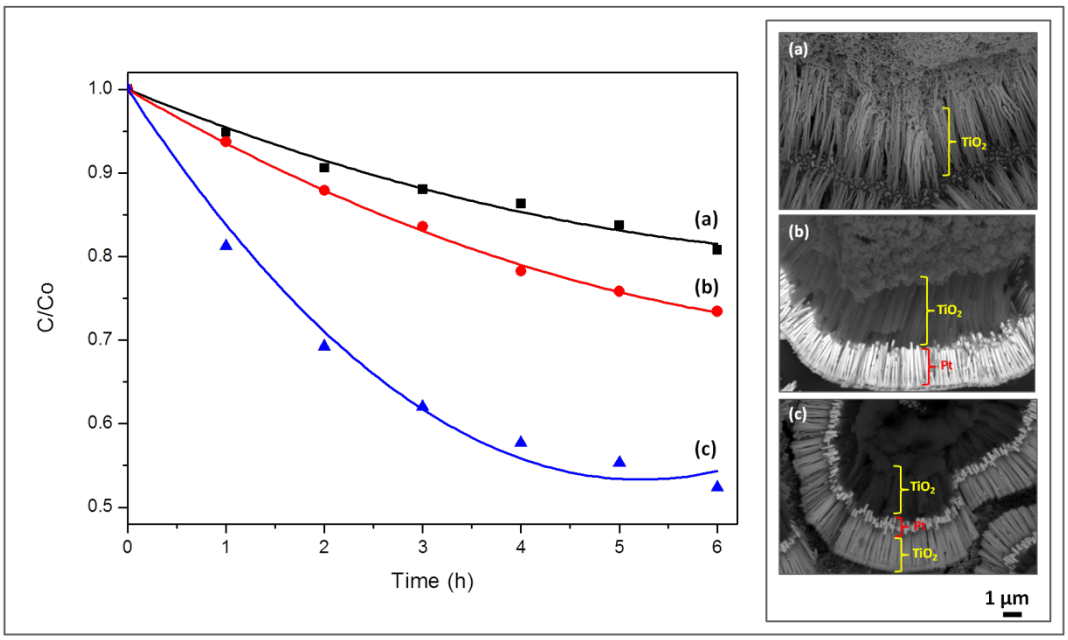

Figure 6-11. Plot reflecting the effect of a) TiO_2, b) Pt-TiO_2, and c) TiO_2-Pt-TiO_2 nanorods on RhB degradation rate under 6 h of continuous UV irradiation; SEM images (a), (b) and (c) shows corresponding nanostructures where the total length of TiO_2 segment are kept approximately constant

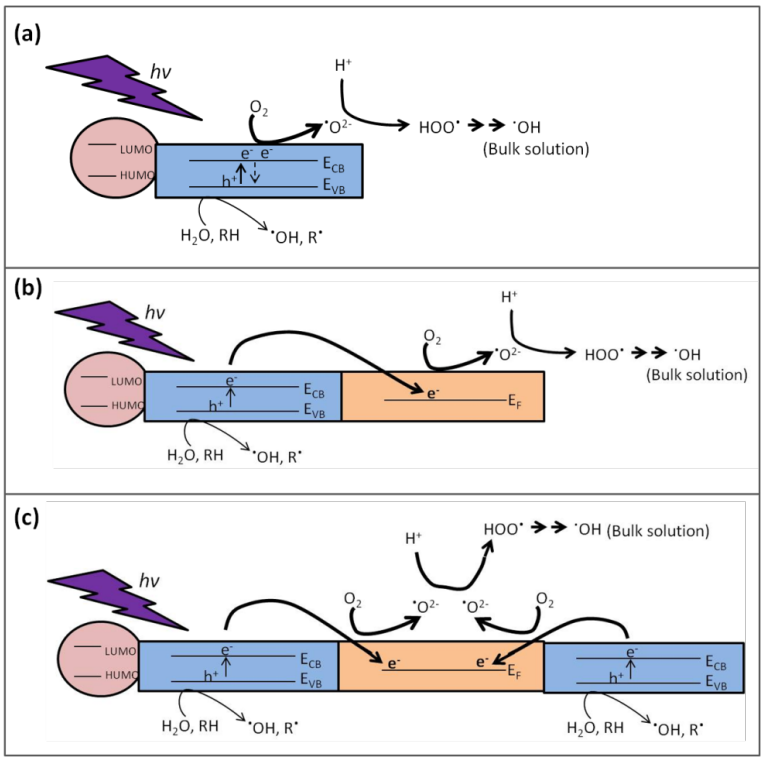

Figure 6-12. Schematic diagram of a) TiO_2, b) Pt-TiO_2, and c) TiO_2-Pt-TiO_2 nanorods illustrating the effect of increasing number of TiO_2/Pt interfaces on its photoactivity in RhB degradation

6.4.5 Effects of Orientation of 2 Segmented TiO_2-Pt Nanorods

As previously discussed in chapter 5 (sections 5.3.3.1.3 and 5.3.3.1.4), the integrity of the TiO_2/Pt interface is affected by the deposition order of material (TiO_2, Pt) into the AAM pores, whereby a sharper interface was achieved when TiO_2 is deposited as a second layer onto a first layer of Pt. Despite differences in the integrity of the TiO_2/Pt interface, the photoactivities of both the bi-segmented TiO_2/Pt nanorods shown in figure 6-13A does not differ significantly. A detailed comparison of the photoactivities of TiO_2-Pt and Pt-TiO_2 nanorods indicates a slightly higher rate constant of 0.053±0.003 h^{-1} for Pt-TiO_2 nanorods than in TiO_2-Pt nanorods (k=0.038±0.002 h^{-1}).

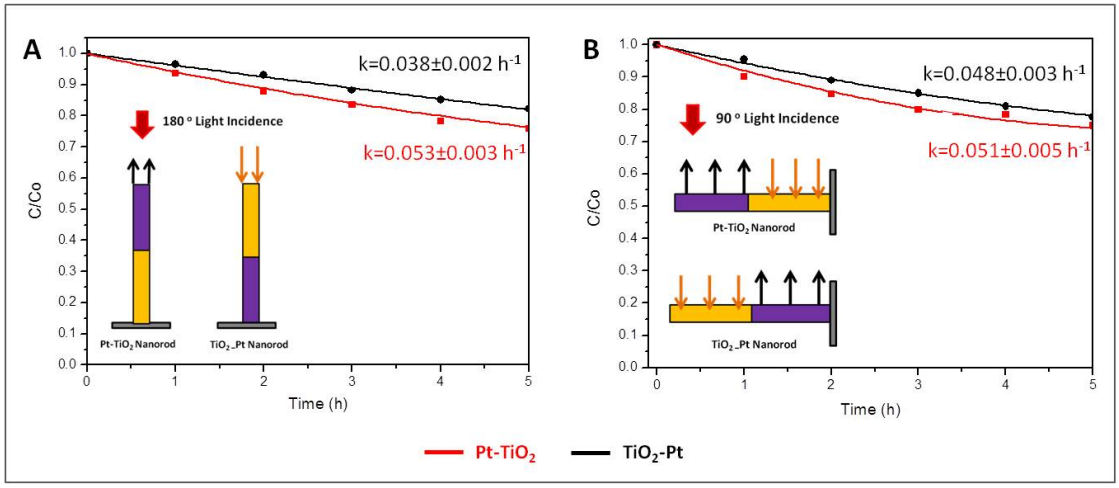

Figure 6-13. Rhodamine degradation on Pt-TiO_2 and TiO_2-Pt bi-segmented nanorods under UV irradiation at A) 180 ^{o} light incidence and B) 90 ^{o} light incidence. Insets show schematic illustration of nanorod orientation to light source.

There are two possibilities to explain why the photoactivity of Pt-TiO_2 bi-segmented TiO_2 nanorods appears slightly higher than that of TiO_2-Pt bi-segmented nanorods. The first possibility may be attributed to a difference between the interfaces of Pt-TiO_2 bi-segmented and TiO_2-Pt bi-segmented nanorods. The less well defined materals interface of TiO_2-Pt bi-segmented nanorods may suggest a higher occurrence of electron-hole recombination as a result of some Pt within the TiO_2 segments. In contrast to this, Pt-TiO_2 bi-segmented nanorod consisting of a sharper interface and minimal diffusion of Pt within the TiO_2 segments would favour a better separation of the photogenerated electrons and holes.

Secondly, the orientation of bi-segment nanorods to the incident light could have played a role. Integrating sphere measurements were performed separately on the same samples of arrays of Pt-TiO_2 and TiO_2-Pt bi-segmented nanorods in order to investigate the effect of sample

orientation to the light source. The two samples were aligned at 180 ^{o} to the incident light source in the integrating sphere as indicated in figure 6-13A (inset), which is similar to the configuration used in the absorption studies. The reflectance measurements in figure 6-15 indicates that the relative % reflectance of Pt-TiO_2 bi-segmented nanorods is approximately twice that of TiO_2-Pt bi-segmented nanorods in the wavelength range of 300 nm to 800 nm. Expectedly, this findings are in agreement with the physical appearances of samples consisting of an array of Pt-TiO_2 nanorods and an array of TiO_2-Pt nanorods, which appears to be white (indicating higher reflectance) and black (indicating lower reflectance) respectively to the naked eyes.

When the light beam comes into contact with the sample within an integrating sphere, the beam may be considered to be reflected, transmitted and absorbed according to equation 6C.

100% = % Reflectance + % Transmittance + % Absorbance (Equation 6C)

Since % transmission for both samples are very low (< 5%) as shown in figure 6-15B, it is assumed that the light transmission through the bi-segmented nanorods is almost negligible. This may therefore suggest that a lower % reflectance is indicative of a higher % absorption. From this, it is proposed that in the case of of TiO_2-Pt bi-segmented nanorods, a higher proportion of light is absorbed by the upper Pt segment such that very little light reaches the lower TiO_2 segment. Conversely, having greater exposure to the light, the upper TiO_2 segments of Pt-TiO_2 nanorods will therefore have higher photo-activation under irradiation. It should be noted that even though the % reflectance of Pt-TiO_2 nanorods is higher than that of TiO_2-Pt nanorods, the low % reflectance values of < 15 % indicates an overall low reflectance of the sample, hence suggesting that the light absorption of the upper TiO_2 segment of Pt-TiO_2 bi-segment is still relatively high. Based on all these, the overall photoactivity of Pt-TiO_2 bi-segment nanorods appears to be higher than that of TiO_2-Pt bi-segmented nanorods.

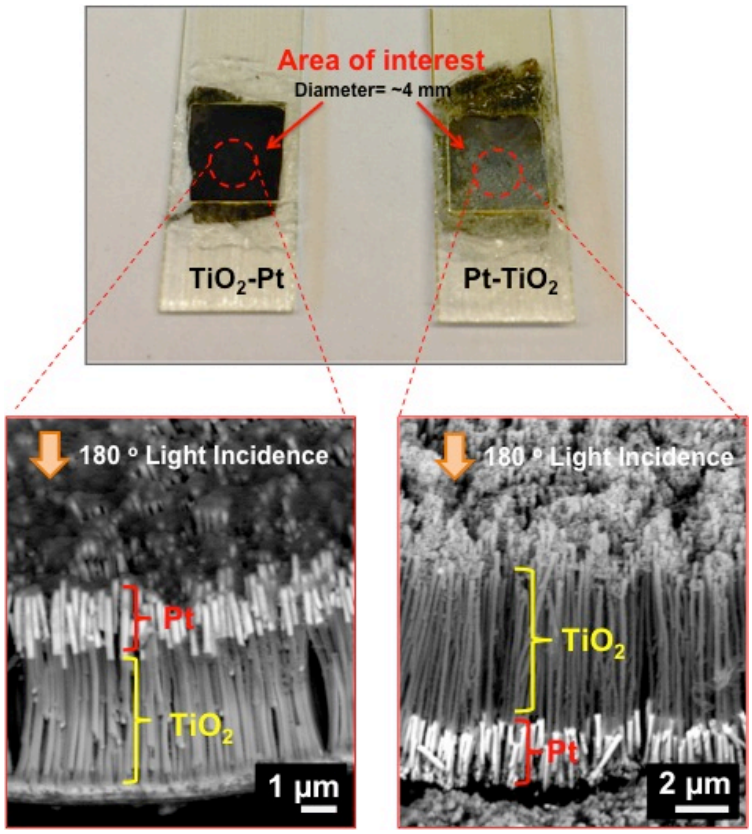

Figure 6-14. Mounted samples consisting of an array of TiO_2-Pt and Pt-TiO_2 freestanding nanorods used for integrating sphere measurements. Angle of light is incident on the nanorods at 180 ^{o}, similar to that in absorption studies.

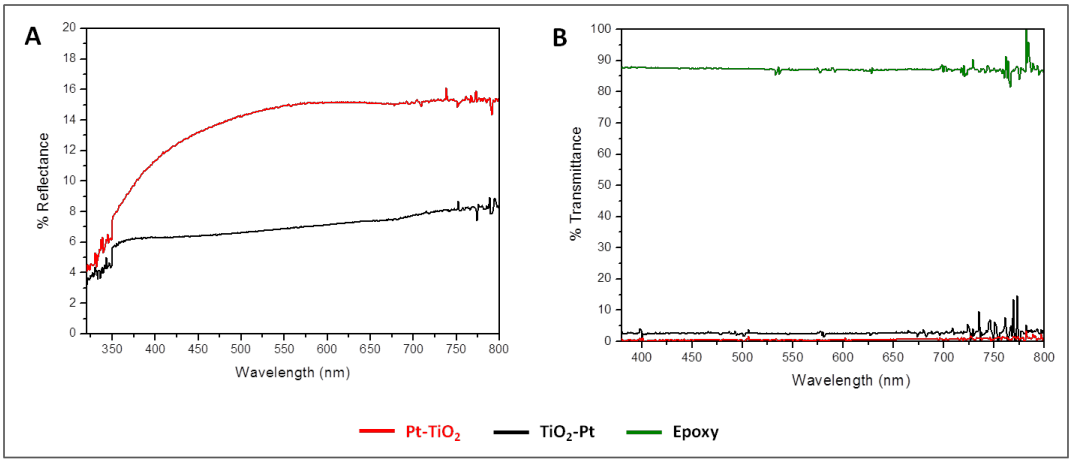

Figure 6-15. Integrating sphere measurements of A) % reflectance and B) % transmittance of samples consisting of TiO_2-Pt and Pt-TiO_2 bi-segmented nanorods. % Transmittance measurements taken against a standard consisting of only epoxy (used as a support for TiO_2/Pt bi-segmented nanorods)

In another set of experiment, the same two samples consisting of Pt-TiO_2 and TiO_2-Pt bi-segmented nanorods were angled at 90 ^{o} to the light as shown in figure 6-13B. Ideally, by comparing between the two setups in which the bi-segmented nanorods are angled at 180 ^{o} and 90 ^{o} to the light source, the latter setup would have both Pt-TiO_2 and TiO_2-Pt bi-segmented nanorods possess similar photoactivities since the total surface area of the material exposed to light are the same for both samples. This would be true if the chemical compositions of the TiO_2 and Pt segments are the same for both Pt-TiO_2 and TiO_2-Pt bi-segmented nanorods. However, since the chemical compositions of the TiO_2 segments are clearly different (owing to Pt diffusion into TiO_2 segments of TiO_2-Pt nanorods), the observable contrast between the photoactivities of the Pt-TiO_2 bi-segmented and TiO_2-Pt bi-segmented nanorods may hence be attributed to the differences between their interfaces. In figure 6-13B, a small difference is seen between the photoactivities of Pt-TiO_2 and TiO_2-Pt bi-segmented nanorods, in which their respective first order rate constants are 0.051 ± 0.005 h^{-1} and 0.048 ± 0.003 h^{-}. Therefore by assuming that the surface areas of both samples are equally exposed to light, it is concluded that the effect of the Pt-diffused TiO_2 segment on the photoactivity of TiO_2/Pt bi-segmented nanorods is hardly significant.

6.5 Conclusion

The employment of a simple photodegradation system of RhB under visible and UV illumination and the comparison between photo-absorptions of various highly ordered 1D striped nanorods of TiO_2/Pt have revealed several pertinent characteristics of the photoactivities of the TiO_2/Pt nanostructures. Compared to the bulk structure of TiO_2, an array of TiO_2 nanorods have shown to exhibit a higher photocatalytic effect on RhB degradation. The addition of a Pt segment to the TiO_2 nanorods further increased the photoactivity of TiO_2, demonstrating the advantages of noble metals as an electron sink to facilitate electron-hole separation and prolong the lifetime of electron-hole pairs. Enhanced photodegradation of RhB was also reflected in the increase in the number of TiO_2/Pt interfaces, which represents important active sites for TiO_2/Pt photocatalysis.

Besides these, an interesting trend in the photoactivities of TiO_2/Pt nanorods were observed as the TiO_2 length segments of Pt-TiO_2 nanorods were varied. Three different regions with distinct characteristics were proposed, in which were described as the ‘addition effect’, ‘competition effect’ and ‘shielding effect’. This experiment reveals the interplay between light absorption and the amount of light reaching the TiO_2/Pt interface. Additionally, differences in the orientation of bi-segmented TiO_2/Pt nanorods to the light source were presented, which may serve as a useful guide for any future work involving the investigation on photoactivities of nanostructure arrays

6.6 References

[1] H. Tang, K. Prasad R. Sanjinès, P. E. Schmid, and F. Lévy, Electrical and optical properties of TiO_2 anatase thin films, J. Appl. Phys., 75 (1994) 2042-2047.

[2] A. L. Linsebigler, and G. Lu J. T. Yates, Photocatalysis on TiO_2 Surfaces: Principles, Mechanisms, and Selected Results, Chem. Rev., 95 (1995) 735–758.

[3] H. Kisch, Semiconductor Photocatalysis for Organic Synthesis, John Wiley & Sons, Inc, 2007.

[4] A. J. Bard and M. S. Wrighton, Thermodynamic Potential for the Anodic Dissolution of n-Type Semiconductors: A Crucial Factor Controlling Durability and Efficiency in Photoelectrochemical Cells and an Important Criterion in the Selection of New Electrode/Electrolyte Systems, J. Electrochem. Soc., 124 (1977) 1706-1710.

[5] H. Gerischer, On the stability of semiconductor electrodes against photodecomposition, J. Electroanal. Chem., 82 (1977) 133–143.

[6] A. J. Bard, A. B. Bocarsly, F.-R. F. Fan, E. G. Walton, and M. S. Wrighton, The Concept of Fermi Level Pinning at Semiconductor/Liquid Junctions. Consequences for Energy Conversion Efficiency and Selection of Useful Solution Redox Couples in Solar Devices, J. Am. Chem. Soc., 102 (1980) 3671-3676.

[7] A. Cremades and J. Piqueras R. Plugaru, The effect of annealing in different atmospheres on the luminescence of polycrystalline TiO_2, J. Phys.: Condens. Matter, 16 (2004) S261–S268.

[8] A. T. Paxton and L. Thien-Nga, Electronic structure of reduced titanium dioxide, Phys. Rev. B, 57 (1998) 1579-1584.

[9] P. J. D. Lindan and N. M. Harrison, Mixed Dissociative and Molecular Adsorption of Water on the Rutile (110) Surface, Phys. Rev. Lett., 80 (1998) 762-765.

[10] J.M. Pan, B. L. Maschhoff, U. Diebold, and T. E. Madey, Interaction of water, oxygen, and hydrogen with TiO_2(110) surfaces having different defect densities, JVST A 10 (1992) 2470-2476.

[11] M. B. Hugenschmidt, L. Gamble and C. T Campbell, The interaction of H2O with a TiO_2(110) surface, Surf. Sci., 302 (1994) 329–340.

[12] W. Göpel, Surface defects of TiO_2(110): A combined XPS, XAES AND ELS study, Surf. Sci., 139 (1984) 333–346.

[13] M. Addamo, M. Bellardita, A. D. Paolaa and L. Palmisano, Preparation and photoactivity of nanostructured anatase, rutile and brookite TiO_2 thin films, Chem. Commun., 47 (2006) 4943-4945.

[14] B. Ohtani, Y. Ogawa and S. Nishimoto, Photocatalytic Activity of Amorphous-Anatase Mixture of Titanium(IV) Oxide Particles Suspended in Aqueous Solutions, J. Phys. Chem. B, 101 (1997) 3746-3752.

[15] Y. Li, T. Sasaki, Y. Shimizu, and N. Koshizaki, Hexagonal-Close-Packed, Hierarchical Amorphous TiO_2 Nanocolumn Arrays: Transferability, Enhanced Photocatalytic Activity, and Superamphiphilicity without UV Irradiation, J. Am. Chem. Soc., 130 (2008) 14755–14762.

[16] S. Nakade, Y. Saito, W. Kubo, T. Kitamura, Y. Wada, and S. Yanagida, Influence of TiO_2 Nanoparticle Size on Electron Diffusion and Recombination in Dye-Sensitized TiO_2 Solar Cells, J. Phys. Chem. B, 107 (2003) 8607-8611.

[17] S.-K. Kim and S.-J. Kim H. D. Jang, Effect of particle size and phase composition of titanium dioxide nanoparticles on the photocatalytic properties, J. Nanopart. Res., 3 (2001) 141–147.

[18] K. D. Benkstein, N. Kopidakis, J. van de Lagemaat, and A. J. Frank, Influence of the Percolation Network Geometry on Electron Transport in Dye-Sensitized Titanium Dioxide Solar Cells, J. Phys. Chem. B, 107 (2003) 7759-7767.

[19] M. Takeuchi, K. Sakamoto, G. Martra, S. Coluccia, and M. Anpo, Mechanism of Photoinduced Superhydrophilicity on the TiO_2 Photocatalyst Surface, J. Phys. Chem. B, 109 (2005) 15422-15428.

[20] Z. Ding, G. Q. Lu and P. F. Greenfield, Role of the Crystallite Phase of TiO_2 in Heterogeneous Photocatalysis for Phenol Oxidation in Water, J. Phys. Chem. B, 104 (2000) 4815-4820.

[21] C. B. Almquist and P. Biswas, Role of Synthesis Method and Particle Size of Nanostructured TiO_2 on Its Photoactivity, J. Catal., 212 (2002) 145–156.

[22] G. R. Bamwenda, S. Tsubota T. Nakamura and M. Haruta, The influence of the preparation methods on the catalytic activity of platinum and gold supported on TiO_2 for CO oxidation, Catal. Lett., 44 (1997) 83-87.

[23] S.Yurdakal, G. Palmisano V. Loddo, V. Augugliaro, and L. Palmisano, Nanostructured Rutile TiO_2 for Selective Photocatalytic Oxidation of Aromatic Alcohols to Aldehydes in Water, J. Am. Chem. Soc., 130 (2008) 1568-1569.

[24] T. Kawahara, Y. Konishi, H. Tada, N. Tohge, J. Nishii, and S. Ito, A Patterned TiO_2(Anatase)/ TiO_2(Rutile) Bilayer-Type Photocatalyst: Effect of the Anatase Rutile Junction on the Photocatalytic Activity, Angew. Chem., 114 (2000) 2935-2937.

[25] D. C. Hurum, A. G. Agrios and K. A. Gray, Explaining the Enhanced Photocatalytic Activity of Degussa P25 Mixed-Phase TiO_2 Using EPR, J. Phys. Chem. B, 107 (2003) 4545-4549.

[26] J. Zhang, Q. Xu, Z. Feng, M. Li and C. Li Importance of the Relationship between Surface Phases and Photocatalytic Activity of TiO_2, Angew. Chem. Int. Ed., 47 (2008) 1766 –1769.

[27] N. Xu, Z. Shi Y. Fan, J. Dong, J. Shi, and M. Z.-C. Hu, Effects of Particle Size of TiO_2 on Photocatalytic Degradation of Methylene Blue in Aqueous Suspensions, Ind. Eng. Chem. Res., 38 (1999) 373-379.

[28] M. Anpo, T. Shima, S. Kodama, and Y. Kubokawa, Photocatalytic hydrogenation of propyne with water on small-particle titania: size quantization effects and reaction intermediates, J. Phys. Chem. B, 91 (1987) 4305-4310.

[29] Z. Zhang, C.-C. Wang, R. Zakaria, and J. Y. Ying, Role of Particle Size in Nanocrystalline TiO_2-Based Photocatalysts, J. Phys. Chem. B 102 (1998) 10871-10878.

[30] N. Serpone and D. Lawless, Spectroscopic,Photoconductivity,and Photocatalytic Studies of TiO_2 Colloids: Naked and with the Lattice Doped with Cr^{3+}, Fe^{3+}, and V^{5+} Cations, Langmuir, 10 (1994) 643-652.

[31] G. Rothenberger, J. Moser, M. Gratzel, N. Serpone, and D. K. Sharma, Charge Carrier Trapping and Recombination Dynamics in Small Semiconductor Particles, J. Am. Chem. Soc., 107 (1985) 8054-8059.

[32] K. Zhu, T. B. Vinzant, N. R. Neale, and A. J. Frank, Removing Structural Disorder from Oriented TiO_2 Nanotube Arrays: Reducing the Dimensionality of Transport and Recombination in Dye-Sensitized Solar Cells, Nano Lett., 7 (2007) 3739-3746.

[33] L. Forro, O. Chauvet, D. Emin, L. Zuppiroli, H. Berger and F. Lévy, High mobility n-type charge carriers in large single crystals of anatase (TiO_2), J. Appl. Phys., 75 (1994) 633.

[34] A. A. Nadaa, M. H. Barakat, H. A. Hamed, N. R. Mohamed, T. N. Veziroglu, Studies on the photocatalytic hydrogen production using suspended modified TiO_2 photocatalysts, Int. J. Hydrogen Energy, 30 (2005) 687–691.

[35] K. Sayama and H. Arakawa, Significant effect of carbonate addition on stoichiometric photodecomposition of liquid water into hydrogen and oxygen from platinum–titanium(IV) oxide suspension, J. Chem. Soc., Chem. Commun., (1992) 150-152.

[36] H. Kominami, A. Furusho, S. Murakami, H. Inoue, Y. Kera and B. Ohtani, Effective photocatalytic reduction of nitrate to ammonia in an aqueous suspension of metal-loaded titanium(IV) oxide particles in the presence of oxalic acid, Catal. Lett., 76 (2001) 31-34.

[37] B. K. Vijayan, N. M. Dimitrijevic, J. Wu, and K. A. Gray, The Effects of Pt Doping on the Structure and Visible Light Photoactivity of Titania Nanotubes, J. Phys. Chem. C, 114 (2010) 21262–21269.

[38] W. Choi, A. Termin and M. R. Hoffmann, The Role of Metal Ion Dopants in Quantum-Sized TiO_2: Correlation between Photoreactivity and Charge Carrier Recombination Dynamics, J. Phys. Chem. B, 98 (1994) 13669-13679.

[39] G. Wu, T. Nishikawa, B. Ohtani, and A. Chen, Synthesis and Characterization of Carbon-Doped TiO_2 Nanostructures with Enhanced Visible Light Response, Chem. Mater., 19 (2007) 4530-4537.

[40] S. Liu, L. Yang, S. Xu, S. Luo, Q. Cai, Photocatalytic activities of C–N-doped TiO_2 nanotube array/carbon nanorod composite, Electrochem. Commun., 11 (2009) 1748–1751.

[41] Z. Wu, F. Dong, W. Zhao, H. Wang, Y. Liu and B. Guan, The fabrication and characterization of novel carbon doped TiO_2 nanotubes, nanowires and nanorods with high visible light photocatalytic activity, Nanotechnology, 20 (2009) 235701-235710.

[42] E. Bae and W. Choi, Highly Enhanced Photoreductive Degradation of Perchlorinated Compounds on Dye-Sensitized Metal/TiO_2 under Visible Light, Environ. Sci. Technol., 37 (2003) 147-152.

[43] J. Wang and Z. Lin, Dye-Sensitized TiO_2 Nanotube Solar Cells with Markedly Enhanced Performance via Rational Surface Engineering, Chem. Mater. , 22 (2010) 579–584.

[44] S. Sakthivel, M. V. Shankar M. Palanichamy, Banumathi Arabindoo, D. W. Bahnemann, V. Murugesan, Enhancement of photocatalytic activity by metal deposition: characterisation and photonic efficiency of Pt, Au and Pd deposited on TiO_2 catalyst, Water Res., 38 (2004) 3001–3008.

[45] V. Subramanian, E. E. Wolf, and P. V. Kamat, Catalysis with TiO_2/ Gold Nanocomposites. Effect of Metal Particle Size on the Fermi Level Equilibration, J. Am. Chem. Soc., 126 (2004) 4943-4950.

[46] H.-J. Choi, and M. Kang. Hydrogen production from methanol/water decomposition in a liquid photosystem using the anatase structure of Cu loaded TiO_2, Int. J. Hydrogen Energy, 32 (2007) 3841–3848.

[47] J. Yu and J. Ran, Facile preparation and enhanced photocatalytic H_2-production activity of $Cu(OH)_2$ cluster modified TiO_2, Energy Environ. Sci., (2011) 1364-1371.

[48] J. M. White S. Sato, Photodecomposition of water over Pt/TiO_2 catalysts, Chem. Phys. Lett., 72 (1980) 83–86.

[49] A. J. Bard and B. Kraeutler, Heterogeneous Photocatalytic Preparation of Supported Catalysts. Photodeposition of Platinum on TiO_2 Powder and Other Substrates, J. Am. Chem. Soc., 100 (1978) 4317-4318.

[50] J. Lee and W. Choi J. Kim, Synergic effect of simultaneous fluorination and platinization of TiO_2 surface on anoxic photocatalytic degradation of organic compounds, Chem. Commun., (2008) 756–758.

[51] X. Z. Li and F. B. Li, Study of Au/Au^{3+}-TiO_2 Photocatalysts toward Visible Photooxidation for Water and Wastewater Treatment, Environ. Sci. Technol., 35 (2001) 2381-2387.

[52] B. Yang C. Ren, M. Wu, J. Xu, Z. Fu, Yan lv, T. Guo, Y. Zhao, C. Zhu, Synthesis of Ag/ZnO nanorods array with enhanced photocatalytic performance, J. Hazard. Mater., 182 (2010) Journal of Hazardous Materials.

[53] S. Gao W. Lu, and J. Wang, One-Pot Synthesis of Ag/ZnO Self-Assembled 3D Hollow Microspheres with Enhanced Photocatalytic Performance, J. Phys. Chem. C, 112 (2008) 16792–16800.

[54] D. C. Northrop and E. H. Rhcderick, Variable Independence Devices, Wiley, New York, 1978.

[55] A. Yamakata, T. Ishibashi and H. Onishi, Water- and Oxygen-Induced Decay Kinetics of Photogenerated Electrons in TiO_2 and Time-Resolved Infrared Absorption Study, J. Phys. Chem. B, 105 (2001) 7258-7262.

[56] K. Iwata, T. Takaya, H. Hamaguchi, A. Yamakata, T. Ishibashi, H. Onishi, and H. Kuroda, Carrier Dynamics in TiO_2 and Pt/TiO_2 Powders Observed by Femtosecond Time-Resolved Near-Infrared Spectroscopy at a Spectral Region of 0.9-1.5 μm with the Direct Absorption Method, J. Phys. Chem. B, 108 (2004) 20233-20239.

[57] J. Bardeen, Surface States and Rectification at a Metal Semi-Conductor Contact, Phys. Rev., 71 (1947) 717-727.

[58] J. S. Curran and D. Lamouche, Transport and kinetics in photoelectrolysis by semiconductor particles in suspension, J. Phys. Chem. B, 87 (1983) 5405–5411.

[59] A. Wood, M. Giersig and P. Mulvaney Fermi Level Equilibration in Quantum Dot−Metal Nanojunctions, J. Phys. Chem. B, 105 (2001) 8810–8815.

[60] T. Hurlen and S. Hornkjøl, Anodic growth of passive films on titanium, Electrochim. Acta, 36 (1991) 189–195.

[61] D. J. Blackwood and L. M. Peter The influence of growth rate on the properties of anodic oxide films on titanium, Electrochim. Acta, 34 (1989) 1505–1511.

[62] M. Pujadas and P. Salvador, EER and Photocurrent Transient Investigation of the Photoassisted Evolution of Hydrogen at an Electroplatinized TiO_2 Single Crystal Implications to Water Splitting at an Electroplatinized TiO_2 single crystal J. Electrochem. Soc., 136 (1989) 716-723.

[63] J. J.Yang, M. D. Pickett, X. Li, D. A. A. Ohlberg, D. R. Stewart, and R. S. Williams, Memristive switching mechanism for metal/oxide/metal nanodevices, Nature Nanotechnology, 3 (2008) 429-433.

[64] R. Konenkamp, Carrier transport in nanoporous TiO_2 films, Phys. Rev. B, 61 (2000) 11057-11063.

[65] S. X. Wu, L. M. Xu, X. J. Xing, S. M. Chen, Y. B. Yuan, Y. J. Liu, Y. P. Yu, X. Y. Li, and S. W. Li, Reverse-bias-induced bipolar resistance switching in Pt/ TiO_2/ $SrTi_{0.99}Nb_{0.01}O_3$/ Pt devices, Appl. Phys. Lett., 93 (2008) 43502.

[66] H.Kim, D.-W. Kim and S.-H. Phark, Transport behaviours and nanoscopic resistance profiles of electrically stressed Pt/TiO_2/Ti planar junctions, J. Phys. D: Appl. Phys., 43 (2010) 505305.

[67] N. Braslau, Alloyed ohmic contacts to GaAs, J. Vac. Sci. Technol., 19 (1981) 803-807.

[68] W. Zhao, C. Chen X. Li, and J. Zhao, Photodegradation of Sulforhodamine-B Dye in Platinized Titania Dispersions under Visible Light Irradiation: Influence of Platinum as a Functional Co-catalyst, J. Phys. Chem. B, 106 (2002) 5022-5028.

[69] J. Lee and W. Choi, Photocatalytic Reactivity of Surface Platinized TiO_2: Substrate Specificity and the Effect of Pt Oxidation State, J. Phys. Chem. B, 109 (2005) 7399-7406.

[70] S. Nishimoto, B. Ohtani, H. Shirai and T. Kagiya, Photolysis of Aqueous Poly(vinyl Alcohol) Solution by Heterogeneous TiO_2/Pt Catalyst, J. Polymer Sci. C Polymer Lett. , 23 (1985) 141–145.

[71] S. Kim and W. Choi, Dual Photocatalytic Pathways of Trichloroacetate Degradation on TiO_2: Effects of Nanosized Platinum Deposits on Kinetics and Mechanism, J. Phys. Chem. B, 106 (2002) 13311-13317.

[72] F. B. Li and X. Z. Li, The enhancement of photodegradation efficiency using Pt–TiO_2 catalyst, Chemosphere 48 (2002) 1103–1111.

[73] Y. Li, G. Lu, and S. Li, Photocatalytic transformation of rhodamine B and its effect on hydrogen evolution over Pt -TiO_2 in the presence of electron donors, J. Photochem. Photobiol. A, 152 (2002) 219–228.

[74] N. Zhang, S. Liu, X. Fu, and Y.-J. Xu, Synthesis of M@TiO_2 (M = Au, Pd, Pt) Core Shell Nanocomposites with Tunable Photoreactivity, J. Phys. Chem. C, 115 (2011) 9136–9145.

[75] H. Chen, S. Chen, X. Quan, H. Yu, H. Zhao, and Y. Zhang, Fabrication of TiO_2-Pt Coaxial Nanotube Array Schottky Structures for Enhanced Photocatalytic Degradation of Phenol in Aqueous Solution, J. Phys. Chem. C, 112 (2008) 9285–9290.

[76] V. F. Stone, Jr. and R. J. Davis Synthesis, Characterization, and Photocatalytic Activity of Titania and Niobia Mesoporous Molecular Sieves, Chem. Mater. , 10 (1998) 1468-1474.

[77] D. P. Colombo Jr. and R. M. Bowman, Femtosecond Diffuse Reflectance Spectroscopy of $Ti0_2$ Powders, J. Phys. Chem. B, 99 (1995) 11752- 11756.

[78] D. P. Colombo Jr., K. A. Roussel, J. Saeh, D. E. Skinner, J. J. Cavaleri, R. M. Bowman, Femtosecond study of the intensity dependence of electron-hole dynamics in TiO_2 nanoclusters, Chem. Phys. Lett., 232 (1995) 207-214.

[79] B. M. Kayes, H. A. Atwater and N. S. Lewis, Comparison of the device physics principles of planar and radial p-n junction nanorod solar cells, J. Appl. Phys., 97 (2005) 114302.

[80] W. Zhai, S. Xue, A. Zhu, Y. Luo, and Y. Tian, Plasmon-Driven Selective Oxidation of Aromatic Alcohols to Aldehydes in Water with Recyclable Pt/TiO_2 Nanocomposites, ChemCatChem, 3 (2011) 127 – 130.

[81] E. D. Palik, Handbook of Optical Constants of Solids, Elsevier, United States of America, 1998.

Chapter 7: Conclusion

7.1. Thesis Conclusion

In this thesis, the aim of fabricating water-splitting materials consisting of multi-component nanorods of TiO_2 and Pt had been achieved by employing templated electrodeposition into AAM. This method facilitates the preparation of ordered arrays of multisegmented nanorods with control in size and composition. Through stepwise development of the protocols on the synthesis of Pt nanorods and TiO_2 nanorods via templated electrodeposition, highly-ordered 1D multi-segmented TiO_2/Pt nanostructures were successfully prepared and reported for the first time.

In the process of developing a protocol for the templated electrodeposition of TiO_2, two different Ti precursors, $TiOSO_4$ and $TiCl_3$ were employed. TiO_2 nanorods were successfully fabricated from $TiOSO_4$ precursor at a low potential -1.2 V (vs. 3 M Ag/AgCl), but difficulty was experienced in using this precursor to deposit on Pt due to hydrogen evolution; while lowering the potentiostatic voltages resulted in the growth of TiO_2 nanotubes. For the first time, detailed mechanisms of the respective growth of TiO_2 nanorods and nanotubes from $TiOSO_4$ were reported; in which the high regeneration of NO_3- species occurring at more negative deposition voltages was the differentiating factor to the formation of TiO_2 nanorods and nanotubes.

The electrodeposition mechanism by which TiO_2 is formed from $TiOSO_4$ and $TiCl_3$ differs greatly. Despite the use of both precursors in successfully fabricating highly ordered TiO_2 nanorods, $TiCl_3$ precursor was a more suitable precursor for the fabrication of multi-segmented TiO_2/Pt nanorods because it involved a higher deposition voltage that would facilitate the deposition of TiO_2 on Pt. A protocol for the electrodeposition of TiO_2 nanorods at a low deposition voltage of -0.1 V (vs. 3 M Ag/AgCl) from $TiCl_3$ precursor was established, enabling the synthesize TiO_2 nanostructures from a stable $TiCl_3$ solution prepared under normal ambient conditions, hence provides the flexibility and ease for $TiCl_3$ (which is highly sensitive to moisture and air) to be handled even without an argon or nitrogen environment.

An important application of the multi-segmented TiO_2/Pt nanorods in water-splitting materials was explored through photo-absorption studies *via* a classic photodegradation system of RhB under visible and UV light. Reported for the first time, these studies reveal several pertinent characteristics of the photoactivities of the TiO_2/Pt nanostructures, where the nanostructural morphology, addition of Pt metal and TiO_2/Pt interfaces had positive enhancements in TiO_2 photoactivity. Additionally, the interplay between light absorption and the amount of light reaching the TiO_2/Pt interface was revealed through

the effects of varying TiO_2 length segments of Pt-TiO_2 nanorods on the photoactivities of TiO_2/Pt nanorods.

With the ability to customize TiO_2/Pt length segments and reproduce TiO_2/Pt interfaces, photocatalytic activity of 1D TiO_2/Pt nanostructures can be conveniently manipulated and effectively evaluated against parameters such as the length segments, structural integrity and number of TiO_2/Pt pair sites. Overall, the development of these 1D multi-segmented TiO_2/Pt nanostructures offers great potential as materials for the enhancement of catalytic activities and as incorporation into water-splitting devices. Beyond this, an equally compelling opportunity lie in the use of these TiO_2/Pt novel nanostructures for nano-scale electronics and photonics, magnetic and electronic building blocks, and bio-sensing applications.

7.2. Future Directions

In this research, the fabrication protocol of the multi-segmented TiO_2/Pt nanostructures is at its infant stage, suggesting that there lie great opportunities for further understanding, improvement and development of the multi-segmented TiO_2/Pt nanostructures used for water-splitting.

At the nanoscale, several improvements may be made to the integrity of the TiO_2/Pt nanostructures. Presently, a diffuse TiO_2-Pt interface has been achieved due to the slightly porous nature of the TiO_2 nanorod, which allowed the infiltration of some Pt into the TiO_2 nanostructure. Further understanding of the growth of TiO_2 "particles" in the AAM may allow development of ways to increase the density of the TiO_2 nanorods so as to achieve a sharper TiO_2-Pt interface, thereby increasing the consistency of TiO_2-Pt and Pt-TiO_2 interfaces along the length of each multi-segmented TiO_2/Pt nanorod.

Besides this, the architecture of the nanorod arrays may be improved to minimize the collapse of nanorods during the drying process. This improvement will produce a more accurate result from employing these nanorod arrays for photoabsorption studies, as light is more able to reach a greater surface area of the nanorods and are more uniformly absorbed across all TiO_2/Pt nanorod samples. This will in turn improve the accuracy of comparison between samples of nanorod arrays. Surface ligands may be introduced to "repel" individual nanorods, but to what extent will it affect the surface adsorption and light absorption of the photocatalytic nanorods?

In addition to the proposed method of employing nanorod arrays in photoabsorption studies, free TiO_2/Pt nanorods can be suspended in RhB solution in an alternative setup. This may entail

encapsulating free TiO_2/Pt nanorods in a semi-permeable "bag", which functions to allow light through, facilitates the exchange of RhB molecules and catalysed products, and at the same time, prevent the loss of photocatalytic nanorods due to washing processes as samples of RhB solution is being withdrawn for absorption measurements.

The synthetic procedures involving the repeat electrodeposition to achieve a multi-segmented nanostructure consisting of a few segment layers is feasible and simple, but can be highly time-consuming and cumbersome as the number of required segments increases. In this case, an automated system would be useful in facilitating the exchange of electrolyte solution in and out of the cell to achieve multiple segments consisting of the desired material compositions, rinsing of the cell, etc. In another case, a "tipping" device could also be employed for the batch addition of powder hydrogen carbonate to the aqueous solution in the preparation of the $TiCl_3$ precursor bath solution, thus ensuring consistency in the amount of powder hydrogen carbonate added in each batch and the time intervals between each batch addition.

Above all, it is of interest to quantify the photocatalytic efficiency of the as-prepared multi-segmented TiO_2/Pt nanorods for hydrogen production based on the irradiated energy. This can be conducted via a simple setup involving a Plexigas cell or through design of a pilot-scale light-irradiated fluidized bed photoreactor, both of which are presently used in the testing for photocatalytic materials and their functional designs are under constant improvements.

With continuous research and development on new photocatalysts materials, there is promise and hope in the advancements of this "green" technology towards realizing the "dream reaction" for hydrogen evolution- the ability to harness hydrogen production from water and sunlight on a larger scale, thus eventually replacing the production of hydrogen through petrochemical routes; and the generation of power from the produced hydrogen.

Appendix

Appendix 3-1: Derivation of graph and error bars in figure 3-3

From current-time plot, total charge passed= area under I-t graph

Total no. of moles of deposited specie, N= Q/zF

Total mass of species deposited, m= N*Mr

Assume 10^9 to 10^{11} pores/cm^2,

Total no. of nanorods, n = Area of AAM used for deposition * 10^9-10^{11} nanorods.cm^{-2}

Mass of 1 nanorod, m_1= m/n

Based on derivation of Faraday's law of electrodeposition, theoretical length of nanorod, $L=4QM/Fz\rho\pi d^2$

1. At each applied voltage of -0.1 V, -0.2 V, -0.3 V, -0.4 V and -0.5 V, theoretical lengths of Pt, L are calculated from the equations presented above.

   e.g. At applied voltage of -0.1 V

   -According to current-time plot in figure 3-4A, total charge passed for deposition of Pt (iii) = area under I-t graph= 1.49 C

   -Density of Pt=21. 45 g cm^{-3}

   Assume no. of pores/cm^2=10^9, area of deposition=0.79 cm^2

   Theoretical length of 1 Pt nanorod = $4.44*10^{-15}$/ $(7.86*10^{-15})$=5.65 μm

2. Actual length of Pt measured from figure 3-3A (averaged over 20 Pt nanorods) = 1.46 μm
3. Corresponding standard deviation (95% Confidence Interval) (over 20 Pt nanorods)= 0.10 μm and represents the error bar shown in figure 3-3.
4. % Charge efficiencies = Actual Pt length/ Theoretical Pt length = 1.46/5.65 = 26.0 %
5. Similarly, values of actual length of Pt and % charge efficiencies at -0.2 V, -0.3 V, -0.4 V and -0.5 V are obtained by repeating steps 1-4.

Appendix 3-2: 'Life-time' calculation of [$PtCl_6^{2-}$] precursor solution

Total volume of 1 Pt nanorod $= \pi r^2 h = (3.142)\left(\frac{200*10^{-7}}{2}\right)^{-}(15*10^{-6}) = 4.71*10^{-19}\ \mathbf{m^3}$

Mass of 1 Pt nanorod= ρ*v= $(21.45\ \frac{g}{cm^3} * (10^{-2})^3\ \frac{cm^3}{m^3})(4.71*10^{-19})\ m^3 = 1.01*10^{-23} g$

Total mass of 10^{11} nanorods = $(1.01*10^{-23})*10^{11} = 1.01*10^{-12}$ g

Total no. of mols of Pt deposited= $\frac{M}{Mr} = \frac{1.01*10^{-12} g}{195.07\ g/mol} = 5.17*10^{-15}\ mols$

From $PtCl_6^{2-} + 2H_2O \rightarrow Pt(0) + 6Cl^- + 4H^+ + O_2$

No. of moles of $PtCl_6^{2-}$ consumed= **no. of moles of Pt deposited=** $5.17*10^{-15}\ mols$

Initial no. of moles of $PtCl_6^{2-}$ present in a freshly prepared Pt solution

$= \frac{M}{Mr} = \frac{0.55\ g}{561.87\ g/mol} = 0.098\ mols$

(Initial no. of moles of $PtCl_6^{2-}$ - no. of moles of $PtCl_6^{2-}$ consumed)/ **Initial no. of moles of** $PtCl_6^{2-}$

$$\frac{\textbf{Initial no. of moles of } PtCl_6^{-2} - \textbf{no. of moles of } PtCl_6^{-2} \textbf{ consumed}}{\textbf{initial no. of moles of } PtCl_6^{-2}} \leq 1$$

$$\frac{(0.0979) - (5.17*10^{-15})x}{0.0979} \leq 1$$

By iteration, $x \approx 10^9$ **(nearest integer)**

Appendix 4-1: Derivation of plot and error bars in figure 4-3

From current-time plot, total charge passed= area under I-t graph

Total no. of moles of deposited specie, N= Q/zF

Total mass of species deposited, m= N*Mr

Assume 10^9 to 10^{11} pores/cm^2,

Total no. of nanorods, n = Area of AAM used for deposition * 10^9-10^{11} nanorods.cm^{-2}

Mass of 1 nanorod, m_1= m/n

Based on derivation of Faraday's law of electrodeposition, theoretical length of nanorod, $L=4QM/Fz\rho\pi d^2$

1. At each deposition time of 1 h, 2 h, 3 h and 5h, theoretical lengths of TiO_2 (deposited from $TiOSO_4$ precursor), L are calculated from the equations presented above.

   e.g. For TiO_2 deposition time of 1 h

   -According to current-time plot in figure 4-4A, total charge passed for deposition of TiO_2 = area under I-t graph= 3.14 C

   -Density of TiO_2 = 4.23 g cm^{-3}

   -Assume no. of pores/cm^2=10^{11}, area of deposition=0.79 cm^2

   -Theoretical length of 1 TiO_2 nanorod = 14.67 μm

2. Actual length of TiO_2 nanorod measured from figure 4-3a (averaged over 100 TiO_2 nanorods)= 9.30 μm
3. Corresponding standard deviation (95% Confidence Interval) (averaged over 100 TiO_2 nanorods)= 2.21 μm and represents the error bar shown in plot (i) figure 4-3.
4. Similarly, values of length of Pt at 2 h, 3 h and 5 h are obtained by repeating steps 1-7.

Appendix 4-2: Derivation of plot and error bars in figure 4-3

From current-time plot, total charge passed= area under I-t graph

Total no. of moles of deposited specie, N= Q/zF

Total mass of species deposited, m= N*Mr

Assume 10^9 to 10^{11} pores/cm^2,

Total no. of nanorods, n = Area of AAM used for deposition * 10^9-10^{11} nanorods.cm^{-2}

Mass of 1 nanorod, m_1= m/n

Based on derivation of Faraday's law of electrodeposition, theoretical length of nanorod, $L=4QM/Fz\rho\pi d^2$

1. At each varying charge of 0.93 C, 2.77 C, 3.31 C and 6.36 C passed, theoretical lengths of TiO_2 (deposited from $TiCl_3$ precursor), L are calculated from the equations presented above.

   E.g. for TiO_2 deposition time of 0.93 C

-According to current-time plot in figure 4-14A, total charge passed for deposition of TiO_2 = area under I-t graph= 0.93 C

-Density of TiO_2 = 4.23 g cm^{-3}

-Assume no. of pores/cm^2=10^{10}, area of deposition=0.79 cm^2

-Theoretical length of 1 TiO_2 nanorod = 2.32 μm

2. Actual length of TiO_2 nanorod measured from figure 4-3a (averaged over 100 TiO_2 nanorods)= 1.52 μm
3. Corresponding standard deviation (95% Confidence Interval) (averaged over 100 TiO_2 nanorods) = 0.16 μm and is represented by the error bar shown in plot (i) figure 4-3.
4. Similarly, values of length of Pt at 2.77 C, 3.31 C and 6.36 C are obtained by repeating steps 1-3.

Appendix 5-1: Estimation of % Pt in TiO_2 segment of Pt-TiO_2-Pt nanorod system

From current-time plot, total charge passed= area under I-t graph

Total no. of moles of deposited specie, N= Q/zF

Total mass of species deposited, m= N*Mr

Assume 10^9 to 10^{11} pores/cm^2,

Total no. of nanorods, n = Area of AAM used for deposition * 10^9-10^{11} nanorods.cm^{-2}

Mass of 1 nanorod, m_1= m/n

Based on derivation of Faraday's law of electrodeposition, theoretical length of nanorod, $L=4QM/Fz\rho\pi d^2$

1. Theoretical length of Pt, L calculated from the equations above.

-According to current-time plot in figure 5-7, total charge passed for deposition of Pt (iii) = area under I-t graph= 1.43 C

-Density of Pt = 21.45 g cm^{-3}

-Assume no. of pores/cm^2=10^9, area of deposition=0.79 cm^2

-Theoretical length of 1 Pt nanorod = $4.26*10^{-14}/(7.86*10^{-15})$ =5.42 μm

2. Based on 33.2% charge efficiency of Pt deposition, expected length of Pt = 33.2%*5.42 = 1.80 μm

3. Actual length of Pt (iii) as shown in figure 5-7A (averaged over 20 Pt nanorods) = 1.71 ± 0.13 μm
4. Difference in expected and actual length of Pt ≈ 0.088 μm
5. % Pt (iii) in TiO_2-(ii) segment ≈ 5 %

Appendix 6-1: Derivation of rate constant, k

Rate constants, k in this chapter are derived by the following steps:

1. Data for absorbance values from 0 to 5.5 h are taken with respect to peak values from respective absorption spectrum as indicated in figure A.

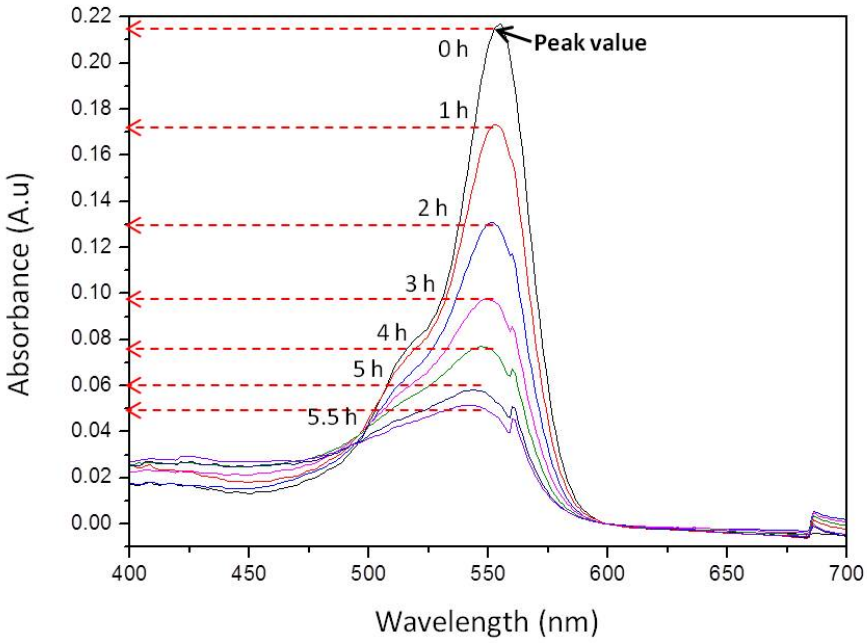

Figure A: Absorption spectra for RhB degradation on Pt-TiO_2 bi-segment nanorods with TiO_2 length segment of 3.5 μm

2. Absorbance values are normalized to 1 by dividing respective absorbance by initial absorbance value presented at 0 h.
3. Assuming RhB degradation to be of first-order reaction, expressed by the following exponential decay equation A1:

$A = A_O e^{-kt}$ (Equation A1)

Where A = absorbance at a particular time of measurement

A_o = Initial absorbance at 0 h

k = rate constant of RhB degradation under illumination

t= time duration of RhB degradation

4. Integrating first-order rate equation A1,

   ln [A] = - k t + ln [A_o] (Equation A2)

5. ln [A] is plotted against t to give a best fit line where the rate constant, k can be obtained from the slope of the linear graph

Table A: Conversion of normalized absorbance values obtained from absorption spectra to ln[C]

Time/ h	Absorbance/ A.u	Normalized absorbance/ A.u	ln[A]
0.0	0.217	1.000	0.000
1.0	0.173	0.797	-0.227
2.0	0.131	0.604	-0.505
3.0	0.097	0.447	-0.805
4.0	0.077	0.355	-1.036
5.0	0.058	0.267	-1.319
5.5	0.051	0.235	-1.448

6. Standard errors of k are generated by the Origin software (data shown in figure B) and are represented in the y-axis error bars in figure 6-10, section 6.4.3.

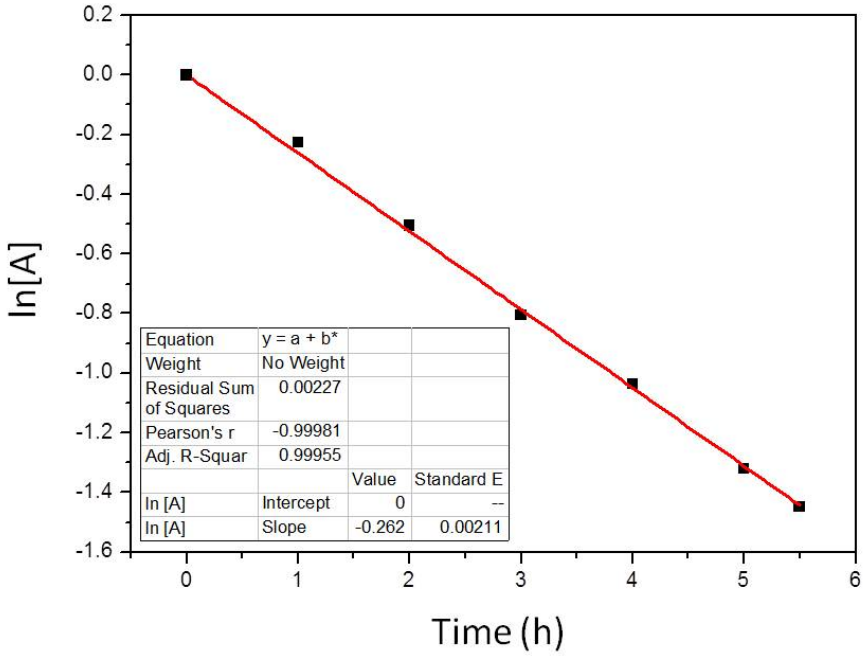

Figure B. Linear plot (best fit) of ln [A] against time duration of RhB degradation. Details of plot are generated using the Origin software